Doctoral Dissertation

Joachim Lundberg

Image-based sizing techniques for fire water droplets

Telemark University College
Faculty of Technology

Joachim Lundberg

Image-based sizing techniques for fire water droplets

Thesis for the degree of Doctor Philosophiae

Telemark University College
Faculty of Technology

Telemark University College

Telemark University College
Faculty of Technology
Department of Process-, Energy and Environmental Technology
Postboks 203
N – 3901 Porsgrunn

www.hit.no

Doctoral Dissertations at TUC
PhD Thesis 2015:5

ISBN 978-82-7206-402-9
ISSN 1893-3068
Printed by the Copy Center TUC - Bø

Abstract

The Norwegian petroleum industry has developed a standard for the technical safety of offshore installations (NORSOK S-001, 2008). When dimensioning accidental load with this standard, the deluge or fire water spray may be considered as a risk reducing measure for equipment and pipes, but not for the structural elements or fire partition (NORSOK S-001, 2008). Proper documentation of the suppression effect and reliability has to be provided when water is used as a fire risk reduction measure in risk evaluation. The standard states that the deluge system shall be automatically activated upon confirmed gas detection when used for explosion mitigation.

Full-scale fire experiments with fire on offshore platforms are limited by practical and economic considerations. Instead, numerical simulations are used for risk analyses. To get a good representation of the effect of the fire water deluge system, the properties of the water spray need to be known.

In the literature, the availability of data on fire water spray is limited. Often the spray is described only by the orifice diameter of the fire water nozzles and spray angle. However, the flow properties of the spray (i.e., size and velocity distribution of the droplets) are known to influence the suppression efficiency. Small droplets will follow the convective forces in the gas flow, evaporate quickly, cool the fire gases and screen for heat radiation. In contrast, large droplets have high momentum and are more likely to reach the source of the fire and to cool objects such as process equipment and pipes.

Presently the most used technique for measuring droplet size and velocity in fire water spray is the Phase Doppler Anemometry (PDA). This technique will provide online measurements of both size and velocity at the same time, but the technique has some limitations and practical problems.

In this doctoral thesis, a laser-based shadow-imaging technique by a high-speed camera and a laser is used. To analyze the shadow-images, an in-house image-processing tool in Matlab has been developed to find droplet size- and velocity distribution.

The results from the experiments in this thesis show the location in the spray to have a large effect on the water flux($dm^3/(m^2 \cdot min)$), i.e. the water flux is not uniform and varies with water supply pressure. The geometry of the nozzle and the frame arms affects the applied water flux extensively at low pressures. This effect is taken into account when the applied water flux is measured.

The results show the water pressure to have the following effects:

- The radial coverage will decrease with increasing water supply pressure
- The applied water flux will be less uniform for different azimuthal angles at low water pressures than at high water pressures. The number of large droplets will decrease with increasing pressure
- The velocity of the droplets will in general increase with increasing pressure.

The research provides unique experimental data of droplet size- and velocity distribution for the fire water nozzle and an image processing software to analyze shadow-images from a laser-based shadow-imaging technique.

The results have been facilitated for adoption to CFD-tools.

Acknowledgements

The research project has been carried out at Telemark University College (HiT), Faculty of Technology in cooperation with Tel-Tek. The financial support of Statoil ASA is gratefully acknowledged.

I want to thank my professor Dag Bjerketvedt for excellent guidance and for our discussions on various topics. Thank for always giving good support when I was struggling.

I would also like to thank my co-Supervisors, Associate Professor Knut Vågsæther and Associate Professor Marius Lysaker. I appreciate all the knowledge you contribute to my research.

I want to give a special thanks to Stian Høiset and Ole Kristian Sommersel, my contacts at Statoil ASA. I appreciate all your help and support.

I want to thank Comput IT for being helpful.

These people deserve a big thanks: André Gaathaug, Per Morten Hansen, Mathias Henriksen, Eivind Fjeldalen and Talleiv Skredtvedt.

Without the support of my family this task would not be possible. So a big thanks to my wife Maria for help and understanding. And of course my two kids Lukas and Jørgen, you're the best.

Porsgrunn, July 2015

Joachim Lundberg

Table of contents

Symbol list

Latin symbols:

Symbol	Description	Unit
A	Area of droplet	[µm^2]
B	Background of an image	
C	Penalty matrix	
d(…)	Differential	
d_{10}	Arithmetic mean diameter	[µm]
d_{32}	Sauter mean diameter	[µm]
d_{43}	De Brouckere mean diameter	[µm]
DV_{50}	Volume median diameter	[µm]
d	Diameter of particle or droplet	[µm]
inf	In-focus parameter	
I	Original image	
J	Background subtracted image	
K	Nominal discharge coefficient	[dm^3/(min$\sqrt{bar(g)}$)]
l	Line through a droplet	
n	Number of droplets of a certain size	
N	Total number of droplets	
p	Position of droplet in image number $i-1$	
P	Position of all droplets in image number $i-1$	
p_w	Supply water pressure	[bar(g)]
q	Position of droplet in image number i	
$\dot{q}_{tot}$	Water flux of all the droplets	[dm^3/(m^2·min)]
Q	Position of all droplets in image number i	
$\dot{Q}_s$	Volumetric flow of water to the nozzle	[dm^3/min]
q^*	Estimated position	
r	Position of droplet in image number $i+1$	
R	Position of all droplets in image number $i+1$	
t	Threshold value	
T	Thresholded image	
$\bar{v}$	Mass-averaged velocity	[m/s]
v	Droplet velocity	[m/s]
v^*	Estimated velocity	[m/s]

w	Predicted movement of droplet
x, y	Position in image
Y	Gray scale value of pixels at line l

Greek symbols:

Symbol	Description	Unit
α	Acceleration term in Λ	
δ, λ, γ	Constants in penalty matrix C	
Δ	Smoothness penalty matrix	
ε	Vector of $\partial\Omega$	[µm]
Γ	Area difference penalty matrix	
Λ	Velocity penalty matrix	
σ	Normalized deviation in ε	
ς	Min divided by max of ε	
$\partial\Omega$	Distance from center to perimeter in a droplet	[µm]

Subscripts/superscripts:

c	Critical value
i	Image number in the movie
j	All the droplets in a movie
k	Number of pixels on the droplet perimeter
k, l, m	Number of droplets in $i-1, i$ and $i+1$, respectively
n	Number of images in the movie
w, e	Crossing of a line l and the perimeter of a droplet

Abbreviations:

CFD	Computational fluid dynamics
COM	Center of mass
CVL	Copper vapor laser
DOF	Depth of field
FOV	Field of view
GUI	Graphical user interface
HSE	Health, safety and the environmental
PDA	Phase Doppler Anemometry
PIV	Particle image velocimetry
TV	Total variation
VC	Value of contrast

Chapter 1

Introduction

1.1 Background

The Norwegian petroleum industry has developed a standard for the technical safety of offshore installations (NORSOK S-001, 2008). When dimensioning accidental load with this standard, the deluge or fire water spray may be considered as a risk reducing measure for equipment and pipes, but not for the structural elements or fire partition (NORSOK S-001, 2008). In risk evaluation, proper documentation of the suppression effect and reliability has to be provided when water is used as a fire risk reduction measure. The standard states that the deluge system shall be automatically activated upon confirmed gas detection when used for explosion mitigation.

Full-scale fire experiments with an actual fire on offshore platforms are limited by practical and economic considerations. Instead, numerical simulations are used for risk analyses. To get a good representation of the effect of the fire water deluge system, the properties of the water spray need to be known.

In the literature, the availability of data on fire water spray is limited. Often the spray is described only by the orifice diameter of the fire water nozzles and spray angle. However, the flow properties of the spray (i.e., size and velocity distribution of the droplets) are known to influence the suppression efficiency. Small droplets will follow the gas flow, evaporate quickly, cool the fire gases and screen for heat radiation. In contrast, large droplets have high momentum and are more likely to reach the source of the fire and to cool objects such as process equipment and pipes. In explosion mitigation, the sizes of the droplets are important where small droplets can contribute to extinction and the large droplets have a high inertia and can reduce the local gas velocities (Thomas 2000; Bjerketvedt & Bjørkhaug 1991). Thus, to evaluate the efficiency of a deluge system it is necessary to know the size and velocity distribution of the droplets.

Presently, the most used technique for measuring droplet size and velocity in fire water spray is the Phase Doppler Anemometry (PDA). This technique will provide online measurements of both size and velocity at the same time, but has some limitations and practical problems. Measurement errors regarding non-spherical droplets is one of the most crucial problems (Wighus, 2012).

A method not requiring spherical droplets is shadow-imaging. This method is based on a high-speed camera capturing movies of the spray. The light source is placed behind the spray relative to the camera, showing the droplets in focus as shadows.

To expand the knowledge of fire water sprays, this PhD project will find the size and velocity distribution of the spray from a commonly used fire water nozzle. This is the Tyco MV34-110 medium velocity fire water nozzle. Instead of doing field measurements, an experimental rig is made for testing the fire water nozzle. The rig is equipped with all the necessary measurement equipment.

A laser-based shadow-imaging technique will be used with a high-speed camera and a laser. This technique basically captures movies of the spray, and the information is extracted from the movies by analyzing the movies frame by frame. Typically, the number of frames to be analyzed are several millions. This requires an automatic routine for the extraction process.
The automatic routine is an image processing software. The droplets will be recognized and the properties measured. One of the challenges in shadow-imaging is the depth of field (DOF). The DOF is the thickness of the focus plane. A large droplet can be further away from focus than a small droplet and still be recognized. This has to be taken into account by the image processing software.

This PhD project will develop an image processing program instead of using commercially available ones. This will have advantages in overview and control of the solving algorithm.

This project is in the field of process safety and can be applied to industrial risk evaluations in general.

1.2 Objective

The main objective of this PhD project is to determine characteristic data, such as droplet size- and velocity distribution, from a typical medium velocity fire water nozzle (Tyco MV34-110). The results will be used as input data for computer simulations, such as the CFD software KFX® by ComputIT.

The strategy was:

1. Build a test rig with a fire water nozzle.
2. Use high-speed camera and shadow-imaging with a high frequency laser.
3. Measure the spray properties at various locations for different water pressures.
4. Develop in-house image processing tool in Matlab to find droplet size- and velocity distribution.

The novelty of the project can be summarized as follows:

- Provides unique experimental data based on high-speed shadow-imaging.
- All the measurement equipment is placed outside the fire water spray to preserve the fluid dynamic properties of the flow (non-intrusive).
- An image processing software developed exclusively for fire water spray. The code will be addressed exclusively to the fire water images to tune the parameters optimally.

- The user will have control of the algorithm in the image processing software to monitor the behaviour and check the accuracy.
- The droplet tracking will be done with a Hungarian algorithm based on three frames. The tracking will be solved as an assignment problem using a penalty function based on the physical properties of the spray.

The measurements will output size and velocity distributions from the spray in addition to other parameters, like mean diameter and spray direction.

1.3 Organization of thesis

The thesis is organized as follows:

- Chapter 2: The related previous research is presented in this chapter. The chapter presents different techniques for measuring droplets in sprays, how to measure the "K-factor" of a nozzle, and some background information on image processing in sprays.

- Chapter 3: This chapter presents the making and design of the experimental rig. It also presents detailed information on all the equipment used. An HSE plan is made for the project and presented here.

- Chapter 4: This chapter presents the image processing software and how the code is developed. It presents how the equipment is calibrated and how it is implemented.

- Chapter 5: This chapter presents the experimental results.

- Chapter 6: The chapter shows how the experimental result is converted into input for to CFD-software.

- Chapter 7: Conclusion.

- Chapter 8: Implications for further research.

Chapter 2

Related previous research

Droplet sizes in sprays from sprinklers and deluge nozzles have been measured by several papers (Yu 1986; Jackman 1992; Sheppard 2002). The droplet sizes are important to know when calculating the suppression efficiency of fire water spray. Larger droplets can penetrate the fire plume and smaller droplets can cool the fire gas and screen for heat radiation.

This chapter will give a brief introduction to the parameters and distributions used for describing the fire water spray. Some techniques have been developed to measure droplet size- and velocity distributions, and these are explained in this chapter. One of the parameters describing the fire water nozzles is the nominal discharge coefficient or the "K-factor". The process for finding the "K-factor" is also described in this chapter. Finally, this chapter contains some methods for image processing of droplets.

2.1 Measurement parameters and distributions

When describing sprays, it is always convenient to use a representative or mean diameter. This diameter is intended to represent the physics of the spray.

The usage of the different mean diameters is related to the application area. The arithmetic diameter is used for comparisons, the Sauter mean diameter is used for mass transfer and reactions and the De Brouckere mean diameter is used for combustion equilibrium. Sauter mean diameter is the sum of the volume of droplets divided by the sum of surface areas. This will give a mean diameter with the same volume to surface area as the volume to surface area of the whole spray (Grant et al., 2000).

Table 2.1 shows how the different mean diameters are calculated. The notation is taken from the general expression for discrete distributions

$$d_{pq} = \left[\frac{\sum_{j=1}^{\infty}\left(n_j d_j^p\right)}{\sum_{j=1}^{\infty}\left(n_j d_j^q\right)}\right]^{1/(p-q)} . \qquad (2.1)$$

Another commonly used representative diameter is the volume median diameter, D_{V50}. This is the diameter where half of the volume is contained in the droplets with a larger diameter (Grant et al., 2000).

Table 2.1: Methods for calculation of mean diameters

Type of Mean Diameter	Equation
Arithmetic mean	$d_{10} = \frac{1}{N}\sum_{j=1}^{N} n_j d_j$
Sauter mean	$d_{32} = \frac{\sum_{j=1}^{N} n_j d_j^3}{\sum_{j=1}^{N} n_j d_j^2}$
De Brouckere mean	$d_{43} = \frac{\sum_{j=1}^{N} n_j d_j^4}{\sum_{j=1}^{N} n_j d_j^3}$

In a fire water spray, the cooling process of the flue gases and the quenching of chemical reactions are the essential mechanisms. The Sauter mean diameter will be the key parameter for this. It balances the convective heat transfer (a function of the surface area) to the heating of the droplet (a function of droplet volume) (Sheppard, 2002). The De Brouckere mean diameter describes the weight of the droplets (Lefebvre, 1989). D_{V50} is the key parameter for water distribution in sprays.

The water-flux is the amount of water per area and time that can be found from the images from the experiments by using

$$\dot{q}_{tot} = \sum_{j=1}^{N} \frac{\pi d_j^3 v_j}{6FOV \cdot DOF_j} \tag{2.2}$$

to calculate the total flux in every image (Zhou et al., 2012). $\dot{q}_{tot}$ is the water flux of all the droplets in the image, d_j and u_j are the diameter and velocity of a single droplet in the image. FOV is the field of view of the image (the height and width of the image). DOF_j is the depth of field. It is a droplet size and lens dependent parameter. FOV multiplied with DOF_j is a volume. Since the water flux measurements are for discrete locations, they are interpolated to find the fluxes at all positions. The total amount of water in the spray is summed up to be compared with the amount of water being put into the nozzle.

The range of droplet sizes in the fire water spray is often represented by a distribution. The distribution can be expressed by analytical expressions. The most used expression is the Rosin-Rammler (or Weibull) distribution, originally developed for coal particles (Grant et al., 2000). Other distributions like log-normal can also be used (Sheppard, 2002).

Sheppard (2002) has not found any correlation between the measured data and analytical expressions for droplet distribution. The parameters for the analytical expressions of the distribution change for all locations of the spray. Sheppard (2000) claims the only method of determining droplet size distribution is to do measurements at multiple locations of the spray at a variety of supply water pressures.

The velocity of the droplets is known to be size dependent. But for droplets with the same size is expected to have a varying velocities. This implies all the droplet sizes at a given location in the spray to have a separate velocity distribution. To give a representative velocity distribution all the droplets are divided in droplet size intervals (can be referred to as classes or phases). A mass-averaged velocity is found by

$$\overline{v_j} = \frac{\sum d_j^3 v_j}{\sum d_j^3} \tag{2.3}$$

for every droplet size interval and the mass-averaged velocity is related to the droplet size. In (2.3) n_j is the number of droplets in droplet size interval and v_j is the velocity of the droplets. The velocity is in general shown to increase with increasing droplet diameter (Tolfo, 1976).

2.2 Early studies of droplet distributions

In the early studies of droplet size distributions in deluge spray, they used a method of either freezing the droplets in liquid nitrogen or isolating them in glycerol and counting them manually afterwards. This method had a problem with the largest droplets scattering and the smallest droplets agglomerating. Still-photography was also used to analyze the spray, but this was highly time consuming and not accurate (Yu, 1986).

2.3 Electro-optical technique

Knollenberg (1970) published an article on an electro-optical technique for measuring size distributions of droplets in clouds and precipitate particles. This technique was based on a linear array of photodetectors on one side of a measurement cell or probe and laser-light on the other side pointing towards the detectors. When a particle or droplet passed between the laser light and the photodetectors, the light would be scattered and the detectors sensed less or no light. The number of photodetectors that sensed less or no light in a row, represent the diameter of the droplet.

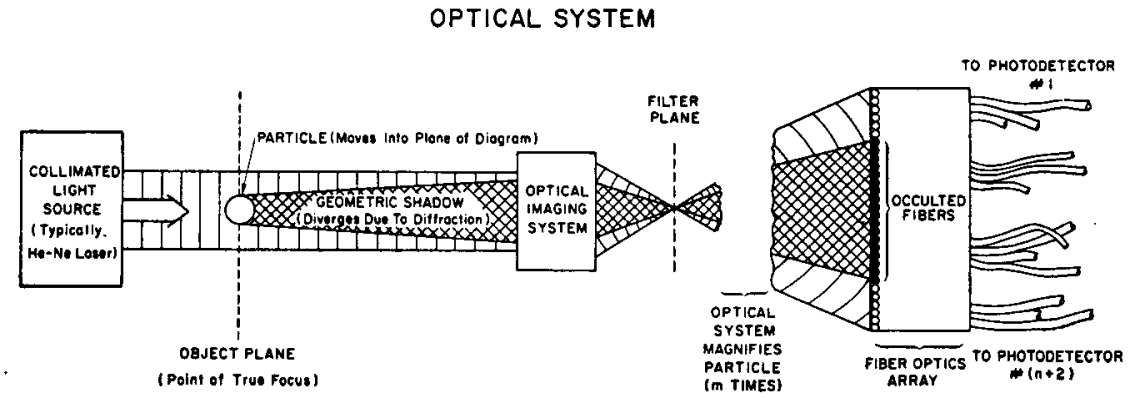

Figure 2.1: Probe setup for Knollenberg's experiment. Image taken from Knollenberg (1970).

Figure 2.1 shows a conceptual illustration of the probe used in Knollenberg (1970). It shows the light source that is typically a laser, the optical imaging system and the coupling to the sensors. The sensors were large photomultipliers instead of small photodiodes and had to be placed in a rack and be coupled to the optical system with fibre optics. The diffraction of the light and depth of field, gave a gradient between the shadow of the droplet and the light passing through. The gradient that was handled by a fully analog logic circuit given a threshold value

to give a binary value to a register. This was done for all the array and over time the droplets or particles were counted and the size and velocity determined (Knollenberg, 1970).

The equipment from Knollenberg's paper was acquired by FM-Global research in the late 70's where the probe, software and hardware were modified to measure on sprinkler spray. It could measure droplets in the range of 100 to 6000 µm with the step size of 30 µm (Yu, 1986). It was measured on selected sprinklers at 3.05 and 6.10 meters below the nozzle. Yu (1986) found droplet size distribution for the selected sprinklers. One example from the research is shown in Figure 2.2.

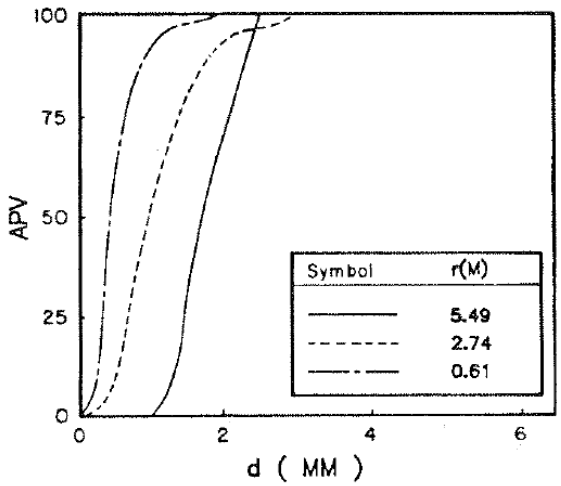

Figure 2.2: Radial variation of droplet size distribution in a common upright sprinkler at 2.06 bar(g) located 3.05 meters below nozzle from (Yu, 1986). APV is the accumulative percent by volume.

2.4 Phase Doppler Anemometry

At about the same time as Knollenberg (1970) presented the electro-optical system, Durst and Zaré (1975) presented the method of Phase Doppler Anemometry (PDA) for suspended spherical particles.

The original setup by Durst and Zaré (1975) used for visualization of the fringe pattern for large particles is shown in Figure 2.3.

The PDA has two purposes. It measures the velocity and the size of the droplets using two different principles. The velocity is measured with a "Laser Doppler technique" and the size is measured according to the Lorentz-Mie theory.

The "Laser Doppler technique" method uses two intersected phase-shifted laser beams. This will make a measurement volume with an optical interference pattern. When a particle or droplet passes this volume, the interference pattern will be affected. This is called a "Doppler burst" and can be related to the velocity of the particle or droplet (Husted, 2007).

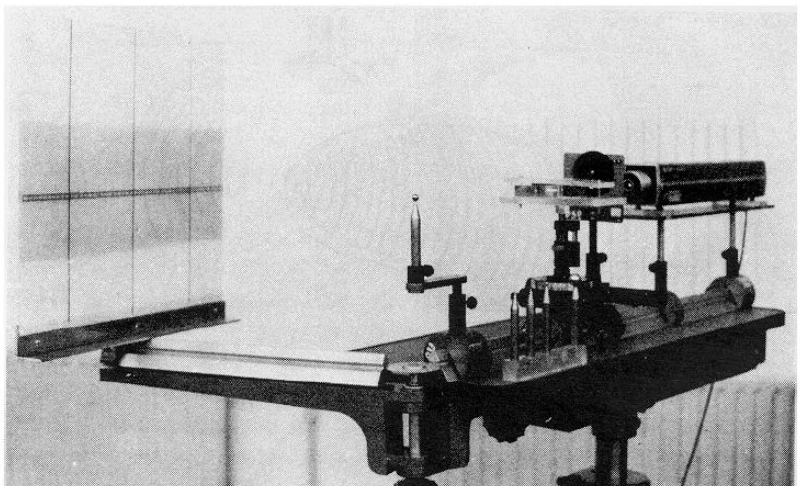

Figure 2.3: The setup used by Durst & Zaré (1975) for visualization of fringes produced by large particles. Image is from Durst & Zaré (1975).

The Lorentz-Mie theory is describing the scattering of an electromagnetic wave (in this case laser-light). An illustration of how the PDA works is in Figure 2.4. The incident light ray is both reflected and refracted given that the particle or droplet is somewhat transparent to the wavelength of the light. The illustration shows that the incident light rays will be reflected and refracted in different directions dependent on where they hit the droplet or particle. If two or more sensors measure the light rays at the same time, the frequency shift of the light is a measure of the difference in length the light has travelled. The frequency shift is then related to a diameter assuming spherical shape.

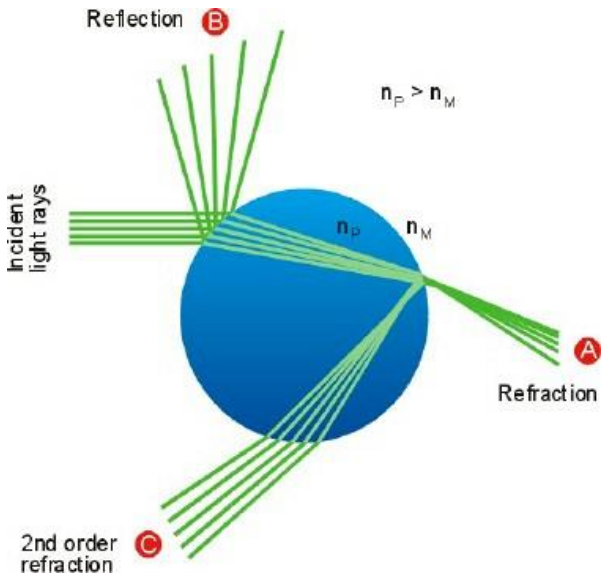

Figure 2.4: Principle of scattering of light in a spherical droplet. Image from Dantec (2014)

Widman (2001) used Phase Doppler Anemometry for characterizing some residential sprinklers and studied the effect of varying the water pressure. It was found that the outer region of the spray was dominated by the large droplets due to insufficient momentum in the smallest droplets. The theoretical relation between the mean droplet size and the water pressure given by Yu (1986) was found to be of limited validity. Figure 2.5 shows the experimental setup used in the article by Widman (2001).

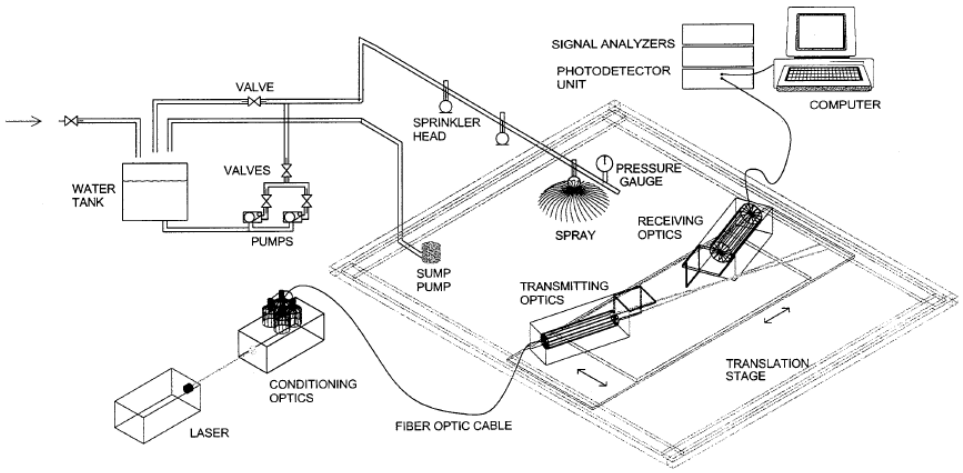

Figure 2.5: Experimental setup used by Widman (2001) using PDA technique. Image is from Widman (2001).

Sheppard (2002) found the velocity field and droplet sizes for many commercially available sprinklers using particle image velocimetry (PIV) and Phase Doppler Anemometry (PDA). The goal of this work was to find the characteristics of sprinkler spray required by computational models. PIV was used to measure the velocity field close to the nozzle and PDA was used a certain distance from the nozzle to measure the droplet size distribution. It was found that in general sprinkler spray the largest number of droplets were less than 250 µm and that most of the water volume were in the droplets larger than 300 µm. In some of the experiments, it was found that a few large droplets contained a dominant fraction of the water in the spray. Dundas (1974) postulated that the volumetric median droplet size would be found proportional to the inverse cube root of the Weber number of the flow, times a constant. Sheppard (2002) found this constant to be dependent on both sprinkler design and location in spray.

Figure 2.6 is a typical result from Sheppard (2002) and shows droplet size distribution from one of the cases. The figure shows both the graph of the cumulative (number) percentage and the volume percentage. By comparing the cumulative number of droplets and the volume percentage, it is found that 50 % of the volume of the droplets represent nearly 100 % of the number of droplets. This points out the important role of the largest droplets in the spray and the uncertainties they can make. Sheppard (2002) used the same experimental setup as Widman used shown in Figure 2.5.

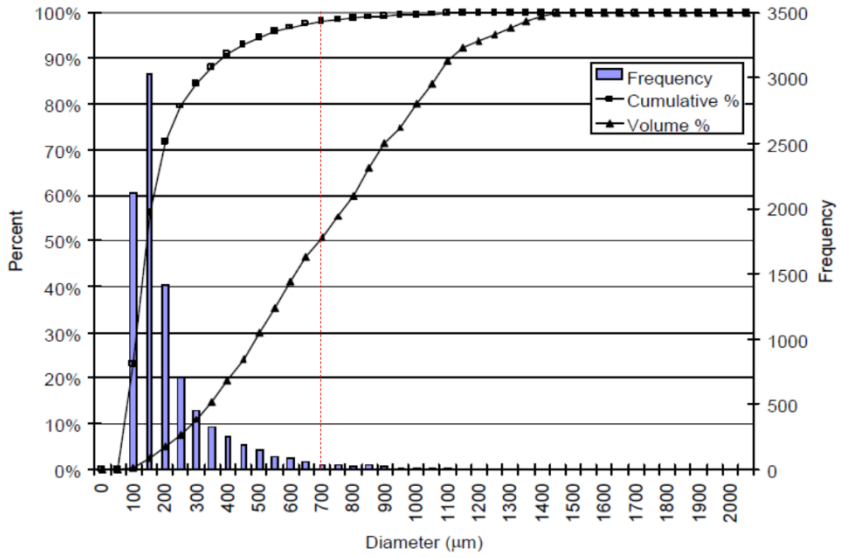

Figure 2.6: Droplet size distribution with both histogram and cumulative percentage for a typical nozzle from Sheppard (2002). A red line indicates where 50 % of the volume of droplets is.

In reports (Wighus 2012; Sæbø & Wighus 2015), medium velocity nozzles for fire water spray have been characterized by various techniques. In Wighus (2012), two parallel tests were performed at two different laboratories. Size- and the velocity characterization of the spray was performed using PDA techniques. The two results had some discrepancies regarding droplet distribution.

Wighus (2012) comments on the usage of PDA technique for fire water spray and claims that the technique may give unrealistic droplet sizes if droplets are non-spherical.

2.5 Analog film techniques

Jackman (1992) used a laser-based shadow-imaging technique to characterize sprinkler nozzles similar to Yu (1986), but instead of using a photodetector-array, Jackman used a high-speed camera with 16 mm analog film. The laser used for backlight in the experiments was a copper vapor laser that pulsed continuously up to 10 kHz. The camera was a film based rotating prism camera capable of capturing 10 000 frames per second at full resolution. To analyze the frames, the photographic film was projected onto a monitor. A crosswire linked with an electronic positioning device was superimposed onto the monitor to quantify the droplet size and velocity. The procedure was done for all droplets in every movie. The degree of focus was determined by the operator. 30 000 droplets were registered in the study by Jackman (1992).

Analog film was used because digital imaging was not yet common.

Figure 2.7 is taken from an analog film from one of Jackman's experiments. It shows a droplet moving from image to image. The black vertical line in the image is a 500 µm thick hypodermic needle used as a sizing standard.

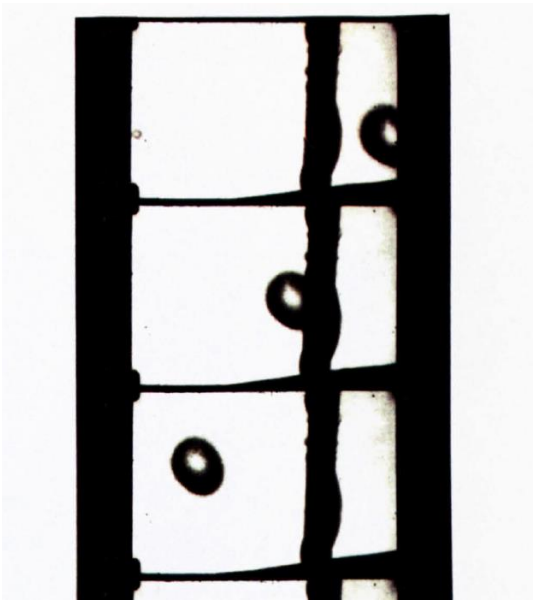

Figure 2.7: Photograph of a part of an analog film showing a typical droplet. The black vertical line is a sizing standard. The figure is from Jackman (1992).

2.6 Laser-based shadow-imaging

Ren et al. (2011) used a laser-based shadow-imaging technique for characterization of sprinkler spray. The equipment used was a digital camera with a high-speed laser from LaVision. This study measured the droplet size- and velocity distribution of the droplets in the spray. Figure 2.8 shows the setup used for the experiments.

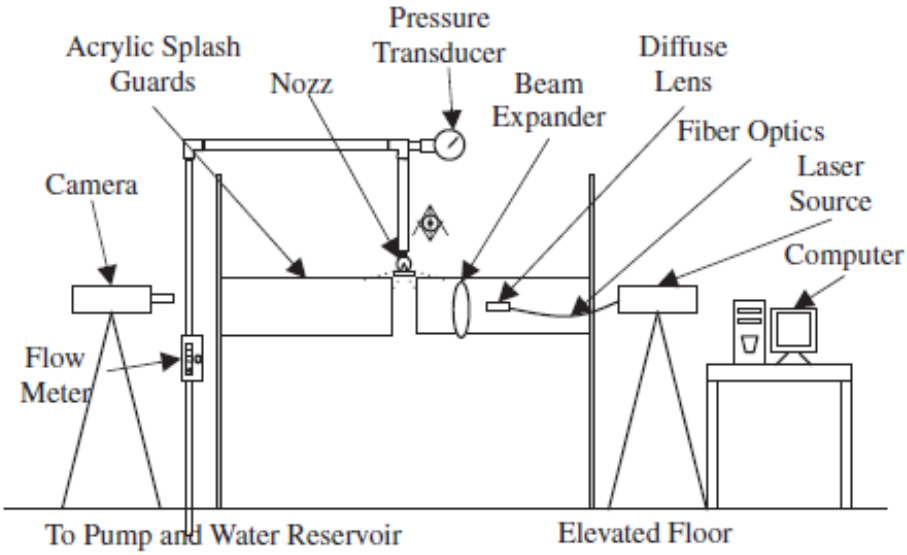

Figure 2.8: Experimental setup of laser-based shadow-imaging from Ren et al. (2011).

The basic principle of shadow-imaging is that the camera will have a narrow depth of field that will make a sheet of droplets in focus while droplets in front of or behind this sheet will be blurred away. The thickness of the DOF sheet is dependent on the size and has to be calibrated

as explained in Chapter 4.3. The laser-based shadow-imaging technique used by Ren et al. (2011) uses acrylic splashguards that will remove some of the droplets in front and behind the DOF.

Ren et al. (2011) found a strong connection between sprinkler geometry and spray pattern. This means the measurements were highly dependent on location in spray. The article included determination of analytical functions for implementation of sprinkler data in CFD tools.

Zhou & Yu (2011) investigated the dependence of the sprinkler geometry on the spray formation in sprinklers at low pressures. It was used custom-made sprinklers with geometrical variations like deflector plate diameter or slot thickness. Figure 2.9 shows an image from the experiment. The results from this study are intended to be used for quantifying geometrical features of sprinklers.

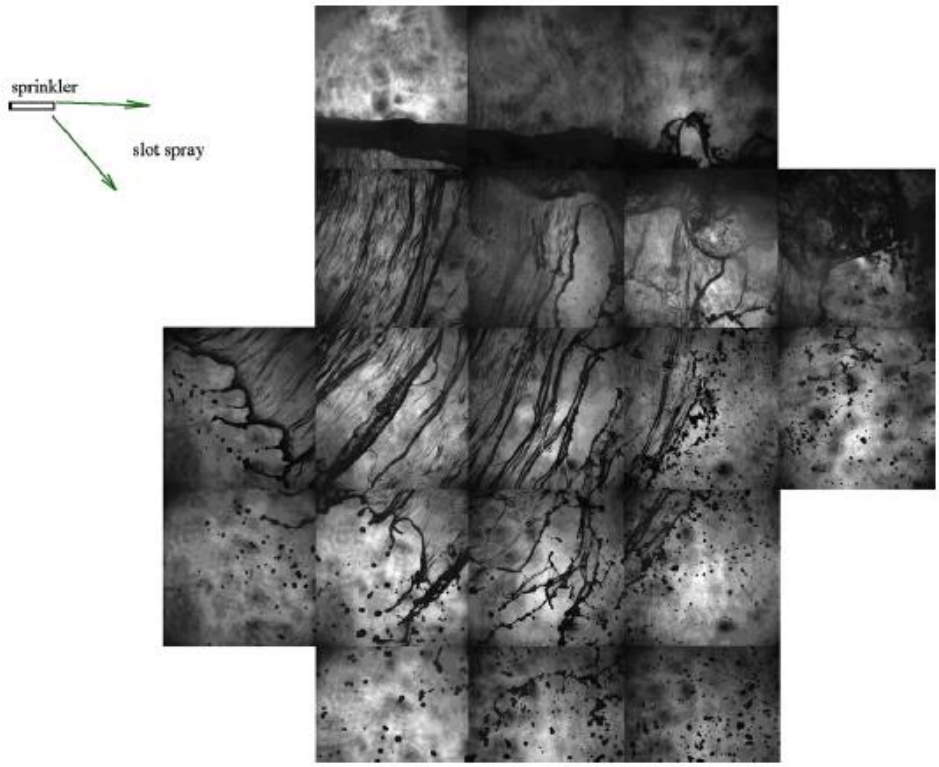

Figure 2.9: Illustration of breakup from a fire water nozzle. From a study to investigate geometrical variations in sprinkler construction. Image is from Zhou & Yu (2011).

Zhou et al. (2012) used a laser-based shadow-imaging method to characterize the spray from a sprinkler spray in the near and far field of the sprinkler tip. The near field measurements provided input that could be used in numerical fire models. An array of water collectors equipped with pressure transducers were used to manually measure the volume-flux. This was compared to the volume-flux from the shadow-imaging method.

Recently, Zlatanovic et al. (2014) published characterization of residential sprinkler spray at low water pressures. It showed a strong dependence of the sprinkler geometry, and a small dependence on water temperature on the initial spray characteristics. The paper shows good

agreement between calculated and experimentally determined droplet sizes, given some assumptions.

Sæbø & Wighus (2015) concludes that it seems like the shadow-imaging technique is the most appropriate measurement technique for fire water spray.

2.7 K-factor measurement

The fire water nozzles are designed to provide a known flow rate at a given pressure. To relate the flow rate to the pressure, Bernoulli's orifice equation is rewritten to

$$\dot{Q}_s = K\sqrt{p_w}\,. \tag{2.4}$$

where $\dot{Q}_s$ denotes the volumetric flow of water, p_w is the supply water pressure (gage) and K is the nominal discharge coefficient known as the fire water nozzle "K-factor" (Sheppard, 2002).

Two commonly referred standards for testing the "K-factor" are "Approval Standard for Sprinkler System Alarm Test Devices" by FM-Approvals (2009) and ISO 6182-1:2004 (ISO-Standard, 2004). Both the standards do not specify:

- whether the pressure is the gauge- or absolute pressure
- whether the water is fresh, salt or has other additives
- the temperature of the water

The pressure is assumed to be gauge pressure, the water is assumed to be fresh with no addition and the temperature is assumed to be room temperature.

FM-Approvals (2009) does the tests in the pressure interval from 1.75 - 12.05 bar with 0.7 bar increments. The pressure is measured in a 6" pipe in front of the nozzle. The number of repetitions at each point is not specified. The "K-factor" is found from the average value.

The ISO-Standard (2004) specifies the pressure tests in the interval from 0.5 – 6.5 bar with 1.0 bar increments. The pressure is measured in a pipe with nominal diameter of 40 mm. The "K-factors" are found by doing the reading from pressures low to high and then the opposite to avoid hysteresis in the nozzle. The "K-factor" shall be calculated both for each point in each series and as an average, where all results shall be within certain boundaries.

2.8 Image processing techniques for analyzing sprays

Image processing techniques are currently being used for analyzing sprays because they are relatively simple and economical compared to other methods like PDA (Koh, 2001). They also have advantages to other techniques regarding non-spherical droplets. However, it can be demanding due to the number of frames to be analyzed to get a statistically meaningful distribution (Lee & Kim, 2004). In shadow-imaging techniques, the depth of field effect is one of the major contributions to measurement error. (Lee & Kim, 2004).

To analyze a large number of images, an automatic method must be applied. Yule et al. (1978) published a method for determining the degree of image focus from the intensity gradient across a droplet shadow-image using an automatic method.

The intensity gradient at the edge of a droplet can represent the distance to the focus plane. When the droplets move from the focus plane, the droplets will be surrounded by a gray "halo". Yule et al. (1978) defined this by two intensity levels and related the diameter of the droplet and the widths of the "halo". This method was later used by others (Fantini 1990; Kashdan et al. 2007). Figure 2.10 is an illustration of Fantini et al. (1990) and shows the principle of the "halo".

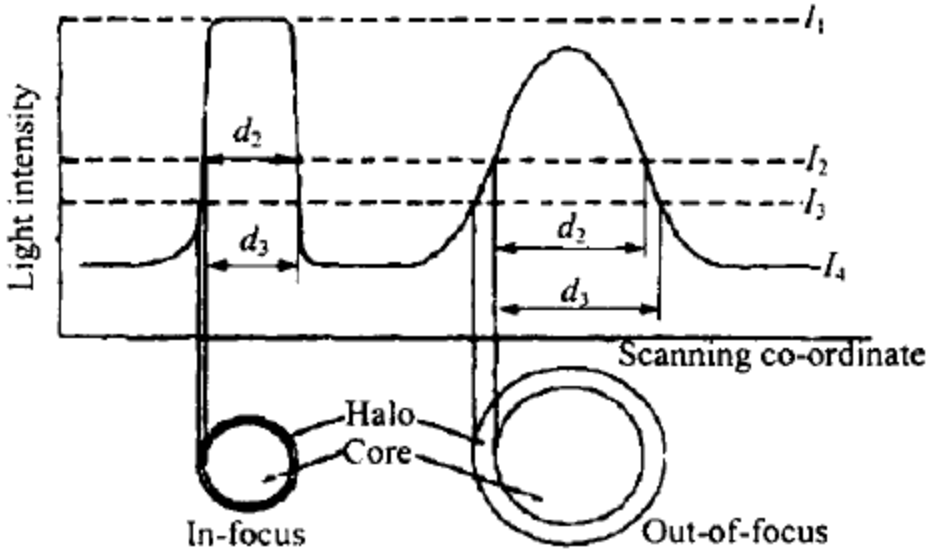

Figure 2.10: Droplet intensity profile with the principles of the "halo" used for describing the degree of focus. Image is from Fantini et al. (1990).

To define the "halo" the relation between the intensities were used:

$$(I_2 - I_4)/(I_1 - I_4) = 0.25 \tag{2.5}$$

$$(I_2 - I_3)/(I_1 - I_4) = 0.12 \tag{2.6}$$

where I_2 and I_3 define the "halo". I_1 is the maximum intensity of the largest in-focus droplet (in an image from a shadow-imaging technique it will be the darkest or minimum of the largest droplet). I_4 is the mean background intensity of the image (Fantini et al. 1990). The original proposition by Yule et al. (1978) was similar to Fantini et al. (1990) but the arbitrary constants of 0.25 and 0.12 in (2.5) and (2.6) were 0.64 and 0.15.

Lecouna et al. (2000) found in a similar way an "in-focus parameter"(inf_c) in a study to find simultaneous measurements of particle sizes and velocities. The inf_c is modeled as explained in Chapter 4.8. Figure 2.11 is from the article by Lecouna et al. (2000) showing the calibration run for known droplet sizes (glass spheres with known diameters).

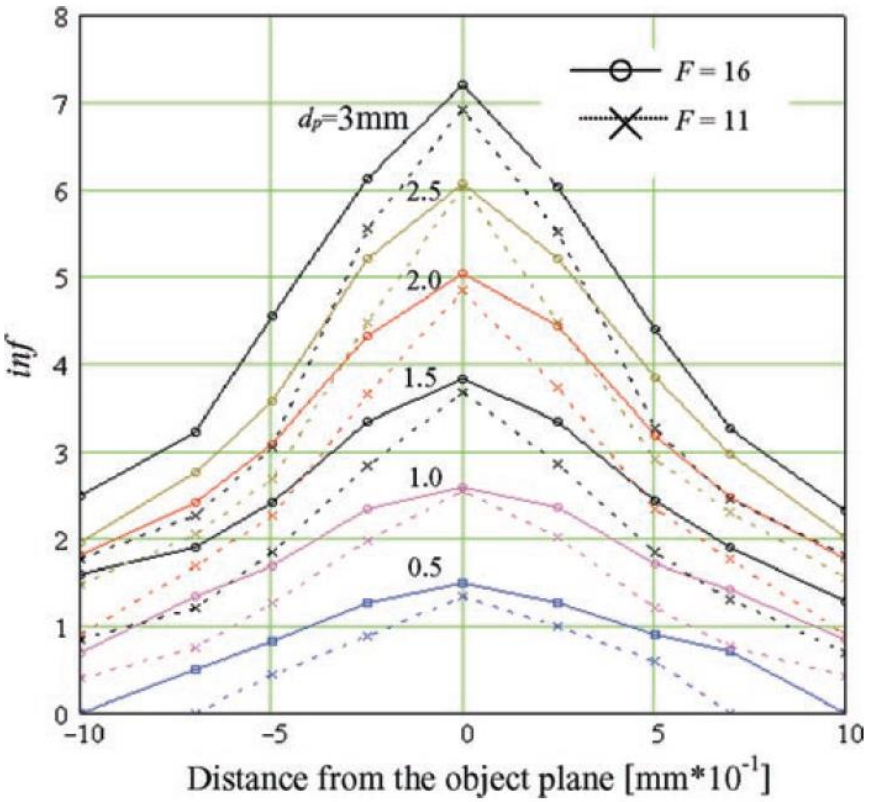

Figure 2.11: Variation of inf with respect to distance to object (focus) plane for different sized particles. Image is taken from Lecouna et al. (2000).

Alternatively, Kim & Kim (1994) defined a concept of the normalized value of contrast (VC) to determine if the droplets are in focus or not. VC can be defined as:

$$VC = \frac{(I_4 - I_1)}{I_4} \tag{2.7}$$

where I_4 and I_1 is defined in the same manner as for (2.5) and (2.6). This criterion is known to be effective for small droplets. Koh et al. (2001) extended this theory to be valid for larger droplets.

Chapter 3

Experimental setup

This chapter will describe how the experimental rig, as shown in Figure 3.2, is made. It gives detailed information about all the utilities of the rig and all the measurement equipment. Two microscope lenses were used in this project. A comparison of these is given here.

A Health, Safety and Environment plan is made to map the different hazards regarding this project and the equipment used.

The experimental setup is located inside a container (see Figure 3.1) and consists of the following equipment: a laser with transmitting optics, a deluge nozzle, a high-speed camera, a long-distance microscope lens, a traverse with nozzle mounting and auxiliary equipment. The deluge nozzle is a Tyco MV34-110 medium velocity nozzle. According to the producer, the nozzle produces a cone-shaped spray that is uniformly filled with medium velocity droplets. The sub image in Figure 3.2 shows a picture of the nozzle.

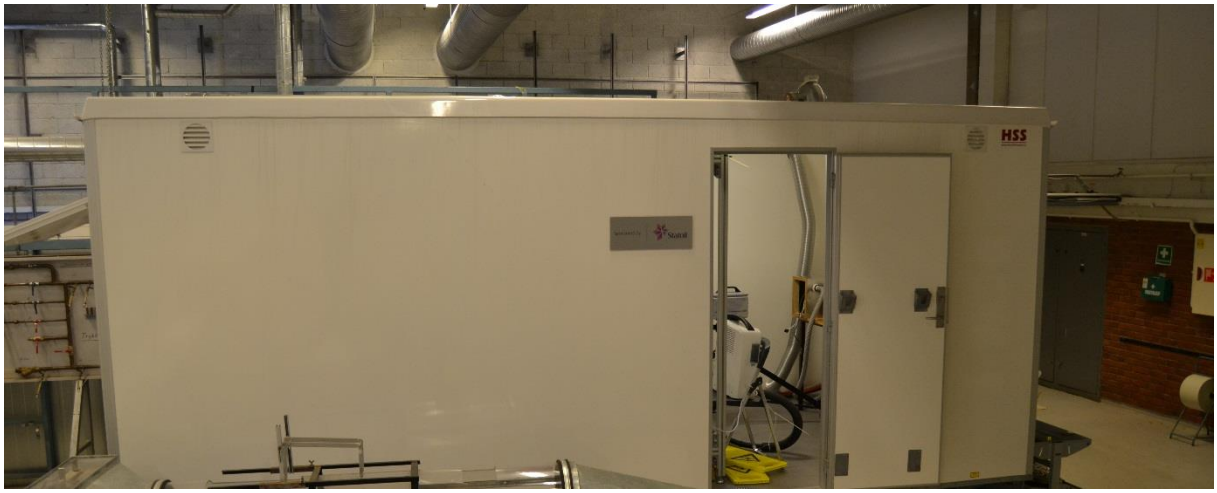

Figure 3.1: The container where the experimental setup is placed.

A high-speed camera with back illumination is used to obtain images of the spray. The back illumination is a copper vapor laser (CVL) from Oxford Lasers. The laser generates short light pulses (25 ns) with high effect (20 W) continually at 12.5 kHz. The camera and laser are synchronized to capture images at 12,500 frames per second. The high-speed camera is a Photron APX-RS monochrome camera. Two high magnification microscope lenses were used (Navitar 12 X with a focus range extender and Questar QM-1). The camera and lens have a narrow focus depth to produce sharp images of droplets in the focus plane with limited visibility of the droplets in front of or behind the plane.

Temperature, pressure, and volumetric flow sensors are mounted on the rig to document the test parameters. The traverse is used to control the position of the nozzle.

The process flow diagram of the setup is shown in Figure 3.3.

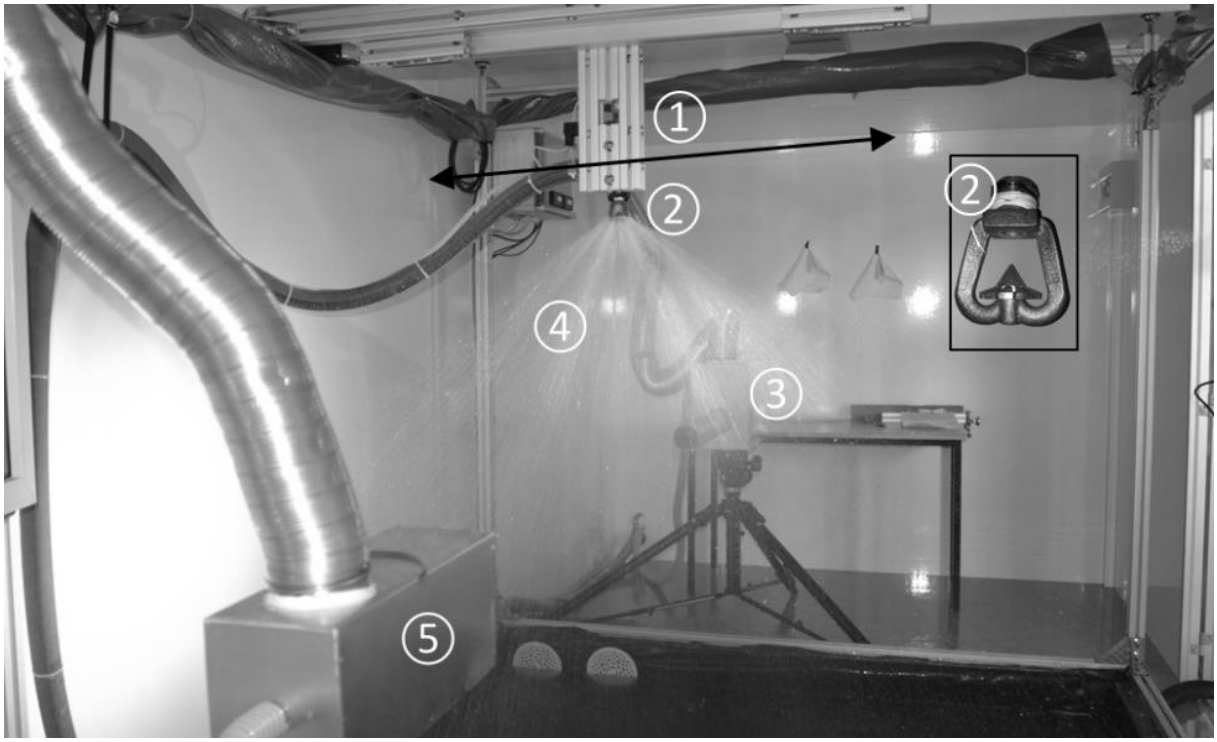

Figure 3.2: The experimental setup for fire water droplet measurement rig: 1) traverse with nozzle mounting, 2) deluge nozzle, 3) high-speed camera and long-distance microscope lens, 4) deluge spray, 5) laser transmitting optics.

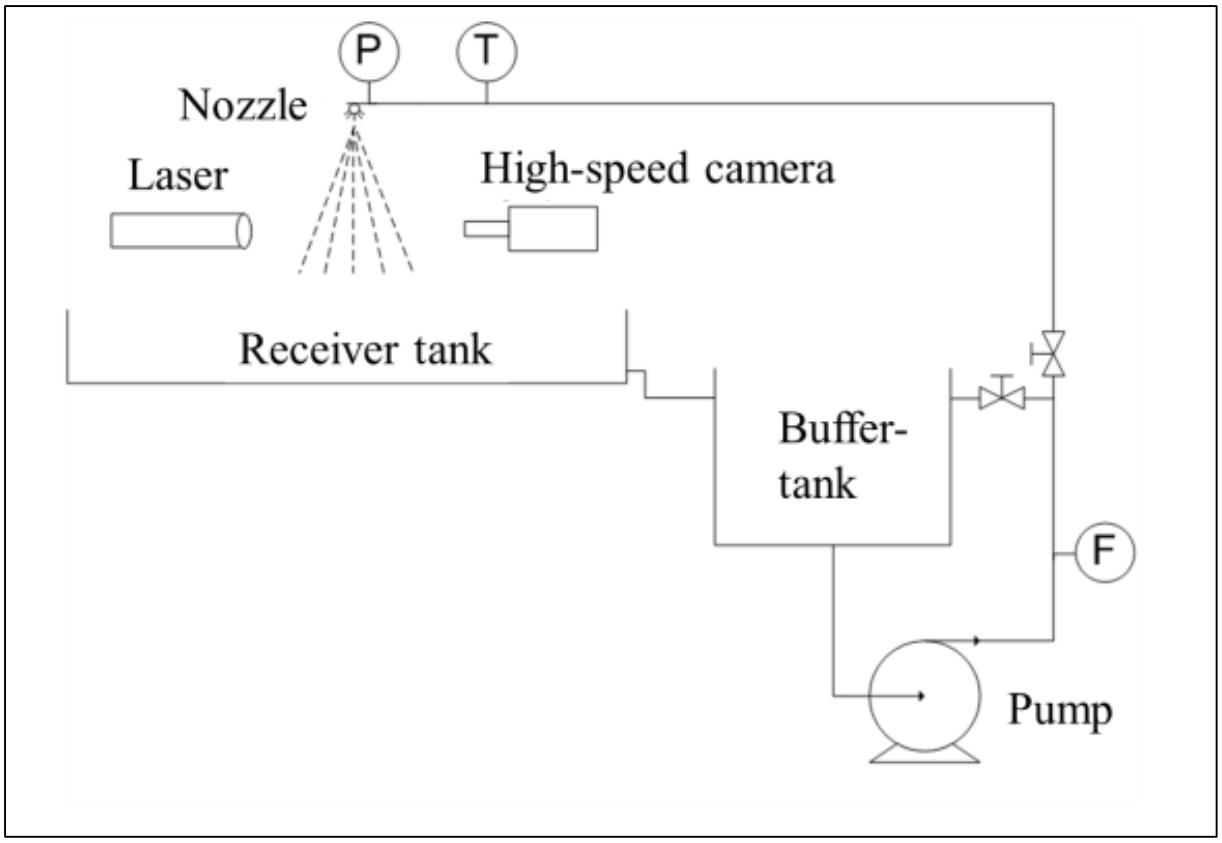

Figure 3.3: Process diagram for the experimental setup.

3.1 Building rig

For measuring the droplet size and velocity distributions, an experimental rig has been made. Technical equipment used in the rig needs to withstand the water from the spray. Figure 3.4 shows the waterproofed cases for the camera and laser diffusor. The laser is placed in a separate room and fiber optic cables connect the laser to the optics on the rig.

The equipment is built inside a container to prevent laser light from entering the room. The computer-controlled nozzle positioning system is shown in Figure 3.5. Utilizing the positioning system, the laser and high-speed camera can be kept still, and the nozzle can be moved to capture images from all radial positions of the spray. The azimuthal angle is controlled manually by rotating the nozzle. Pressure, temperature and volume flow sensors are mounted to measure the conditions of the supply water flow. The accuracy of the measurement equipment is discussed in Chapter 5.6.

Figure 3.4: Waterproof cases for camera and laser diffuser.

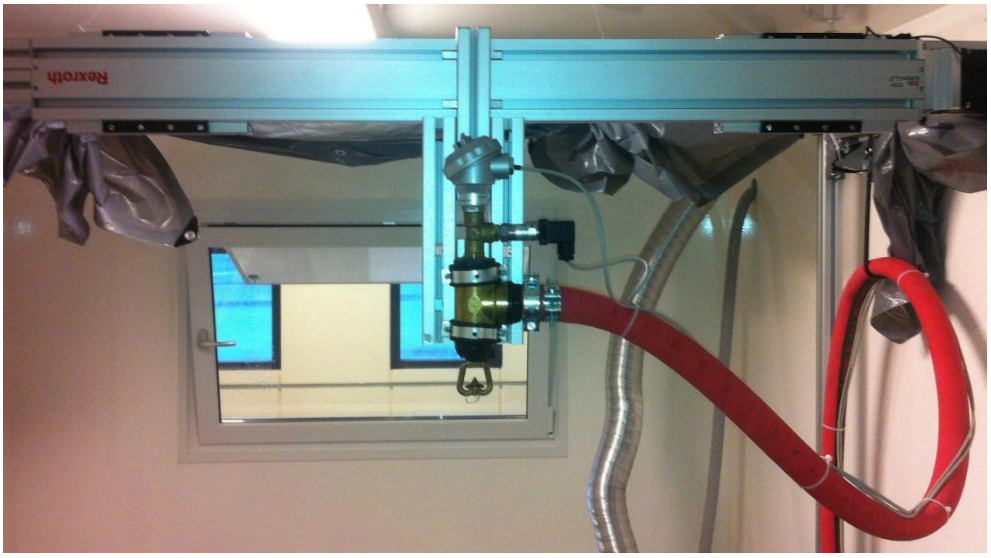

Figure 3.5: Positioning system with fire water nozzle applied.

3.2 Pump

The pump, an Ebara EVML10-10N5/4,0kW, is used to supply water from the buffer tank to the nozzle. It is a ten step centrifugal pump with a maximum head pressure of 11.0 bar(g) and maximum volumetric flow rate of 250 dm^3/min. The pump has an ABB frequency converter to control the effect to the pump. It reduces the effect by reducing the frequency of the electric current. The pump curve is shown for some frequencies in Figure 3.6 together with the pressure-flow correlation of the Tyco MV34 110 nozzle.

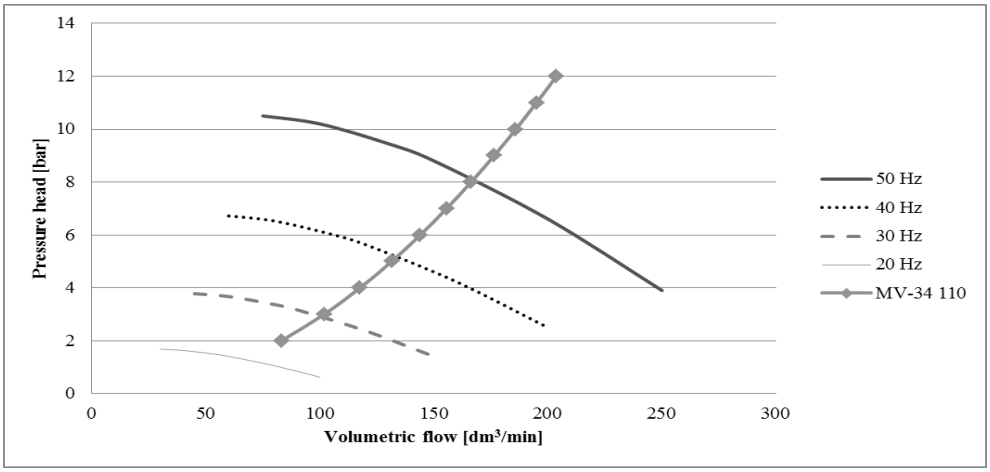

Figure 3.6: Pump curves from the Ebara pump for different frequencies together with the pressure-flow correlation for the Tyco MV34 110 nozzle.

The pump and the frequency converter is mounted on a moveable skid shown in Figure 3.7.

Figure 3.7: Pump and frequency converter on moveable skid.

3.3 Flow measurement

To measure the volumetric flow rate of supply water to the nozzle, a Trimec MP050 positive displacement piston flowmeter is mounted after the pump. Since it is a piston flowmeter, it does not demand developed flow at the inlet for measuring.

The working principle of the flowmeter is that an eccentric ring or piston will be displaced by the liquid. The Trimec MP050 is shown in Figure 3.8. The flow range of the Trimec is 12-330 dm^3/min and the accuracy is 0.5% of the reading.

Figure 3.8: Volumetric flowmeter.

3.4 Temperature sensors

The temperature of the supply water is measured with a PT-100 temperature sensor with a Nokeval temperature transmitter. The temperature sensor is a resistance temperature detector with an accuracy of 1/1 DIN class B. This means ± (0.3+temperature*0.005) °C of the actual temperature. The temperature sensor and the transmitter are shown in Figure 3.9.

3.5 Pressure sensor

A pressure sensor of the type AST 4000 is placed right above the nozzle. The sensor is connected to a pressure transmitter. The accuracy of the sensor is ± 0.25 % of full scale, giving ± 0.04 bar of the read value. The sensor and the transmitter is shown in Figure 3.9.

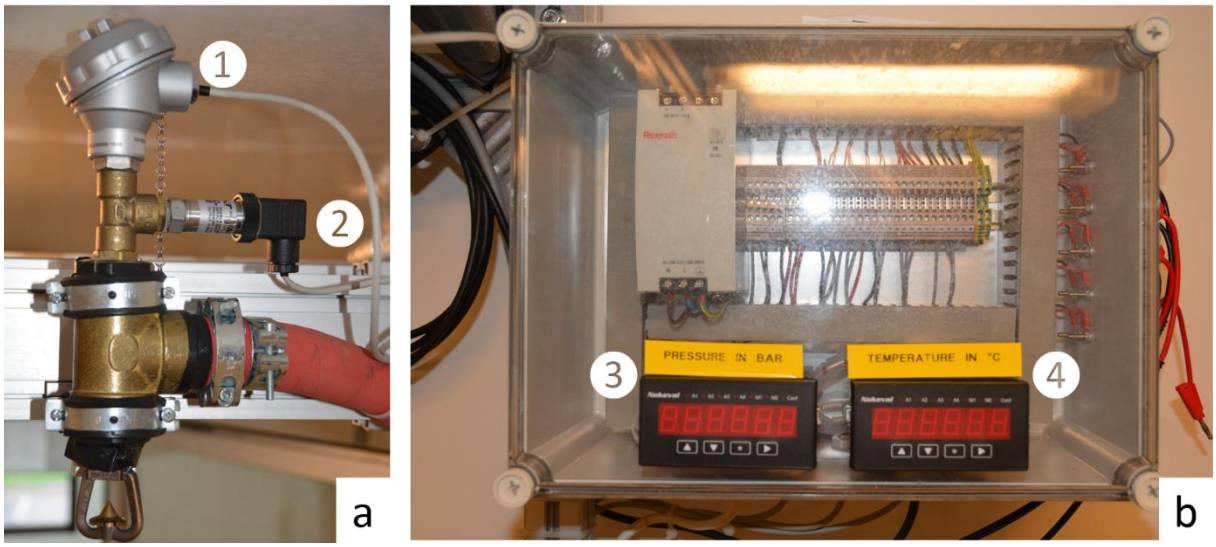

Figure 3.9: a) Temperature sensor (1) and pressure sensor (2) b) pressure transmitter (3) and temperature transmitter (4).

3.6 Nozzle

The nozzle used in this project is a Tyco MV34-110. This is a typical medium velocity offshore nozzle with an external deflector. It provides a uniformly filled cone of medium velocity water droplets. The specifications for the nozzle are found in Table 3.1.

Table 3.1: Specifications for the medium velocity nozzle (Tyco MV34-110).

Parameter	Units	Value
Orifice diameter	mm	9.6
K-factor	$dm^3/(min * \sqrt{bar})$	58.8
Spray angle	deg	110.0
Working pressure	bar(g)	1.4 – 12.1

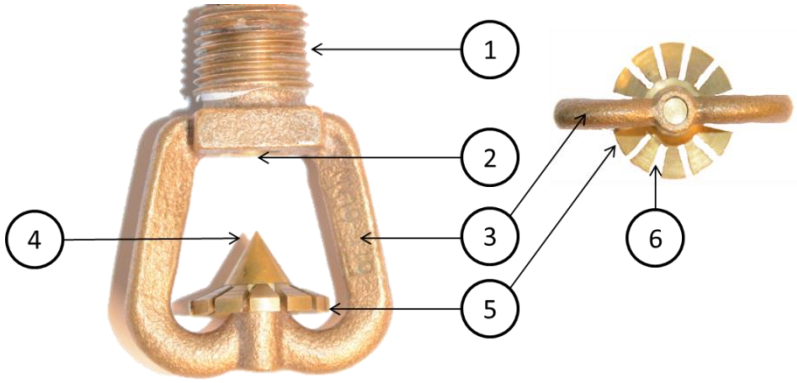

Figure 3.10: Image of the medium velocity nozzle. 1) ½" NPT treaded connection to water pipes, 2) Orifice, 3) Frame arms, 4) Splitter, 5) Deflector plate, 6) Tines.

The medium velocity nozzle, shown in Figure 3.10, consists of a treaded connection that contains an orifice and frame arms that hold the splitter and deflector plate. The deflector plate has 12 tines with 30° angular increase between each tine. The angle between the frame arm and the closest tine is 15°.

Figure 3.11: Medium velocity nozzle before the water is turned on (left), right after (middle) and when the flow is steady (right). The water pressure was 2.0 bar(g).

Figure 3.11 shows the medium velocity nozzle operating. The left image is right before the water is turned on. The central image is right after the water is turned on. Image shows that the water will flow through the tines and some will be spread by the deflector plate. The right image shows established flow where the water flows through the orifice and is directed to the deflector plate by the splitter.

3.7 Camera

The camera used for this project is a Photron APX-RS high-speed camera shown in Figure 3.12. This monochrome camera can capture up to 3000 frames per second at full resolution (1024p x 1024p). It can be used at higher framerates with reduced resolution. The camera has a CMOS sensor with a physical pixel size of 17 µm and a 2 GB memory that can capture about 2000 images at full resolution.

To control the camera, the software Photron FASTCAM Viewer 3 is used. The camera has an internal clock used to synchronize the laser with the camera.

Figure 3.12: Photron APX-RS high-speed camera.

3.8 Laser

The laser used in this project is a Copper vapor laser LS20-50 shown in Figure 3.13. It has high nominal output power (20 W) and short pulse duration (~25 ns). It is a continuous blinking laser with low jitter.

The copper vapor laser will radiate with two different wavelengths: 510.6 nm and 578.2 nm (yellow and green). It is normally operated at 12 500 pulses per second or Hertz (Hz) giving a continuous output, but it can be operated in burst mode up to 50 000 Hz for a limited time.

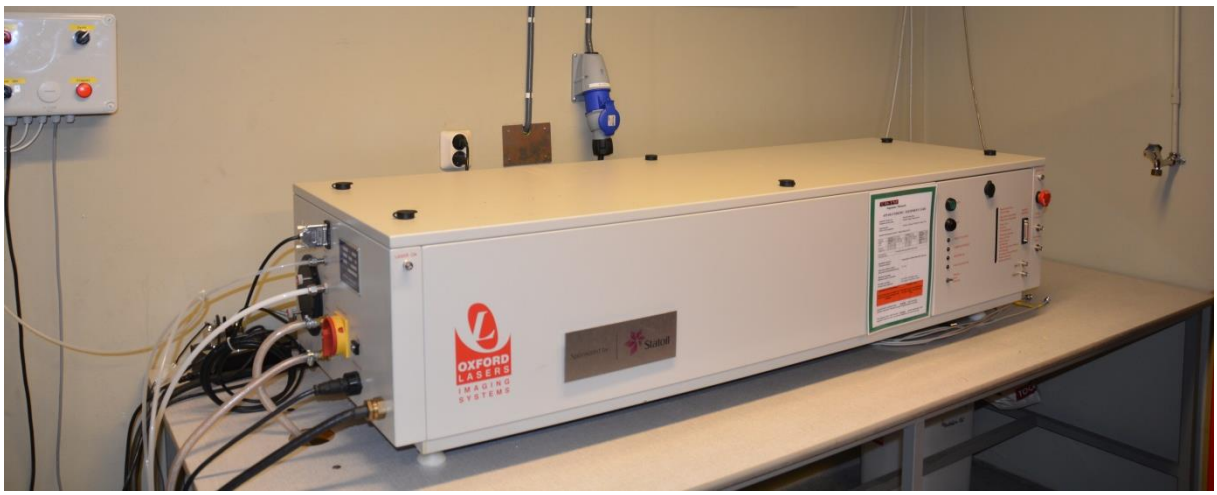

Figure 3.13: Copper vapor laser from Oxford Lasers of the type LS20-50.

The copper vapor laser is highly suited for laser-based shadow-imaging because of the high nominal power and the continuous output.

3.9 Lenses

The droplet sizes in a water spray from a deluge nozzle can range from some tens of µm to some mm. To capture images of this range of droplets, a microscope lens is needed for the high-speed camera. Since the camera should be placed outside the spray, the focus length (distance from the lens tip to the object of interest or focus plane) has to be approximately 100 cm. The crucial factors for a lens in this project are light sensitivity, magnification and depth of field (DOF). The light sensitivity of the camera determines the frame rate and the amount of optical noise. Optical noise is produced by droplets crossing in front of or behind the focus of the lens. The magnification has to be sufficient to get the smallest details of the flow, while at the same time catching the largest droplets.

3.9.1 Navitar 12x zoom

For most of this project, a Navitar 12x zoom high magnification zoom lens with a range extender has been used. This lens can be used with various lens configurations to give the correct magnification at the desired length to focus plane. The magnification can be up to 12 times and is dynamically adjustable. The lens is parfocal, meaning that the focus length will not change when the magnification is adjusted. The lens is normally used for short focus lengths (10 – 30 cm from the lens tip), but in this project the lens has been used with a range extender that extends the focus length up to 100 cm or more. The numerical aperture (N.A.) can be a measurement of the light sensitivity of a lens. The Navitar lens has a typical value for the N.A. of 0.009 at maximum magnification and a focus length of 100 cm. The Navitar lens is shown in Figure 3.14.

Figure 3.14: Navitar 12 X high magnification zoom lens with a range extender.

3.9.2 Questar QM-1

The Questar QM-1 by LaVision is a long distance microscope lens designed to operate at focal lengths from 50-150 cm. An image of the lens is shown in Figure 3.15. It is a Maksutov-Cassegrain Catadioptric mirror based microscope. The principal design of this type of lens is shown in Figure 3.16.

Figure 3.15: Questar QM-1 long distance microscope lens by LaVision.

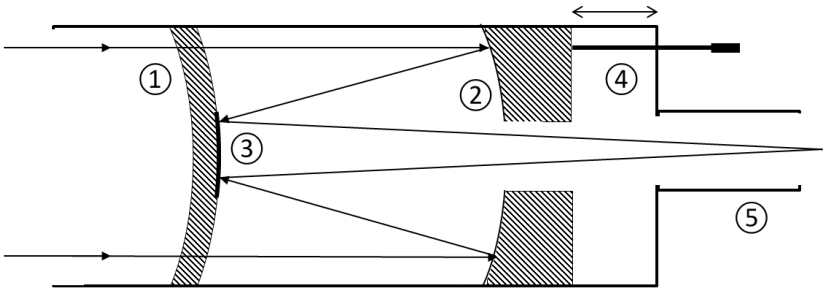

Figure 3.16: Principle of a Maksutov-Cassegrain catadioptric mirror based microscope like the QM-1. The components are: 1) correcting meniscus, 2) primary mirror, 3) secondary mirror, 4) adjustment screw, 5) combinations of lenses and macro rings.

The light will pass through a correcting meniscus lens in the front and to the primary mirror. From this mirror, the light will go to the secondary mirror and out of the back of the lens. At the back of the lens, it is possible to make combinations of macro rings and lenses to adjust the magnification. The distance to the focus plane of the lens is set by the distance between the primary and the secondary mirror.

To set the magnification on the lens, a given configuration of macro rings and lenses has to be used. The lens has to be reassembled to change the magnification, and the focus has to be readjusted.

The QM-1 lens has an alignment torch that simplifies the alignment. The N.A. of the QM-1 is typically 0.04 with the focus length of 100 cm.

3.9.3 Comparison of Questar QM-1 and Navitar 12x zoom

For magnification purposes, the lens needs to give a 1:1 magnification at a distance to the focus plane of 100 cm to give a desired range of droplet sizes. This is possible with both the Questar QM-1 from LaVision and the Navitar 12x-zoom. This is maximum magnification for the Navitar lens. The numerical aperture, N.A., is approximately 0.009 for the Navitar lens and

0.040 for the QM-1 lens. An increase in N.A. will make the lens more light sensitive and the DOF shallower. The decrease in DOF with the QM-1 lens compared to the Navitar lens is shown in Figure 3.17. This figure shows clearly that the QM-1 lens has much shorter DOF than the Navitar 12 X.

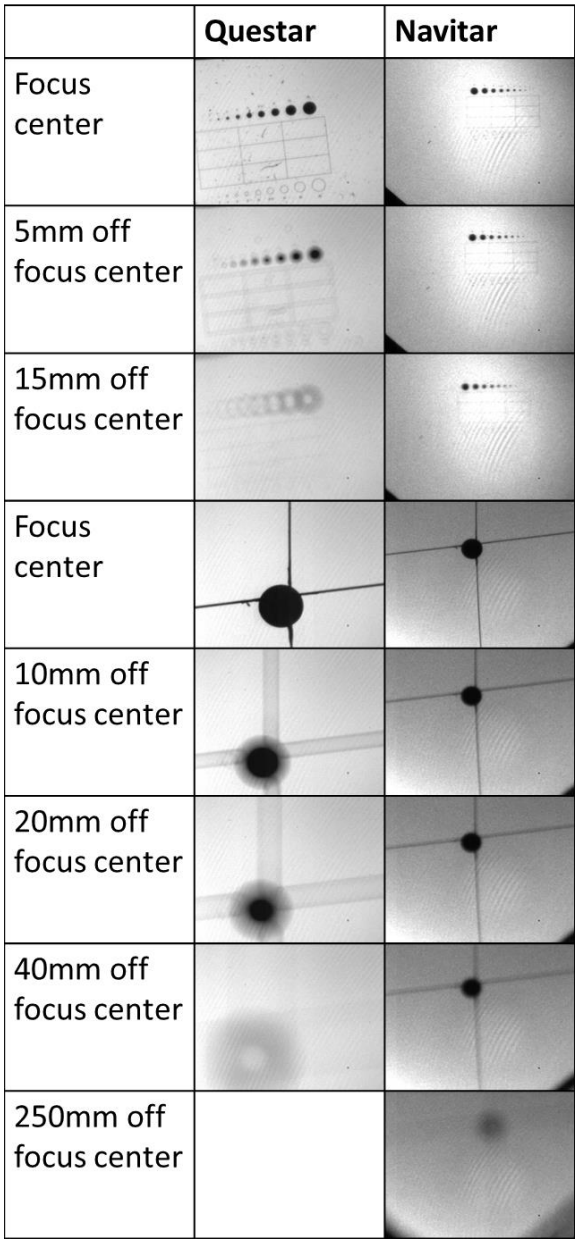

Figure 3.17: Comparison between Navitar 12 X and Questar QM-1.

3.10 HSE

The research equipment acquired for this project had to be adapted to the laboratory. Whenever a new type of equipment is used in a laboratory this represents a risk. To clarify the risk represented by the fire water droplet rig, a HSE-plan for the project was made. The light radiation hazard from the copper vapor laser was considered the highest hazard in the usage of the rig. It was treated by screening the laser equipment from surroundings. The doors were

equipped with interlocks, and warning signs and lights were placed outside every entrance. The number of approved operators of the rig was highly limited, assuring control of modification and possible dangers.

The plan states that the laboratory is a part of university property and uses their procedures when applicable.

Other potential safety risks that were discussed were:

- Personal safety equipment
- Non-radiational dangers regarding lasers
- High voltages
- Electrical work
- Dangers of stumbling
- Pressurized equipment
- Gas bottles
- General fire
- Environmental issues

In addition to the HSE-plan, the sponsors of the project conducted a safety review of the project. The project was reviewed to satisfy the demands of the sponsors regarding HSE & Quality according to the guidelines in NORSOK S-006 (2003).

Minor nonconformities on reporting of events were found during the review.

Chapter 4

Image processing

The flow properties, like droplet size and velocity, generated with a fire water nozzle are known to vary within the spray (Sheppard, 2002). Therefore, to characterize the flow properties caused by a given fire water nozzle, hundreds of movies must be recorded. Each movie is recorded at a given position in the spray. Since each movie typically consists of 8,000-12,000 frames, millions of images need to be analyzed to obtain the velocity- and size- distribution for all locations of the fire water spray within a certain accuracy. Due to the number of images to be analyzed, an automatic post-processing algorithm is required.

The post-processing algorithm is developed in Matlab and uses Matlab image processing toolbox, (Mathworks, 2011). Established and new image processing techniques are used to extract information about the fire water spray from the movies of the droplets. The size of the droplets can be determined by comparing the droplets in the movie to a calibration standard with a known size. The velocity can be found by comparing the position of the droplets in subsequent frames. By recording the measurements of several droplets, it is possible to find the droplet size- and velocity distribution of the spray.

This chapter will explain how the image processing program works. In Chapter 4.1 schematics of the image processing code are represented, and the subsequent chapters explain the different operations of the program.

The image processing code is implemented in a graphical user interphase in Matlab. This will make the code more user friendly and make it have the appearance of a computer program. The graphical user interface is found in Chapter 4.2

The calibration of the Depth of field (DOF) is shown in Chapter 4.3.

4.1 Image processing schematics

A schematic diagram of the image processing code is shown in Figure 4.1, where the number in the parentheses is the section where it is explained.

Frame *i* is read into the image processing code and the common background is found and subtracted from the original image. The new image is binarized, filtered, and the droplets are qualified. A routine in the image processing code will subsequently check the focus of the droplet and register the diameter with DOF. The same is done in the temporally adjacent frames to get the velocities of the droplets. The coupling of the droplets is done by solving an assignment problem that determines the droplets' paths by solving a penalty matrix. The information is recorded and the same is done for all time step intervals.

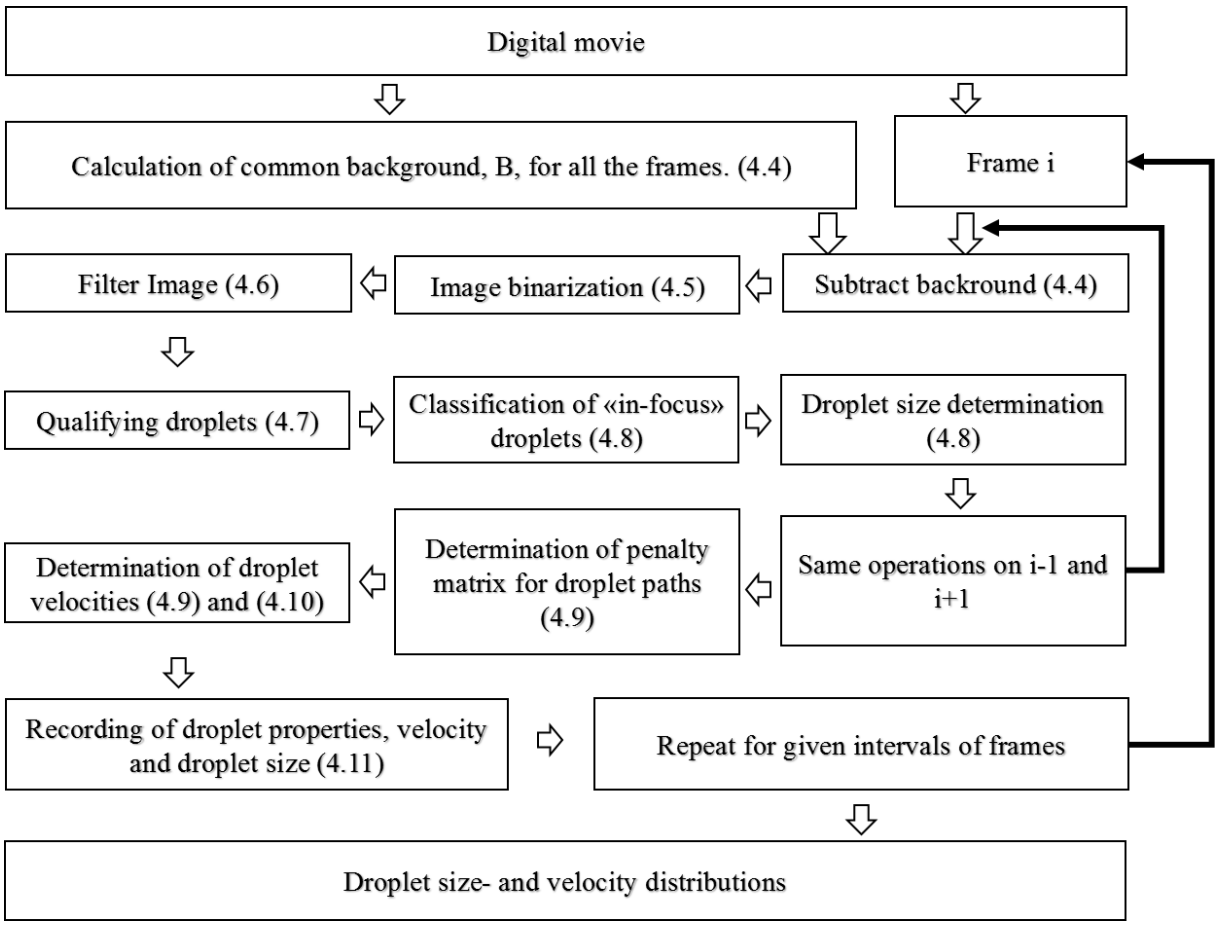

Figure 4.1: Schematics for the image processing code. Numbers in brackets refer to subchapters in the report.

4.2 Image processing software

Graphical user interphases (GUI) for running the image processing code has been developed. The benefit of having a user interface to the code is the flexibility and overview of the output. To separate the operations, the software is divided into three sheets: parameter testing, excluding and results sheet.

The program has been developed to manage the image processing on three parallel images at the same time. This will show how an adjustment will affect three images at the same time to give a more unified impression of how the change will affect the entire movie. Panels are used to group several objects and functions. This is shown by the rectangular frames in the sheet, as shown in Figure 4.2.

The following chapters will explain the purpose of the three sheets of the software.

4.2.1 Image processing program: Parameter testing

The parameter testing sheet will complete the following operations: background subtraction, filtering, binarization and pre-qualifications of the velocity field. The sheet is shown in Figure 4.2

The first panel is the “Image reading” panel. Here the movie file is defined and the original image is displayed. It can read either random frames from the movies or fixed images.

The next panel is the “Filters, Background Removal and Thresholding” panel. Here the image will evolve when clicking the buttons on the right hand side in the figure. The “Remove background” button will remove the background. This is explained in Chapter 4.4.

“Noise const. removal” will set all pixels higher than the limit to be background. The “TV-filter” uses total variation filter on the images, and the constants can be adjusted. The filters used are explained in Chapter 4.6.

The “Thresholding” button will threshold or binarize the image. This is explained in Chapter 4.5.

The “Sphericity Check” box evaluates the shape of the droplets, explained in Chapter 4.7.

“Display” is just for illustrational purposes. It is possible to display the original or the output image from all the operational stages and superimpose the contours of the thresholded image or the thresholded image after the sphericity check.

The last panel is for prequalification of the velocity field and is just for illustrative purposes.

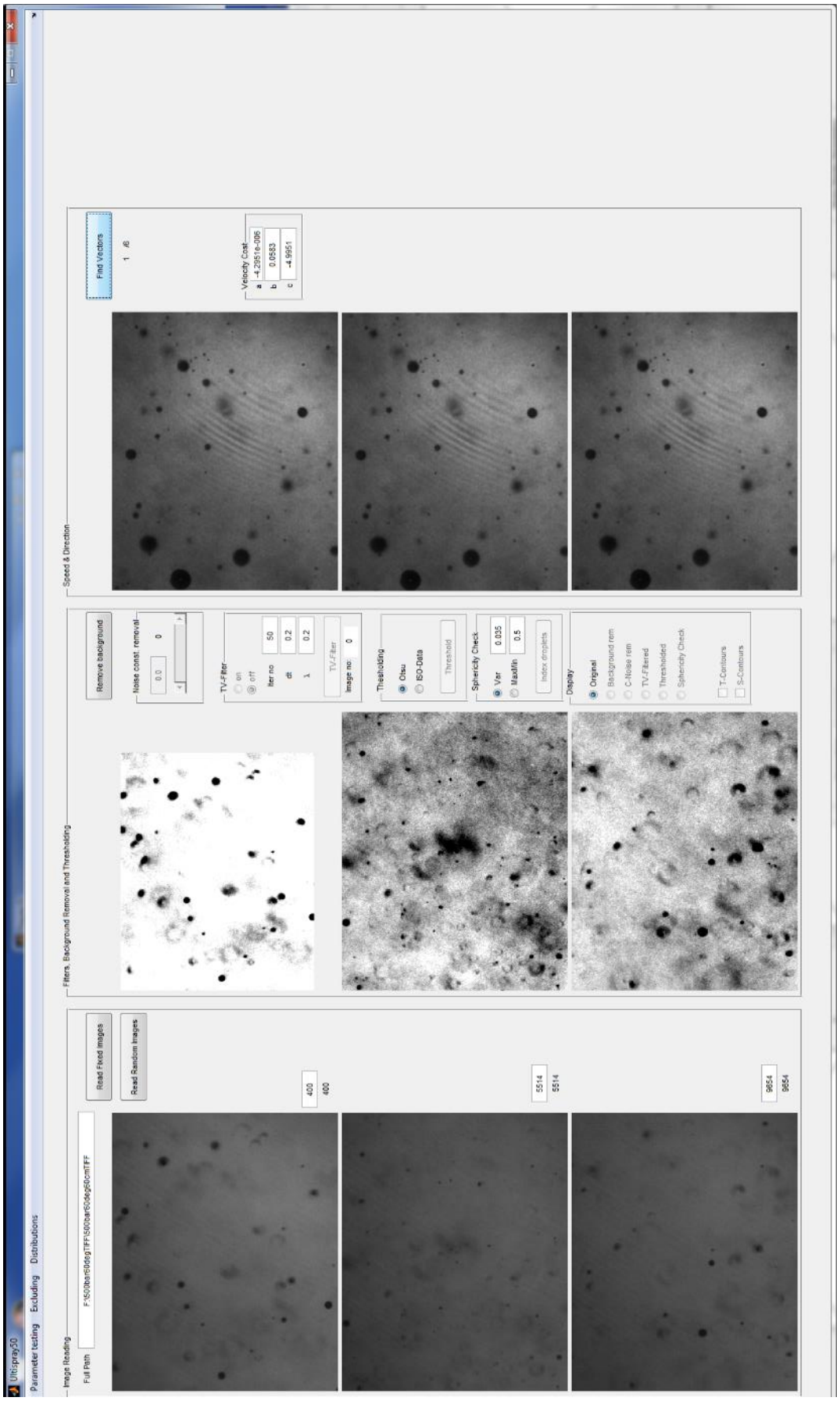

Figure 4.2: First sheet of image processing software. It is divided into three panels (columns).

4.2.2 Image processing program: Excluding

The second sheet is an adjustment sheet for the Hungarian algorithm parameter explained in Chapter 4.10.

The second sheet of the GUI has just one panel, which is the Hungarian algorithm parameter. In this panel, the parameters explained in Chapter 4.10 are possible to tune to find the velocity field of the highest number of droplets without getting unreal paths. It is here just one image, but by pressing the buttons "Upper, Middle or Lower" one can choose the different parallels from sheet one. There are sliders for all the parameters to adjust, but the one called "Median Cut-off" is currently not in use. With the box marked "Velocity cost" it is possible to control the ideal velocity explained in Chapter 4.10. The matrix or spreadsheet contains the different costs going into the Hungarian algorithm with a droplet number that can be found in the image. The droplet number is displayed with a number in parentheses. This number explains why the droplet is rejected or a zero is displayed if the droplet is used. Most of the rejected droplets are not shown.

The graph on the right-hand side of Figure 4.3 is an illustration of the in-focus parameter explained in Chapter 4.2. The red line is the gray-scale value in the processed image from right before the thresholding and the green lines are the values that go into the in-focus equation by Lecouna et al. (2000) explained in Chapter 4.8.

4.2.3 Image processing program: Results

The third is the results sheet, shown in Figure 4.4, where the run parameters are set up and intermediate results can be observed while running the code.

The parameters e.g. how many images the code is going to use and the frame rate are input in this sheet. The physical parameters can be changed later as well. The image shows in real time how and which droplets are registered by showing the velocity vector. The graph under the image shows a histogram of the droplet sizes found in the current movie compared to a distribution function. The graph to the right of Figure 4.4 is the relationship of droplet diameter and velocity. In the lower-right box, some parameters from the run are shown in real time.

The "Sequence" button can be programmed to run several movies. This can be quite practical when a measurement series can consist of hundreds of movies.

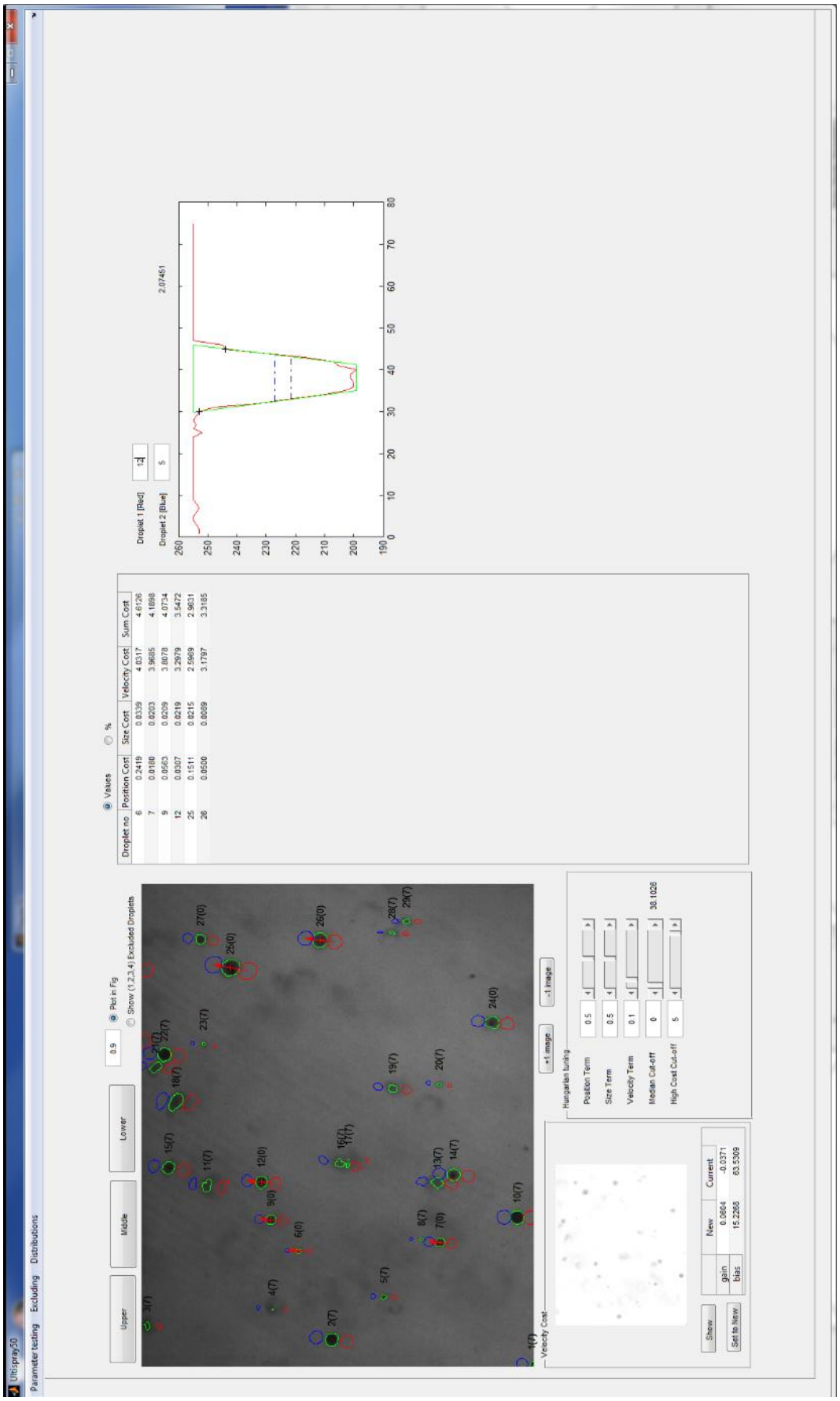

Figure 4.3: Second sheet of image processing GUI.

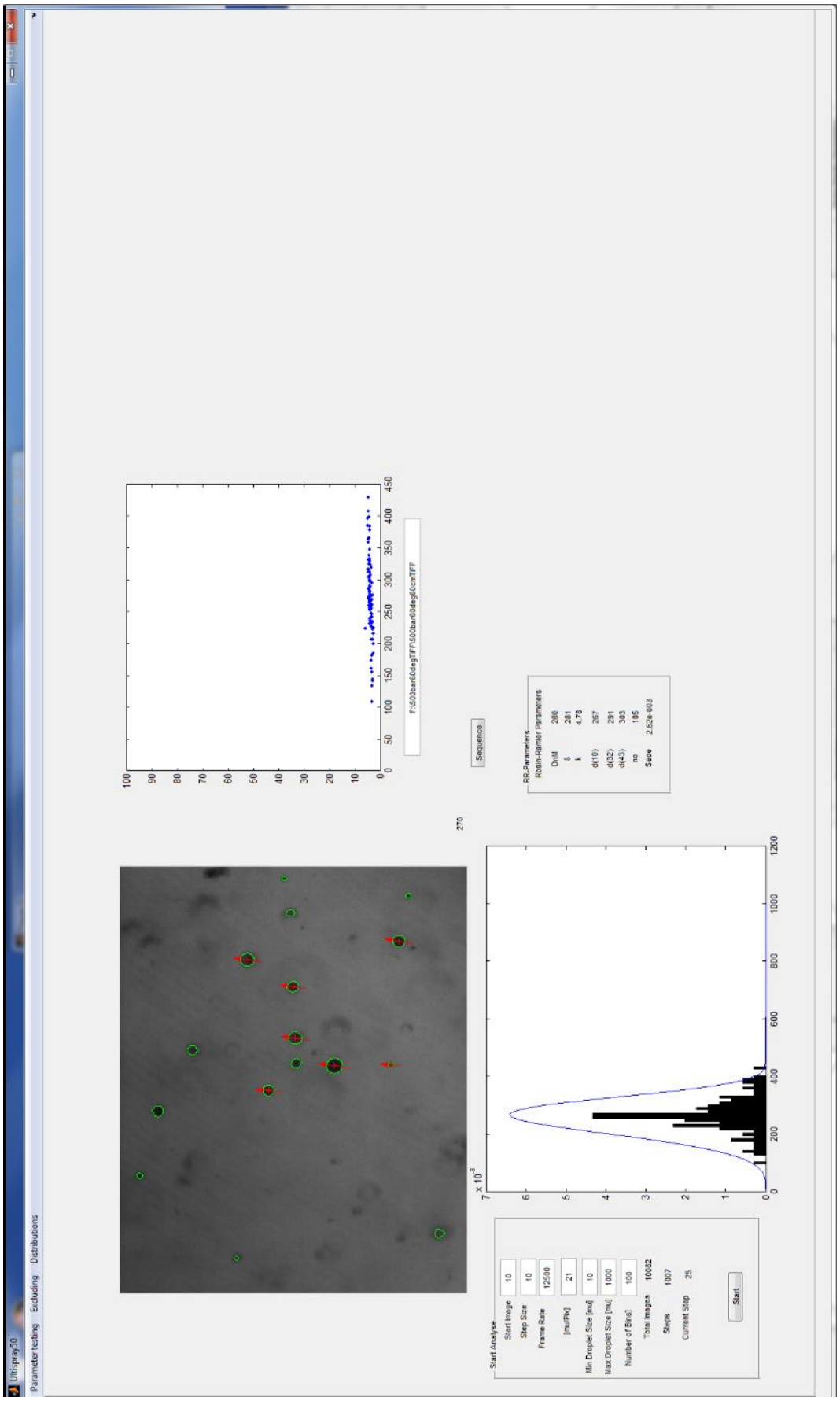

Figure 4.4: Third sheet of image processing GUI.

4.3 Depth of field (DOF) calibration

The lens for a given setup has a given field of view and a given depth of field (DOF). The field of view is dependent on the setup, but the DOF is also droplet size dependent. In Figure 4.5 from Lee et al. (2009), the principles of the DOF is shown. The study is done for particles, but droplets will have the same effect. Figure 4.5 shows different sized particles and illustrates that a large droplet will have a larger field of view than a small one. For quantitative measurements, the field of view and the DOF are multiplied to get a control volume. This implies that a large droplet has a larger control volume than a small droplet. The DOF can be defined as the distance a droplet can be moved out of focus, while still being recognized as a droplet.

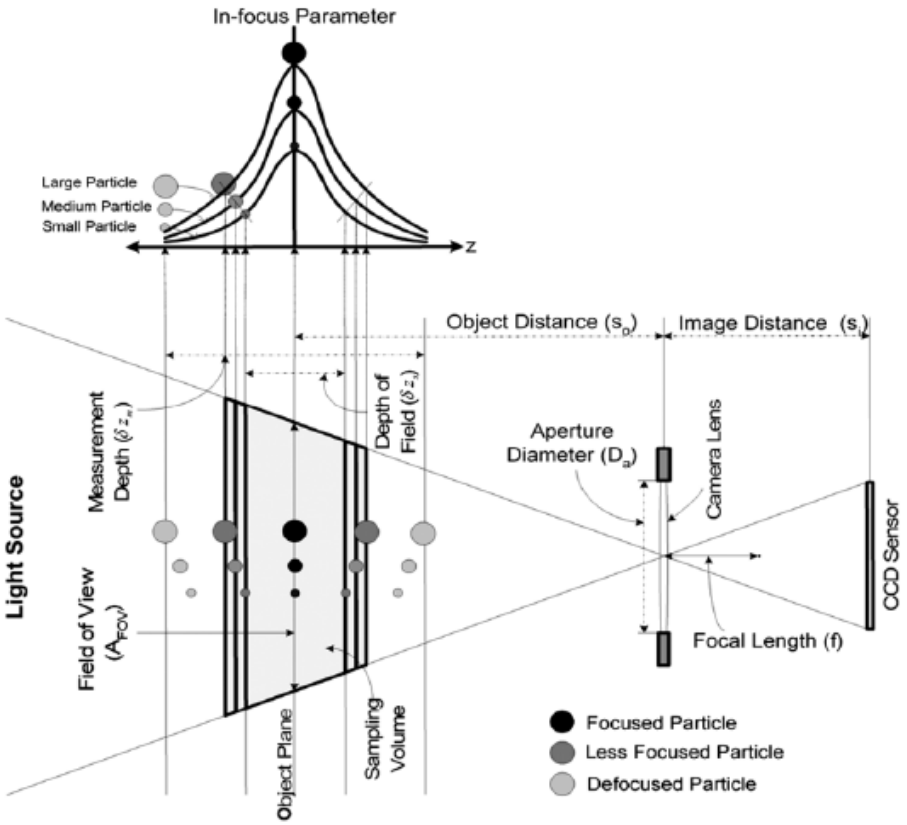

Figure 4.5: Principles of DOF from Lee et al. (2009).

A measure for the droplet's position in the DOF is the inf-parameter by Lecouna et al. (2000) explained later in this chapter. The inf-parameter compares the maximum and minimum gray-scale level of the droplets to the gradient at the edges of the droplets. Figure 4.6 shows the gray-scale value through the center of a calibration standard. The standard is a 1.5 mm steel ball placed on a cross of glass strings. The numbers 0 to 30 in Figure 4.6 are the displacement from the focus plane in mm for the calibration standard. At 0 mm, the "droplet" has steep gradients at the edges. At 15 and 25 mm off center, the black center will disappear more and more and be completely blurred out at 30 mm. The images in Figure 4.6 have to be seen in context with the graphs. The inf-parameter will have a high value for deep U-shaped gray-scale profiles and a low value for shallow V-shaped profiles.

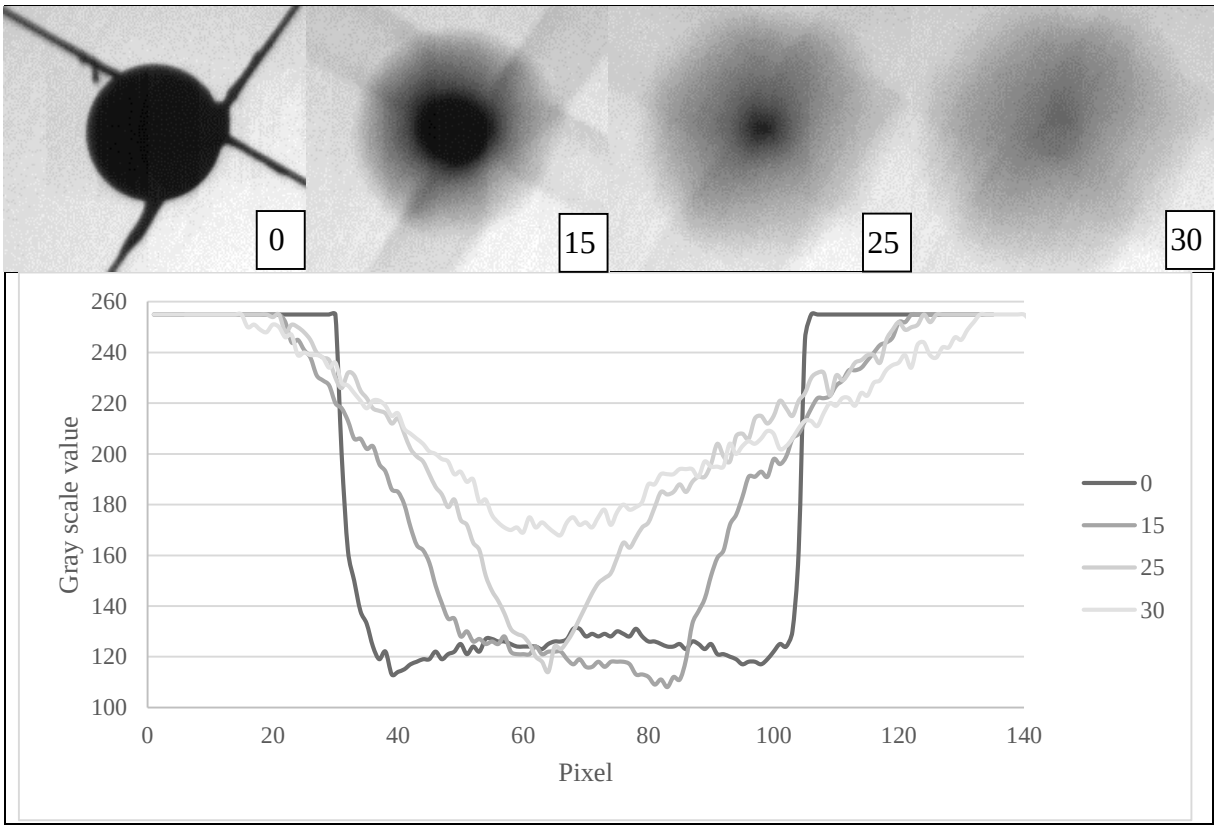

Figure 4.6: Gray-scale profile on a line through the droplet sizing at different distances from the focus plane. The small images on the top of the figure has the gray-scale values in the graph.

To compensate for droplet size dependency of the DOF, a calibration was made of the setup. The calibration of the setup was done by keeping the settings for the camera, lens and laser the same for the experiments with the water spray and the experiments with the standards. A sizing standard was placed in the field of view and mounted on a translation screw perpendicular to it. The sizing standard was a Patterson globe and a spherical steel ball with the diameter of 1.5 mm. The Patterson globe is a glass plate with filled circles of different diameters. The setup for calibration and the pattern on the Patterson globe is shown in Figure 4.7.

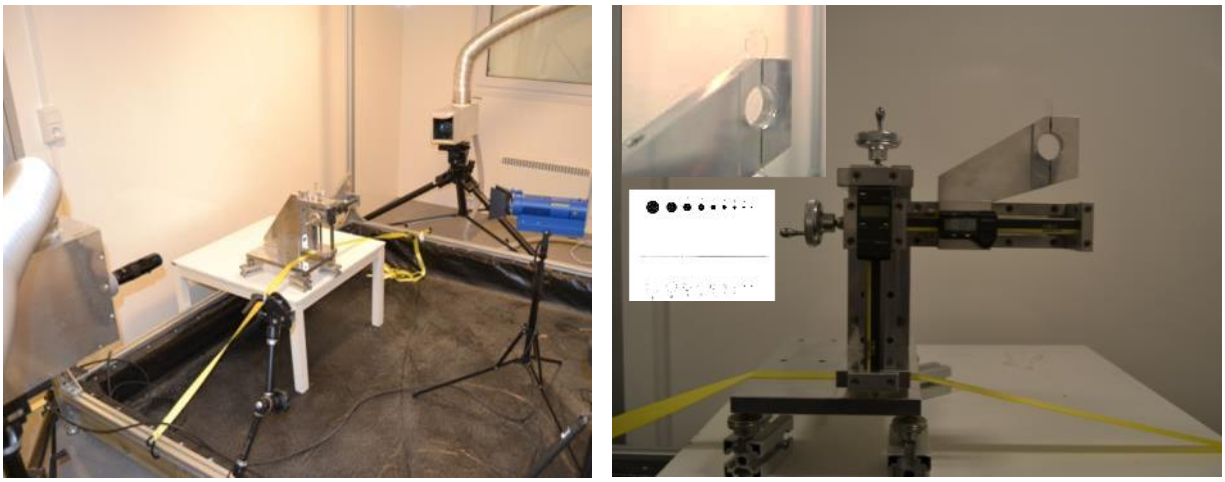

Figure 4.7: Setup with translation screw controlling position of a Patterson globe.

Images of the sizing standard were captured for different DOF. The images were processed in an in-house Matlab code explained in the previous chapters. The run parameters and calculation algorithms of the calibration run and the fire water spray were the same.

According to Lecouna et al. (2000), the degree of focus of the droplets can be found by investigating the intensity gradient at the edge of the droplet. A steep gradient indicates that the droplet is close to the focus plane. By traversing the droplet from the focus plane, the gradient at the edge will be weaker. Lecouna et al. (2000) define an in-focus parameter that correlates the intensity gradient at the edge to the gray-scale value difference between the background and the darkest pixel of the droplet. Chapter 4.8 shows how to calculate the droplet size dependent DOF denoted by the inf-parameter.

Figure 4.8 shows a screen dump from the in-house Matlab program made to calculate the DOF and the inf-parameter. This program imports images from the calibration experiments and finds the gray-scale profile through the object (droplet or standard). The program uses the same image processing code as for the spray experiments, explained in Chapter 4.4-4.11, to find the droplet parameters in order to calculate the inf-parameter. The program can read the gray-scale profile through the object in all directions. The data from the calibration is the inf-parameter and the diameter. Since the size of the standards and the distance from the focus plane is known, it is possible to correlate a size on the image to a physical length and a size of the DOF.

A Patterson globe and a spherical steel ball with the diameter of 1.5 mm made standard sizes of 1500, 450, 360, 270, 225, 180, 145, 110 and 74 µm. The experiment contained 38 images of the Patterson globe and 107 images of the steel ball from different positions perpendicular to the field of view. Not all of the images where used due to blurred images far from the focus plane. The readings for the DOF calibration was based on 92 readings of droplets and 3 measurements on every reading.

Figure 4.9 shows the in-focus parameter from the calibration experiments to the distance from the focus plane for all the standards used. It shows the in-focus parameter to increase with increasing size and decreasing distance from the focus plane. The larger the size of the standards or droplets is, the higher the in-focus parameter is.

A straight line going through the circles measures the diameter of the standards in the image as a number of pixels. The number of pixels through the different standards is shown as a function of the distance to the focal plane in Figure 4.10. At one distance to the focus plane, the diameter in pixels has a rapid increase in value. This is the point where the different standards get too blurred to measure. This is found, by trial and error, to be where the in-focus parameter has the value about 1.25. This value is the criterion to determine if the droplet is in focus or not. The value will be used for both calibration and experiments.

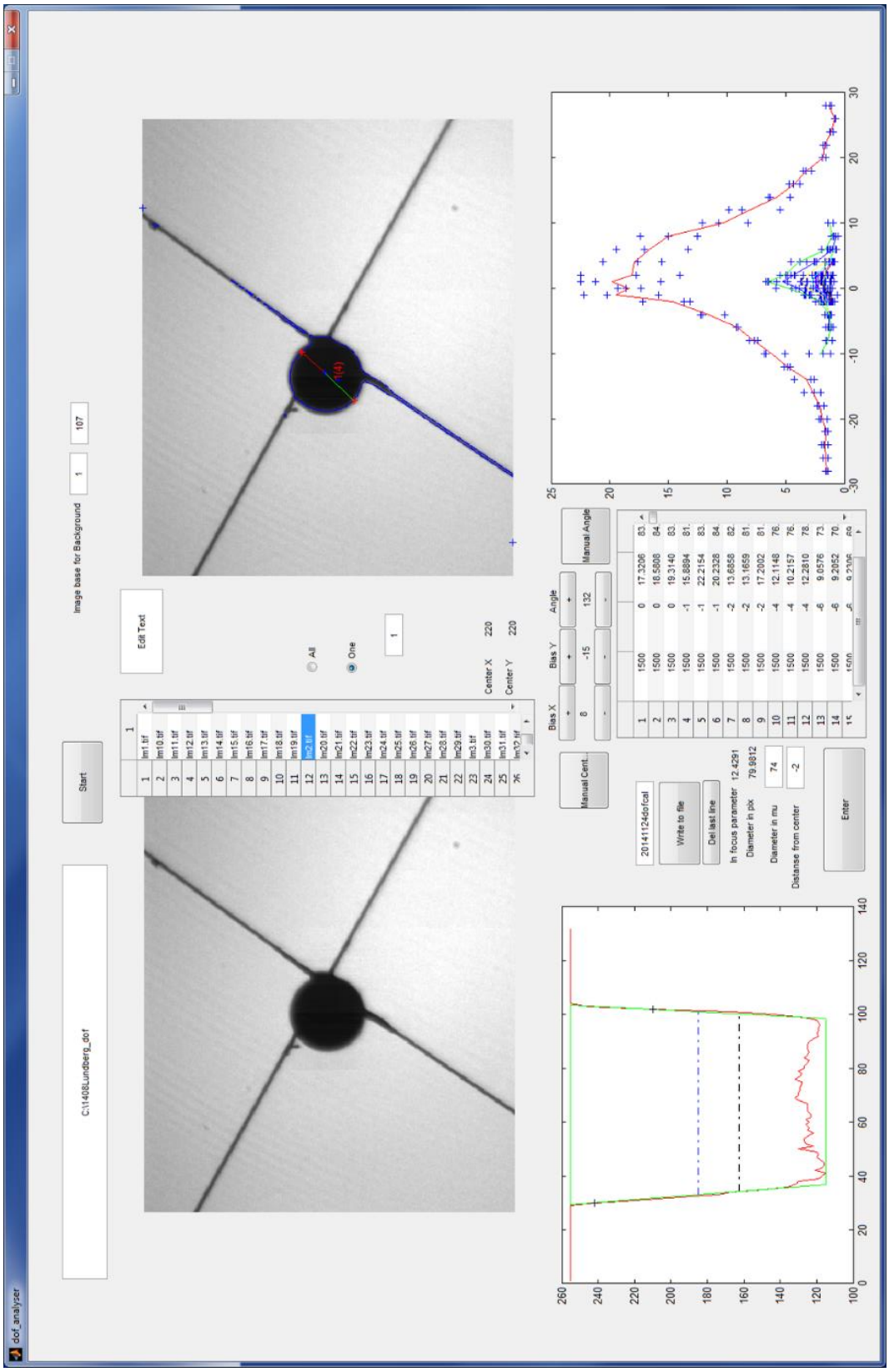

Figure 4.8: Graphical user interface for calculating the DOF from the images from the calibration.

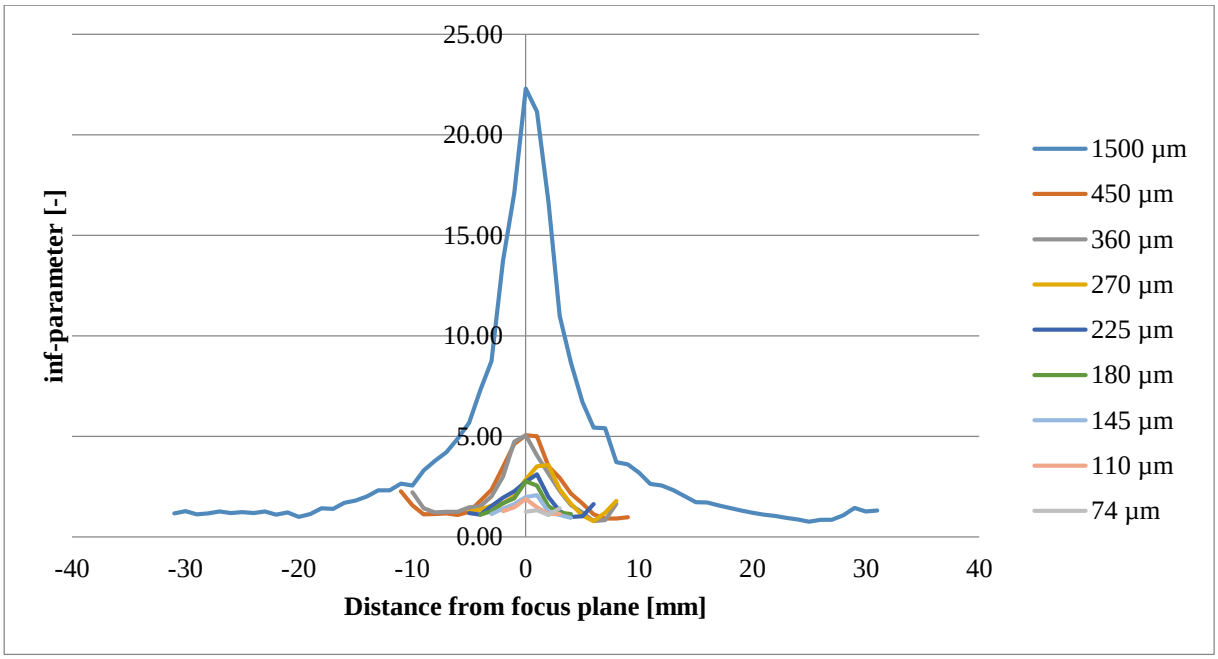

Figure 4.9: inf-parameter to the distance from the focus plane for different sized standards.

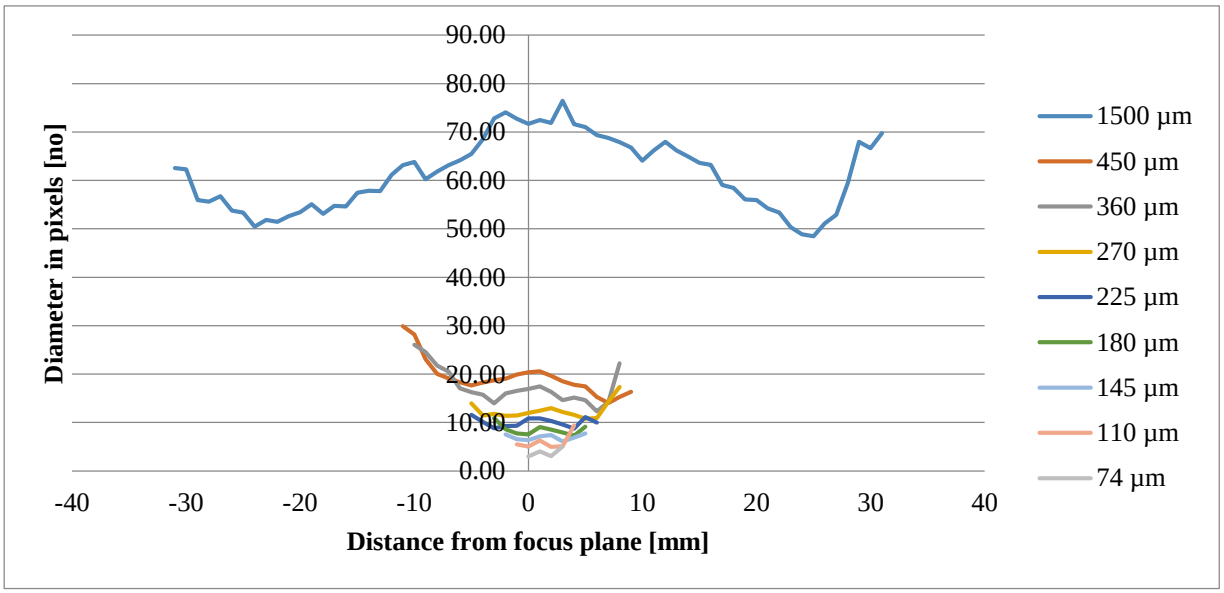

Figure 4.10: Diameter in number of pixels to the distance from the focus plane for different sized standards.

By averaging the number of pixels through the different standards, by using the measurements qualified to be in focus, a correlation between the size of the standard and the number of pixels is found. This correlation is shown in Figure 4.11.

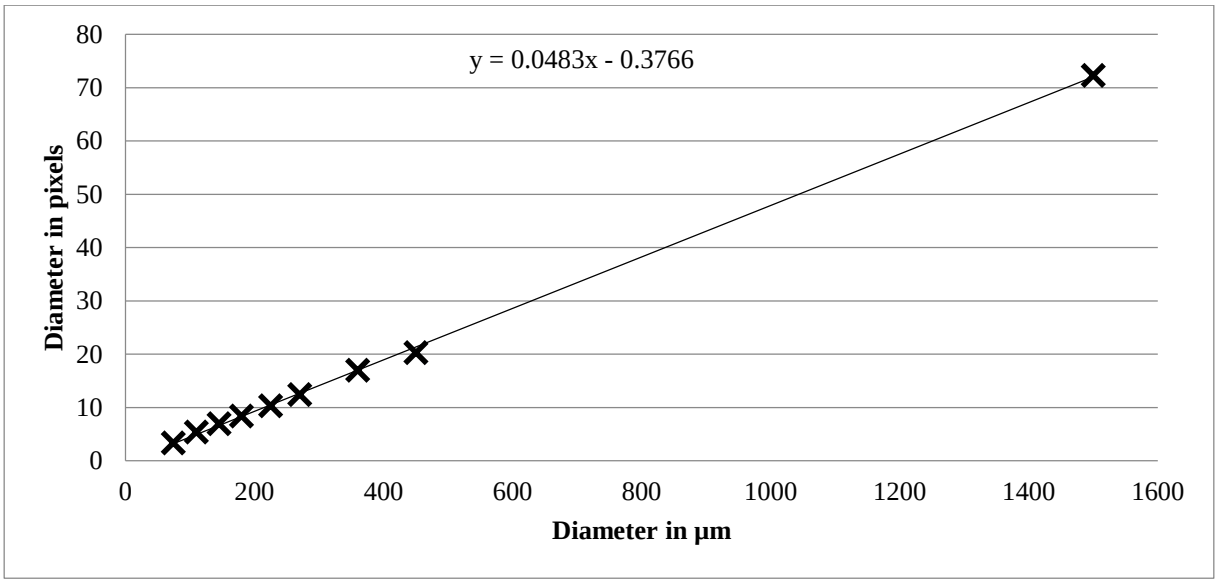

Figure 4.11: Results from calibration with sizing standards and the correlation curve.

Figure 4.12 shows the correlation between the DOF and actual size of the standards in µm.

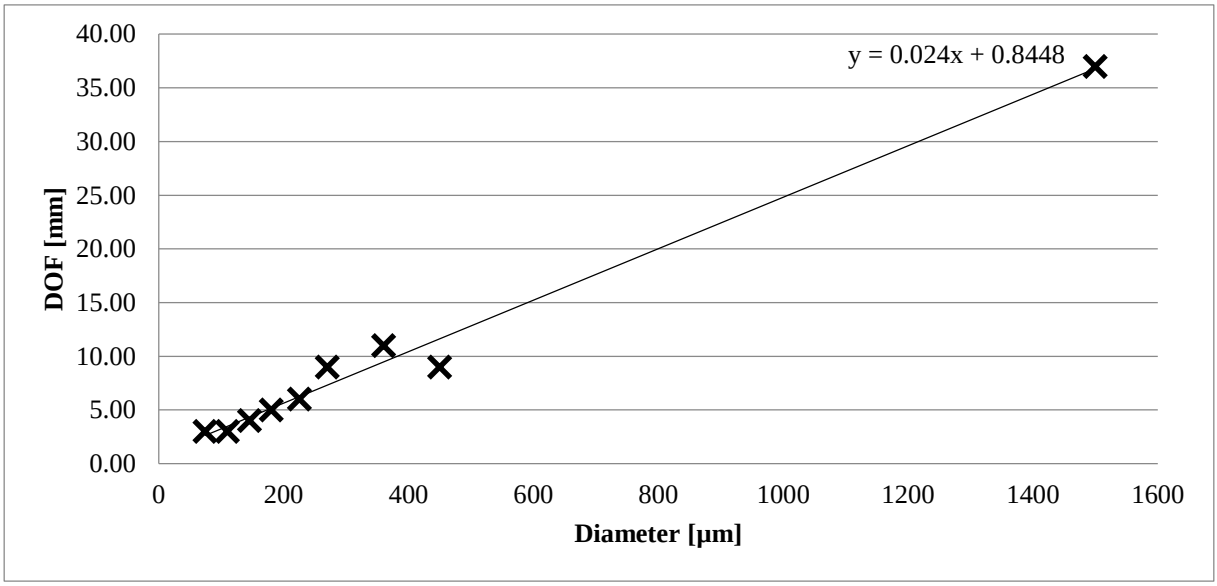

Figure 4.12: DOF to diameter of the standards.

4.4 Background subtraction

The recorded images consist of droplets (both “in focus” and “out of focus” droplets), noise and the background. In an ideal image, the “in focus” droplets are black, the “out of focus” droplets are gray and the background is white, meaning that it is easy to identity the “in focus” droplets. However, in real measurements, due to varying illumination and optical phenomena, the background appears uneven and there is a smooth transition from “in focus” to “out of focus” droplets, see Figure 4.13.

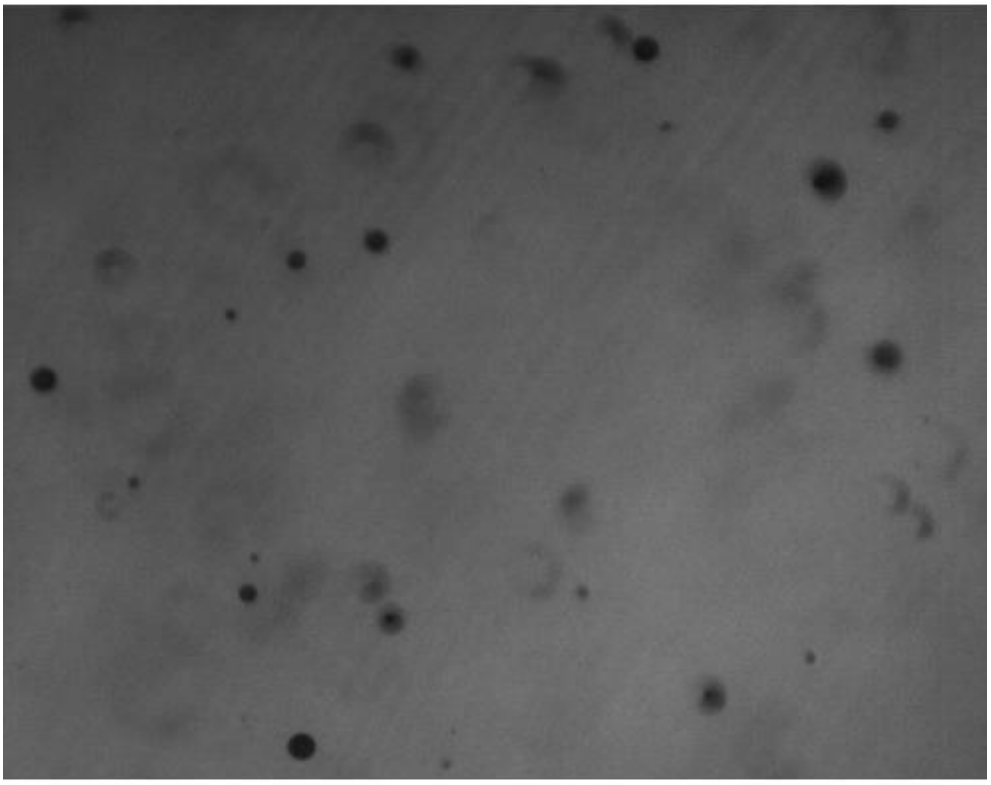

Figure 4.13: Original image from spray, I_i.

An estimate for the uneven background B is found by averaging all frames of a movie, i.e.

$$B = \frac{1}{n}\sum_{i=1}^{n} I_i \tag{4.1}$$

where I_i is the image at frame i and n is the total number of frames in the movie. Then, for each image in the movie, the background is subtracted:

$$J_i = I_i - B, \quad i = 1{:}\,n. \tag{4.2}$$

After the background subtraction routine, the images will mainly consist of noise and droplets, see Figure 4.14. The figure is just for illustrative purposes where the gray-scale value is adjusted.

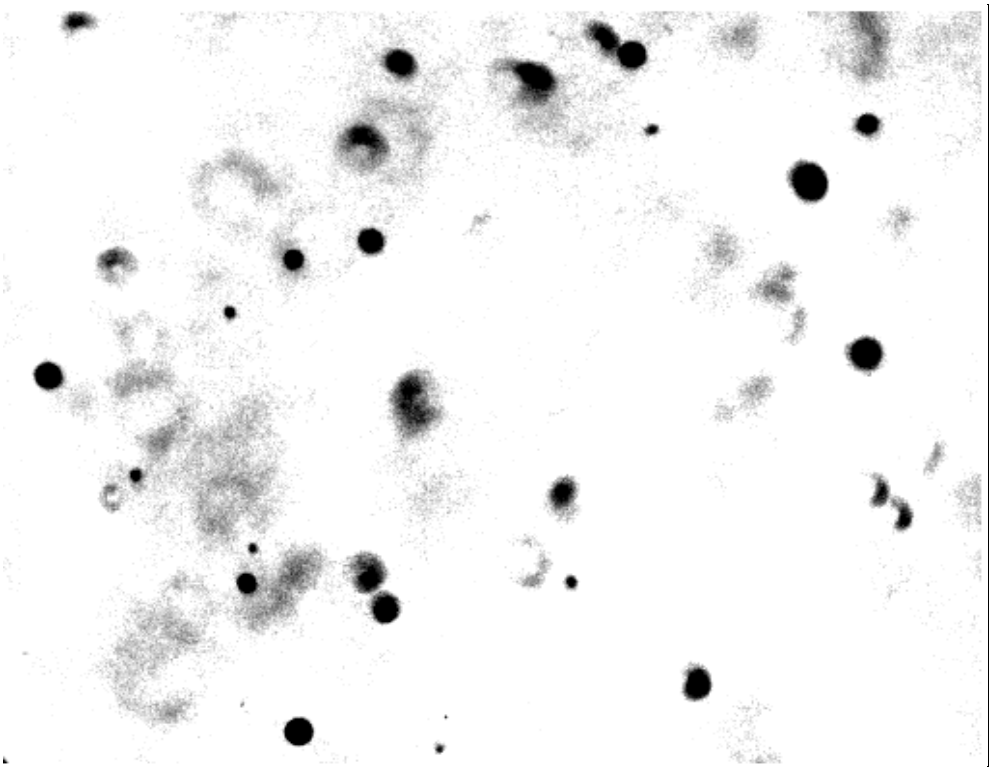

Figure 4.14: Image processed image J_i, where the background is removed from the original image, showed in Figure 4.13.

The background B, is subtracted from all of the images, as shown in Figure 4.15.

Figure 4.15: Background found by Equation (4.1).

4.5 Image binarization

The droplets can be isolated by applying a thresholding algorithm that divide the image into droplets and background (including noise). The Otsu (1979) algorithm is used to find the threshold value t. The optimal solution of t maximizes the inter-class variance between the droplets and the background (Gonzales & Woods, 2008). The threshold value is then used to divide the gray-scale image $J_i(x, y)$ into background and droplets, where (x, y) represents the pixel coordinates. Every pixel value above the threshold t is classified as background, and pixel value below t is identified as droplets, yielding the binary image

$$T_i(x, y) = \begin{cases} 0 & \text{if } J_i(x, y) < t \\ 1 & \text{if } J_i(x, y) \geq t \end{cases}. \tag{4.3}$$

The threshold algorithm can be used both globally and locally, and can thereby determine one global threshold value over an entire image, or one local for each defined area. The output of the threshold algorithm is a binary image, i.e. droplets and background, see Figure 4.16.

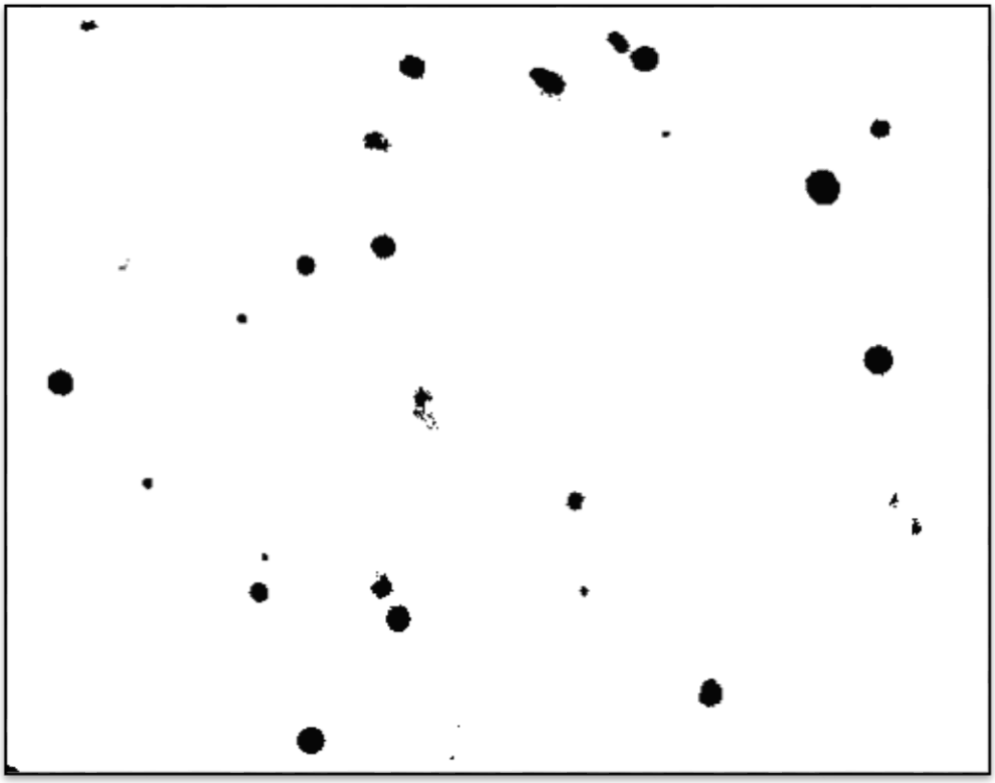

Figure 4.16: Thresholded image T_i found with (3.3) showing droplets (black) and background (white).

Figure 4.17 shows the gray-scale or intensity of the original image in Figure 4.15. It shows a histogram of the number of pixels with the gray-scale value. The scale of the x- axis is removed because the shape of the histogram is the determinative to the threshold value t using the Otsu (1979) algorithm from the image processing toolbox (Mathworks, 2011).

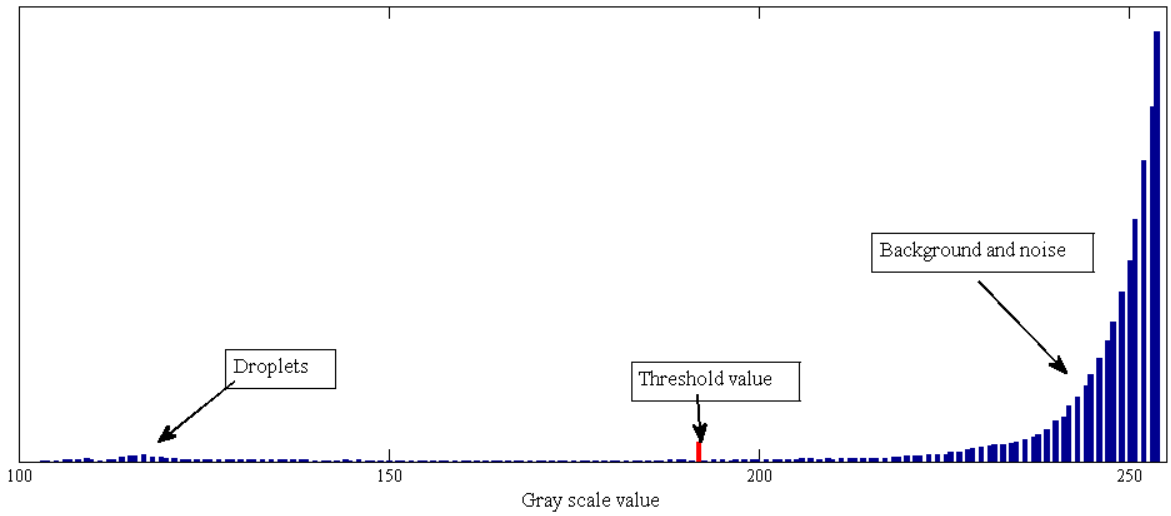

Figure 4.17: Illustration of the principles of the Otsu (1979) method.

An iterative algorithm, IsoData by Ridler & Calvard (1978), has been tested for this project. In short, the algorithm works as follows:

1. Make an initial guess for the threshold value
2. Find the mean gray-scale value for the background and the droplets
3. Iterate to find the threshold value t that gives

$$t = \frac{\left(\overline{J_l(x,y)<t} + \overline{J_l(x,y)\geq t}\right)}{2}. \tag{4.4}$$

For this project the IsoData (Ridler & Calvard, 1978) algorithm did not differ significantly from the Otsu (1979) method and is not used.

To improve the image quality before the image is thresholded, an iterative total variation (TV) filter by Rudin, Osher & Fatemi (1992) was tested. This reduced the background noise and at the same time kept the steep gradients in the image. The TV-filter made the image processing code too time consuming without affecting the result significantly.

4.6 Filter image

Salt and pepper noise is single black pixels on white background or the opposite in binary images. It will occur in the thresholded images from the measurement series. The method used is a median filter that also removes highly uneven droplet edges. Figure 4.18a is a thresholded image before the salt and pepper removal and Figure 4.18b is after. The red ring in the image illustrates where the code removes noise and the blue illustrates where it smoothens highly uneven droplets.

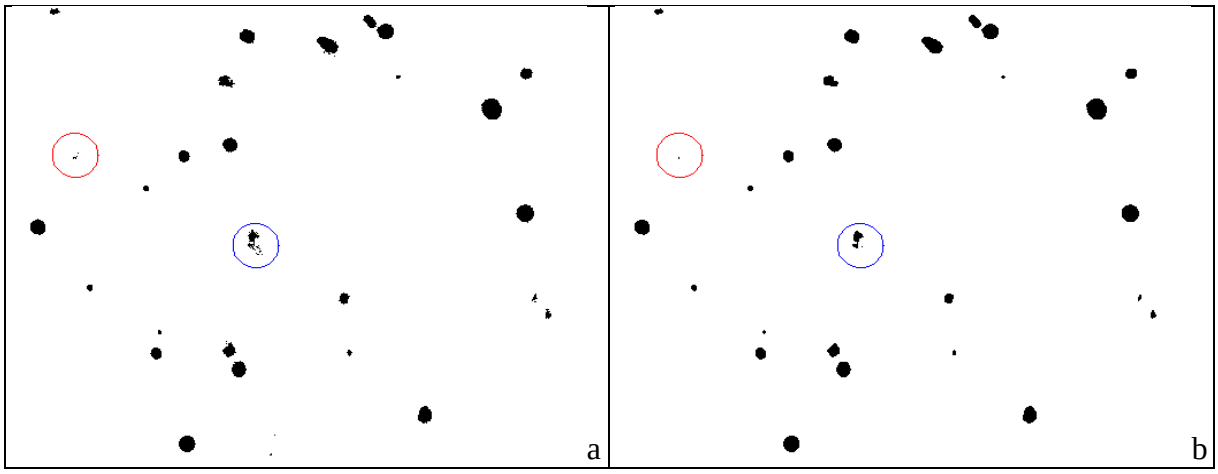

Figure 4.18: a) A thresholded image before the salt and pepper removal, b) after salt and pepper removal.

If there is a white spot in the black droplet, it will be changed to black. This can occur due to optical phenomena.

4.7 Qualifying droplets

Although the droplets are found with a threshold algorithm, false droplets may still exist. The droplets or possible droplets are found purely based on a gray-scale value in the image. The shape of the droplets needs to be considered to distinguish between real droplets and noise.

The image is run through an object recognition algorithm that will index all the droplets and measure the properties of the object. This is done with the built-in Matlab routine "bwconncomp"combined with "regionprops" from the image processing toolbox (Mathworks, 2011).

The image processing code can recognize non-real droplets from background noise, droplets consisting of several droplets or droplets and background interfering. From visual considerations of the images, the characteristic feature of a non-real droplet is found to often have either an uneven edge or an non-circular shape.

Let $\partial\Omega = \{x_1, x_2, \dots, x_k\}$ denote the k number of coordinates along the boundary of a given droplet ($k$is the number of pixels of the perimeter of the droplet). The center of mass of the droplet is denoted COM. The distance from the center of mass to each point in $\partial\Omega$ is

$$\varepsilon = d(COM, \partial\Omega). \tag{4.5}$$

By comparing the standard deviation of ε around $\partial\Omega$ the droplet is compared to the number of elements in ε. This can be expressed as a parameter σ found by:

$$\sigma = \frac{st.dev(\epsilon)}{k}. \tag{4.6}$$

To determine if the droplets are non-circular, we calculate the ratio between the largest and smallest radius in the droplet. This can be expressed as:

$$\varsigma = \frac{\min(\epsilon)}{\max(\epsilon)}. \tag{4.7}$$

This is done for all the droplets and just the ones that pass both criteria will be used further.

Figure 4.19 shows examples of droplets that pass or are excluded in the criteria.

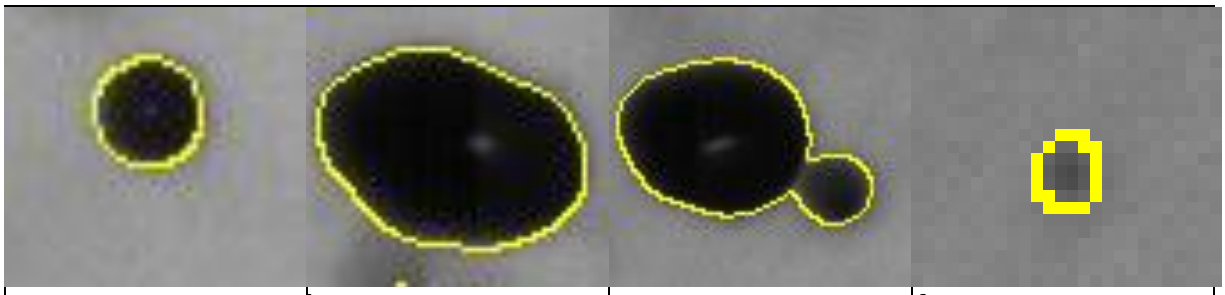

Figure 4.19: Examples of droplets with a) circular shape, b) oval shape, c) double droplet shape, d) droplet with un-even edge.

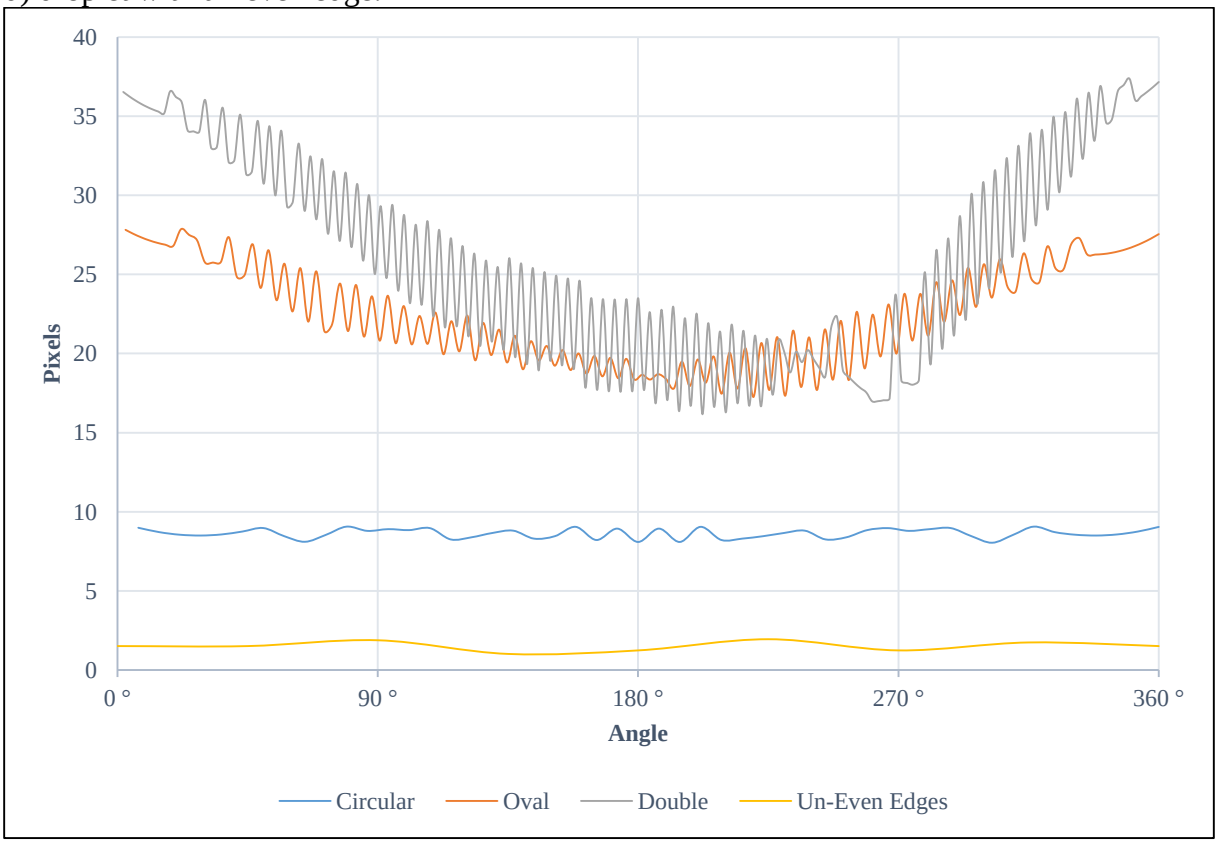

Figure 4.20: The distance from the center of mass to perimeter of the droplet for the different examples of droplets from Figure 4.19 for all angles.

As shown in Figure 4.20, ϵ will behave different for different droplets and give different values for the characteristic σ and ς. The limit value for σ and ς is found by trial and error to be 0.035 and 0.5, respectively. Table 4.1 shows the numerical value for the four cases (circular, oval, double and un-even edge) and a red cell indicates rejection while green indicates accept. Both σ and ς have to be accepted for the droplet to pass.

Table 4.1: σ and ς values for different droplets.

	Circular	Oval	Double	Un-Even Edges
σ	0.885	0.619	0.4324	0.5193
ς	0.006	0.0243	0.0374	0.0417

4.8 Qualifying of "in-focus" droplets

To qualify the "in-focus" droplets the concept of gray-scale gradient at the boundary by Lecouna et al. (2000) is adopted. This method compares the gray-scale or intensity gradient at the boundary of the droplets to the intensity difference of the minimum of the droplet and the background. The comparison is the expression of the "in-focus parameter" inf described by equation (4.8). The inf is droplet diameter dependent. For a constant value for inf, the depth of field will increase with increasing droplet size. An equipment dependent limit is found for inf where all droplets with values above this limit inf_c is in-focus. The same limit is used for both the calibration and experiments where the calibration is explained in Chapter 4.3. The inf will be found for all droplets in every image and the droplets below a limit will be rejected.

To determine the inf, the gray-scale profile through the droplets is used. The red line in Figure 4.21 is shown as an example. The yellow circle is the edge of the droplet defined in the binarization routine in Chapter 4.5.

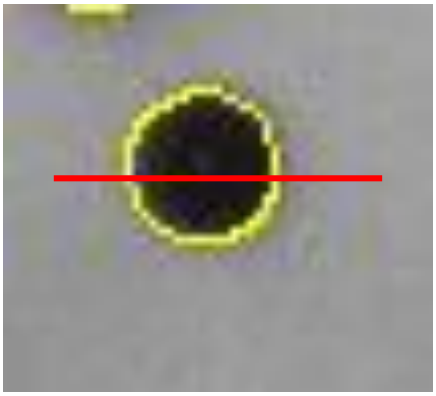

Figure 4.21: Illustration of a circular droplet where the red line indicates where the gray-scale values are found (line l).

The reason the line starts outside the droplet is to insure that the profile starts in the background and goes through the droplet. The line in this thesis is horizontal, but it is possible to investigate all the directions through the droplets.

The line l is defined as $l = \{x_1, x_2, \dots, x_n\}$ where x is the positions along the line. The center COM and the position of the droplets edges is x_w and x_e where$(COM, x_w, x_e) \in l$. The gray-scale profile from the background-subtracted image J_i described in Chapter 4.3 is given by $Y = J_i(l)$. Figure 4.22 shows the profile Y along the line l.

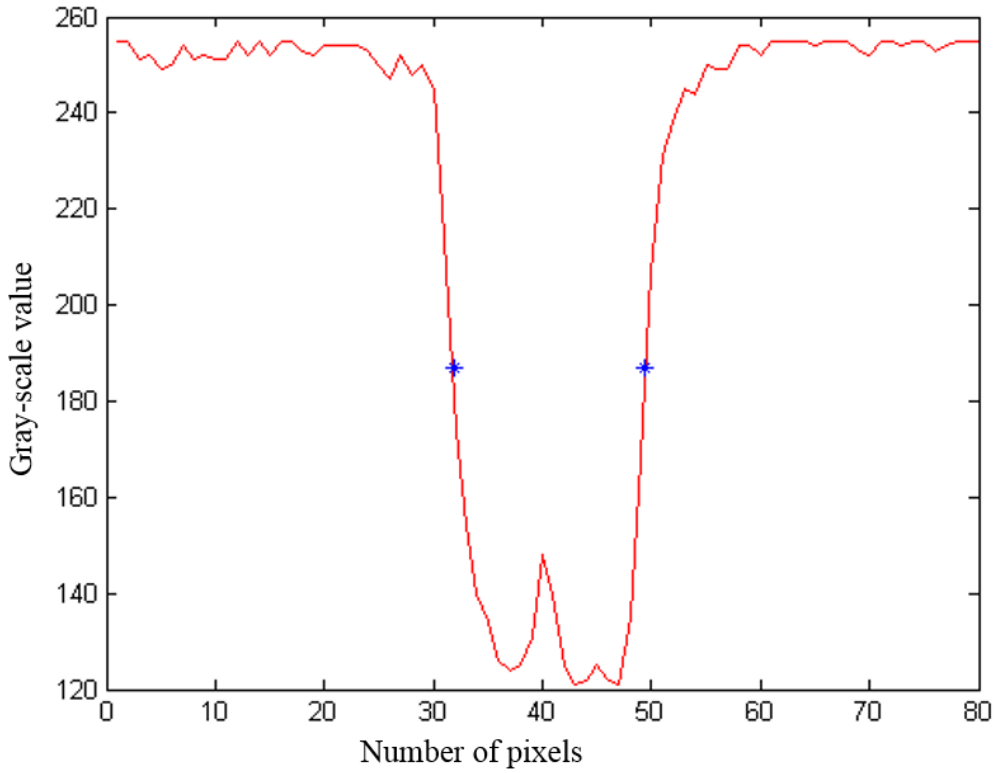

Figure 4.22: Gray-scale profile through droplet. The blue stars indicate where the edges of the droplet are.

The inf-parameter is modeled by Lecouna et al. (2000) like

$$inf = K \frac{d_j grad_{max}}{(Y_{max} - Y_{min})} \tag{4.8}$$

where

$$grad_{max} = \frac{\left|\left(\frac{\partial Y}{\partial l}\right)_w\right| + \left|\left(\frac{\partial Y}{\partial l}\right)_e\right|}{2} \tag{4.9}$$

The minimum and maximum gray-scale value of the profile is respectively $Y_{min} = \min(Y)$ and $Y_{max} = \max(Y)$. The gradient at the edges of the droplet is found by the derivative of the profile at the edges, $\left(\frac{\partial Y}{\partial l}\right)_w$ and $\left(\frac{\partial Y}{\partial l}\right)_e$. The diameter, d_j, is the Euclidean norm from x_w to x_e.

Figure 4.23 shows the gray-scale value (red) compared to the modeled droplet by the parameters from the Lecouna et al. (2000) equation (green).

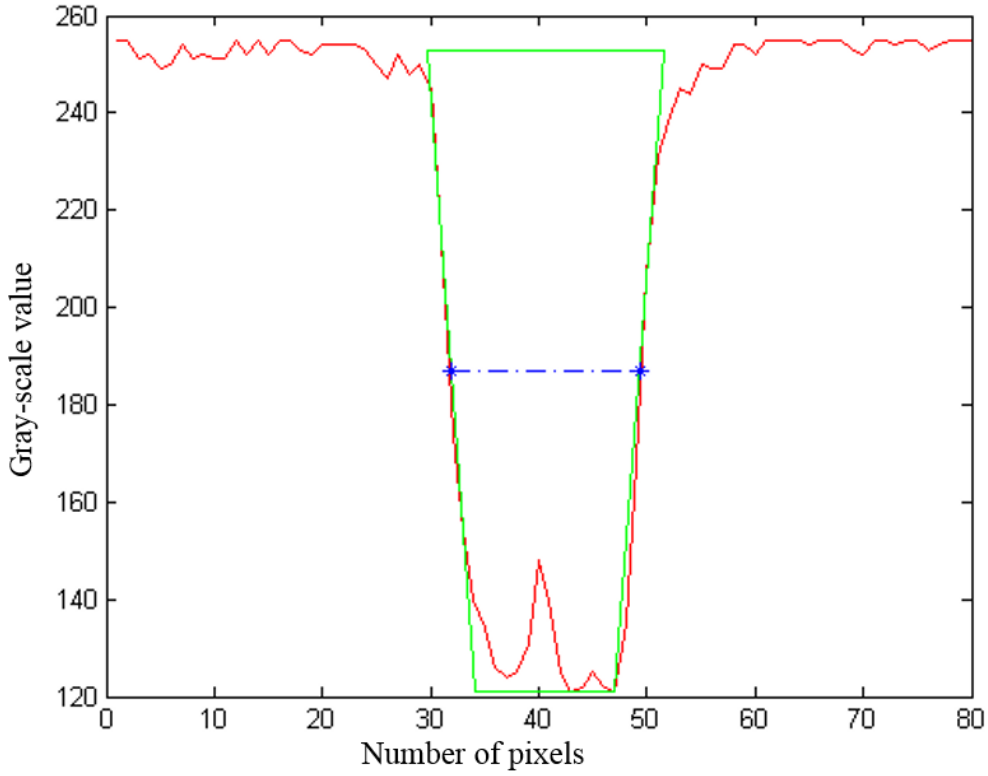

Figure 4.23: Gray-scale value through droplet compared to modeled droplet by parameters from the Lecouna et al. (2000) equation.

The inf is found for all the droplets and the one below the limit inf_c is rejected. Figure 4.24 shows the qualified droplets (yellow) and the rejected (green). The diameter of the droplets is the same diameter as used in Lecouna et al. (2000).

The same procedure (from the background subtraction routine) is completed for the image before and after the current to be used in the algorithm for velocity calculation.

4.9 Droplet matching and velocity calculation

To find the velocity of the droplets, the position of each droplet in a given frame of a movie is compared with the position of the same droplet in subsequent frames. In this thesis, the velocity of the droplets in frame T_i is calculated with the use of three frames, i.e. T_{i-1}, T_i and T_{i+1}. The velocity distribution of the droplets is then obtained by comparing the physical position in the temporally adjacent frames.

Therefore, to calculate the droplet velocity, all "in-focus" droplets have to be tracked between the frames. However, this is a challenging problem, since several possible droplet paths may exists for a given set of droplets, see Figure 4.25. By using brute-force search, the number of possible configurations of droplet paths for n droplets are $n!$. By using the Hungarian algorithm, the number will be only n^2(Kuhn, 1955).

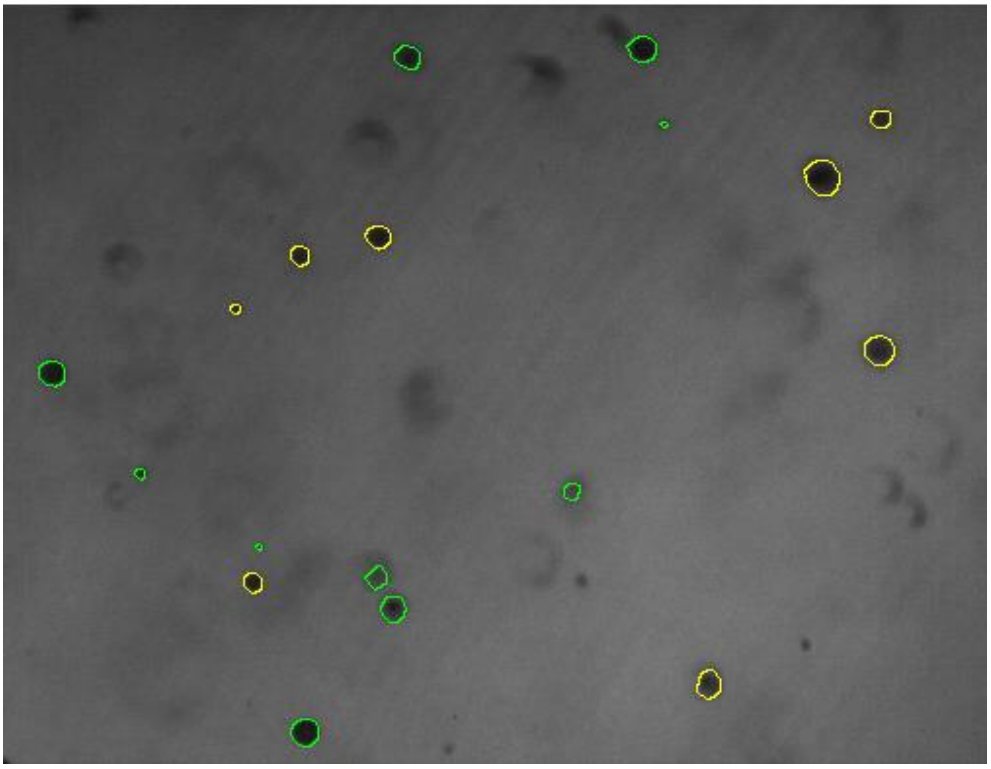

Figure 4.24: Figure shows qualified (yellow) and rejected (green) droplets.

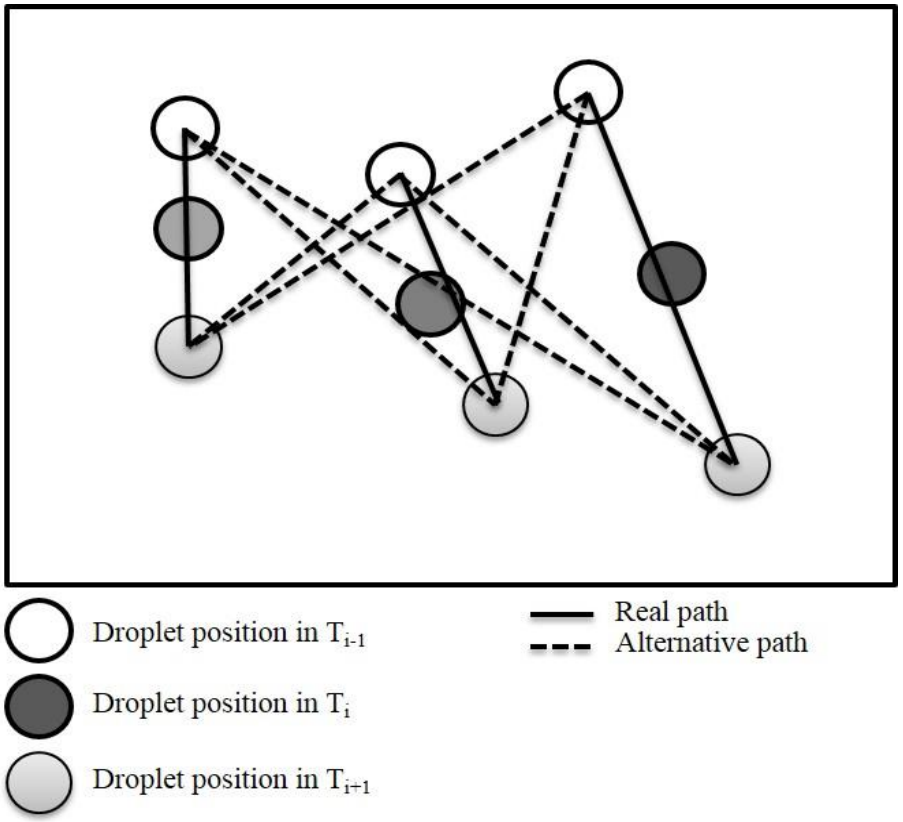

Figure 4.25: Droplet combinations for illustrations. Possible paths for three droplets in three sub sequential frames.

Please note that, with respect to the flow properties, each droplet has exactly one path, i.e. one single droplet cannot be assigned to several paths. Moreover, the number of "in-focus" droplets may change from frame to frame, as droplets might emerge or disappear in subsequent frames. To overcome these challenges, a multiple tracking framework is applied. Multiple tracking considers all possible paths, and selects the optimal combination. Such an optimization problem can be solved efficiently by, e.g. the Hungarian algorithm (Kuhn, 1955).

4.10 Tracking as an assignment problem

In terms of mathematics, a path between the positions of droplets in subsequent frames can be assigned a cost. In this thesis, the cost for a given path is defined by a combination of the following constraints:

- The direction of the path should not change appreciably from frame to frame
- The droplet velocity should not deviate much from an average droplet velocity
- The droplet size should not differ appreciably from frame to frame
- A droplet cannot be assigned to several paths

To find the optimal association of all the droplets in adjacent frames, a cost must be calculated for each individual path. Let $P = \{p_1, p_{2,\dots,} p_k\}$, $Q = \{q_1, q_{2,\dots,} q_l\}$ and $R = \{r_1, r_{2,\dots,} r_m\}$ denote the sets of k, l and m points (droplets) detected in frame $i-1, i$ and $i+1$, respectively. The total cost of each path from $p \in P$ to $r \in R$ via $q \in Q$ is given by the penalty matrix $C_{k\times m}$, where

$$C_{k\times m} = \delta\Delta_{k\times m} + \lambda\Lambda_{k\times m} + \gamma\Gamma_{k\times m} \tag{4.10}$$

and δ, λ and γ are positive constants and the subscript $k \times m$ represents the dimension of the matrixes, i.e. the matrixes have k rows and m columns. In the following, the three matrixes $\Delta_{k\times m}$, $\Lambda_{k\times m}$ and $\Gamma_{k\times m}$ are discussed in more detail.

The elements in $\Delta_{k\times m}$ represent a measure of the smoothness of each path, and paths that change direction from one frame to another are penalized. To calculate the direction of a path, it is utilized the fact that every convex combination of two points lies on the line segment between the two points, i.e. $w = \alpha p + (1-\alpha)r$, with $0 \le \alpha \le 1$. By using $\alpha = 0.5$ (assuming no acceleration), a point halfway between p and r is thereby simply given by $w = \frac{p+r}{2}$. If $w \in Q$, it means that there is a droplet in frame i positioned halfway between a droplet $p \in P$ and a droplet $r \in R$, indicating a non-changing direction of the path. Otherwise, with $w \notin Q$, the path changes direction from one frame to another, and the changes is measured as the shortest distance from w to any $q \in Q$, i.e.

$$\Delta_{k\times m} = \begin{bmatrix} d\left(\frac{p_1 + r_1}{2}, q^*\right) & \cdots & d\left(\frac{p_1 + r_m}{2}, q^*\right) \\ \vdots & \ddots & \vdots \\ d\left(\frac{p_k + r_1}{2}, q^*\right) & \cdots & d\left(\frac{p_k + r_m}{2}, q^*\right) \end{bmatrix} \tag{4.11}$$

where $d(w, q^*)$ denotes the shortest distance from w to any $q \in Q$.

All droplets will move a certain distance between the frames. However, the droplet velocity depends on the droplet size, i.e. larger droplets move in general with a higher velocity than smaller droplets. Each element in $\Lambda_{k\times m}$ in (4.11) give the deviation between the velocity along a given path and a size dependent (priori calculated) velocity distribution by

$$\Lambda_{k\times m} = \begin{bmatrix} |d(p_1, r_1) - v^*| & \cdots & |d(p_1, r_m) - v^*| \\ \vdots & \ddots & \vdots \\ |d(p_k, r_1) - v^*| & \cdots & |d(p_k, r_m) - v^*| \end{bmatrix} \tag{4.12}$$

where $|d(p,r) - v^*|$ denotes the absolute value of the distance (velocity) by moving from p to r, minus a size dependent velocity, v^*, which is based on droplet p and r.

Finally, the elements in $\Gamma_{k\times m}$ is a measure of the mismatch in the size of the droplets connected along a given path. First, let us introduce the following notation

$$A(p,q,r) = \frac{|A(p) - A(q)| + |A(p) - A(r)| + |A(q) - A(r)|}{A(p) + A(q) + A(r)} \tag{4.13}$$

where $A(p), A(q)$ and $A(r)$ denotes the area of droplets p, q and r , respectively. With this notation at hand, the matrix $\Gamma_{k\times m}$ is given by

$$\Gamma_{k\times m} = \begin{bmatrix} A(p_1, q^*, r_1) & \cdots & A(p_1, q^*, r_m) \\ \vdots & \ddots & \vdots \\ A(p_k, q^*, r_1) & \cdots & A(p_k, q^*, r_m) \end{bmatrix} \tag{4.13}$$

where q^* is the droplet $q \in Q$ with the shortest distance to the midpoint between the given p and r.

Please note that all elements in the matrixes $\Delta_{k\times m}$, $\Lambda_{k\times m}$ and $\Gamma_{k\times m}$ are greater or equal to zero. Consequently, all elements, i.e. costs, in the penalty matrix $C_{k\times m}$ are greater or equal to zero. The Hungarian algorithm takes the penalty matrix $C_{k\times m}$ as its only argument and returns the optimum path assignment; see (Kuhn, 1955) for details. The running time of the Hungarian algorithm is $O(n^3)$ compared to brute-force search of $O(n!)$.

Figure 4.26 shows the droplet paths with a red vector found with the Hungarian algorithm. The contours of the segmented droplets and the segmented droplets of the temporally adjacent frames are superimposed for illustrational purposes.

4.11 Recording of droplet properties

For every calculation, the droplet properties are saved as entries to a spreadsheet. The entries are location of droplet in frame, diameter, velocity, area, direction, sphericity and inf.

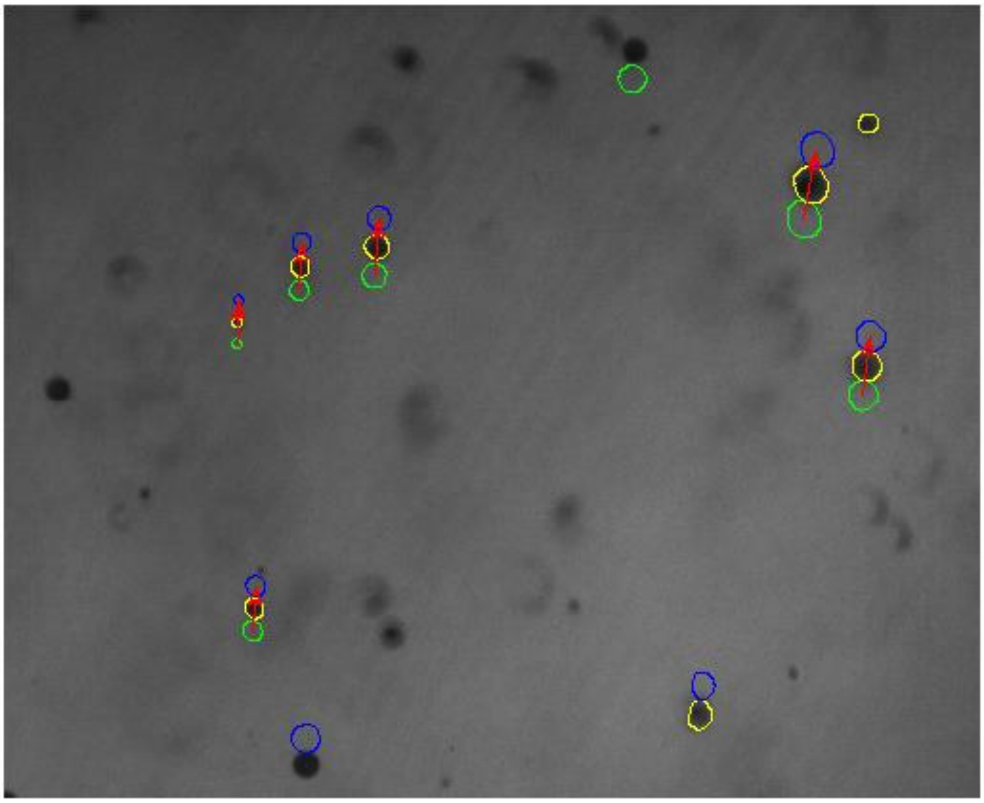

Figure 4.26: Vectors of droplet paths showing movement from frame $i + 1$ (blue contour) to frame $i - 1$ (green contour) of the droplets in frame i (yellow contour).

Chapter 5

Experimental results and discussion

This chapter describes the results from the experiments providing droplet size- and velocity distribution, mean droplet diameters and application water flux. The "K-factor" will be presented. In the end of the chapter, the results will be discussed and the accuracy of the method presented.

The fire water nozzle characterized in this research project is the Tyco MV34-110. The parameters varied are the supply water pressure, radial position and azimuthal angle where the range of the experiments and the intervals are shown in Table 5.1. The measurements are performed 100 cm below the tip of the nozzle because this is a reference location for comparison and a wish from our sponsors.

Table 5.1: Range of parameters for the experiments

Parameter	Range	Interval
Water pressure	2.0-8.0 bar(g)	3.0 bar
Radial distance	0-150 cm	10 cm
Azimuthal angle	0-90°	15°

The location of the measurement points are shown in Figure 5.1 where the lines cross (dotted circles and lines). The experimental results are presented in one chapter for each water pressure series. For each pressure series, 112 measurements are performed giving measurements for every azimuthal angle and radial position.

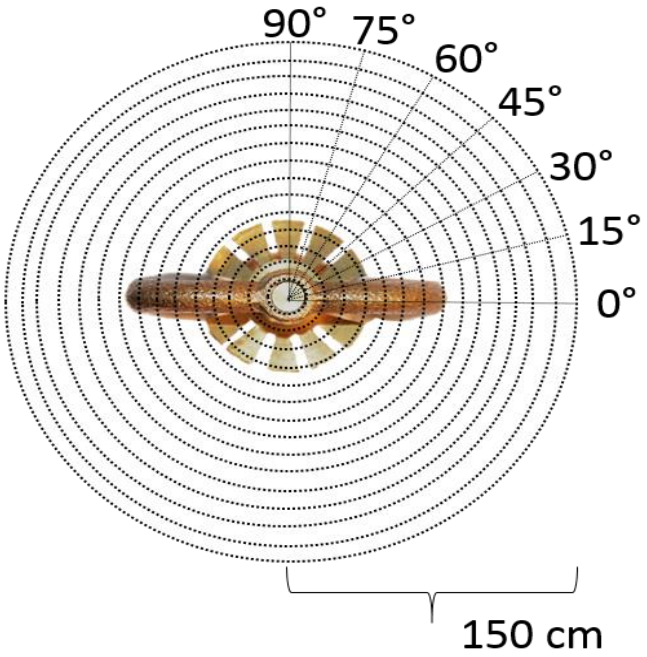

Figure 5.1: The location of the measurement points where the lines cross. Nozzle is included for illustration of the orientation.

To illustrate the orientation of the tines and frame arms, the fire water nozzle is included in Figure 5.1. This geometrical feature is expected to affect the measurements.

The results are found using the image processing code described in Chapter 4.

The results will report the following parameters:

- Mean diameters (arithmetic- (d_{10}), Sauter- (d_{32}) and De Brouckere mean (d_{43}))
- Applied mass flux
- Arithmetic mean angle of the droplet path
- Mass weighted velocity
- Droplet size distribution
- Total droplet size distribution azimuthal
- Total droplet size distribution radial
- Mass weighted velocity distribution

Figure 5.2 shows images of the fire water spray from the different pressure series. The images show a denser spray with increasing pressure.

Preliminary results from this research project are published in two papers. These are provided in appendix 1 and 2.

2.0 Bar(g)

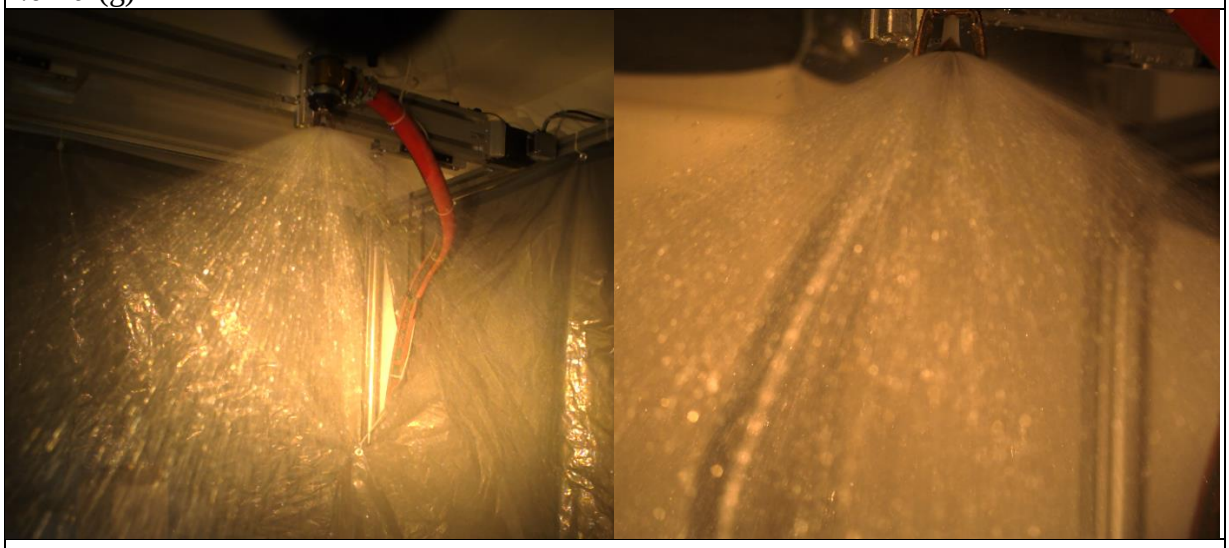

5.0 bar(g)

8.0 Bar(g)

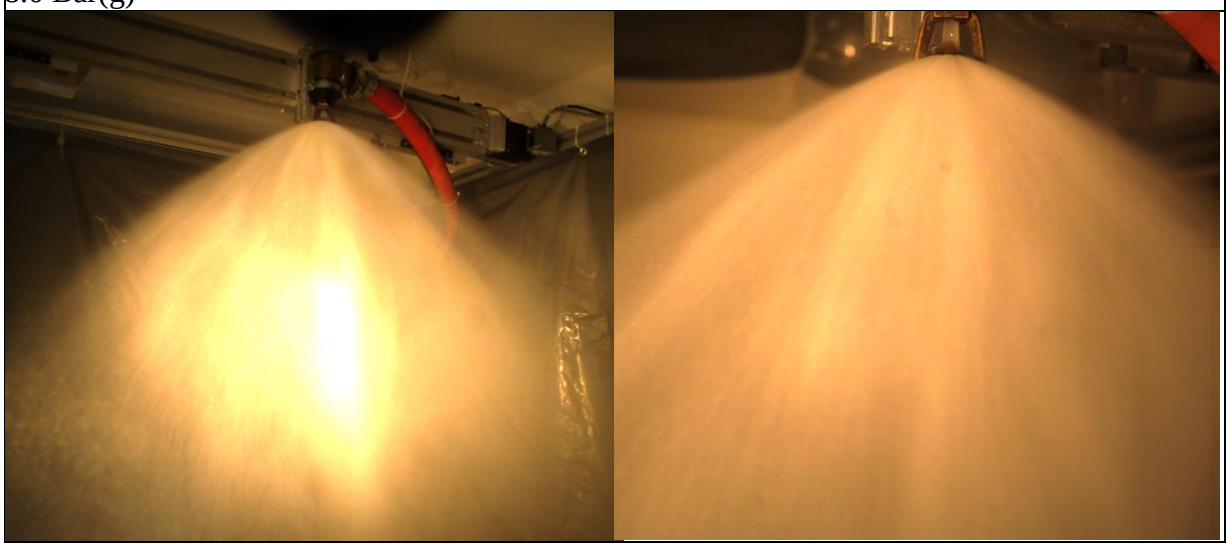

Figure 5.2: Images of the spray at different supply water pressures (pressure indicated above).

5.1 Experimental results 2.0 bar(g)

The water pressure of 2.0 bar(g) on the Tyco MV34-110 fire water nozzle was measured to give a volumetric flow rate of 80 dm^3/min. The temperature of the water used was 12° C, and the water was normal tap water without additions.

Table 5.2: The number of droplets counted in the 2.0 bar(g) measurement series. Columns for every azimuthal angle and rows for radial distance.

no / cm	2.0bar0deg	2.0bar15deg	2.0bar30deg	2.0bar45deg	2.0bar60deg	2.0bar75deg	2.0bar90deg
0	1276	1949	1357	1734	1510	2116	2510
10	1940	1572	1858	1757	1458	1643	2411
20	1825	1648	1949	1639	1836	1481	1581
30	1109	1622	1690	2214	1595	1573	1918
40	1015	1758	1645	1617	1771	1347	1978
50	1803	1460	1686	1374	1099	1463	1667
60	505	1417	1046	1373	854	1119	1244
70	336	728	979	952	866	859	714
80	169	564	709	631	557	520	612
90	89	414	585	397	355	484	410
100	88	313	381	332	277	401	286
110	65	340	336	363	479	332	317
120	51	179	303	177	331	225	339
130	8	91	174	120	207	72	216
140	38	26	62	16	120	24	65
150	5	12	26	13	29	13	14

Table 5.2 reports the number of droplets in the readings for every location in the 2.0 bar(g) measurement series. The arithmetic mean diameter from 2.0 bar(g) series is shown in Table 5.3.

Table 5.4 shows the Sauter mean diameter and Table 5.5 shows the De Brouckere mean diameter for the 2.0 bar(g) measurement series.

Table 5.6 shows the applied water flux for the 2.0 bar(g) measurement series. In Figure 5.3, the results are presented in polar coordinates and are mirrored on both axes to illustrate the pattern of the spray.

The arithmetic mean angle of the droplets and the mass-weighted velocities in measurement series 2.0 bar(g) are shown in Table 5.7 and Table 5.8, respectively.

Table 5.3: Arithmetic mean diameter of 2.0 bar(g) measurement series. Columns for every azimuthal angle and rows for radial distance.

µm / cm	2.0bar0deg	2.0bar15deg	2.0bar30deg	2.0bar45deg	2.0bar60deg	2.0bar75deg	2.0bar90deg
0	249	246	290	270	262	263	277
10	231	264	262	260	271	252	251
20	237	235	224	255	233	231	219
30	307	250	276	251	249	261	242
40	309	271	301	288	250	294	287
50	280	279	296	296	291	286	294
60	340	326	325	285	311	308	292
70	439	380	363	350	321	351	332
80	471	468	447	425	385	497	360
90	527	535	501	535	441	539	418
100	510	578	680	604	535	575	524
110	688	865	641	511	427	553	556
120	370	1187	778	638	578	714	585
130	1420	1276	1066	578	737	763	663
140	153	1475	1148	952	894	1164	939
150	124	1690	784	674	1081	630	1150

Table 5.4: Sauter mean diameter of 2.0 bar(g) measurement series. Columns for every azimuthal angle and rows for radial distance.

µm / cm	2.0bar0deg	2.0bar15deg	2.0bar30deg	2.0bar45deg	2.0bar60deg	2.0bar75deg	2.0bar90deg
0	599	878	1176	1086	762	641	834
10	454	609	785	628	637	622	461
20	454	464	775	457	523	418	408
30	589	425	552	454	426	500	445
40	538	560	733	548	492	608	627
50	406	556	593	644	433	558	521
60	472	612	623	557	455	588	456
70	590	664	749	606	452	623	468
80	606	737	717	616	550	872	454
90	738	856	944	928	585	841	490
100	784	862	1076	894	790	826	600
110	2144	1579	1146	861	678	775	737
120	3047	2116	1665	939	796	948	850
130	1695	2268	1953	1044	1126	975	1041
140	155	2113	1492	1143	1147	1351	1228
150	125	2423	1980	1391	1194	1291	1236

Table 5.5: De Brouckere mean diameter of 2.0 bar(g) measurement series. Columns for every azimuthal angle and rows for radial distance.

µm / cm	2.0bar0deg	2.0bar15deg	2.0bar30deg	2.0bar45deg	2.0bar60deg	2.0bar75deg	2.0bar90deg
0	925	1683	1920	2103	1301	1180	1660
10	639	964	1325	1125	1017	1010	794
20	729	737	1796	609	1046	547	542
30	792	590	785	648	539	674	594
40	699	891	1405	784	696	873	915
50	536	831	887	936	555	835	736
60	567	878	882	755	576	963	608
70	757	908	1115	825	588	848	581
80	662	905	854	743	682	1222	514
90	849	1091	1329	1378	675	1080	529
100	940	1018	1255	1017	987	949	635
110	2488	1854	1366	970	766	859	835
120	3831	2422	2085	1016	849	1022	957
130	1780	2601	2319	1146	1320	1018	1215
140	156	2323	1595	1203	1232	1479	1315
150	125	2716	2259	1459	1248	1393	1279

Table 5.6: Applied water flux of 2.0 bar(g) measurement series. Columns for every azimuthal angle and rows for radial distance.

$dm^3/(m^2 \cdot min)$ / cm	2.0bar0deg	2.0bar15deg	2.0bar30deg	2.0bar45deg	2.0bar60deg	2.0bar75deg	2.0bar90deg
0	10.1	17.5	20.2	18.0	12.3	15.3	21.3
10	10.5	13.8	17.8	12.9	14.0	13.5	13.2
20	12.1	10.8	15.3	13.2	12.3	8.5	9.7
30	13.8	10.9	17.8	21.4	14.0	16.8	17.3
40	11.4	20.5	23.0	19.4	17.2	21.0	32.0
50	11.2	16.8	19.3	22.1	8.8	18.3	18.7
60	4.8	21.1	12.1	17.8	6.1	14.0	10.4
70	4.8	14.7	13.1	14.3	6.5	14.2	6.8
80	3.1	18.1	12.2	14.1	6.7	19.0	6.3
90	2.5	17.0	14.3	16.1	5.7	18.6	5.1
100	2.5	14.4	16.2	17.5	7.5	16.9	7.3
110	6.2	38.4	15.8	14.3	9.6	12.6	11.3
120	1.9	40.4	28.6	9.4	13.2	14.4	14.4
130	1.0	23.3	30.0	6.0	15.3	5.1	13.1
140	0.0	6.9	10.2	1.7	11.7	4.0	7.9
150	0.0	3.8	3.7	1.2	3.5	0.9	2.1

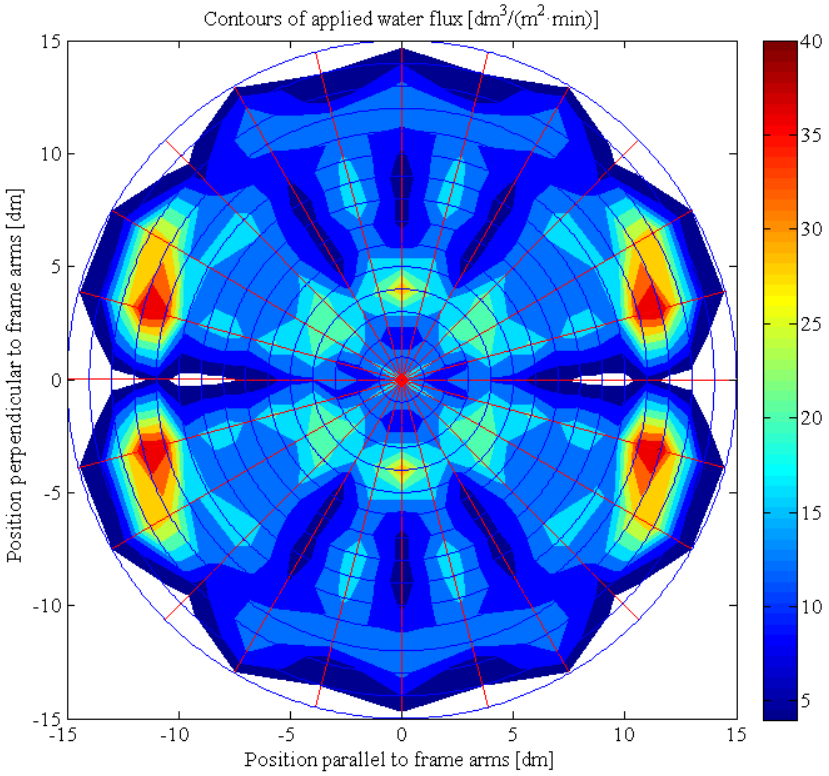

Figure 5.3: Applied water flux, $\dot{q}_{tot}$, in $[dm^3/(m^2 \cdot min)]$ at 2.0 bar(g).

Table 5.7: Mean angle of the droplets in the 2.0 bar(g) measurement series. Columns for every azimuthal angle and rows for radial distance.

deg / cm	2.0bar0deg	2.0bar15deg	2.0bar30deg	2.0bar45deg	2.0bar60deg	2.0bar75deg	2.0bar90deg
0	10.7	2.0	2.9	6.0	3.6	0.1	-1.5
10	3.4	-4.3	0.1	4.9	2.9	5.9	3.9
20	0.2	3.4	3.8	-1.3	6.2	9.8	8.6
30	-0.1	1.9	2.8	4.7	3.6	3.8	6.8
40	1.1	6.7	9.5	14.3	7.0	3.2	8.1
50	6.6	13.1	13.6	13.1	8.2	8.1	18.5
60	9.2	15.2	12.3	15.3	12.2	15.0	16.1
70	8.6	17.2	14.7	16.6	17.1	21.7	16.8
80	16.4	17.9	19.1	21.8	17.6	20.2	22.8
90	18.4	25.5	20.8	24.3	22.0	25.7	22.9
100	26.1	30.8	23.8	28.9	22.2	27.8	25.8
110	35.9	35.9	30.3	32.1	19.9	30.3	31.7
120	23.4	35.9	32.7	32.5	35.4	33.5	31.2
130	-1.1	41.0	40.7	49.1	38.0	40.1	37.0
140	90.5	68.3	47.3	51.3	45.2	43.4	41.6
150	127.5	40.5	56.5	69.7	26.9	49.8	88.7

Table 5.8: Mass-weighted mean velocity in the 2.0 bar(g) measurement series. Columns for every azimuthal angle and rows for radial distance.

m/s / cm	2.0bar0deg	2.0bar15deg	2.0bar30deg	2.0bar45deg	2.0bar60deg	2.0bar75deg	2.0bar90deg
0	5.8	5.8	5.8	5.5	5.2	5.0	5.1
10	5.1	5.8	5.6	5.4	5.9	5.7	4.7
20	6.0	5.9	6.5	6.4	5.9	5.4	6.4
30	6.4	6.0	7.0	8.9	7.6	8.0	8.2
40	6.2	9.7	8.9	9.0	9.1	9.8	10.6
50	5.2	8.9	7.5	10.2	6.1	9.1	8.3
60	4.8	8.8	6.1	9.1	4.7	8.8	6.6
70	4.2	8.5	5.6	7.8	4.7	8.3	5.7
80	4.6	8.6	4.3	7.7	4.5	8.7	5.0
90	5.9	8.7	5.1	8.4	4.7	7.9	4.3
100	6.7	8.2	4.4	8.4	5.2	7.7	5.9
110	6.6	7.5	5.7	8.4	6.4	7.6	7.5
120	6.9	7.7	7.1	7.6	7.4	7.9	7.4
130	3.7	7.9	7.9	7.9	8.0	7.8	8.1
140	0.5	6.8	8.0	8.0	8.4	9.1	9.1
150	0.7	7.0	9.5	8.9	8.1	8.8	8.9

The local droplet size distribution for every measurement point in the 2.0 bar(g) measurement series for one azimuthal angle is shown in Figure 5.4. The local droplet size distributions are shown in Appendix 3.

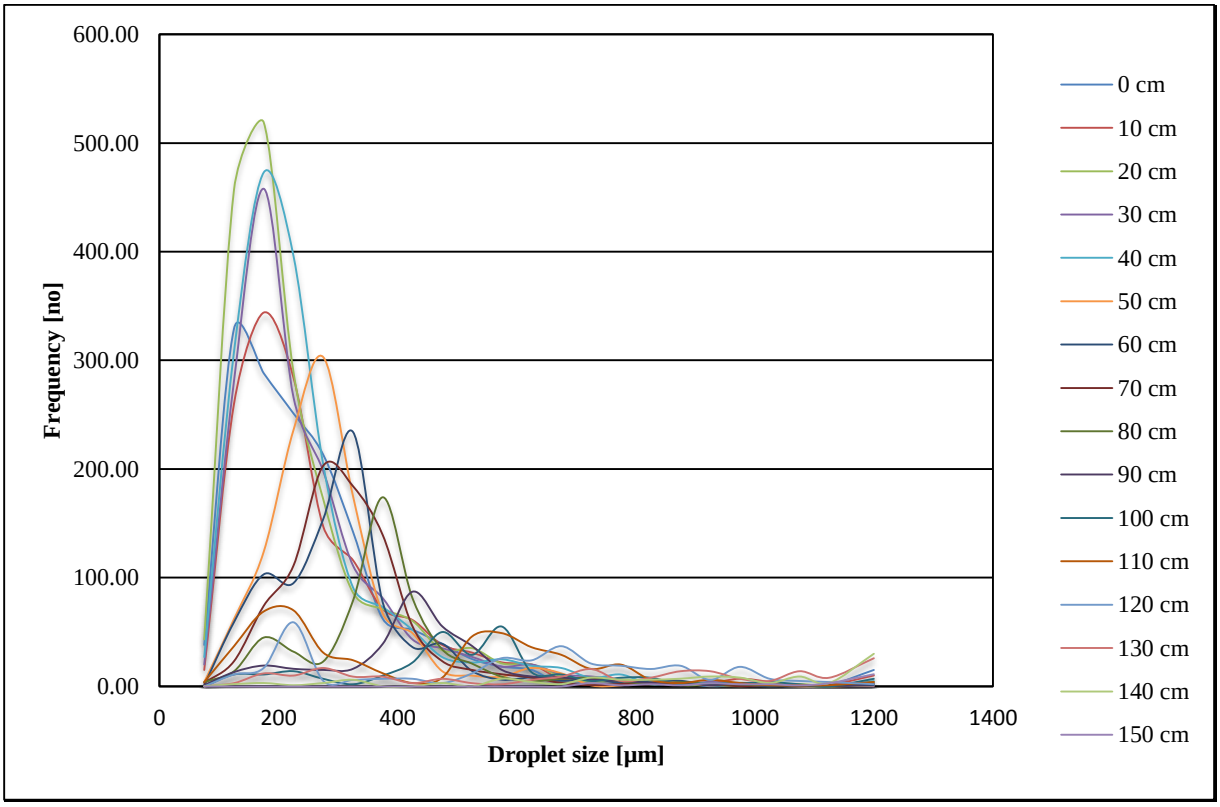

Figure 5.4: Droplet size distribution at 2.0 bar(g) and 60° for different radial positions.

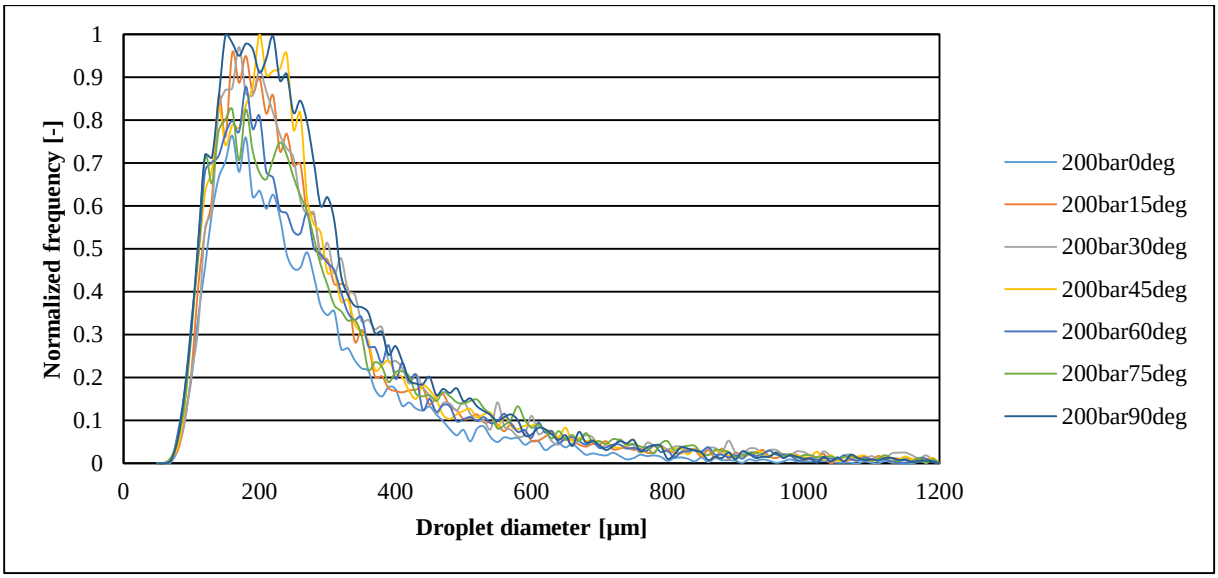

Figure 5.5: Total droplet size distribution for every azimuthal angle for the 2.0 bar(g) measurement series.

Figure 5.5 shows the total size distribution for every azimuthal angle and is normalized by dividing all the readings by the most frequent measurement. The same normalization is done in Figure 5.6 for the total size distribution for every radial distance.

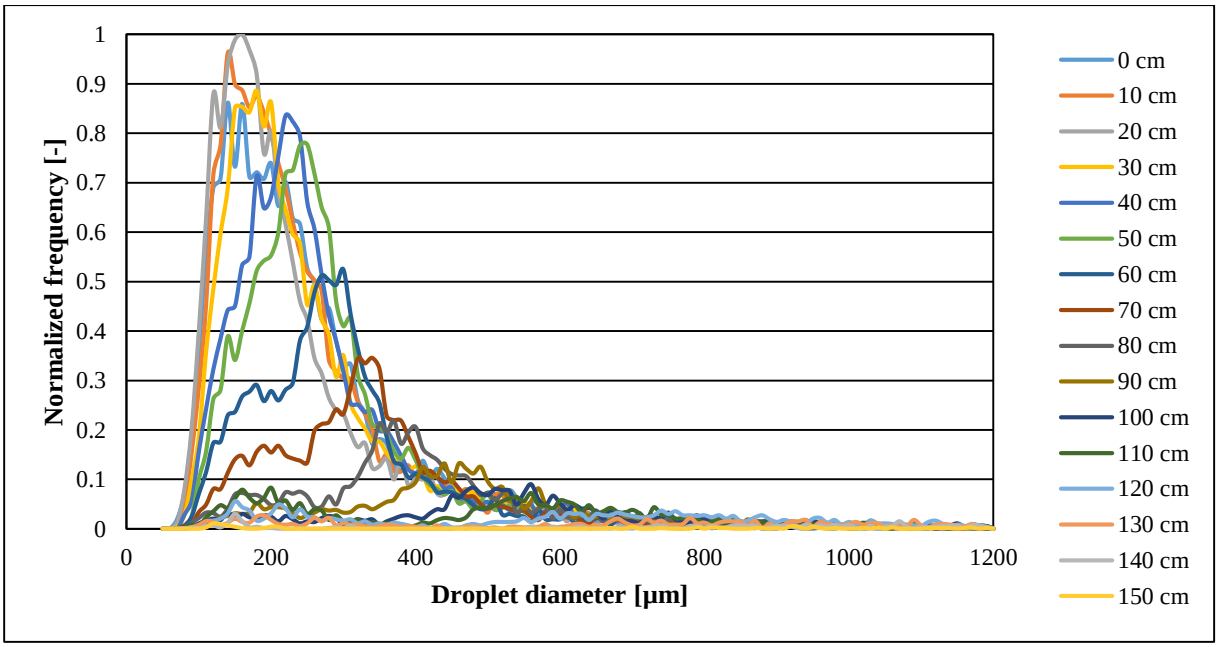

Figure 5.6: Total droplet size distribution for every radial position for the 2.0 bar(g) measurement series.

The mass-weighted mean velocity of the corresponding droplet diameter interval is shown in Figure 5.7 for every azimuthal angle. The figure is from the 2.0 bar(g) measurement series.

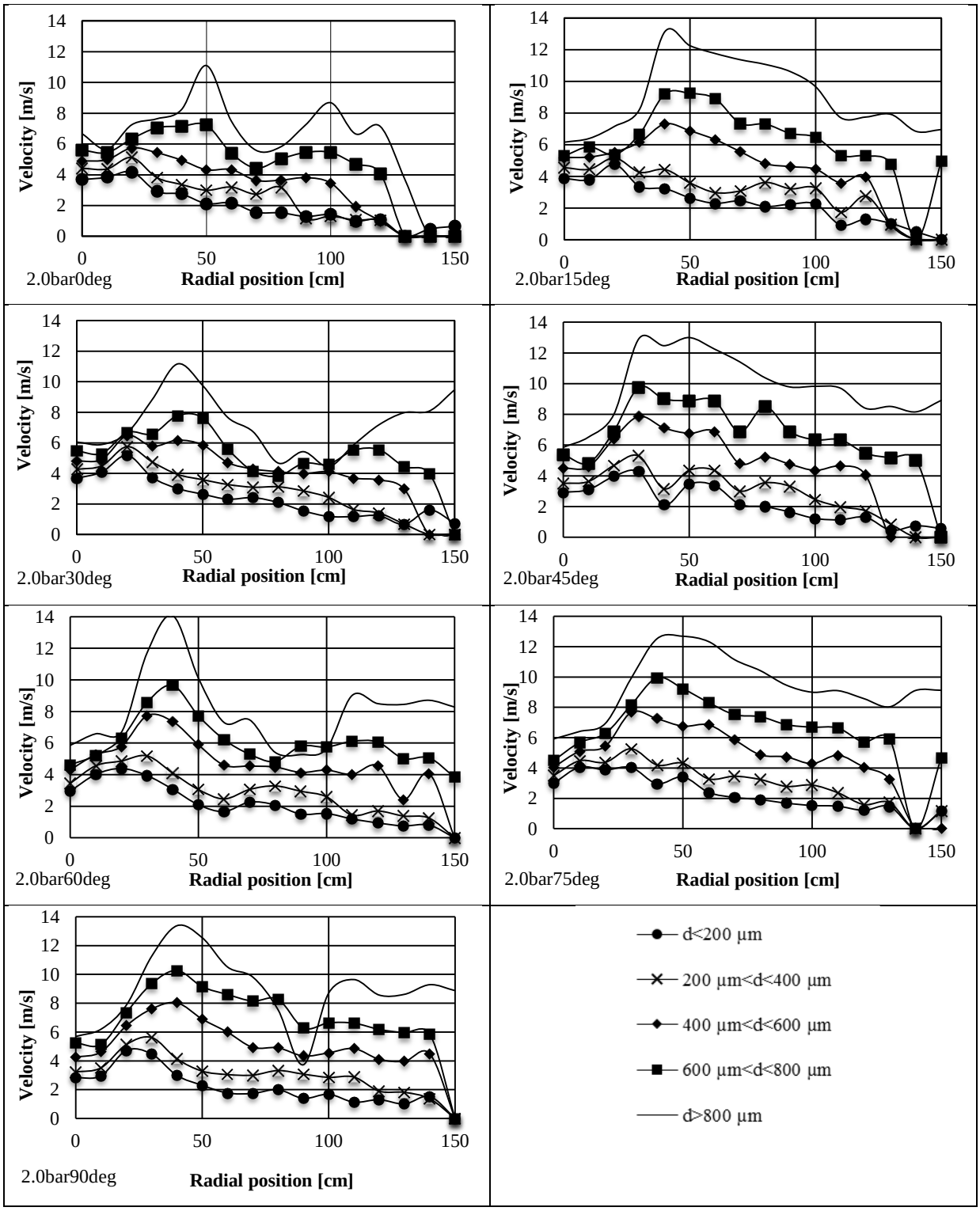

Figure 5.7: Mass-averaged velocity distribution for the 2.0 bar(g) run.

5.2 Experimental results 5.0 bar(g)

The water pressure of 5.0 bar(g) on the Tyco MV34-110 fire water nozzle was measured to give a volumetric flow rate of 126 dm^3/min. The temperature of the water used was 12° C, and the water was normal tap water without additions.

Table 5.9: The number of droplets counted in the 5.0 bar(g) measurement series. Columns for every azimuthal angle and rows for radial distance.

no / cm	5.0bar0deg	5.0bar15deg	5.0bar30deg	5.0bar45deg	5.0bar60deg	5.0bar75deg	5.0bar90deg
0	777	586	816	939	1457	2230	1900
10	1291	1114	919	532	931	1517	1816
20	1219	1136	562	2412	1202	1445	719
30	848	2271	1971	2046	3022	1177	1763
40	1743	1734	2480	1402	3087	1531	2485
50	2931	1702	1945	1941	1308	1914	1657
60	2846	1842	2155	3045	1541	1726	2723
70	1279	1198	1688	3311	2324	2653	1739
80	349	1076	1563	2760	1264	2481	2145
90	313	1146	753	1511	950	1345	2046
100	18	1116	705	679	789	767	875
110	77	719	809	439	579	464	824
120	11	135	238	75	271	170	471
130	34	56	26	18	89	60	139
140	36	35	26	10	20	12	150
150	32	8	6	17	28	9	17

Table 5.9 reports the number of droplets in the readings for every location in the 5.0 bar(g) measurement series. The arithmetic mean diameter from 5.0 bar(g) series is shown in Table 5.10.

Table 5.11 shows the Sauter mean diameter and Table 5.12 shows the De Brouckere mean diameter for the 5.0 bar(g) measurement series.

Table 5.13 shows the applied water flux for the 5.0 bar(g) measurement series. In Figure 5.8, the results are presented in polar coordinates and are mirrored on both axes to illustrate the pattern of the spray.

The arithmetic mean angle of the droplets and the mass-weighted velocities in measurement series 5.0 bar(g) are shown in Table 5.14 and Table 5.15, respectively.

Table 5.10: Arithmetic mean diameter of 5.0 bar(g) measurement series. Columns for every azimuthal angle and rows for radial distance.

µm / cm	5.0bar0deg	5.0bar15deg	5.0bar30deg	5.0bar45deg	5.0bar60deg	5.0bar75deg	5.0bar90deg
0	200	228	188	189	209	200	194
10	230	200	220	238	218	207	216
20	199	209	259	198	236	229	251
30	205	196	218	221	230	226	244
40	185	236	232	244	208	277	215
50	228	265	257	251	251	238	227
60	244	284	235	267	242	256	230
70	263	337	303	287	271	262	292
80	310	404	383	354	355	331	295
90	291	430	484	482	412	451	348
100	397	492	590	496	499	535	502
110	356	532	494	526	530	531	545
120	167	604	752	540	621	545	568
130	191	197	788	175	386	487	530
140	154	411	158	368	621	206	198
150	158	148	869	222	167	196	171

Table 5.11: Sauter mean diameter of 5.0 bar(g) measurement series. Columns for every azimuthal angle and rows for radial distance.

µm / cm	5.0bar0deg	5.0bar15deg	5.0bar30deg	5.0bar45deg	5.0bar60deg	5.0bar75deg	5.0bar90deg
0	341	413	407	502	295	334	350
10	349	339	376	422	353	301	333
20	396	405	472	342	493	393	459
30	300	323	410	425	383	406	416
40	255	383	391	463	324	447	364
50	302	566	430	424	385	425	372
60	312	652	326	417	350	422	310
70	355	643	402	425	345	363	360
80	459	681	561	475	443	441	382
90	462	613	633	639	469	563	433
100	537	619	950	665	567	651	588
110	751	656	728	643	652	686	648
120	203	704	1350	678	734	686	708
130	200	256	1329	181	723	738	733
140	166	1036	204	583	744	570	527
150	171	151	1192	521	472	237	187

Table 5.12: De Brouckere mean diameter of 5.0 bar(g) measurement series. Columns for every azimuthal angle and rows for radial distance.

µm / cm	5.0bar0deg	5.0bar15deg	5.0bar30deg	5.0bar45deg	5.0bar60deg	5.0bar75deg	5.0bar90deg
0	442	546	749	1340	351	444	657
10	436	452	499	547	460	361	429
20	564	602	588	451	753	510	591
30	378	424	549	567	482	517	531
40	312	503	517	639	457	564	466
50	374	876	606	551	495	579	533
60	363	974	417	542	436	562	375
70	417	857	485	517	390	449	407
80	579	876	706	559	502	523	443
90	567	715	773	753	498	630	475
100	562	682	1253	778	602	713	624
110	962	716	889	684	694	790	692
120	218	735	1764	724	770	721	746
130	203	289	1554	183	765	791	762
140	171	1144	227	619	781	707	677
150	177	152	1372	695	679	258	194

Table 5.13: Applied water flux of 5.0 bar(g) measurement series. Columns for every azimuthal angle and rows for radial distance.

$dm^3/(m^2 \cdot min)$ / cm	5.0bar0deg	5.0bar15deg	5.0bar30deg	5.0bar45deg	5.0bar60deg	5.0bar75deg	5.0bar90deg
0	3.4	3.0	2.7	3.2	5.1	7.6	5.4
10	5.9	5.1	4.4	3.7	4.8	5.0	7.2
20	7.9	5.8	5.8	14.9	8.2	7.7	5.8
30	3.8	12.6	17.3	24.5	19.9	5.4	11.7
40	5.3	17.4	22.6	15.5	16.3	15.2	17.1
50	13.4	29.4	18.4	17.3	9.5	15.1	10.2
60	12.1	38.8	11.0	30.1	7.2	14.8	11.5
70	7.7	31.6	13.1	40.9	14.4	17.6	11.3
80	3.0	34.6	22.4	43.5	13.9	31.5	16.1
90	2.2	36.2	17.2	48.3	14.3	32.5	21.7
100	0.3	32.4	27.9	18.0	18.1	27.7	22.0
110	1.2	23.6	21.8	12.2	18.4	14.0	28.5
120	0.0	4.8	17.0	2.1	11.6	5.3	16.4
130	0.0	0.0	2.0	0.0	1.8	1.5	4.2
140	0.0	0.8	0.0	0.1	0.7	0.1	0.5
150	0.0	0.0	0.3	0.0	0.0	0.0	0.0

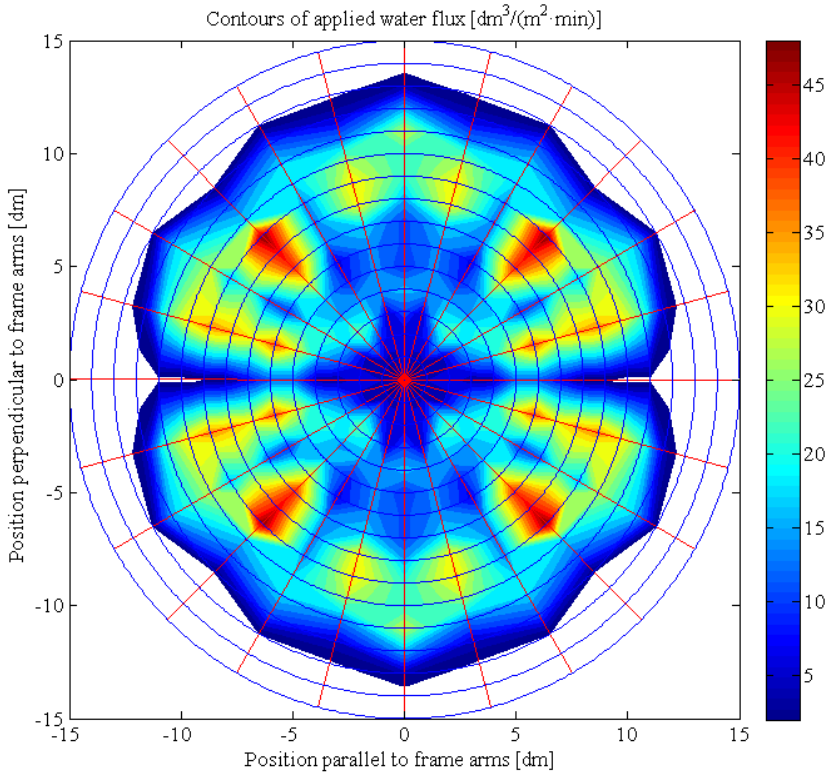

Figure 5.8: Applied water flux, $\dot{q}_{tot}$, in $[dm^3/(m^2 \cdot min)]$ at 5.0 bar(g).

Table 5.14: Mean angle of the droplets in the 5.0 bar(g) measurement series. Columns for every azimuthal angle and rows for radial distance.

deg / cm	5.0bar0deg	5.0bar15deg	5.0bar30deg	5.0bar45deg	5.0bar60deg	5.0bar75deg	5.0bar90deg
0	9.8	6.9	9.5	12.8	-2.0	3.6	0.2
10	0.4	11.5	5.6	11.0	7.9	16.3	14.4
20	2.0	11.7	5.1	3.8	10.2	3.8	13.8
30	-3.2	3.4	7.6	10.6	15.1	30.0	20.5
40	0.0	2.7	12.4	6.4	1.2	26.4	9.8
50	3.7	9.6	6.5	9.6	5.0	15.2	6.9
60	10.2	13.1	15.4	13.0	6.7	12.6	13.0
70	12.9	15.7	12.5	17.4	17.1	16.7	13.1
80	12.7	21.1	17.6	22.0	12.4	22.3	19.9
90	23.7	27.9	20.8	27.4	21.2	24.0	25.9
100	21.6	32.8	30.1	31.4	27.6	29.4	25.6
110	26.1	34.1	35.5	32.6	31.7	28.5	32.8
120	0.7	36.6	40.1	42.7	37.0	32.7	36.4
130	40.9	94.4	61.8	-64.9	37.3	40.5	49.6
140	116.6	28.9	-61.2	74.9	37.3	20.5	74.7
150	87.5	93.0	64.3	61.5	95.5	14.6	-10.6

Table 5.15: Mass-weighted mean velocity in the 5.0 bar(g) measurement series. Columns for every azimuthal angle and row for radial distance.

m/s / cm	5.0bar0deg	5.0bar15deg	5.0bar30deg	5.0bar45deg	5.0bar60deg	5.0bar75deg	5.0bar90deg
0	4.8	5.1	4.7	4.3	4.1	4.0	3.9
10	4.9	5.0	4.8	4.4	5.1	5.0	4.3
20	5.7	5.5	6.3	6.0	5.6	5.2	6.1
30	5.1	5.6	5.6	7.2	7.1	7.1	7.3
40	4.2	6.4	5.5	6.0	6.5	6.5	7.2
50	3.9	5.8	5.2	6.1	4.6	6.0	5.5
60	3.9	5.0	4.1	6.0	3.5	5.5	4.6
70	3.5	4.5	3.7	4.0	3.8	4.8	4.0
80	3.6	4.7	3.7	4.9	4.0	4.7	4.3
90	3.7	4.5	3.8	4.7	4.0	4.7	4.2
100	3.2	4.4	4.0	4.3	4.2	4.2	4.5
110	1.7	3.5	3.6	4.6	3.8	4.8	4.8
120	1.0	3.9	3.3	3.5	4.4	3.7	3.9
130	0.0	1.0	2.5	0.8	2.2	2.8	3.6
140	0.0	0.0	0.0	0.0	3.8	0.0	4.5
150	0.0	0.0	0.0	0.0	0.0	0.0	0.0

The local droplet size distribution for every measurement point in the 5.0 bar(g) measurement series for one azimuthal angle is shown in Figure 5.9. The local droplet size distributions is shown in Appendix 3.

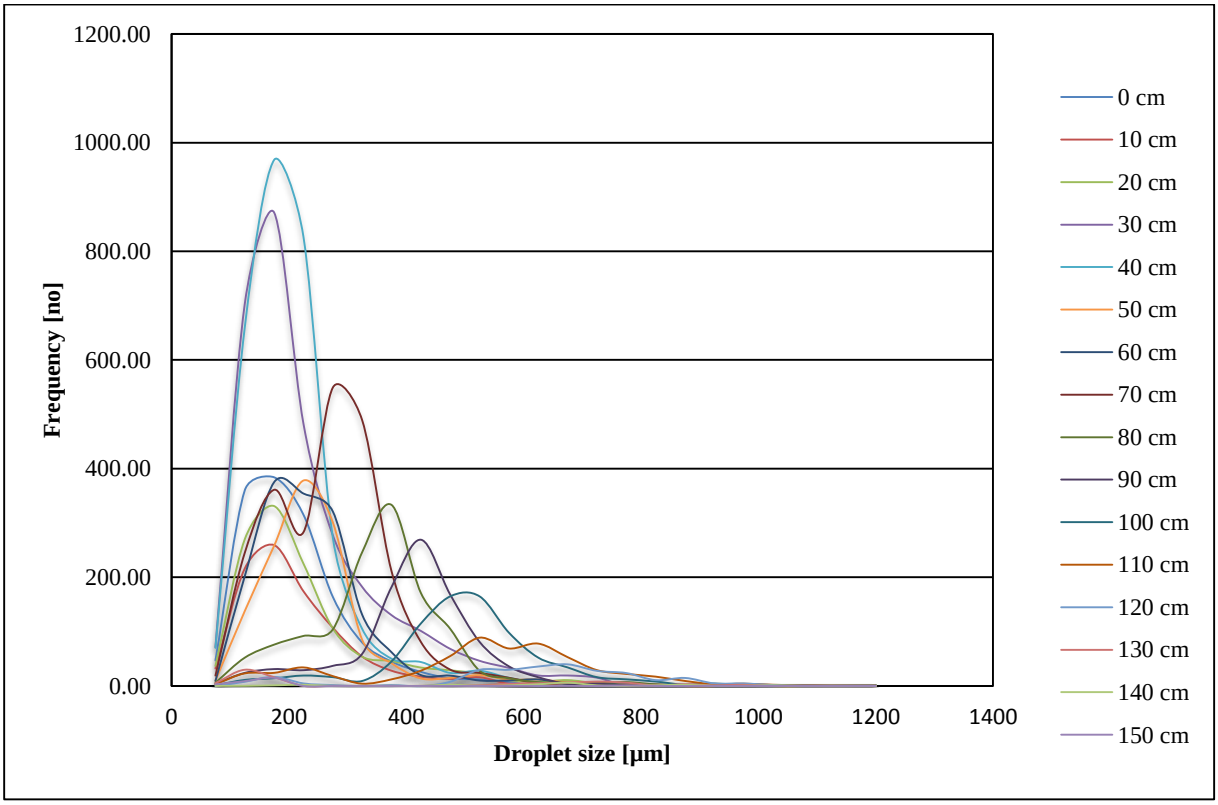

Figure 5.9: Droplet size distribution at 5.0 bar(g) and 60° for different radial positions.

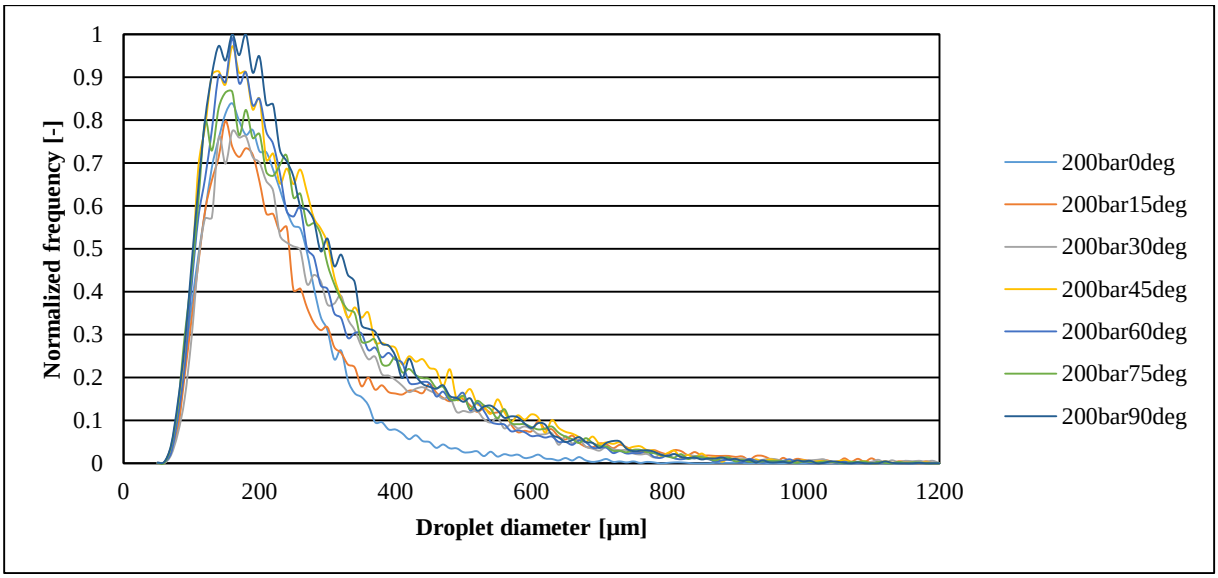

Figure 5.10: Total droplet size distribution for every azimuthal angle for the 5.0 bar(g) measurement series.

Figure 5.10 shows the total size distribution for every azimuthal angle and is normalized by dividing all the readings by the most frequent measurement. The same normalization is done in Figure 5.11 for the total size distribution for every radial distance.

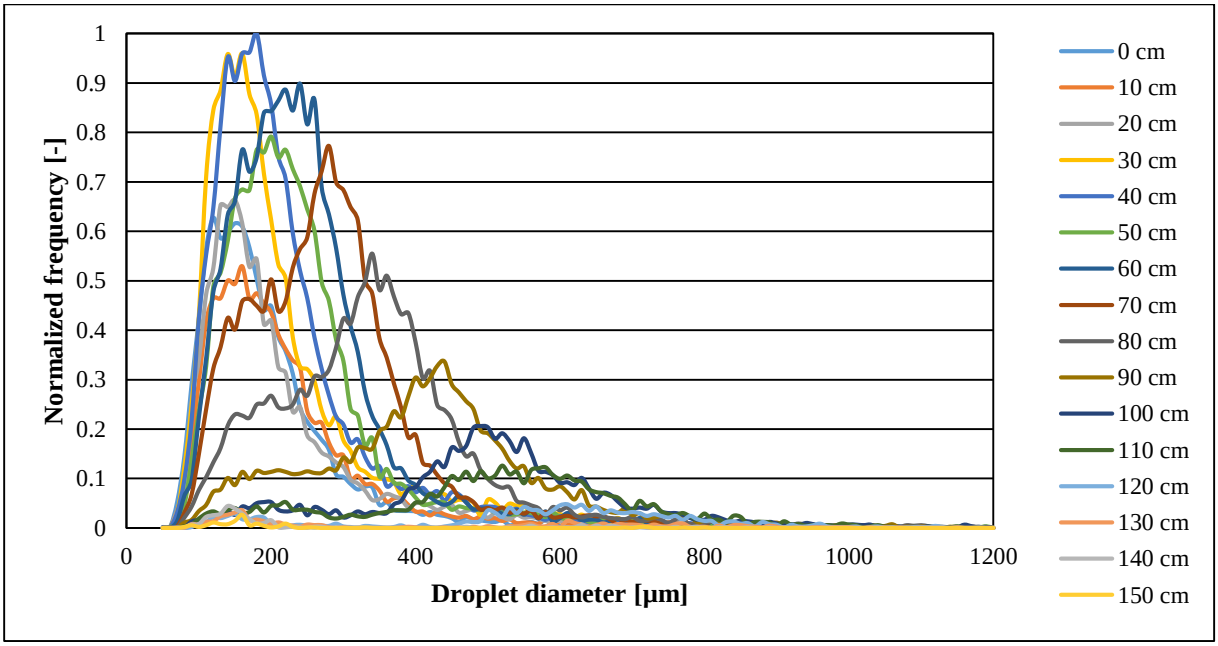

Figure 5.11: Total droplet size distribution for every radial distance for the 5.0 bar(g) measurement series.

The mass-weighted mean velocity of the corresponding droplet diameter interval is shown in Figure 5.12 for every azimuthal angle. The figure is from the 5.0 bar(g) measurement series.

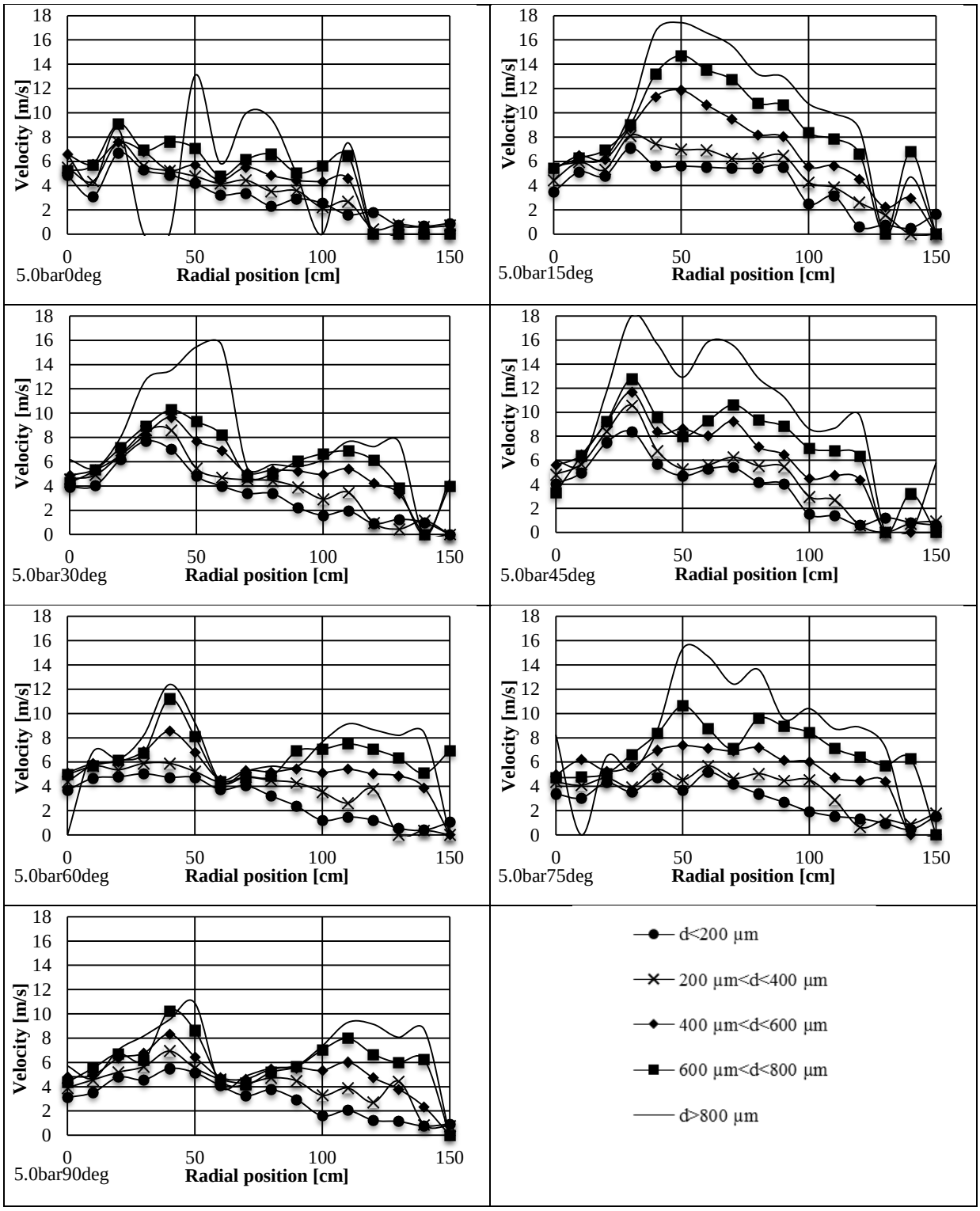

Figure 5.12: Mass-averaged velocity distribution for the 5.0 bar(g) run.

5.3 Experimental results 8.0 bar(g)

The water pressure of 8.0 bar(g) on the Tyco MV34-110 fire water nozzle was measured to give a volumetric flow rate of 161dm^3/min. The temperature of the water used was 12° C, and the water was normal tap water without additions.

Table 5.16: The number of droplets counted in the 8.0 bar(g) measurement series. Columns for every azimuthal angle and rows for radial distance.

no / cm	8.0bar0deg	8.0bar15deg	8.0bar30deg	8.0bar45deg	8.0bar60deg	8.0bar75deg	8.0bar90deg
0	643	600	758	352	555	892	1747
10	115	1104	1400	1208	944	1278	1955
20	216	1070	683	591	333	968	688
30	515	1575	1242	1462	684	278	359
40	615	1915	1536	1590	1786	715	2064
50	2413	1665	3091	2305	2298	2280	1647
60	2636	2256	3484	3125	3236	2243	3103
70	1747	2949	3275	2448	952	2269	4761
80	526	3413	1908	1779	1122	2062	3767
90	348	2829	784	458	914	1180	1932
100	167	707	199	135	203	292	346
110	259	55	126	189	219	308	291
120	56	133	99	35	135	153	112
130	16	58	64	157	42	177	76
140	11	26	43	20	86	61	151
150	27	29	174	12	41	17	8

Table 5.16 reports the number of droplets in the readings for every location in the 8.0 bar(g) measurement series. The arithmetic mean diameter from 8.0 bar(g) series is shown in Table 5.17.

Table 5.18 shows the Sauter mean diameter and Table 5.19 shows the De Brouckere mean diameter for the 8.0 bar(g) measurement series.

Table 5.20 shows the applied water flux for the 8.0 bar(g) measurement series. In Figure 5.13, the results are presented in polar coordinates and are mirrored on both axes to illustrate the pattern of the spray.

The arithmetic mean angle of the droplets and the mass-weighted velocities in measurement series 8.0 bar(g) are shown in Table 5.21 and Table 5.22, respectively.

Table 5.17: Arithmetic mean diameter of 8.0 bar(g) measurement series. Columns for every azimuthal angle and rows for radial distance.

µm / cm	8.0bar0deg	8.0bar15deg	8.0bar30deg	8.0bar45deg	8.0bar60deg	8.0bar75deg	8.0bar90deg
0	180	185	186	203	214	204	191
10	222	196	195	201	196	207	204
20	230	190	176	209	235	234	213
30	193	201	211	212	222	232	235
40	227	223	229	225	234	275	238
50	240	241	249	238	219	232	238
60	248	272	286	258	255	263	257
70	261	316	339	300	313	299	280
80	360	320	374	397	370	386	326
90	388	367	473	422	411	422	378
100	302	495	323	725	472	402	497
110	254	679	281	320	335	409	429
120	297	501	345	270	287	327	371
130	371	412	221	203	333	233	324
140	194	314	142	236	199	195	186
150	143	156	166	219	180	164	229

Table 5.18: Sauter mean diameter of 8.0 bar(g) measurement series. Columns for every azimuthal angle and rows for radial distance.

µm / cm	8.0bar0deg	8.0bar15deg	8.0bar30deg	8.0bar45deg	8.0bar60deg	8.0bar75deg	8.0bar90deg
0	292	288	309	283	292	321	289
10	268	276	286	306	291	322	304
20	315	353	289	359	343	303	347
30	316	344	396	373	415	356	316
40	388	372	377	375	399	454	400
50	369	421	394	373	333	401	410
60	353	490	403	374	327	421	409
70	378	445	441	425	433	421	379
80	525	448	469	474	483	446	428
90	585	540	556	622	542	535	504
100	1489	639	615	1156	774	677	726
110	492	1119	504	499	511	537	591
120	940	1355	491	497	488	515	533
130	1220	1031	350	244	575	357	493
140	254	1605	157	255	297	278	297
150	164	170	212	246	200	176	251

Table 5.19: De Brouckere mean diameter of 8.0 bar(g) measurement series. Columns for every azimuthal angle and rows for radial distance.

µm / cm	8.0bar0deg	8.0bar15deg	8.0bar30deg	8.0bar45deg	8.0bar60deg	8.0bar75deg	8.0bar90deg
0	381	381	412	349	343	408	375
10	294	334	368	388	372	412	380
20	362	469	397	459	409	342	445
30	423	447	496	466	530	414	360
40	505	493	475	492	511	654	484
50	461	569	493	467	425	524	519
60	426	652	475	445	383	519	497
70	461	537	501	488	513	496	443
80	652	529	519	517	540	478	485
90	749	671	605	748	626	583	575
100	1993	719	752	1377	974	841	937
110	662	1359	563	542	555	567	636
120	1233	1818	528	567	537	576	567
130	1365	1276	409	272	614	440	548
140	278	1999	165	261	387	339	424
150	181	176	246	252	210	180	257

Table 5.20: Applied water flux of 8.0 bar(g) measurement series. Columns for every azimuthal angle and rows for radial distance.

$dm^3/(m^2 \cdot min)$ / cm	8.0bar0deg	8.0bar15deg	8.0bar30deg	8.0bar45deg	8.0bar60deg	8.0bar75deg	8.0bar90deg
0	2.6	2.0	2.5	1.2	1.2	2.5	4.8
10	0.2	3.0	3.8	4.0	3.0	5.2	9.4
20	0.8	6.1	2.5	3.2	1.4	2.8	3.9
30	3.5	13.2	12.9	16.3	3.3	0.7	1.3
40	5.3	16.9	14.8	13.6	14.9	2.8	21.0
50	17.1	16.0	30.8	19.7	14.6	20.2	16.3
60	20.2	31.0	37.4	27.2	22.8	18.2	25.8
70	10.7	44.5	37.5	32.4	9.3	24.6	39.2
80	5.6	52.1	27.7	31.9	14.9	35.8	36.8
90	4.4	63.8	14.1	8.6	15.7	23.7	26.8
100	3.0	25.0	2.3	7.5	5.2	5.2	7.6
110	1.0	2.4	1.1	2.2	2.7	6.1	7.6
120	0.6	5.0	0.6	0.2	1.0	1.5	1.4
130	0.1	1.3	0.1	0.1	0.4	0.4	0.5
140	0.0	0.5	0.0	0.0	0.1	0.0	0.1
150	0.0	0.0	0.0	0.0	0.0	0.0	0.0

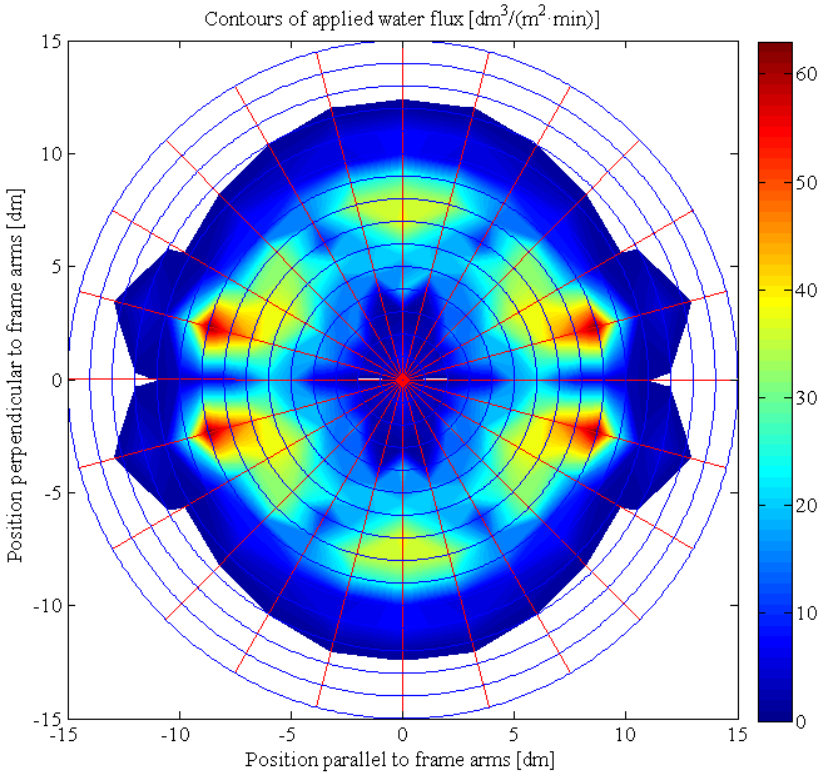

Figure 5.13: Applied water flux, $\dot{q}_{tot}$, in $[dm^3/(m^2 \cdot min)]$ at 8.0 bar(g).

Table 5.21: Mean angle of the droplets in the 8.0 bar(g) measurement series. Columns for every azimuthal angle and rows for radial distance.

deg / cm	8.0bar0deg	8.0bar15deg	8.0bar30deg	8.0bar45deg	8.0bar60deg	8.0bar75deg	8.0bar90deg
0	8.0	5.8	8.1	4.8	44.2	17.5	1.4
10	-38.5	12.2	1.9	12.7	12.8	18.6	8.8
20	18.5	2.9	9.4	8.2	-4.9	23.2	16.7
30	8.8	7.0	6.2	7.6	20.9	-11.0	35.6
40	7.7	7.8	8.3	8.8	3.6	54.0	16.2
50	7.2	12.7	11.8	7.9	6.4	8.7	10.6
60	9.1	9.6	14.3	11.9	9.8	13.9	13.4
70	5.7	15.5	17.2	16.7	11.5	16.0	18.7
80	8.1	22.9	22.1	17.7	19.7	20.3	19.6
90	16.1	24.5	26.4	17.0	17.4	24.6	28.1
100	10.6	28.2	22.4	28.0	18.8	23.9	20.0
110	18.6	27.3	20.1	16.7	19.6	23.7	25.3
120	32.3	58.3	60.1	2.9	16.3	21.6	21.5
130	23.1	77.1	58.7	33.6	0.9	21.4	7.3
140	73.4	76.1	66.4	45.1	66.4	-7.4	56.7
150	106.6	106.2	-49.4	59.1	32.0	70.9	-23.5

Table 5.22: Mass-weighted mean velocity in the 8.0 bar(g) measurement series. Columns for every azimuthal angle and rows for radial distance.

m/s / cm	8.0bar0deg	8.0bar15deg	8.0bar30deg	8.0bar45deg	8.0bar60deg	8.0bar75deg	8.0bar90deg
0	6.8	5.6	5.3	4.9	3.1	4.0	4.2
10	2.5	4.2	4.3	5.0	4.9	5.3	6.3
20	3.9	8.1	7.0	6.1	4.4	3.5	6.8
30	9.9	10.6	10.8	12.1	6.4	2.5	4.2
40	8.2	10.5	10.7	8.6	7.9	4.5	11.6
50	6.3	10.4	8.3	8.0	7.6	9.2	8.8
60	7.0	10.0	7.5	7.0	6.2	6.9	7.3
70	4.9	8.7	5.5	8.0	5.2	6.5	6.0
80	4.2	8.8	6.0	6.9	5.3	7.1	5.1
90	4.4	9.9	4.9	5.6	5.7	6.6	5.7
100	6.2	9.0	5.5	5.4	5.8	5.6	4.8
110	3.9	4.5	6.1	6.2	6.3	6.9	8.1
120	5.9	5.9	3.6	4.7	5.0	5.7	5.6
130	1.6	6.6	2.4	1.1	4.6	3.2	4.2
140	2.1	7.9	1.0	0.6	2.3	1.2	3.2
150	1.0	0.9	0.8	0.5	0.6	1.3	0.8

The local droplet size distribution for every measurement point in the 8.0 bar(g) measurement series for one azimuthal angle is shown in Figure 5.14. The local droplet size distributions are shown in Appendix 3.

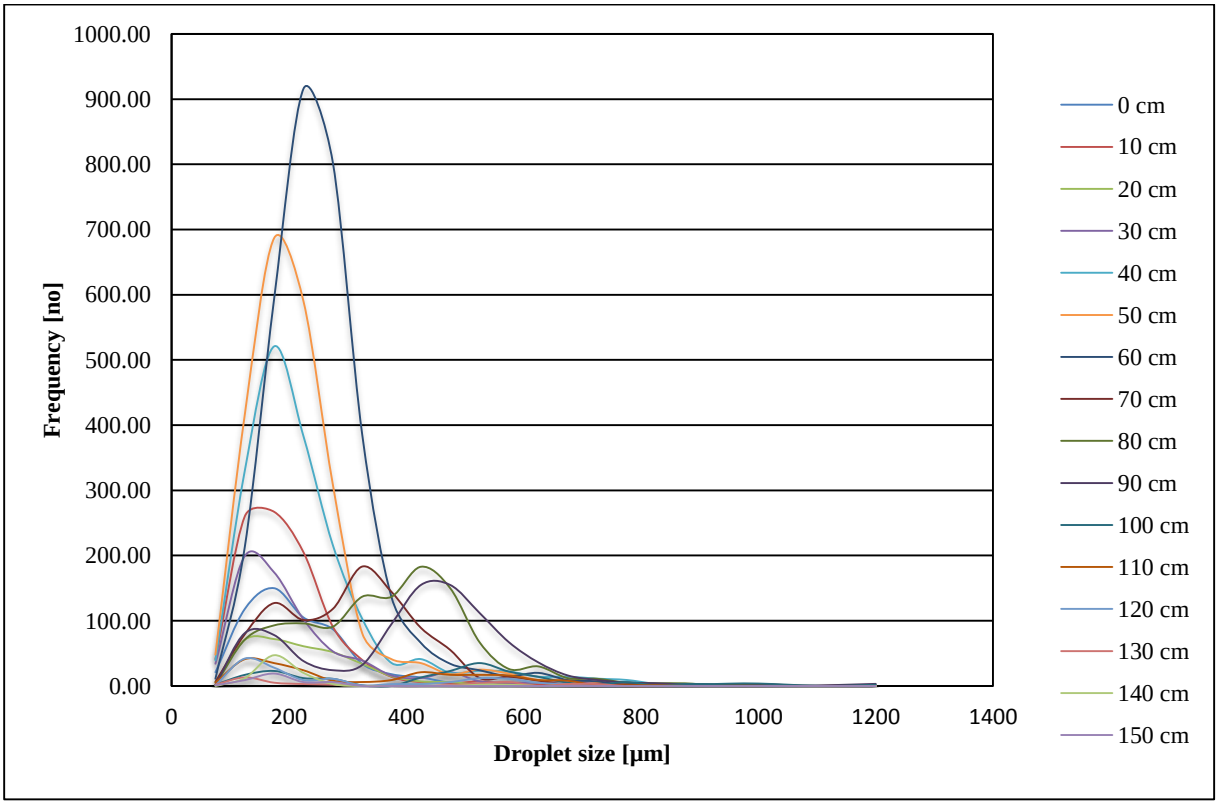

Figure 5.14: Droplet size distribution at 8.0 bar(g) and 60° for different radial positions.

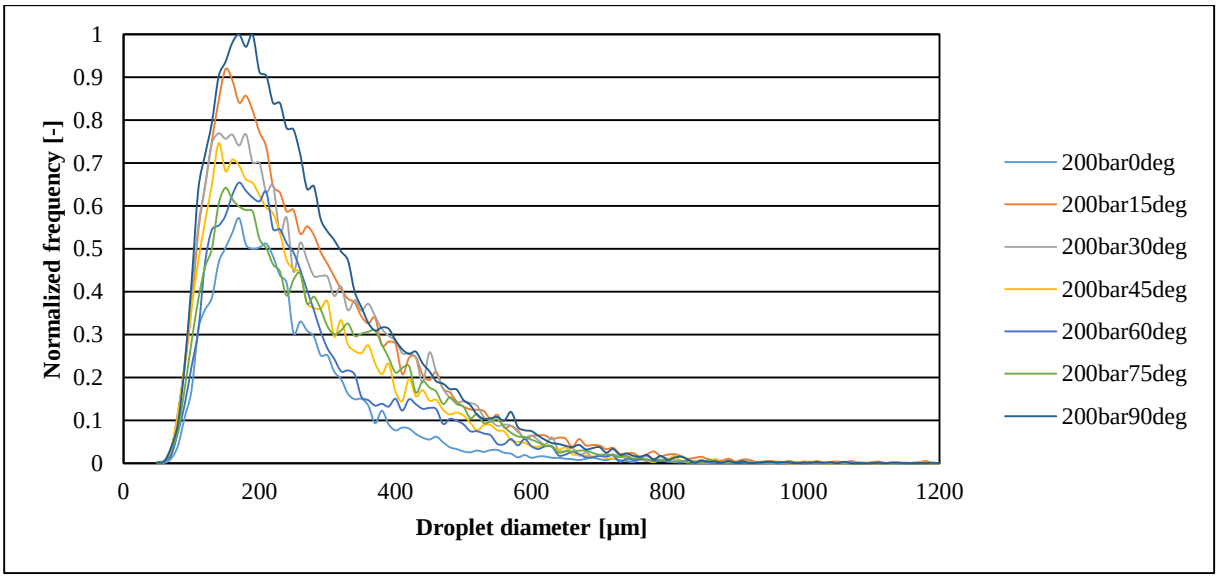

Figure 5.15: Total droplet size distribution for every azimuthal angle for the 8.0 bar(g) measurement series.

Figure 5.15 shows the total size distribution for every azimuthal angle and is normalized by dividing all the readings by the most frequent measurement. The same normalization is done in Figure 5.16 for the total size distribution for every radial distance.

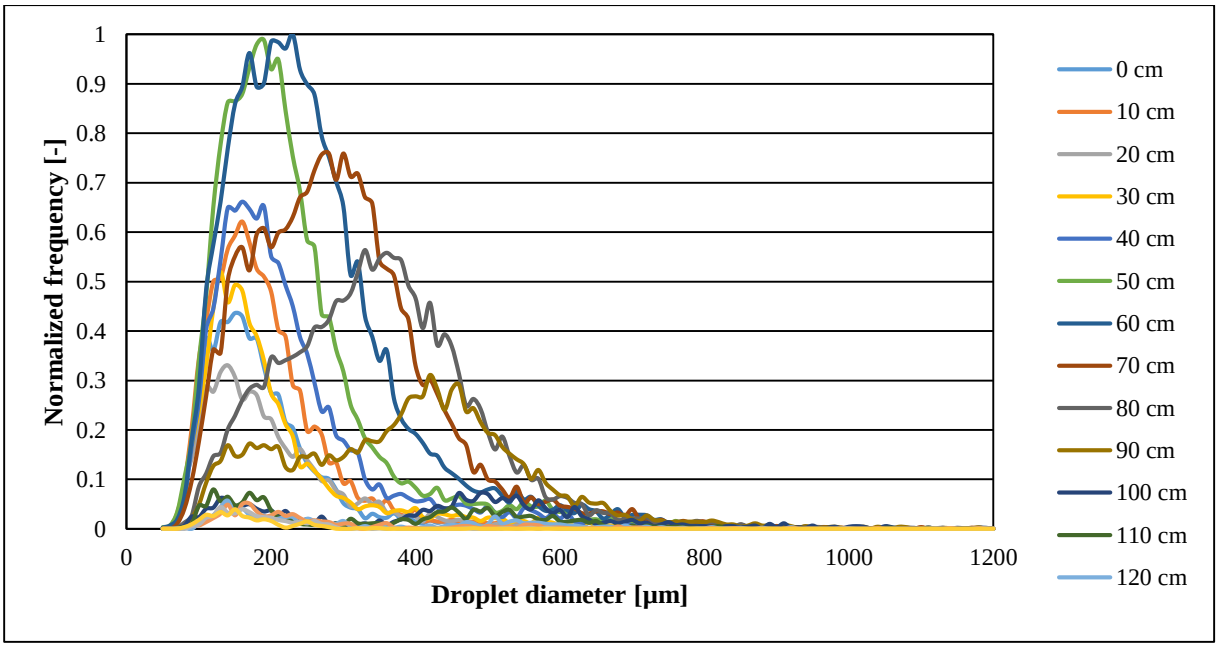

Figure 5.16: Total droplet size distribution for every radial distance for the 8.0 bar(g) measurement series.

The mass-weighted mean velocity of the corresponding droplet diameter interval is shown in Figure 5.17 for every azimuthal angle. The figure is from the 8.0 bar(g) measurement series.

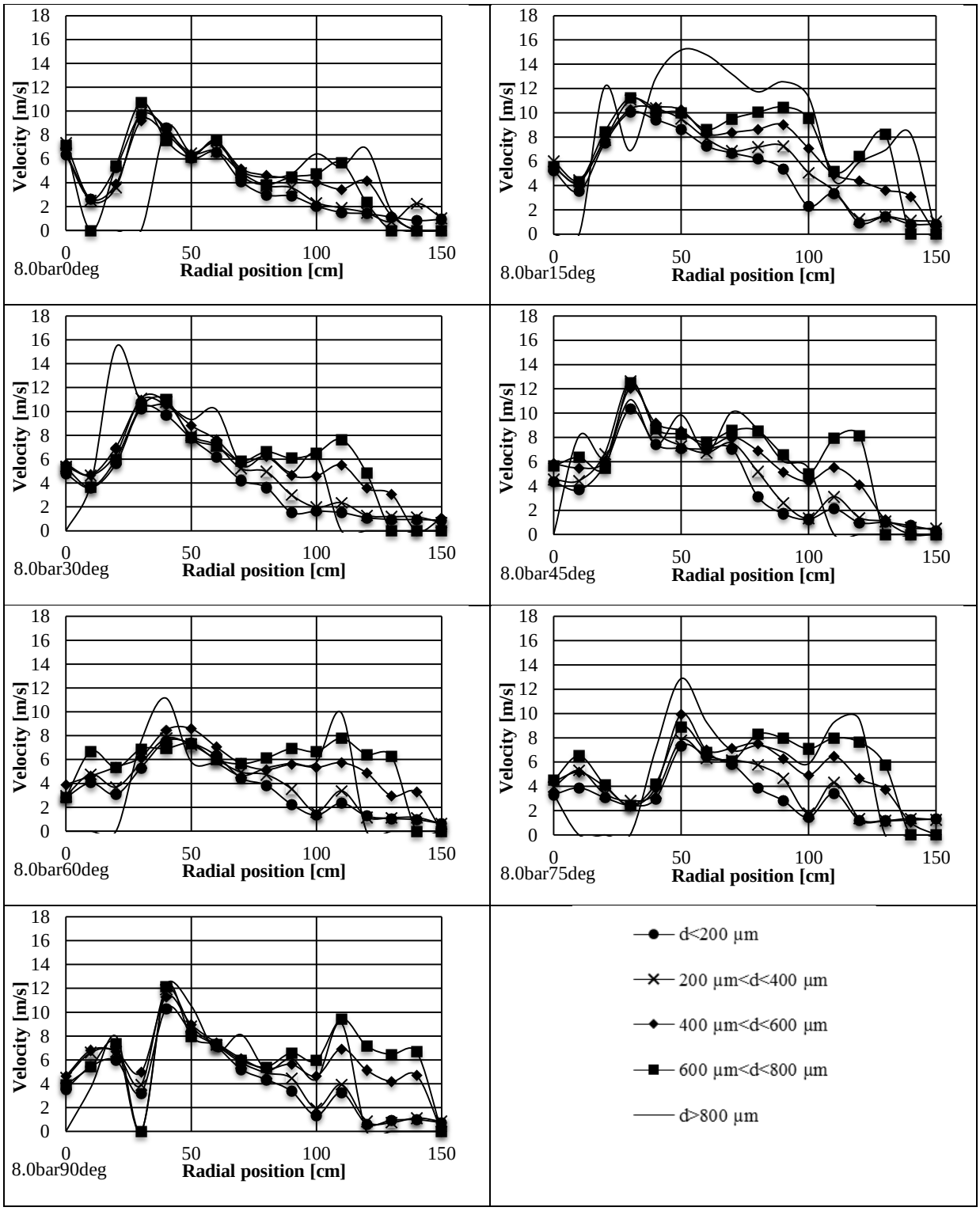

Figure 5.17: Mass-averaged velocity distribution for the 8.0 bar(g) run.

5.4 K-factor

In this project, the "K-factor" is measured by using the total-pressure of the supply water. The water is fresh and at 20 °C with no additives. The "K-factor" is found with the same equipment as described in Chapter 3.

The "K-factor" is obtained by doing measurements at each supply water pressure and finding the max-, min- and average values (one measurement is the average of time series with 600 measurement points using the Trimec volume flowmeter). The supply water pressures ranging from 3.0 – 8.0 bar(g) are performed and shown in Figure 5.18.

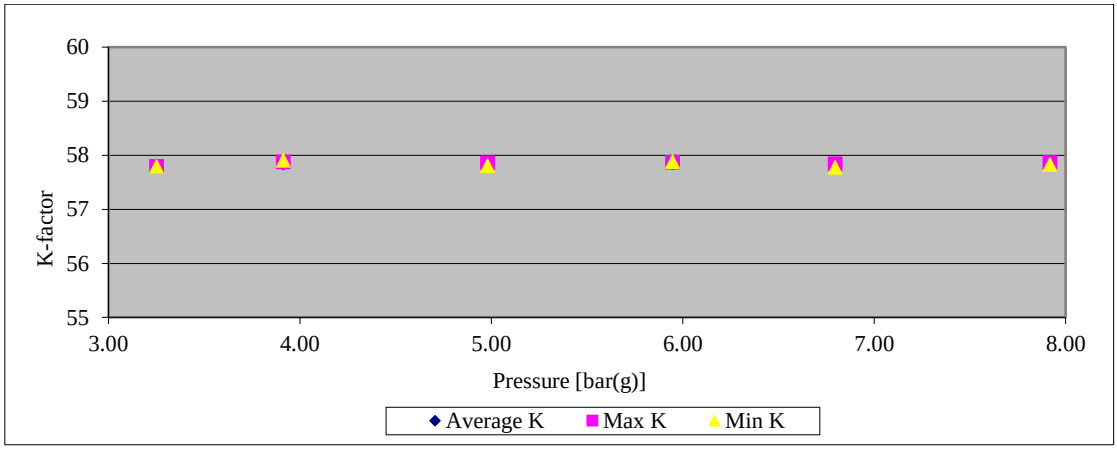

Figure 5.18: Results from Measurements of the "K-factor".

An average of all the pressure series gives the "K-factor" of 57.9 $dm^3/\sqrt{bar}$, which is in acceptable agreement with that of 58.8 $dm^3/\sqrt{bar}$ from the producer (Tyco). The difference is 1.5 %, which is less than the standards referred to in Chapter 2.6 of $\pm$5 %.

5.5 Calculated and measured mass-flows

Laser-based shadow-imaging technique is used in this research project. The main features are that the measurement equipment is placed outside the spray and the images are analyzed with an in-house code. The in-house code uses the Hungarian tracking algorithm to find the droplet paths. By placing the equipment outside the spray, the fluid dynamics of the spray are not affected by the measurement equipment.

The laser-based technique is compared to PDA studies. PDA requires spherical droplets while the technique in this thesis is almost droplet shape independent. The PDA technique has a great advantage of finding the droplet data immediately, while the present imaging technique requires download time from camera to a computer and the image processing time. The PDA technique is an established technique for characterization of sprays.

In the report by Sæbø & Wighus (2015), it is concluded that a shadow-imaging technique is more suited to characterize fire water sprays than PDA since the PDA is highly sensitive to non-spherical shape of droplets.

The droplet size, velocity and direction have been used to calculate mean diameters, size- and velocity distributions and water application flux. The water flux is used further to calculate the mass-flow from the nozzle. By integrating the water flux by the applied area, the mass-flow is found. This is compared to the actual mass-flow of supply water during the experiment. In Table 5.23 the actual and measured mass-flows are compared.

Table 5.23: Comparison of actual to measured mass-flow.

	Unit	2.0 bar(g)	5.0 bar(g)	8.0 bar(g)
Actual mass-flow	[kg/min]	80	126	161
Measured mass-flow	[kg/min]	91	92	73
Percentage of actual	[%]	114%	73%	45%

The calculated mass-flow from the experiments to the measured mass-flow from the flow-meter is ranging from 117 % to 45 %. Over 100 % implies more water from the nozzle than went into the nozzle. The reason for this is expected to be due to the locations of the measurements. The shape of the nozzle will have a higher water flux in the azimuthal angles of the nozzle containing tines. When calculating the flow, the flux measurements have to be interpolated between the measurement locations. This effect will decrease with increasing pressures.

When the calculated mass-flow is lower than the measured mass-flow to the nozzle, it implies that the image processing software does not register all droplets of the spray. This can be due to the amount of water between, in front or behind the focus plane of the camera in the middle of the spray. This will make the images from the experiments more blurred and the droplets harder to isolate. In Figure 5.19, images from the three pressure series are presented.

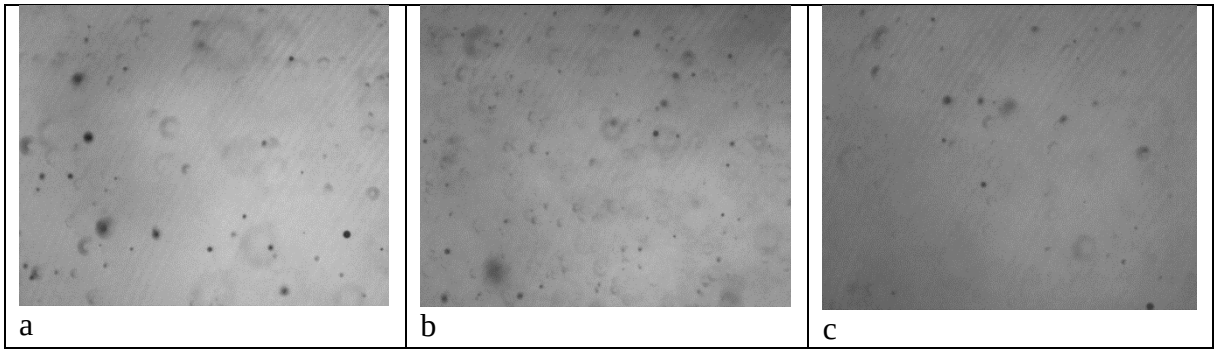

Figure 5.19: Typical images from a) 2.0 bar(g) run, b) 5.0 bar(g) run, c) 8.0 bar(g) run.

To the eye, the images in Figure 5.19 seem to be quite similar to analyze by image processing, but in reality the 8.0 bar(g) pressure series is more demanding. Figure 5.20 illustrates the number of pixels having a given gray-scale value. It shows the 8.0 bar(g) series to have, in general, lower gray-scale values than 5.0 and 2.0 bar(g) series. A lower gray-scale value will have a darker background, and the droplets are harder to detect with the image processing code.

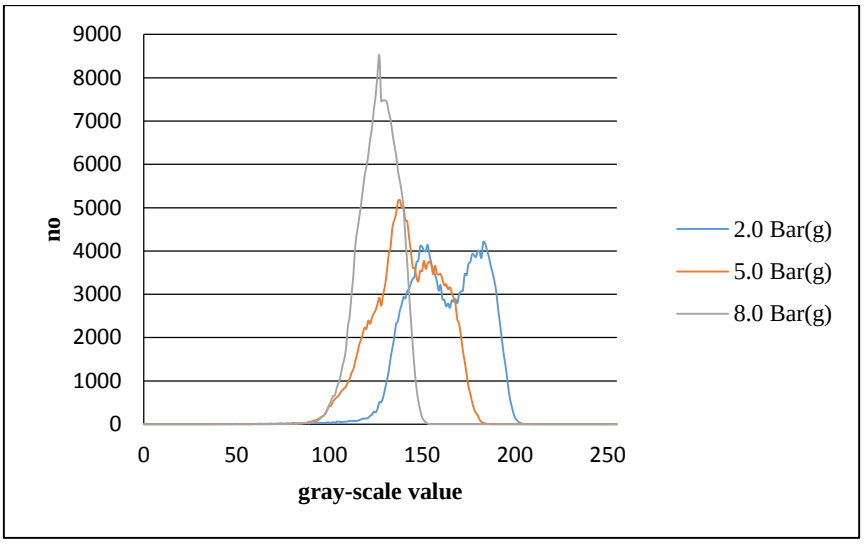

Figure 5.20: Number of detected gray-scale values in the different water pressure runs.

An important factor of the measurements is the dependency of the nozzles geometry on the fire water spray. The measurements from the 2.0 bar(g) series show a high measurement of the applied water flux at azimuthal angle of 15°. By investigating the geometry of the nozzle, in Figure 3.10, the frame arm will focus the water to the sides and this will be at around 15°. In addition to this, 15° will also be at one tine of the deflector plate. By studying the applied water fluxes, we find an increase of water flux in positions with a tine. This effect is stronger in the 2.0 bar(g) series than in series at higher water pressures. The water application flux is found to have large azimuthal differences at low supply water pressures.

The droplet size distribution from all the supply water pressure series shows the mode of the distribution to increase with increasing radial distance. This means that the fraction of smaller droplets will be larger to the center of the spray and the larger droplets will be close to the edge.

The velocity distribution shows the velocity of the droplets to be in general highest between 20 and 60 cm from the center of the spray for all pressures. The velocity will in general increase with increasing droplet size.

5.6 Accuracy of the method

The accuracy of the laser-based shadow-imaging test rig for fire water nozzles made and used in this project is evaluated in this chapter. The accuracy is determined from several factors:

- Sensors (flow, temperature and pressure)
- Image processing code
- DOF calibration
- Spatial resolution of measurement locations.

The different factors will be reviewed and the accuracy of the method will be considered in this chapter. The sensors have the following accuracy:

- Temperature: the deviation of the sensor is ± (0.3+temperature*0.005) °C giving a temperature accuracy of the measurements of 12 ± 0.36 ° C.
- Flow: the deviation of the sensor is ± 0.5 % of measured value giving a flow accuracy of 80 ± 0.4 dm^3/min to 161 ± 0.8 dm^3/min.
- Pressure: the deviation of the sensor is ± 0.25 % of full-scale value giving the accuracy of (2.0 - 8.0) ± 0.04 bar(g).

In the image processing code, the droplet diameters are determined in the images from a gray-scale gradient. When the images are binarized, the pixels are given values 1 or 0. This will give ± 1 pixel as error.

In Chapter 4.3 the calibration of the DOF is explained. A Patterson globe containing circles with a known physical size was used. The read size of these circles compared to their physical size together with the binarization error is shown in Figure 5.21.

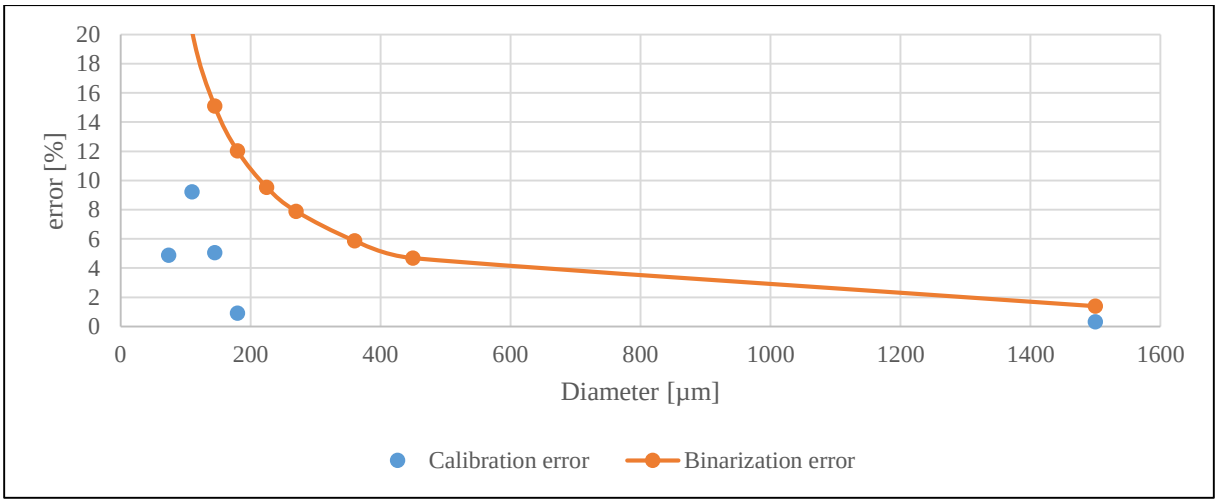

Figure 5.21: Calibration- and Binarization error compared to the real size of a sizing standard.

The measurements of the Patterson globe are performed without any water spray. This will make the image processing more difficult and the uncertainties more difficult to quantify.

When calculating the applied water flux, the measurements from discrete location is used for interpolation. This is expected to reduce the accuracy of the method.

By comparing the applied water flux with the measured amount of water put into the nozzle, this will give a guidance for the amount of the droplets that is registered. This is discussed in Chapter 5.5.

Chapter 6

Facilitating the results to CFD-codes

To utilize the results from this research project for CFD-software such as KFX®, the results need to be adapted to a special setup (Evanger, 2009). The fire water spray is defined as several phases where one phase is a droplet size interval with a representative droplet diameter. It is not beneficial to simulate the trajectory of every droplet, so the spray phase has droplet packages consisting of numerical droplets treated as Lagrangian particles. The number of numerical droplets can be controlled by the input to the software. The mass-flow and velocity of every phase is input to the code as well as the inner and outer angle of the spray. It is also possible to define the temperature and the type of fluid. The user has no options to adjust the input to compensate for azimuthal differences.This chapter will explain how the results from Chapter 5 are converted to useful results for CFD-software. Three different methods are shown.

In Figure 6.1, a screen dump from KFX® is shown. Here all the previously explained parameters can be input to the CFD code.

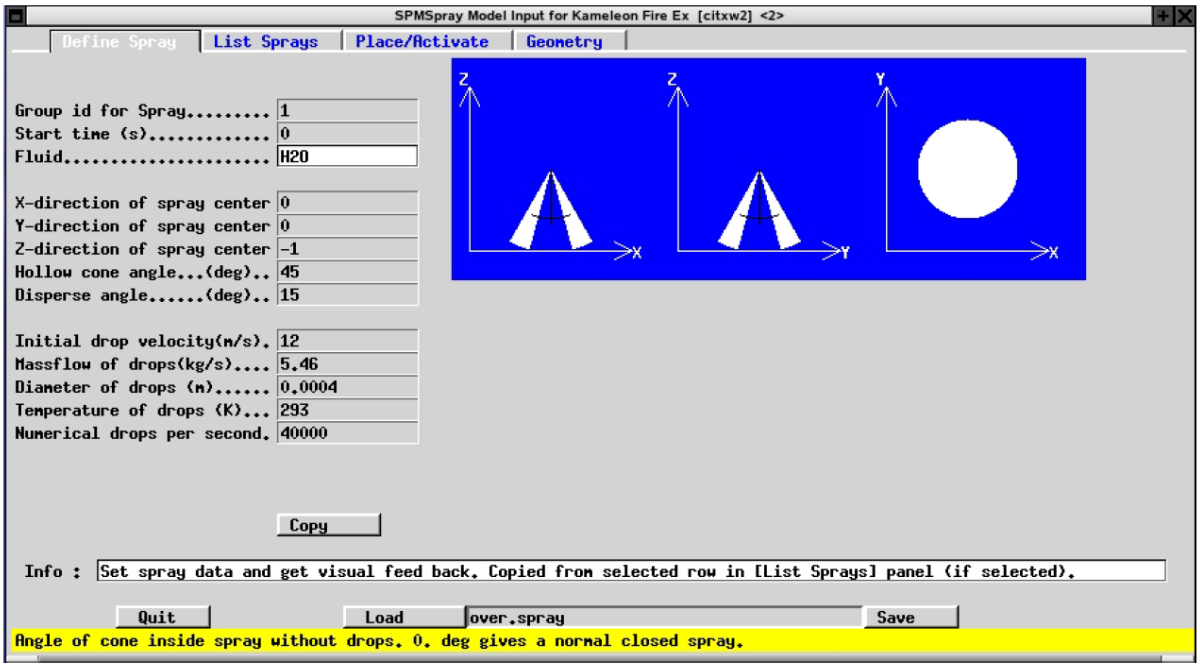

Figure 6.1: The define spray panel in KFX® from Evanger (2009).

To enter all the phases of the spray, it is possible to use the "List Sprays" panel shown in Figure 6.2. It is also possible to set a time variation, direction, location and activation mechanism, but this has more to do with the behavior of the deluge system and is not treated in this research project.

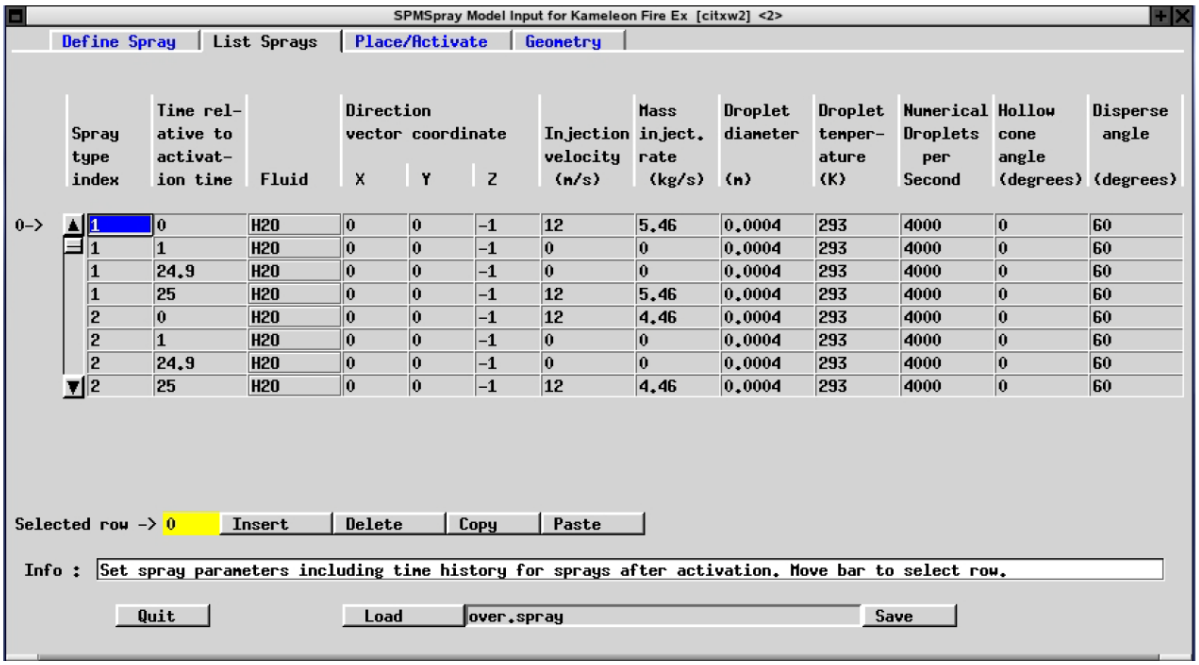

Figure 6.2: The list spray panel in KFX® from Evanger (2009).

The data from the experiments is performed 100 cm below the nozzle tip of the fire water nozzle. The CFD-software needs to define the data from a point source. To compensate for this, the CFD-software has to adjust some parameters to get the measured size distribution, velocity distribution and mass-flow to be the same at 100 cm.

6.1 Converting results to CFD-input: Simplified solution

The experimental results need to be simplified to be appropriate as CFD-input. One method is to assume that all the water is evenly distributed on the area defined by the dispersion angle. The flow rate of each phase is found by multiplying the total flowrate of the nozzle by some percentage found from the experiments. The velocity is found experimentally by finding the mass weighted velocity of the phases calculated by (2.3).

The phases are defined as 10 evenly sized intervals from zero to 1500 µm. Every interval is represented by the droplet size of the center of the interval (e.g. the first interval from zero to 150 µm is represented by the droplet size 75 µm). The droplets larger than 1500 µm are added to the 1500 µm measurement.

To adapt the experimental results to the mass flow, the mass flux from Chapter 5 is sorted into the different droplet size intervals. This means that the mass flux is per phase and for all measured locations in the spray shown in Figure 5.1. Then the mass flux is integrated in both azimuthal and radial distance to find the total mass flow of the phase. The result from the integration is shown in Table 6.1 for the tree different pressure series.

Table 6.1: Mass Flow of different droplet size intervals for different pressures. All values are in $[dm^3/min]$.

	2.0 bar(g)	5.0 bar(g)	8.0 bar(g)
75 µm	0.19	0.63	0.82
225 µm	3.48	8.91	11.44
375 µm	6.68	16.52	20.50
525 µm	8.85	21.24	19.63
675 µm	9.70	18.39	10.20
825 µm	10.13	11.22	4.47
975 µm	9.83	5.54	1.65
1125 µm	8.26	3.11	1.18
1275 µm	6.57	1.87	0.56
> 1425 µm	27.79	4.19	1.40
Total mass flow	91.48	91.62	71.84

By assuming that the measured distribution is representative for the real distribution of the spray, the mass flow for the size interval can be divided by the total mass flow to get a percentage distribution of the different size intervals. This is shown in Table 6.2.

Table 6.2: Mass percent of different droplet size intervals for different pressures.

	2.0 bar(g)	5.0 bar(g)	8.0 bar(g)
75 µm	0.20 %	0.69 %	1.14 %
225 µm	3.80 %	9.73 %	15.93 %
375 µm	7.30 %	18.03 %	28.53 %
525 µm	9.68 %	23.18 %	27.32 %
675 µm	10.61 %	20.07 %	14.20 %
825 µm	11.07 %	12.24 %	6.22 %
975 µm	10.75 %	6.04 %	2.30 %
1125 µm	9.02 %	3.39 %	1.64 %
1275 µm	7.18 %	2.04 %	0.78 %
> 1425 µm	30.38 %	4.58 %	1.94 %

Figure 6.3 shows graphically the results from Table 6.2 giving the simplified size distribution.

To find a representative velocity the mass-averaged velocity is used like in Chapter 5. The mass-averaged velocity is calculated for the same droplet size intervals as for the mass flow. The results are shown in Table 6.3.

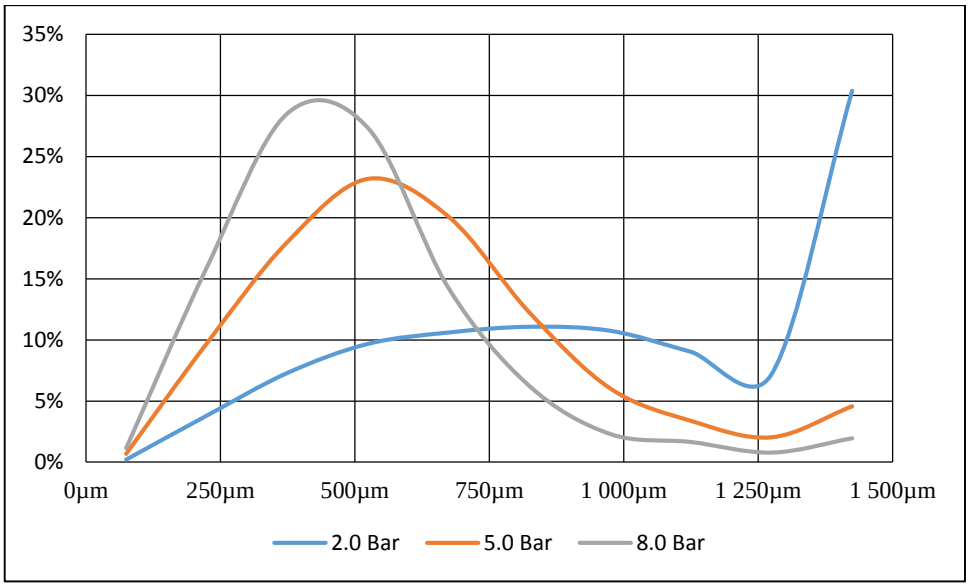

Figure 6.3: Simplified size distribution for CFD input.

Table 6.3: Mass-averaged velocity of different droplet size intervals for different pressures. All values are in [m/s].

	2.0 bar(g)	5.0 bar(g)	8.0 bar(g)
75 µm	2.1	3.2	3.9
225 µm	2.5	3.6	4.2
375 µm	3.6	4.9	4.9
525 µm	5.1	6.0	5.7
675 µm	6.1	6.7	6.9
825 µm	7.2	8.2	7.3
975 µm	8.1	9.4	7.4
1125 µm	8.4	10.0	9.5
1275 µm	8.8	10.7	8.5
> 1425 µm	9.2	9.8	8.9

Figure 6.4 shows the mass-averaged velocities for the different droplet size intervals correlating droplet size to velocity for different pressures. The dispersion angle of the spray is what is specified by the manufacturer of the nozzle and is 55°. This is applied for this "Simplified solution".

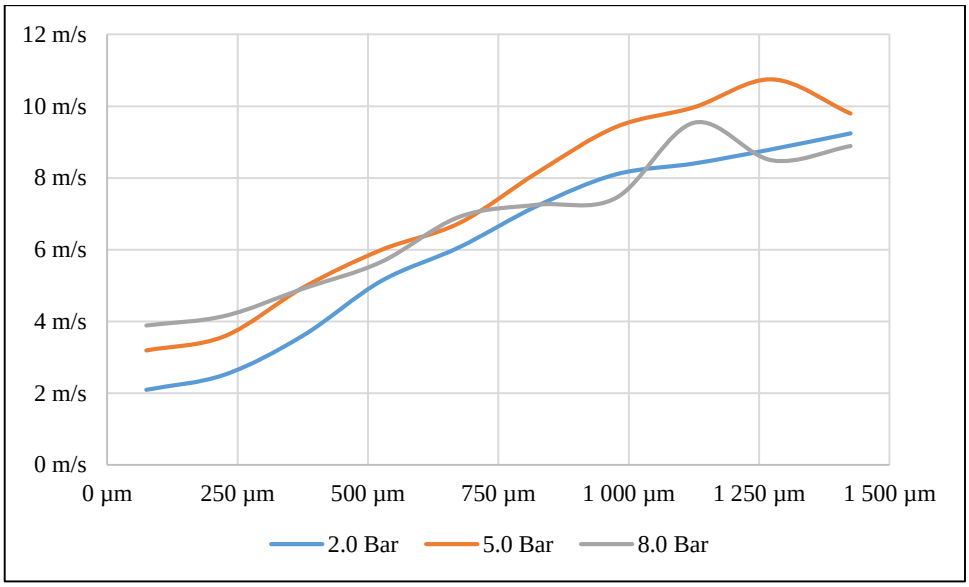

Figure 6.4: Mass-averaged velocities to the different droplet size intervals correlating droplet size to velocity for different pressures.

6.2 Converting results to CFD-input: Radial dependent solution

In Chapter 6.1, the mass-flow of each phase was assumed uniform in all radial positions of the spray. The experiments show the mass-flow of the different phase to be a function of radial and azimuthal position. To input the experiments to CFD code there is currently no possibility to compensate for azimuthal variations, and the mass-fluxes are integrated by azimuthal angle to find the mass-flow for all radial positions.

The phases are divided in the same intervals as in Chapter 6.1. Figure 6.5 shows the mass-flow for five arbitrary mass-flows of the 8.0 bar(g) pressure series. The mass flow is per cm and is found by integrating the interpolated mass-flux measurement for every cm in the radial direction for the azimuthal angles. The unit percentage is percentage of the total mass-flow.

It is assumed that the area where 95% of the water for each phase flow represents the area coverage of the spray. Since there are no azimuthal differences, the area coverage is represented by the inner angle and outer angle of the phase.

Figure 6.6 shows the same graphs as Figure 6.5, but here the lines are cut-off where the outer and inner angle represent 95 % of the total water of the phase.

The mass-flow of water is then assumed constant within the radial limits made by the 95 % criterion. By summing up all the phases, a total mass-flow rate is found. This is shown in Figure 6.7 compared to the total mass-flow from the measurements for the 8.0 bar(g) series.

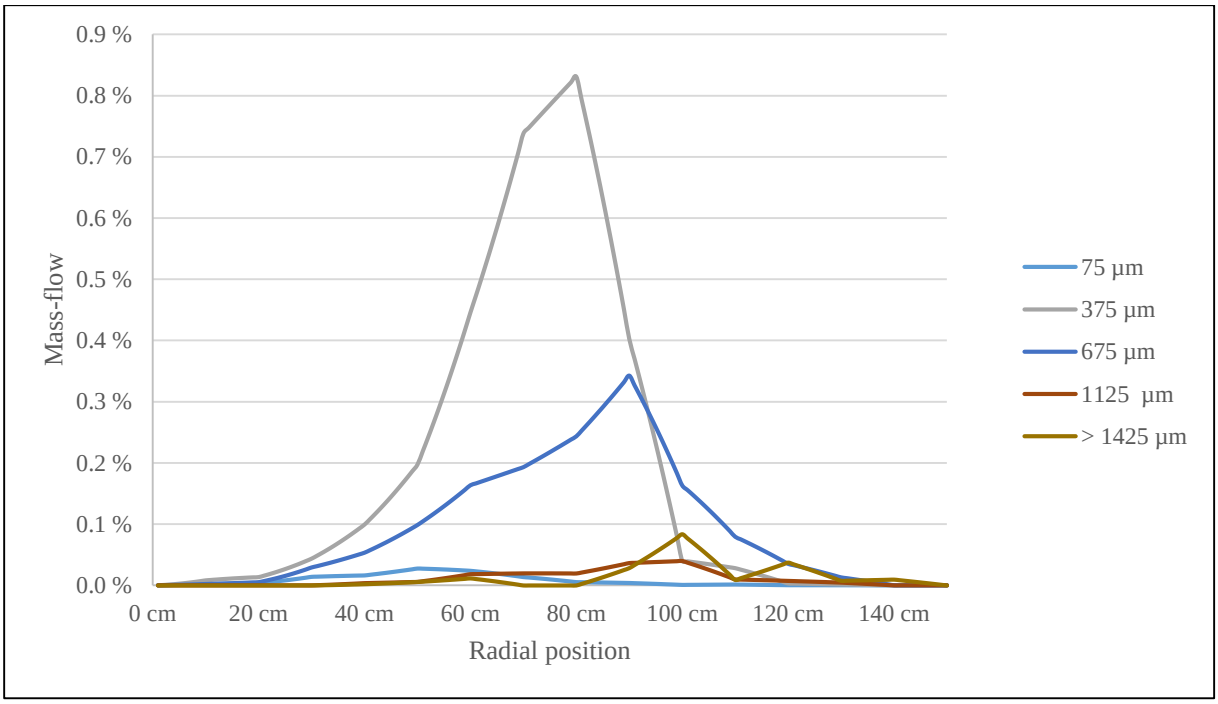

Figure 6.5: Percentage of the total mass-flow to the radial position for arbitrarily measurement at the 8.0 bar(g) water pressure run.

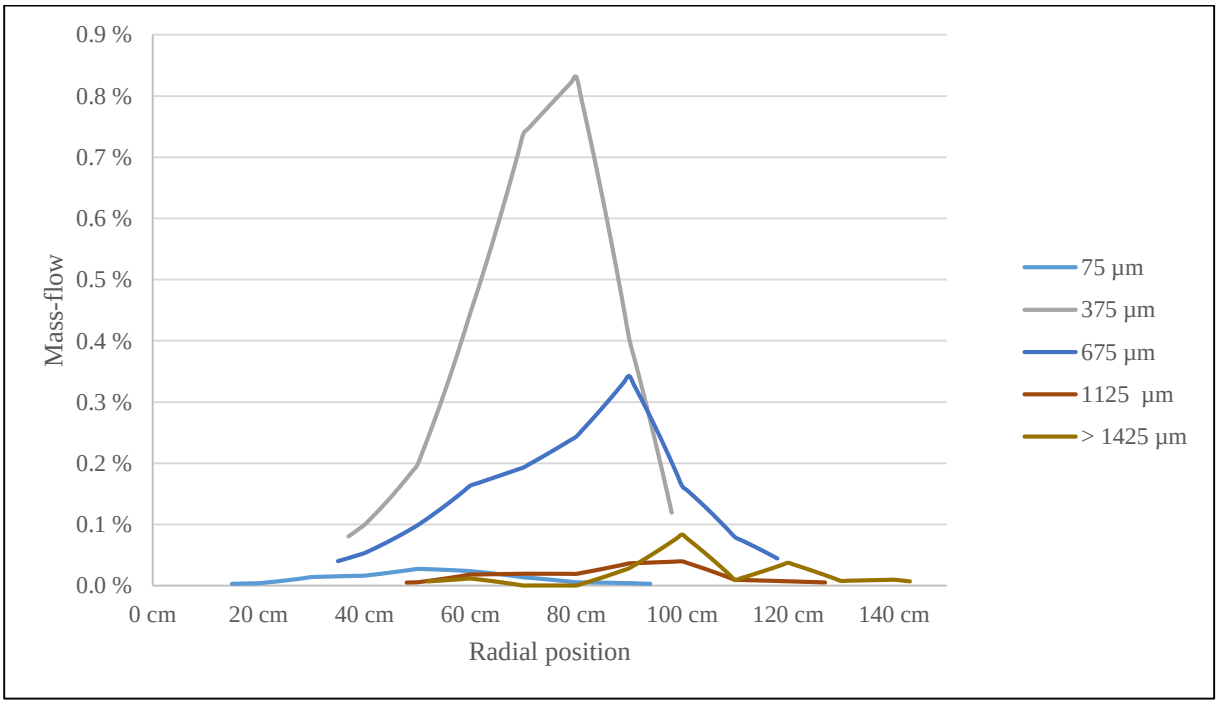

Figure 6.6: Percentage of the total mass-flow to the radial position for arbitrarily measurement at the 8.0 bar(g) water pressure using range obtained by 95 % of the flow.

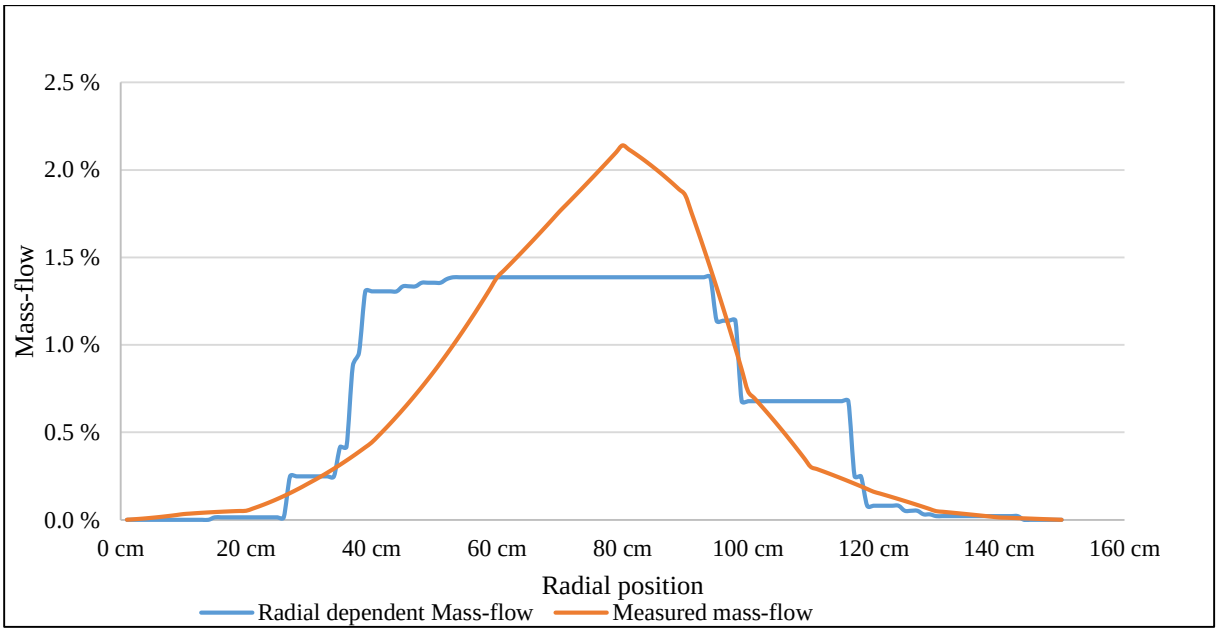

Figure 6.7: Total mass-flow from measurements for the sum of all locations in the 8.0 bar(g) series.

The same procedure is done for the 2.0 bar(g) and 5.0 bar(g) series in Figure 6.8 and Figure 6.9, respectively.

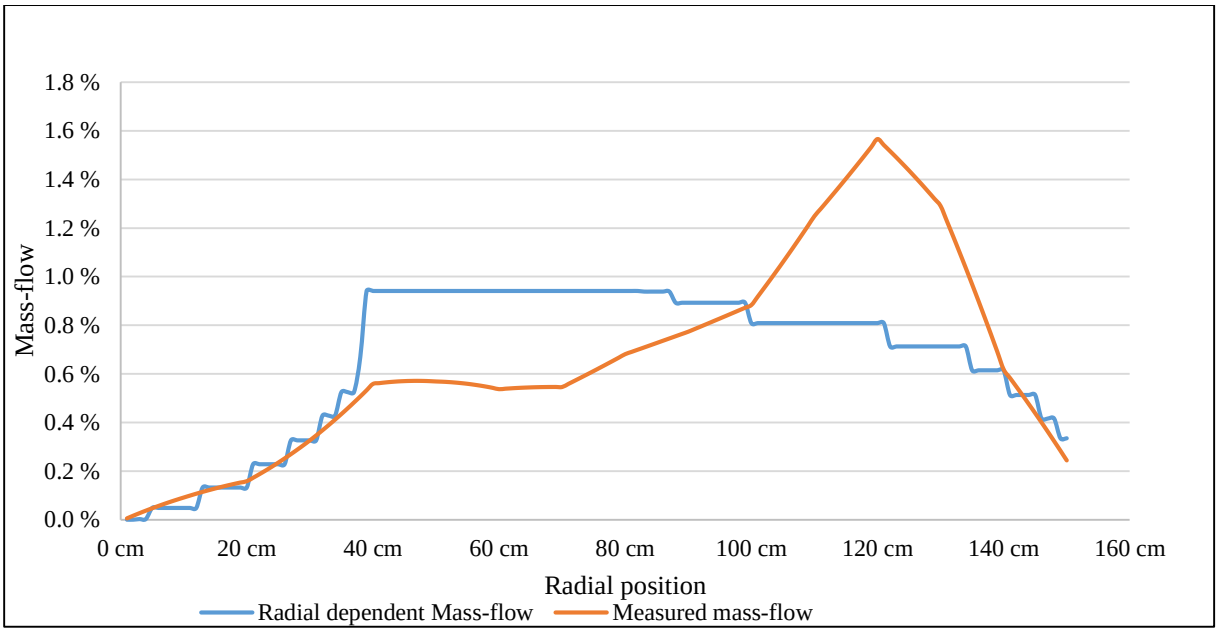

Figure 6.8: Total mass-flow from measurements for all locations for the 2.0 bar(g) series.

The mass-weighted velocity of the droplet size intervals is assumed the same as for the simplified solution in Chapter 6.1.

The inputs for CFD-codes using the radial dependent solution for 2.0, 5.0 and 8.0 bar(g) are shown in respectively Table 6.4, 6.5 and 6.6 where the start and stop positions for the droplet size intervals are listed as hollow cone angle and dispersion angle.

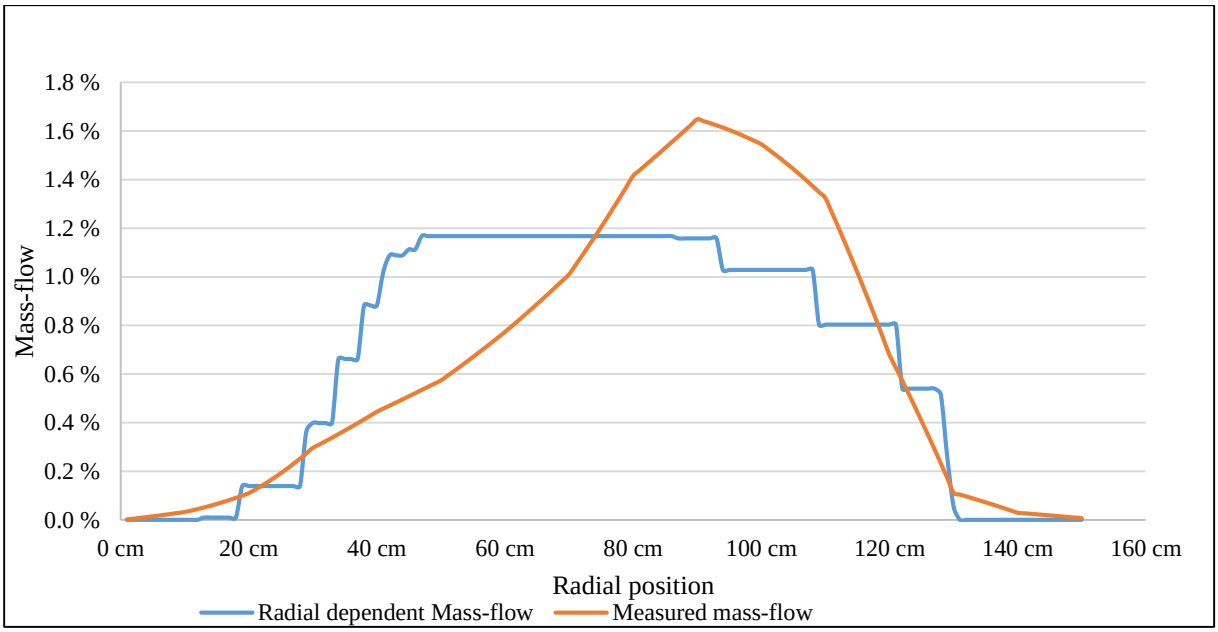

Figure 6.9: Total mass-flow from measurements for all locations for the 5.0 bar(g) series.

Table 6.4: Input parameters to CFD for the 2.0 bar(g) run, assuming simplified solution

Diameter [µm]	Mass-weighted velocity [m/s]	Mass-flow [%]	Hollow cone angle [°]	Dispersion angle [°]
75 µm	2.1	0.2 %	2	39
225 µm	2.5	3.8 %	3	41
375 µm	3.6	7.3 %	7	45
525 µm	5.1	9.7 %	12	50
675 µm	6.1	10.6 %	15	53
825 µm	7.2	11.1 %	18	54
975 µm	8.1	10.7 %	19	55
1125 µm	8.4	9.0 %	21	56
1275 µm	8.8	7.2 %	21	56
> 1425 µm	9.2	30.4 %	21	56

Table 6.5: Input parameters to CFD for the 5.0 bar(g) run, assuming simplified solution

Diameter [µm]	Mass-weighted velocity [m/s]	Mass-flow [%]	Hollow cone angle [°]	Dispersion angle [°]
75 µm	3.2	0.7 %	7	41
225 µm	3.6	9.7 %	11	43
375 µm	4.9	18.0 %	16	47
525 µm	6.0	23.2 %	19	50
675 µm	6.7	20.1 %	21	52
825 µm	8.2	12.2 %	22	52
975 µm	9.4	6.0 %	23	52
1125 µm	10.0	3.4 %	17	52
1275 µm	10.7	2.0 %	24	52
> 1425 µm	9.8	4.6 %	25	52

Table 6.6: Input parameters to CFD for the 8.0 bar(g) run, assuming simplified solution

Diameter [µm]	Mass-weighted velocity [m/s]	Mass-flow [%]	Hollow cone angle [°]	Dispersion angle [°]
75 µm	3.9	1.1 %	9	43
225 µm	4.2	15.9 %	15	43
375 µm	4.9	28.5 %	20	44
525 µm	5.7	27.3 %	21	49
675 µm	6.9	14.2 %	19	50
825 µm	7.3	6.2 %	21	49
975 µm	7.4	2.3 %	24	51
1125 µm	9.5	1.6 %	26	52
1275 µm	8.5	0.8 %	28	52
> 1425 µm	8.9	1.9 %	27	55

6.3 Converting results to CFD-input: Phase splitting

In Chapter 6.2, the mass-flow of water was adopted to CFD-input by dividing the droplet sizes into phases and finding the radial positions where 95 % of the mass-flow of the actual phase will be. This will adapt the measured data to fit the measured data better than using the simplified solution in Chapter 6.1. Fitting it means to represent the same droplet size distribution at the same time as the mass-flow of the phases are added up over the radial distance, to be equal to the measured mass-flow of the spray.

To get a better adaption of the measured data to the CFD-input, the droplet size intervals with the most dominant mass-flow have been divided in two groups.

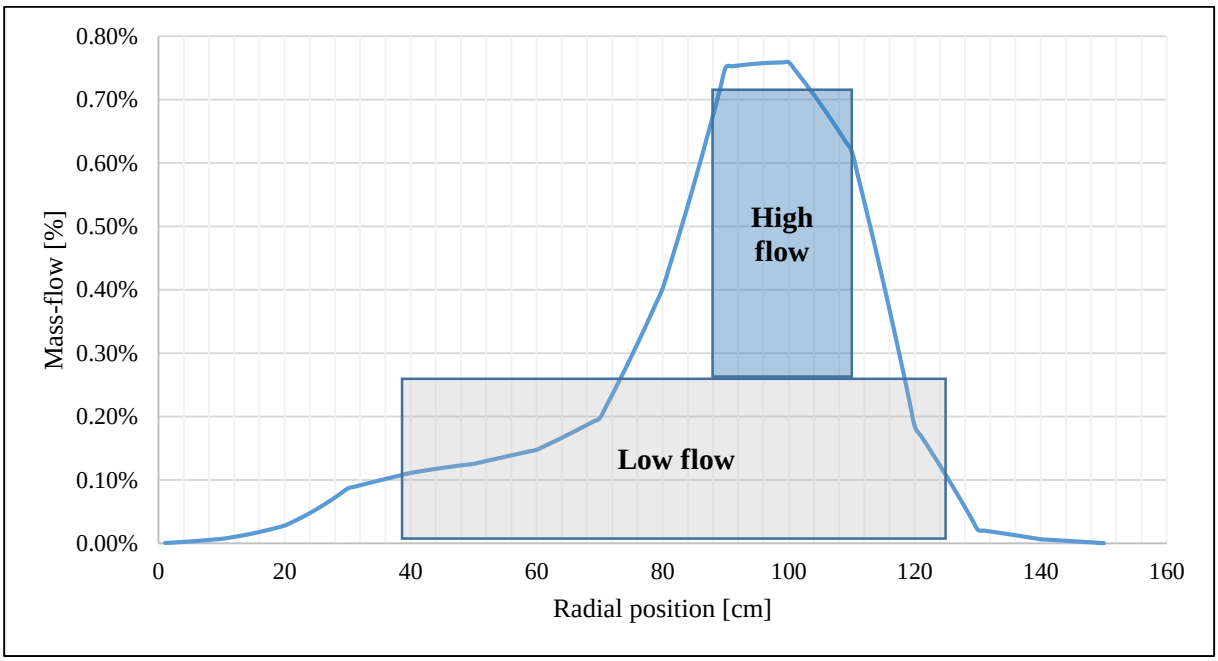

Figure 6.10: The mass-flow for the droplet size interval (or phase) from 450 µm to 675 µm. The data are summed over all the azimuthal angles. In the figure, the phase splitting model is illustrated.

Figure 6.10 shows the mass-flow from the 5.0 bar(g) series and the droplet size interval (or phase) from 450 µm to 675 µm. The measured mass-flow is divided in two groups, "High flow" and "Low flow. The "Low flow" is found by finding the radial interval that will account 50 % of the total mass-flow for the phase. The measurements in this interval are then averaged and the "Low flow" subtracted. The radial position representing the "Low flow" is an interval where the mass-flow accounts for 95 % of the water in the phase. By dividing the phase, we have a more detailed way of representing the location where the different phases will be found.

Figure 6.11 compares the measured mass-flow for the 5.0 bar(g) series with the mass-flows from all the phases added up included the phase splitting.

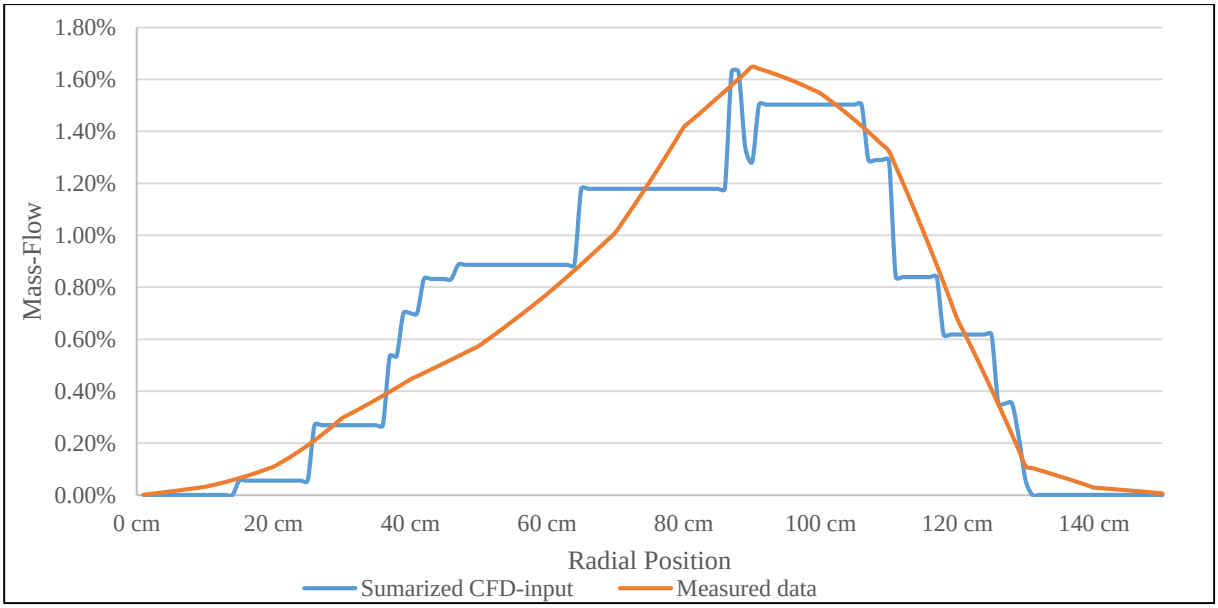

Figure 6.11: The measured mass-flow for the 5.0 bar(g) series with the mass-flows from all the phases added up included the phase splitting.

The same procedure is done for the 2.0 bar(g) series and the 8.0 bar(g) series giving Figure 6.12 and Figure 6.13, respectively.

The inputs for CFD-software using the radial dependent solution with phase splitting for 2.0, 5.0 and 8.0 bar(g) is shown in respectively Table 6.7, 6.8 and 6.9 where the start and stop positions for each phase are listed as hollow cone angle and dispersion angle. The three last rows in each table are the data describing "High flow". The velocity is assumed equal to the simplified case in Chapter 6.1.

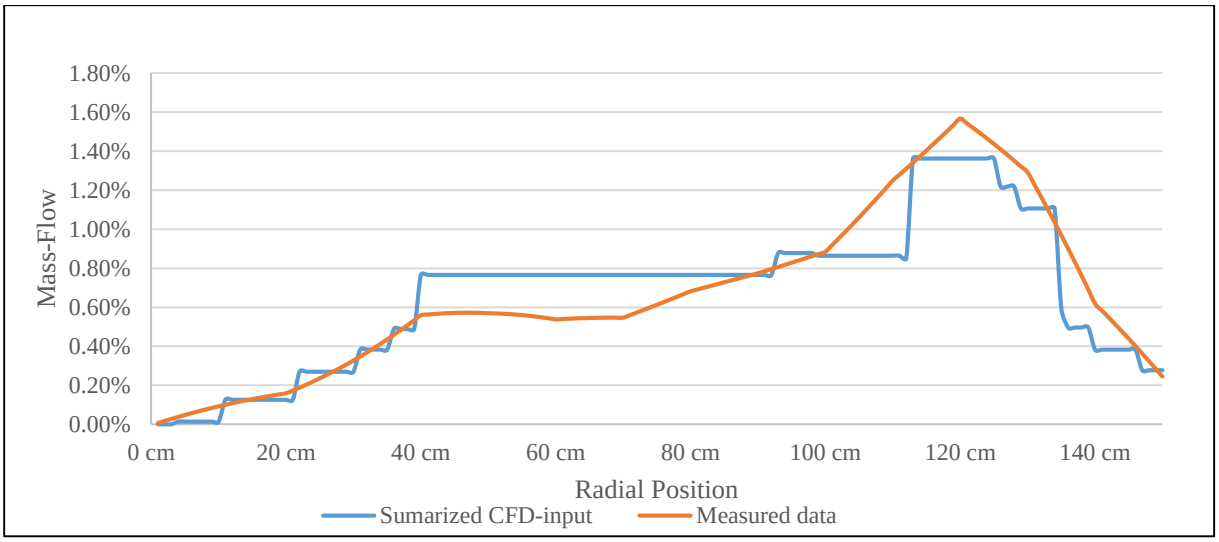

Figure 6.12: The measured mass-flow for the 2.0 bar(g) series with the mass-flows from all the phases added up included the phase splitting.

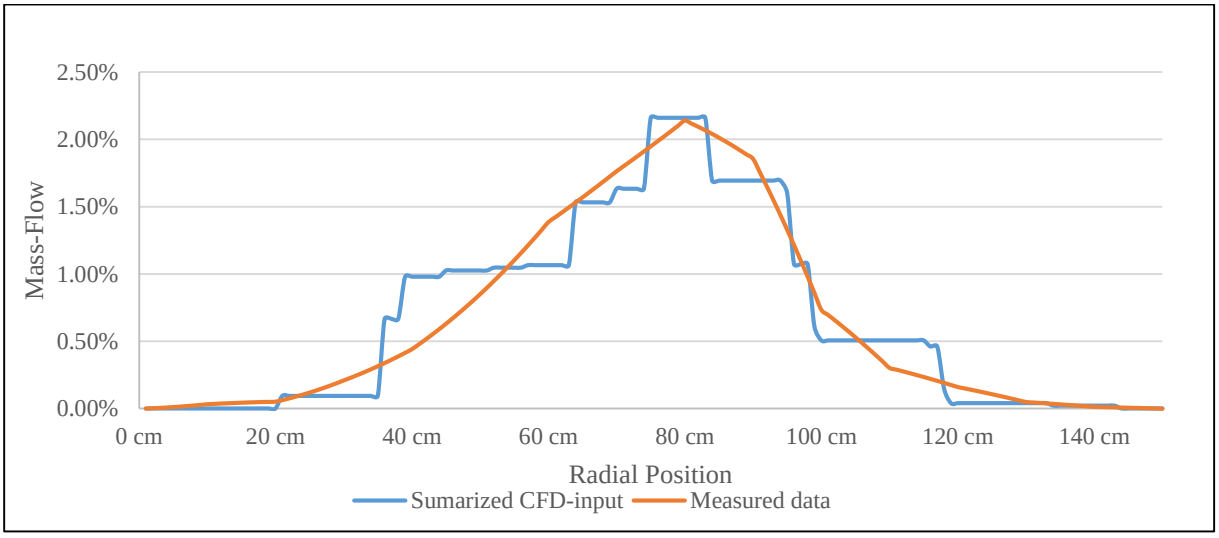

Figure 6.13: The measured mass-flow for the 8.0 bar(g) series with the mass-flows from all the phases added up included the phase splitting.

Table 6.7: Input parameters to CFD for the 2.0 bar(g) run, assuming phase splitting solution

Diameter [µm]	Mass-weighted velocity [m/s]	Mass-flow [%]	Hollow cone angle [°]	Dispersion angle [°]
112 µm	2.3	1.5 %	2	48
338 µm	3.4	9.9 %	6	44
564 µm	5.4	15.0 %	12	51
790 µm	6.9	12.4 %	17	54
1016 µm	8.1	11.7 %	20	56
1242 µm	8.8	11.6 %	22	56
>1468 µm	9.2	19.1 %	22	56
790 µm	6.9	4.0 %	43	52
1016 µm	8.1	3.6 %	45	53
1468 µm	9.2	11.3 %	48	53

Table 6.8: Input parameters to CFD for the 5.0 bar(g) run, assuming phase splitting solution

Diameter [µm]	Mass-weighted velocity [m/s]	Mass-flow [%]	Hollow cone angle [°]	Dispersion angle [°]
112 µm	3.3	4.1 %	9	42
338 µm	4.4	17.3 %	15	47
564 µm	6.3	23.6 %	20	51
790 µm	7.7	15.1 %	21	52
1016 µm	9.6	8.2 %	23	52
1242 µm	9.9	3.3 %	23	52
>1468 µm	9.8	4.6 %	25	52
338 µm	4.4	7.0 %	33	41
564 µm	6.3	10.8 %	41	48
790 µm	7.7	6.0 %	42	49

Table 6.9: Input parameters to CFD for the 8.0 bar(g) run, assuming phase splitting solution

Diameter [µm]	Mass-weighted velocity [m/s]	Mass-flow [%]	Hollow cone angle [°]	Dispersion angle [°]
112 µm	4.0	6.9 %	12	43
338 µm	4.7	29.3 %	20	44
564 µm	5.8	24.7 %	21	49
790 µm	7.0	8.9 %	20	50
1016 µm	7.7	3.3 %	24	49
1242 µm	7.9	1.4 %	30	53
>1468 µm	8.9	1.9 %	27	55
338 µm	4.7	9.3 %	33	40
564 µm	5.8	11.1 %	37	44
790 µm	7.0	3.0 %	35	45

Chapter 7

Conclusion

The main objective of this PhD project was to determine characteristic data for a typical medium velocity fire water nozzle (Tyco MV34-110).

An experimental rig is designed and made for testing the nozzle using with a laser-based shadow-imaging technique. The rig has temperature, pressure and volume-flow sensors, pump and a positioning system. The high-speed camera and laser is placed on opposite sides of the spray, capturing shadow-images of droplets in the fire water spray. All equipment is designed to withstand the water from the fire water spray.

The image processing code is made in Matlab for analysing shadow images. In the code or program, the calibration of the depth of field (DOF) correction is included.

The results from the experiments in this thesis show the location in the spray to have a large effect on the water flux ($dm^3/(m^2 \cdot min)$), i.e. the water flux is not uniform for all locations and is affected by the water supply pressure. This is due to the geometry of the nozzle, and the frame arms are affecting the applied water flux extensively for low pressures. The dominating geometrical features of the nozzle are the frame arms and the tines. This effect is important to take into account when measuring the applied water flux.

The results show the water pressure to have the following effects:

- the radial coverage will decrease with increasing water supply pressure
- the applied water flux will vary less with azimuthal angle than with increasing pressure
- the number of large droplets will decrease with increasing pressure
- the velocity of the droplets will in general increase with increasing pressure.

The PDA technique with commercial software can have problems with closed solution algorithms. It also has optical difficulties with both interference and the non-sphericity of the droplets.

Three alternative methods for converting the results to input for CFD-tools have been presented in this thesis. The best adaption is the radial dependent solution with phase splitting from Chapter 6.3.

The accuracy of the method and the results seem to be in accordance with a calibration run with about 10 % deviation. From Chapter 5.5 the calculated mass-flow from the experiments to the measured mass-flow from the flow-meter is ranging from 117 % to 45 %. Over 100 % implies more water from the nozzle than went into the nozzle. The reason for this is expected to be due to the locations of the measurements. The shape of the nozzle will have a higher water flux in the azimuthal angles of the nozzle containing tines. When calculating the flow, the flux measurements have to be interpolated between the measurement locations. This effect will decrease with increasing pressures. When the calculated mass-flow is lower than the measured mass-flow to the nozzle, it implies that the image processing software does not register all droplets of the spray.

The droplets not registered by the image processing software are assumed to have the same distribution as the measured part. This is just based on visual considerations of how the image processing software works.

To verify the method, the applied water flux could be measured with an isokinetic extractor. This will ensure to capture all the droplets for every location.

By the usage of the Hungarian algorithm, the droplet paths are determined, providing velocity measurements for the droplets in the spray.

The research project has provided unique experimental data of droplet size- and velocity distribution with the strategy from Chapter 1.2.

The novelty of the project can be summarized as follows:

- Provides unique experimental data based on high-speed shadow-imaging
- All the measurement equipment is placed outside the fire water spray to preserve the fluid dynamic properties of the flow
- An image processing software developed exclusively for fire water spray. The code is addressed exclusively to the fire water images to tune the parameters optimally.
- The user will have control of the algorithm in the image processing software to monitor the behaviour and check the accuracy.
- The droplet tracking is done with a Hungarian algorithm based on three frames. The tracking is solved as an assignment problem using a penalty function based on the physical properties of the spray.

Chapter 8

Implications for further research

This research project has measured the spray properties for three supply water pressure series on a medium velocity nozzle. It is suggested to be continued for more pressure series to find the correlation between water pressure and geometrical features (frame arms and tines on fire water nozzle). Other nozzles with smaller "K-factor" should be tested. This will deliver less water and more of the droplets might be captured by the image processing software.

Another type of nozzle should be tested to determine if the method is applicable to other nozzles than the medium velocity nozzle.

Isokinetic extractor measurements should be performed on the spray to determine the actual water distribution (dm^3/m^2s) of the spray.

Chapter 9

Main contributions in the papers

9.1 ISFEH paper (Appendix 1)

The paper gives some information on the image processing and the experimental setup. The results in this article are preliminary and are based on manual readings of the images.

9.2 ISHPMIE paper (Appendix 2)

This paper is based on several experiments at different radial positions and manual readings. The experiments are an experimental preliminary series prior to the series used in this thesis.

References

Bjerketvedt, D., Bjørkhaug, M. (1991). Experimental investigation — Effect of water sprays on gas explosions. Prepared by Chr. Michelsen Institute for the Department of Energy. UK. OTH 90 316. HMSO. London.

Dantec (2014). Home page: http://www.dantecdynamics.com/measurement-principles-of-pda, accessed: 23.9.2014.

Dundas, P.H. (1974). Technical Report Optimization of Sprinkler Fire Protection The Scaling of Sprinkler Discharge : Prediction of Drop Size, FMRC Serial No. 18792 RC73-T-40. Factory Mutual Research Corporation, Norwood, MA, June 1974.

Durst, F., Zaré, M. (1975). Laser-Doppler measurements in two-phase flows. Proceedings of the LDA-Symposium Copenhagen, 403-429.

Evanger, T. (2009). Kameleon FireEx KFX® 2010 User manual. ComputIT ,Trondheim.

Fantini E., Tognotti L., Tonazzini A. (1990). Drop Size Distribution in Sprays by Image-Processing. Computers & Chemical Engineering, 14(11):1201-1211.

FM-Approvals (2009). Approval Standard for Sprinkler System Alarm Test Devices. FM Approval standard.

Gonzalez, R.C. and Woods, R.E. (2008). Digital Image Processing (third ed.). Pearson Prentice Hall, Upper Saddle River, NJ.

Grant, G., Brenton, J., Drysdale, D. (2000). Fire Suppression by Water Sprays, Progress in Energy and Combustion Science, 26: 79-130.

Husted, B.P. (2007). Experimental measurements of water mist systems and implications for modelling in CFD. Doctoral thesis, in Department of fire safety engineering, Lund University.

ISO -standard. (2004). ISO-6182-1:2004. International standard.

Jackman, L.A. (1992). Sprinkler Spray Interactions with Fire Gases. Ph.D. Thesis, Explosion and Fire Unit, South Bank University, London.

Kashdan, J.T., Shrimpton, J.S., Whybrew, A. (2007). A Digital Image Analysis Technique for Quantitative Characterisation of High-speed Sprays. Optics and Lasers in Engineering 45(1): 106-115.

Kim, K. S., Kim, S.S. (1994). Drop Sizing and Depth-of-Field Correction in TV Imaging. Atomization and Sprays, 4:65-78.

Knollenberg, R.G. (1970). The Optical Array: An Alternative to Scattering on Extinction for Airborne Particle Size Determination. J. Applied Meteorology, 1: 86-103.

Koh K.U., Kim J.Y., Lee S.Y. (2001). Determination of in-focus criteria and depth of field in image processing of spray particles. Atomization and Sprays, 11(4):317–333.

Kuhn, H.W. (1955). The Hungarian method for the assignment problem. Naval Research Logistics Quarterly, 2: 83–97.

Lecuona, A., Sosa, P.A., Rodriguez, P.A., Zequeira, R.I. (2000). Volumetric characterization of dispersed two-phase flows by digital image analysis. Measurement Science and Technology, 11: 1152–1161.

Lee S.Y., Kim Y.D. (2004). Sizing of Spray Particles Using Image Processing Technique. KSME International Journal, 18(6): 879-894.

Lee C., Wu C.H., Hoopes J.A. (2009). Simultaneous particle size and concentration measurements using a back-lighted particle imaging system. Flow Measurement and Instrumentation, 20:189-199.

Lefebvre, A.H. (1989). Combustion: An International Series. Atomization and Spray (New York: Hemisphere).

Mathworks (2011). Matlab *User's Guide* (r2011b). 3 Apple Hill Drive Natick, MA.

NORSOK S-001 (2008). Technical Safety S-001 (4th ed). Standards Norway.

NORSOK S-006 (2003). Technical Safety S-006 (2th ed). Standards Norway.

Otsu, N. (1979). A Threshold Selection Method from Gray-Level Histograms. IEEE Transactions on Systems, Man, and Cybernetics 9(1): 62-66.

Ren N., Marshall A.W., Baum H. (2011). A comprehensive methodology for characterizing sprinkler sprays. Proc Combust Inst 33(2): 2547–2554.

Ridler T., Calvard S. (1978). Picture thresholding using an iterative selection method. IEEE Transactions on Systems, Man, and Cybernetics SMC, 8 (8):630–632.

Rudin, L.I., Osher, S., Fatemi, E. (1992). Nonlinear total variation based noise removal algorithms. Physica D, 60: 259–268.

Sheppard, D.T. (2002). Spray Characteristics of Fire Sprinklers. National Institute of Standards and Reporting NIST GCR 02-838, Gaithersburg, MD.

Sæbø, A.O., Wighus, R. (2015). Droplet sizes from deluge nozzles. Report no A15 107453:1 (replaces restricted report NBL F09117, 2009), Trondheim.

Thomas, G.O. (2000). On the Conditions Required for Explosion Mitigation by Water Sprays. Process Safety and Environmental Protection, 78(5): 339-354.

Tolfo, F., Staudt Ph. (1976). Photomicrographic analysis of a spray: Determination of droplet size and velocity spectra by means of diamant's rotating mirror microscope. Journal of Aerosol Science, 7(6): 497-506.

Widmann, J.F. (2001). Phase Doppler interferometry measurements in water spray produced by residential fire sprinklers. Fire Safety Journal 36: 545–567.

Wighus, R. (2012). Droplet size, velocity and area distribution – Deluge nozzles. Report NBL A12114 (replaces restricted report NBL F03113, 2006), Trondheim.

Yu, H.Z. (1986). Investigation of spray patterns of selected sprinklers with the FMRC drop size measuring system. Proceedings of the 1st international symposium on fire safety science. Hemisphere Publishing Corp., 1165–1176.

Yule A.J., Chigier N.A., Cox N.W. (1978). Measurement of particle sizes in sprays by the automated analysis of spark photographs. Particle Size Analysis, Heyden Press, New York, 61-73.

Zhou, X., Yu, H.-Z. (2011). Experimental investigation of spray formation as affected by sprinkler geometry. Fire Safety Journal 46: 140-150.

Zhou, X., D'Aniello, S.P., Yu, H.-Z. (2012). Spray Characterization Measurements of a Pendent Fire Sprinkler. Fire Safety Journal 54: 36-48.

Zlatanovic, L.,Vreeburg, J., van der Hoek, J.P., Poznakovs, I. (2014). An experimental study on the spray characteristics of residential sprinklers under low-flow and low-pressure conditions. Fire Safety Journal 68: 30-40.

List of appendices

Appendix 1: ISFEH paper

Lundberg, J., Lysaker, O.M., Vaagsaether K., Bjerketvedt D. Image-based characterization of a medium velocity fire water nozzle – preliminary results. Seventh international seminar on fire & explosion hazards, pp 492-500, Providence, RI, USA, 5 – 10th of May, 2013.

Appendix 2: ISHPMIE paper

Lundberg, J., Lysaker, O.M., Vaagsaether K., Bjerketvedt D. Characterization of deluge spray with image processing, Tenth international symposium on hazards, prevention and mitigation of industrial explosions. Bergen, Norway 10-14th of June, 2014.

Appendix 3: Droplet size data

Droplet size distributions from all locations at three pressures.

Appendix 3: Droplet size data

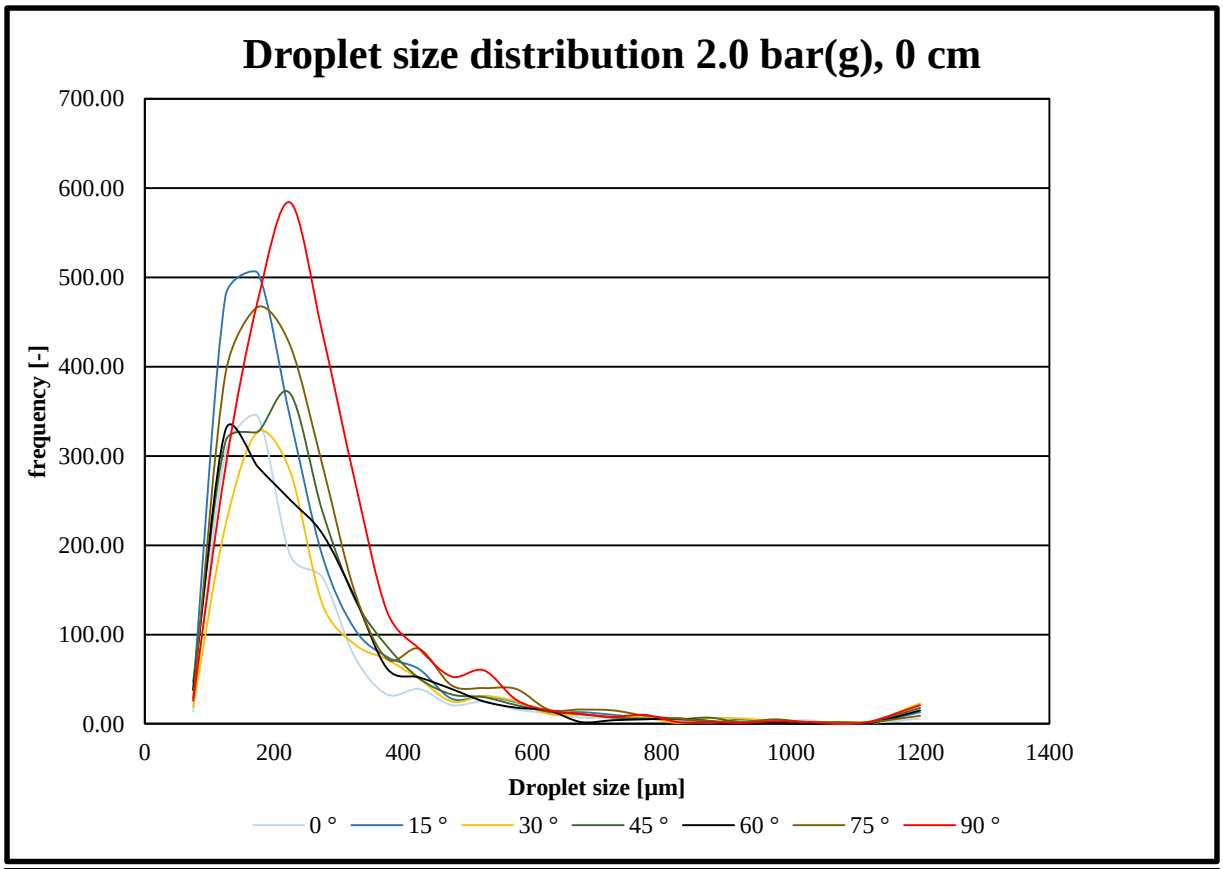
Droplet size distribution 2.0 bar(g), 0 cm
700.00
600.00
500.00
400.00
300.00
200.00
100.00
0.00
frequency [-]
0
200
400
600
800
1000
1200
1400
Droplet size [µm]
0 °
15 °
30 °
45 °
60 °
75 °
90 °

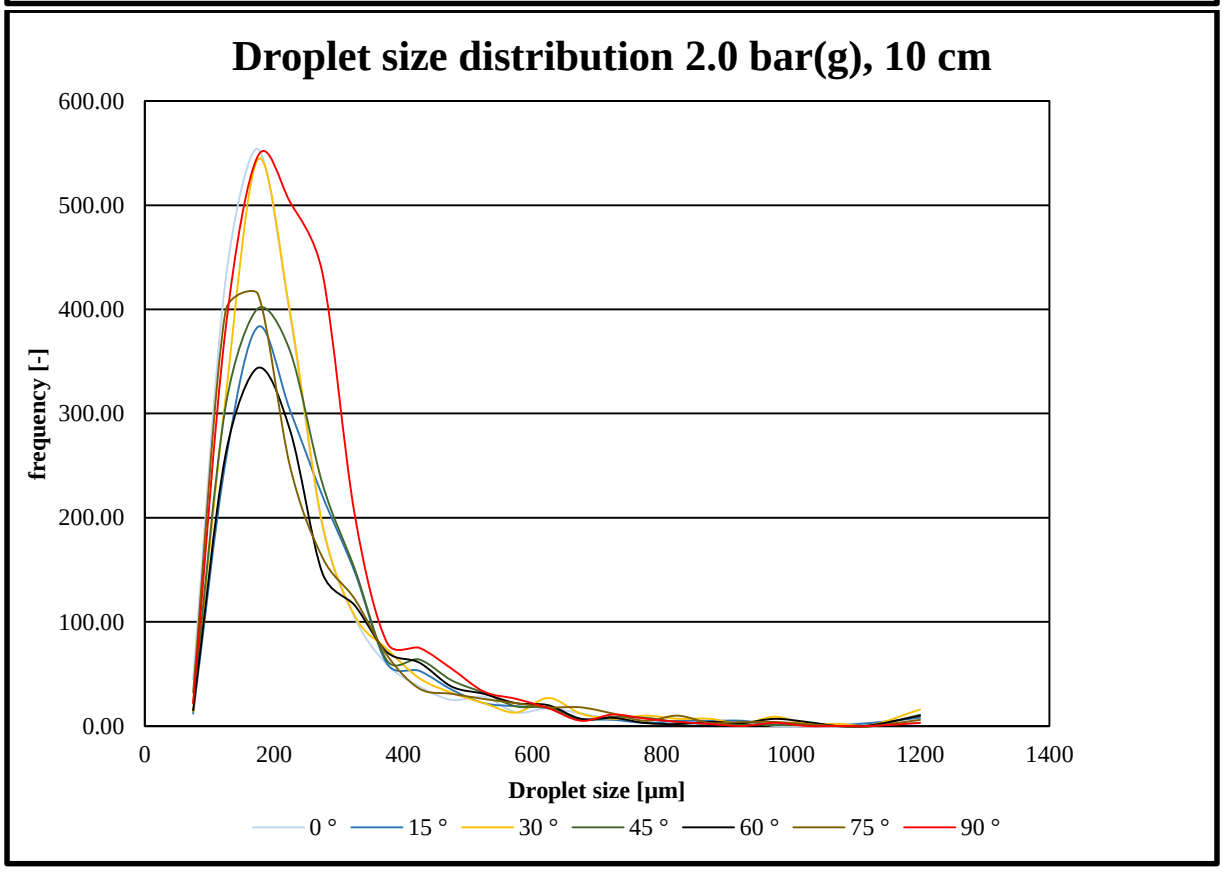
Droplet size distribution 2.0 bar(g), 10 cm
600.00
500.00
400.00
300.00
200.00
100.00
0.00
frequency [-]
0
200
400
600
800
1000
1200
1400
Droplet size [µm]
0 °
15 °
30 °
45 °
60 °
75 °
90 °

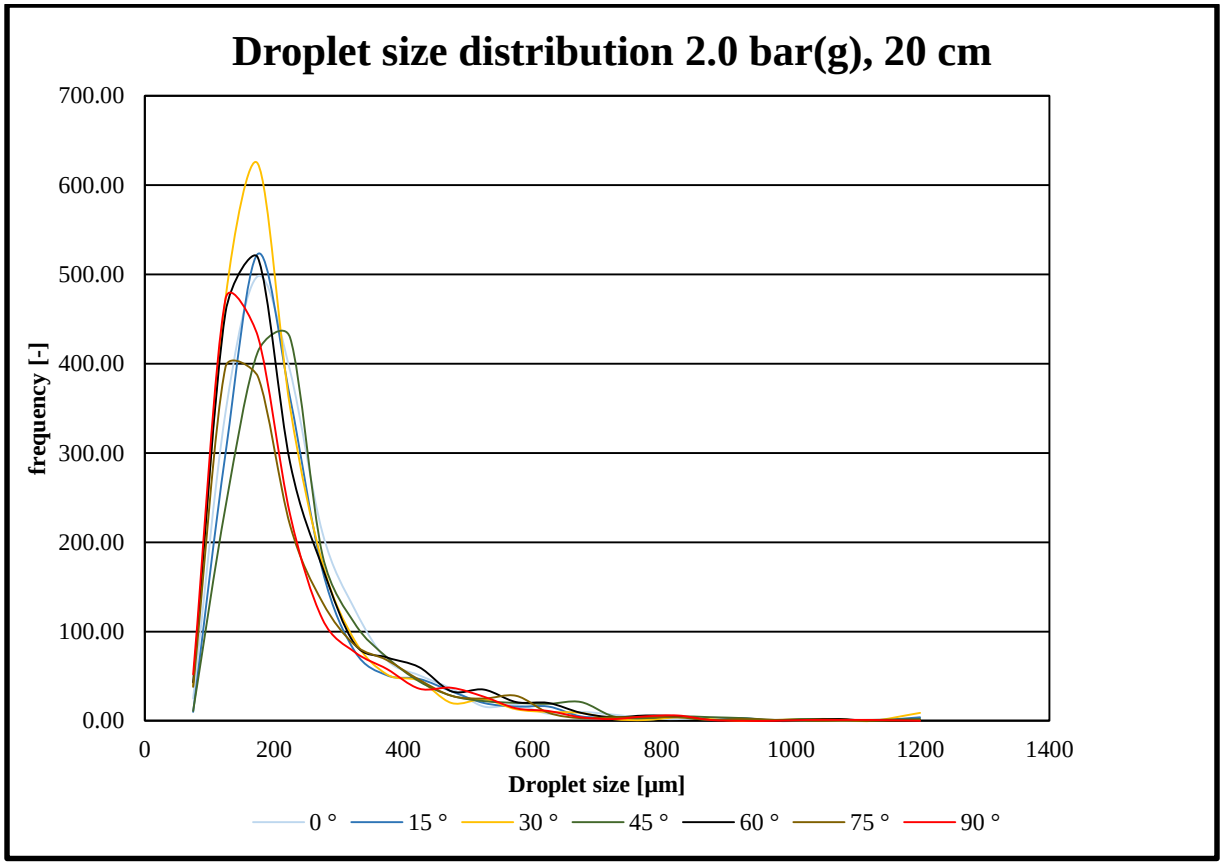
Droplet size distribution 2.0 bar(g), 20 cm
700.00
600.00
500.00
400.00
300.00
200.00
100.00
0.00
frequency [-]
0
200
400
600
800
1000
1200
1400
Droplet size [µm]
0 °
15 °
30 °
45 °
60 °
75 °
90 °

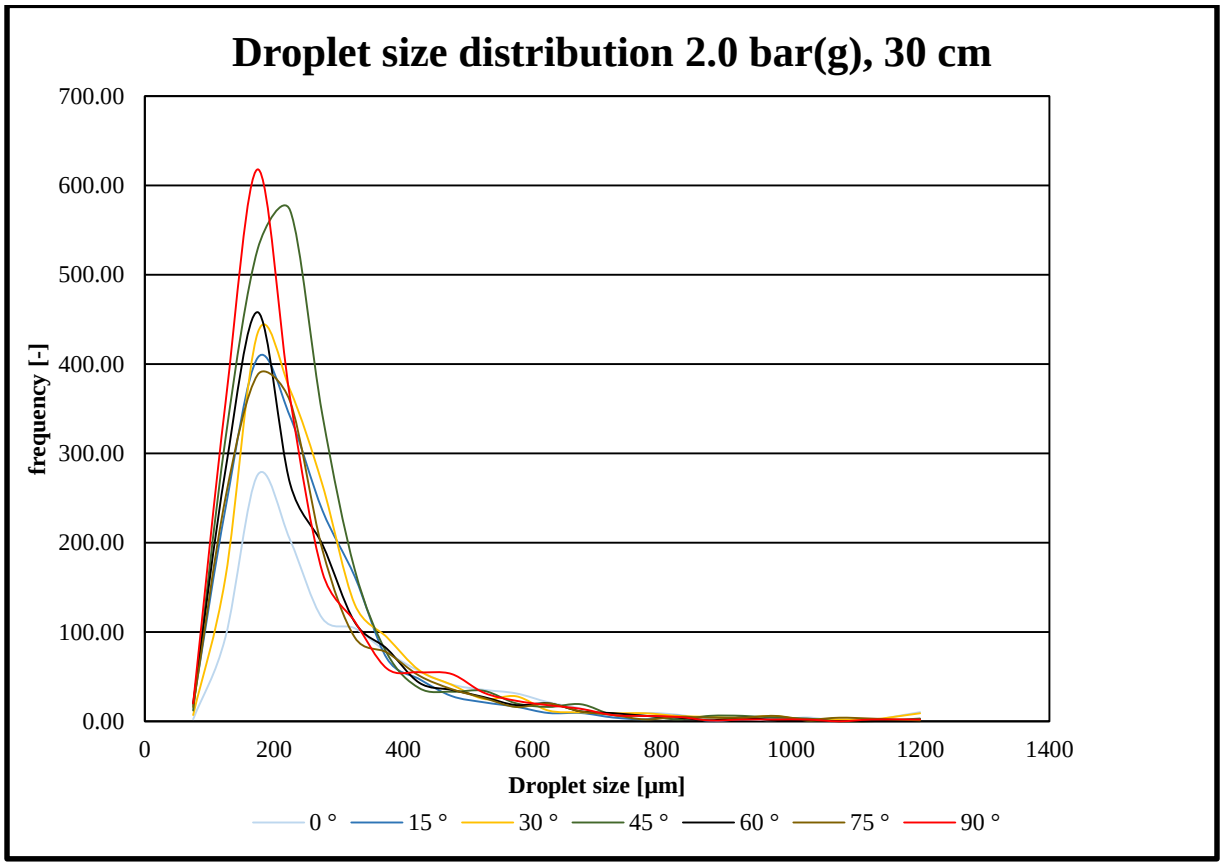
Droplet size distribution 2.0 bar(g), 30 cm
700.00
600.00
500.00
400.00
300.00
200.00
100.00
0.00
frequency [-]
0
200
400
600
800
1000
1200
1400
Droplet size [µm]
0 °
15 °
30 °
45 °
60 °
75 °
90 °

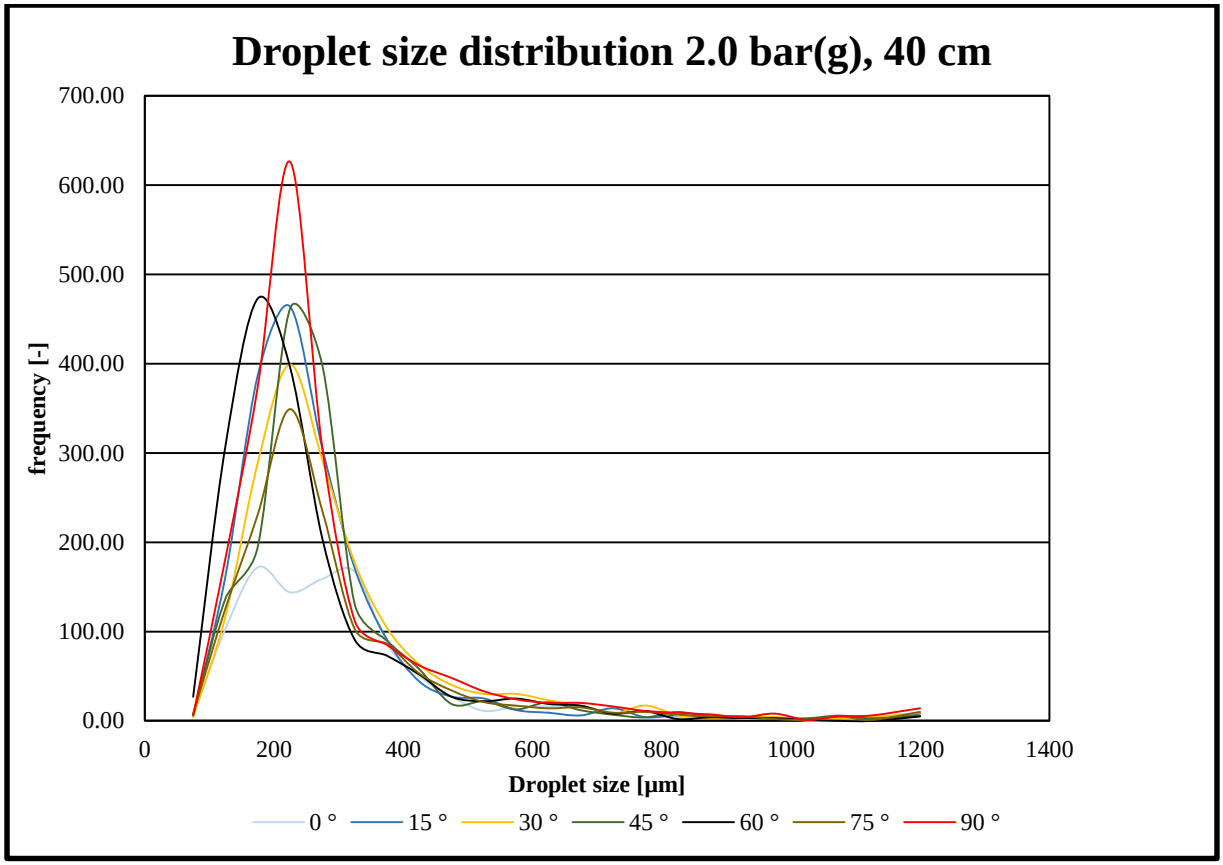
Droplet size distribution 2.0 bar(g), 40 cm
700.00
600.00
500.00
400.00
300.00
200.00
100.00
0.00
frequency [-]
0
200
400
600
800
1000
1200
1400
Droplet size [µm]
0 °
15 °
30 °
45 °
60 °
75 °
90 °

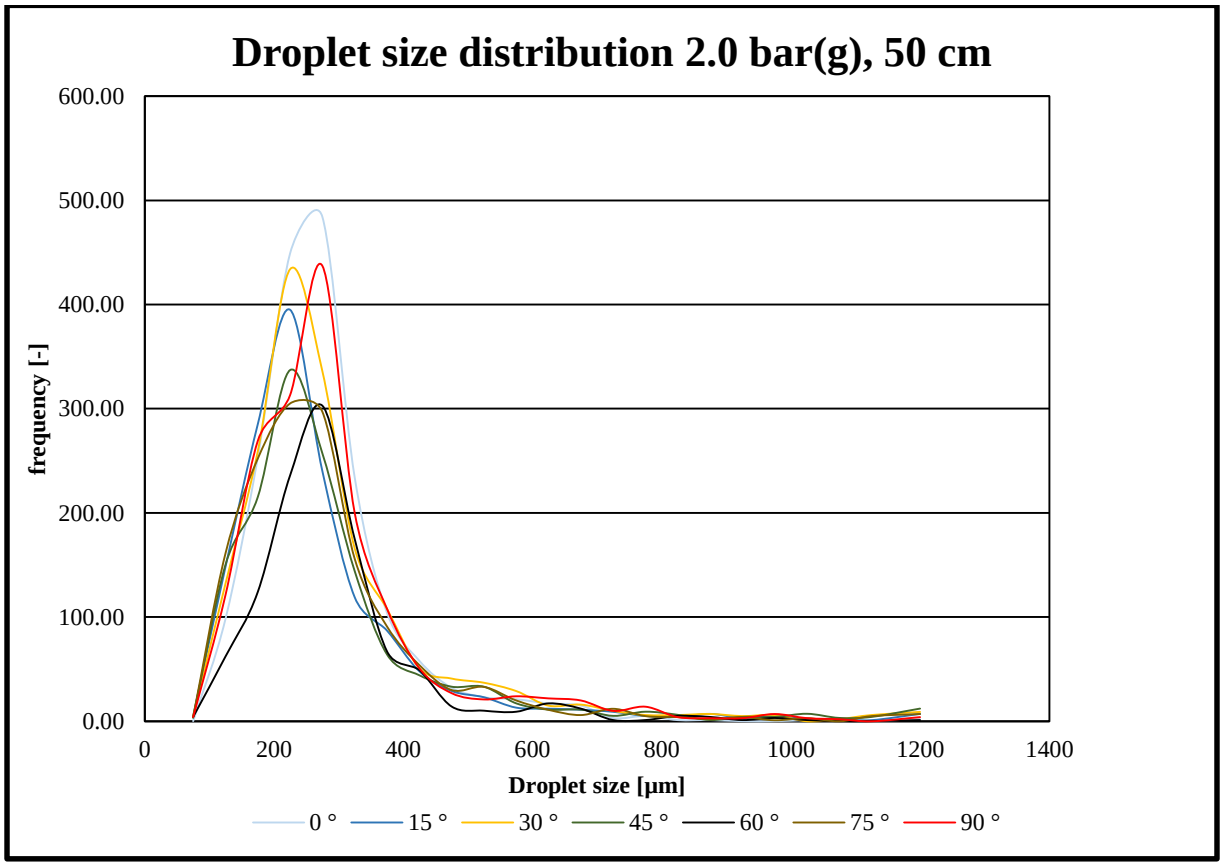
Droplet size distribution 2.0 bar(g), 50 cm
600.00
500.00
400.00
300.00
200.00
100.00
0.00
frequency [-]
0
200
400
600
800
1000
1200
1400
Droplet size [µm]
0 °
15 °
30 °
45 °
60 °
75 °
90 °

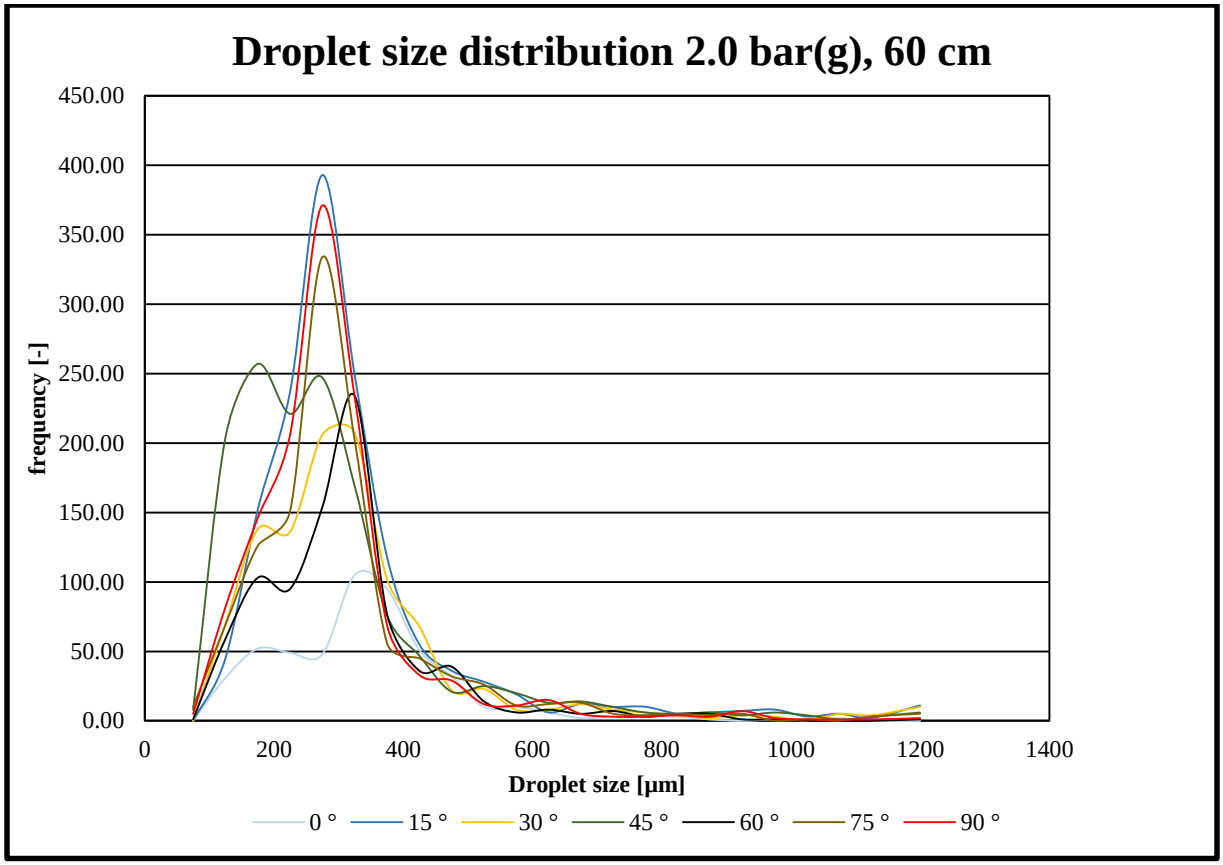
Droplet size distribution 2.0 bar(g), 60 cm
450.00
400.00
350.00
300.00
250.00
200.00
150.00
100.00
50.00
0.00
frequency [-]
0
200
400
600
800
1000
1200
1400
Droplet size [µm]
0 °
15 °
30 °
45 °
60 °
75 °
90 °

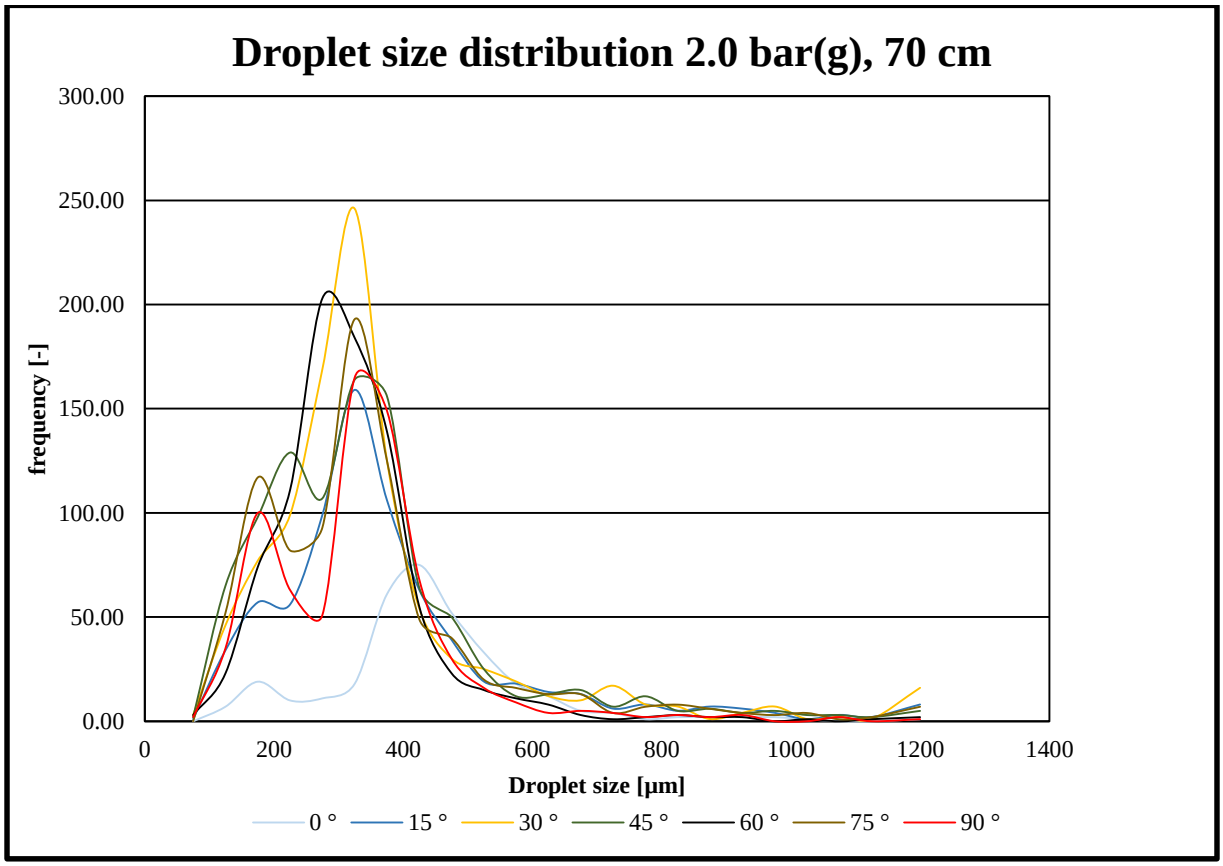
Droplet size distribution 2.0 bar(g), 70 cm
300.00
250.00
200.00
150.00
100.00
50.00
0.00
frequency [-]
0
200
400
600
800
1000
1200
1400
Droplet size [µm]
0 °
15 °
30 °
45 °
60 °
75 °
90 °

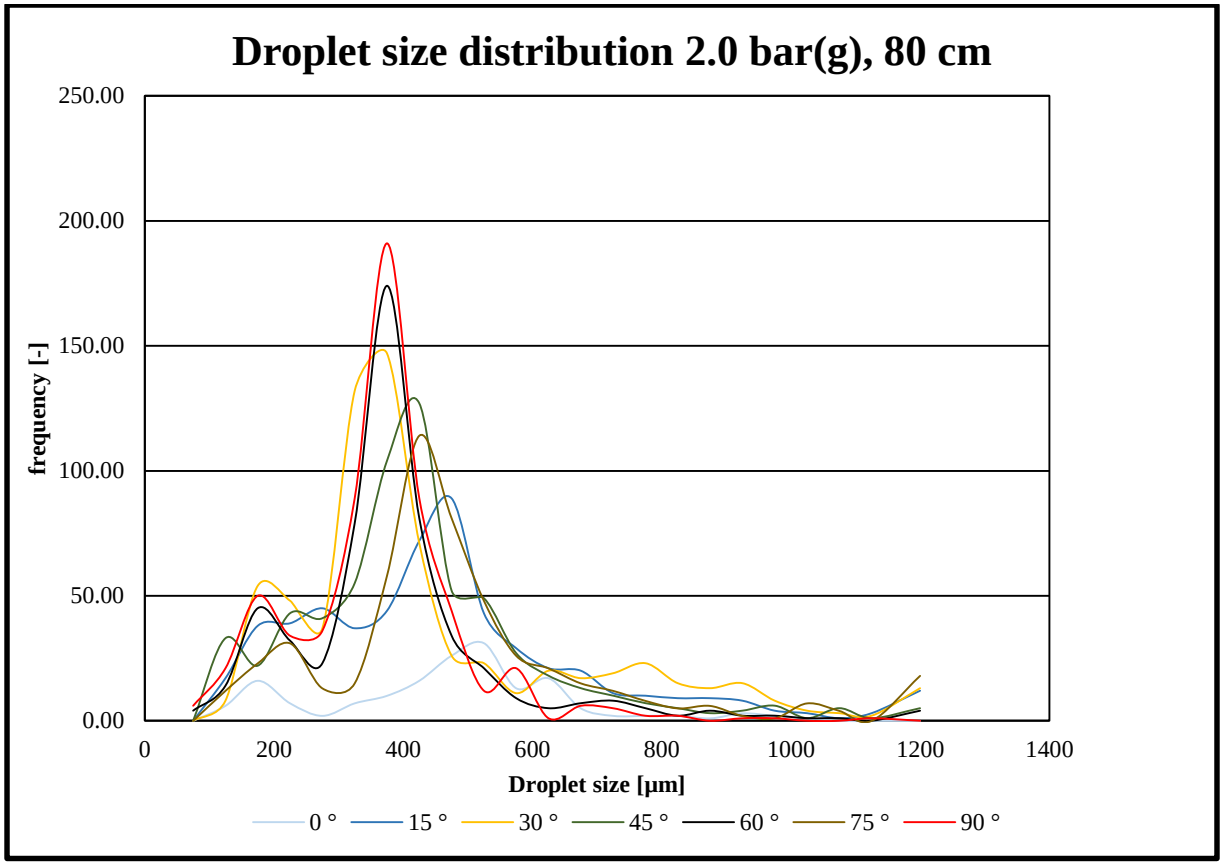
Droplet size distribution 2.0 bar(g), 80 cm
250.00
200.00
150.00
100.00
50.00
0.00
frequency [-]
0
200
400
600
800
1000
1200
1400
Droplet size [µm]
0 °
15 °
30 °
45 °
60 °
75 °
90 °

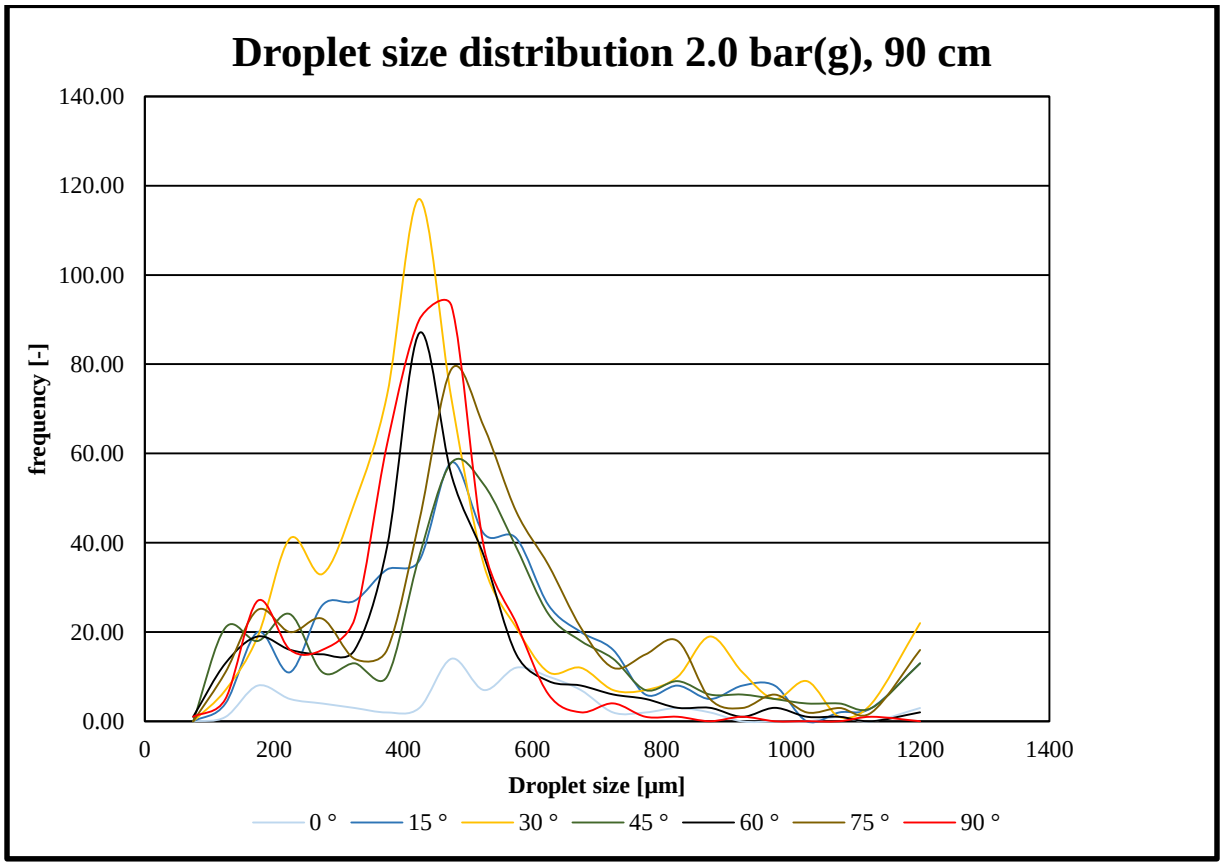
Droplet size distribution 2.0 bar(g), 90 cm
140.00
120.00
100.00
80.00
60.00
40.00
20.00
0.00
frequency [-]
0
200
400
600
800
1000
1200
1400
Droplet size [µm]
0 °
15 °
30 °
45 °
60 °
75 °
90 °

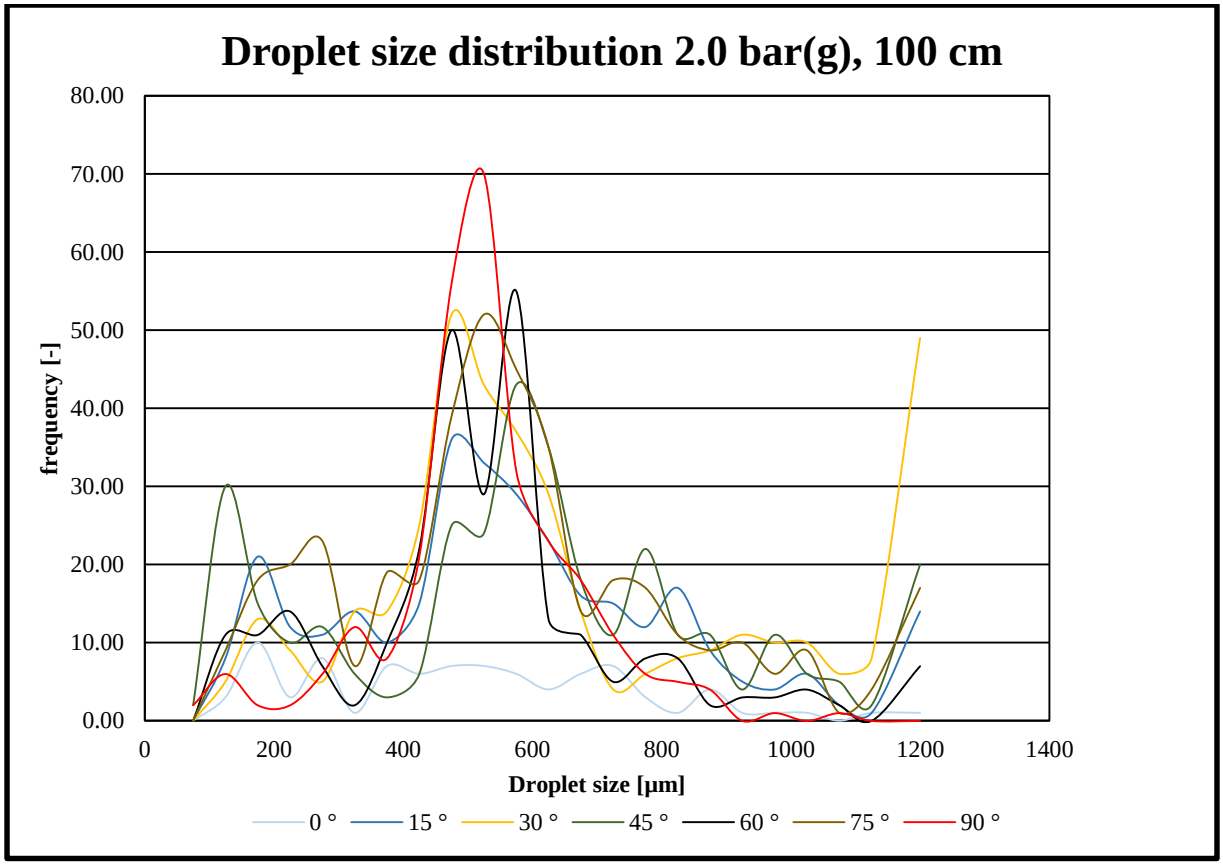
Droplet size distribution 2.0 bar(g), 100 cm
frequency [-]
80.00
70.00
60.00
50.00
40.00
30.00
20.00
10.00
0.00
0
200
400
600
800
1000
1200
1400
Droplet size [µm]
0 °
15 °
30 °
45 °
60 °
75 °
90 °

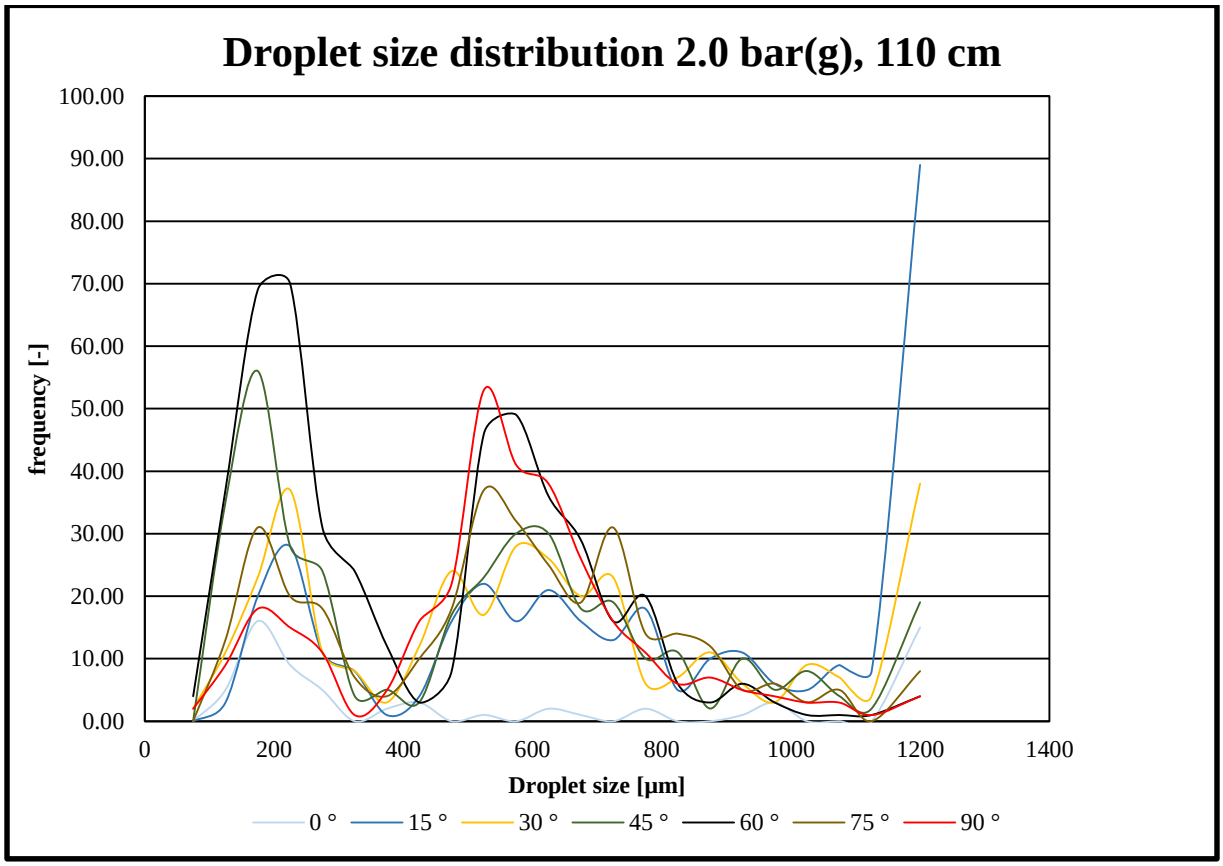
Droplet size distribution 2.0 bar(g), 110 cm
frequency [-]
100.00
90.00
80.00
70.00
60.00
50.00
40.00
30.00
20.00
10.00
0.00
0
200
400
600
800
1000
1200
1400
Droplet size [µm]
0 °
15 °
30 °
45 °
60 °
75 °
90 °

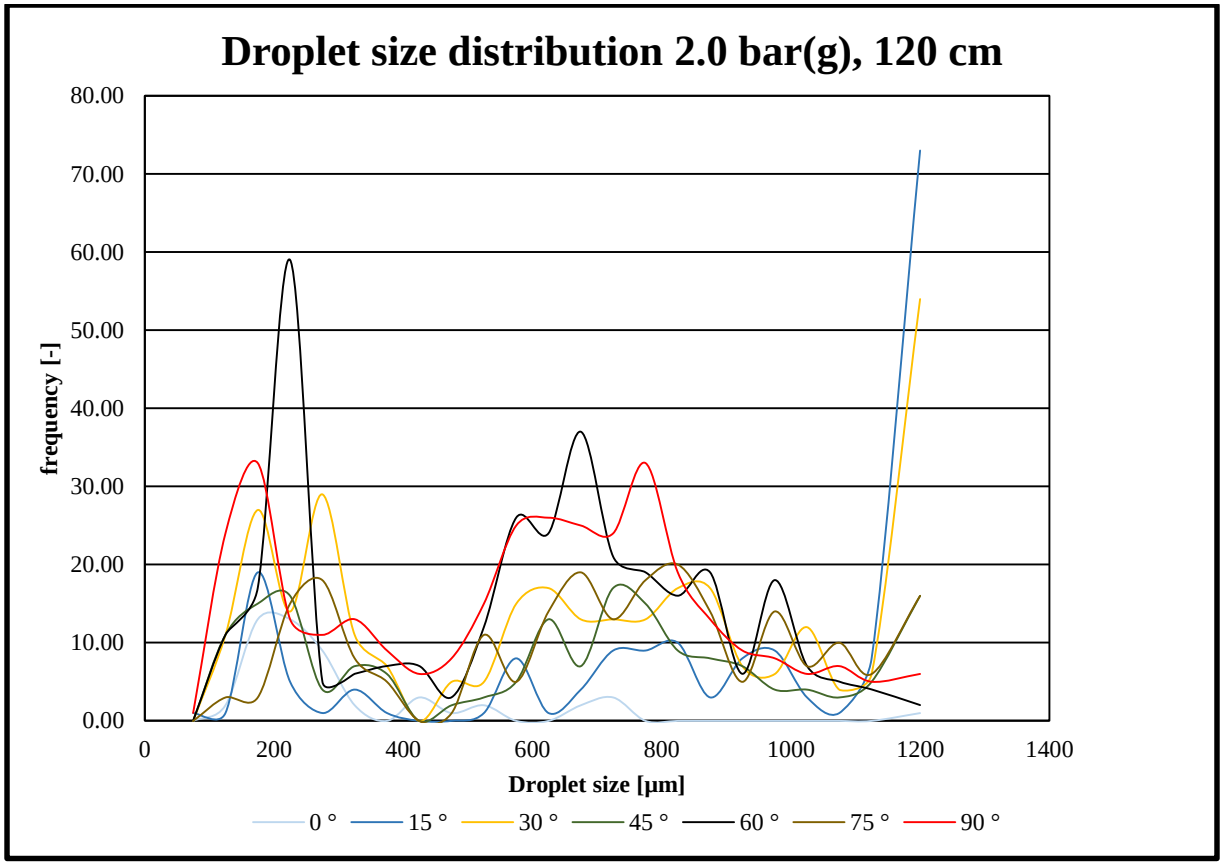
Droplet size distribution 2.0 bar(g), 120 cm
80.00
70.00
60.00
50.00
40.00
30.00
20.00
10.00
0.00
frequency [-]
0
200
400
600
800
1000
1200
1400
Droplet size [µm]
0 °
15 °
30 °
45 °
60 °
75 °
90 °

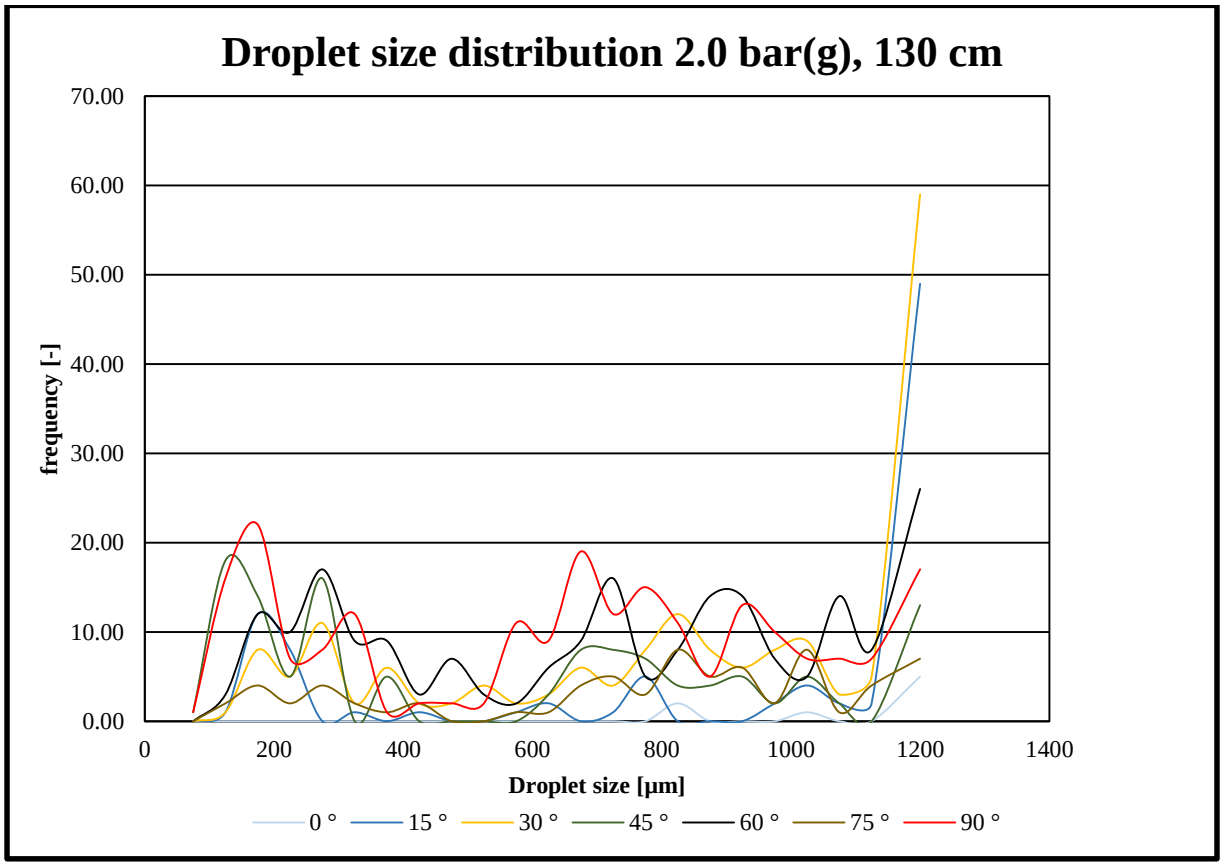
Droplet size distribution 2.0 bar(g), 130 cm
70.00
60.00
50.00
40.00
30.00
20.00
10.00
0.00
frequency [-]
0
200
400
600
800
1000
1200
1400
Droplet size [µm]
0 °
15 °
30 °
45 °
60 °
75 °
90 °

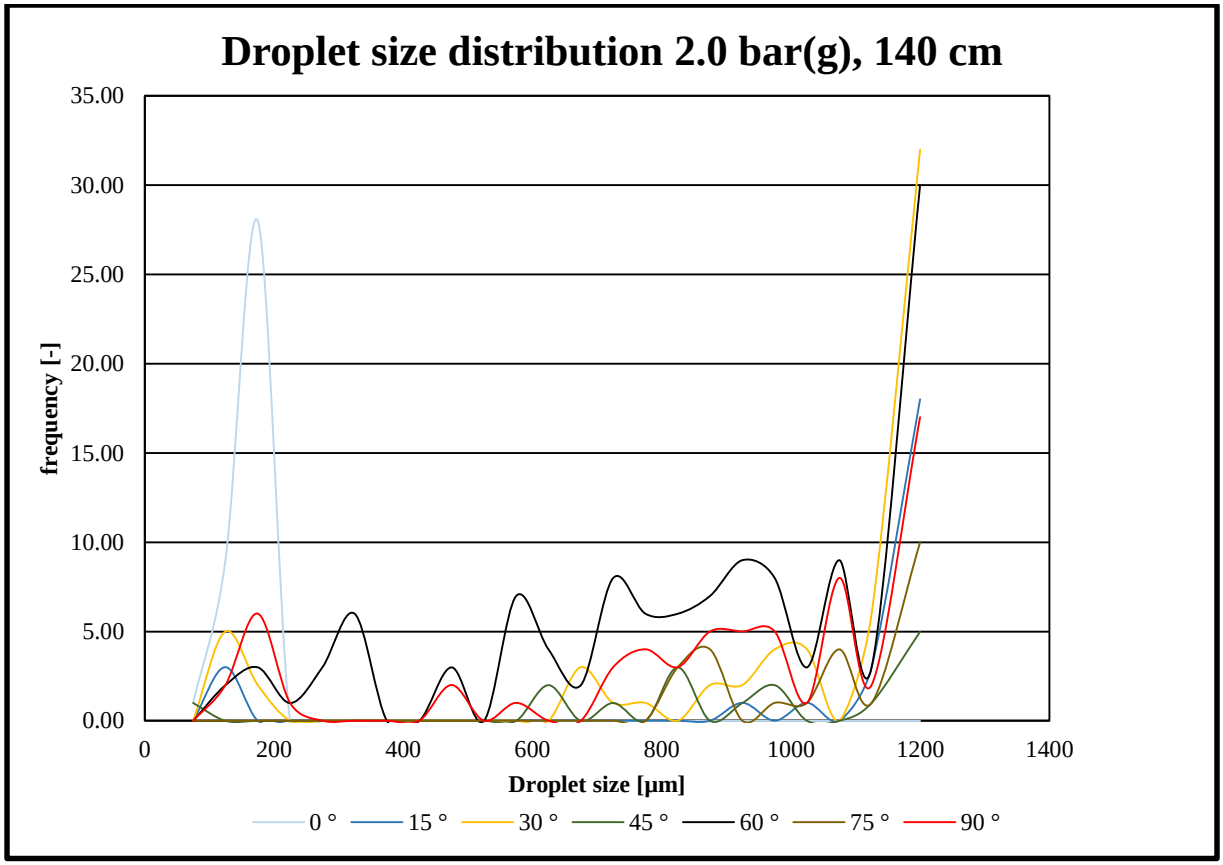
Droplet size distribution 2.0 bar(g), 140 cm
35.00
30.00
25.00
20.00
15.00
10.00
5.00
0.00
frequency [-]
0
200
400
600
800
1000
1200
1400
Droplet size [µm]
0 °
15 °
30 °
45 °
60 °
75 °
90 °

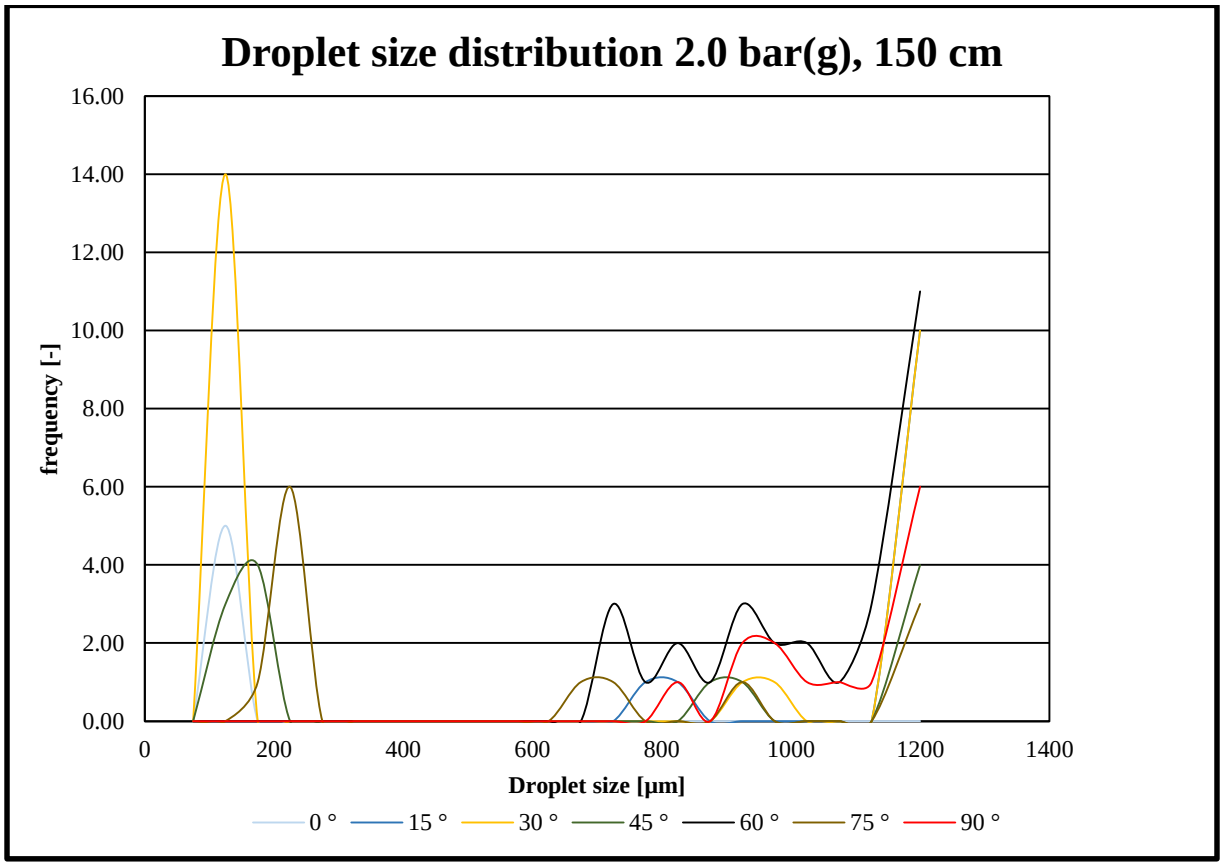
Droplet size distribution 2.0 bar(g), 150 cm
16.00
14.00
12.00
10.00
8.00
6.00
4.00
2.00
0.00
frequency [-]
0
200
400
600
800
1000
1200
1400
Droplet size [µm]
0 °
15 °
30 °
45 °
60 °
75 °
90 °

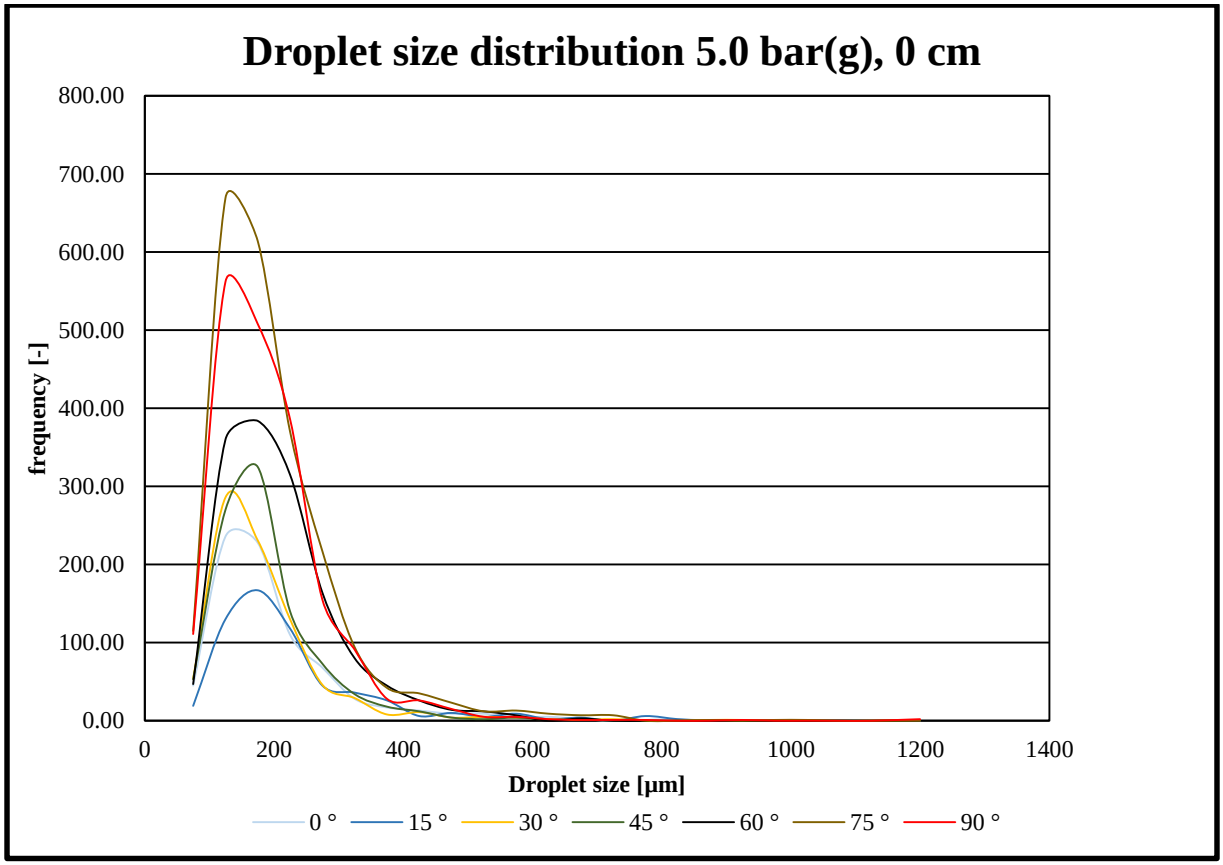
Droplet size distribution 5.0 bar(g), 0 cm
800.00
700.00
600.00
500.00
400.00
300.00
200.00
100.00
0.00
frequency [-]
0
200
400
600
800
1000
1200
1400
Droplet size [µm]
0 °
15 °
30 °
45 °
60 °
75 °
90 °

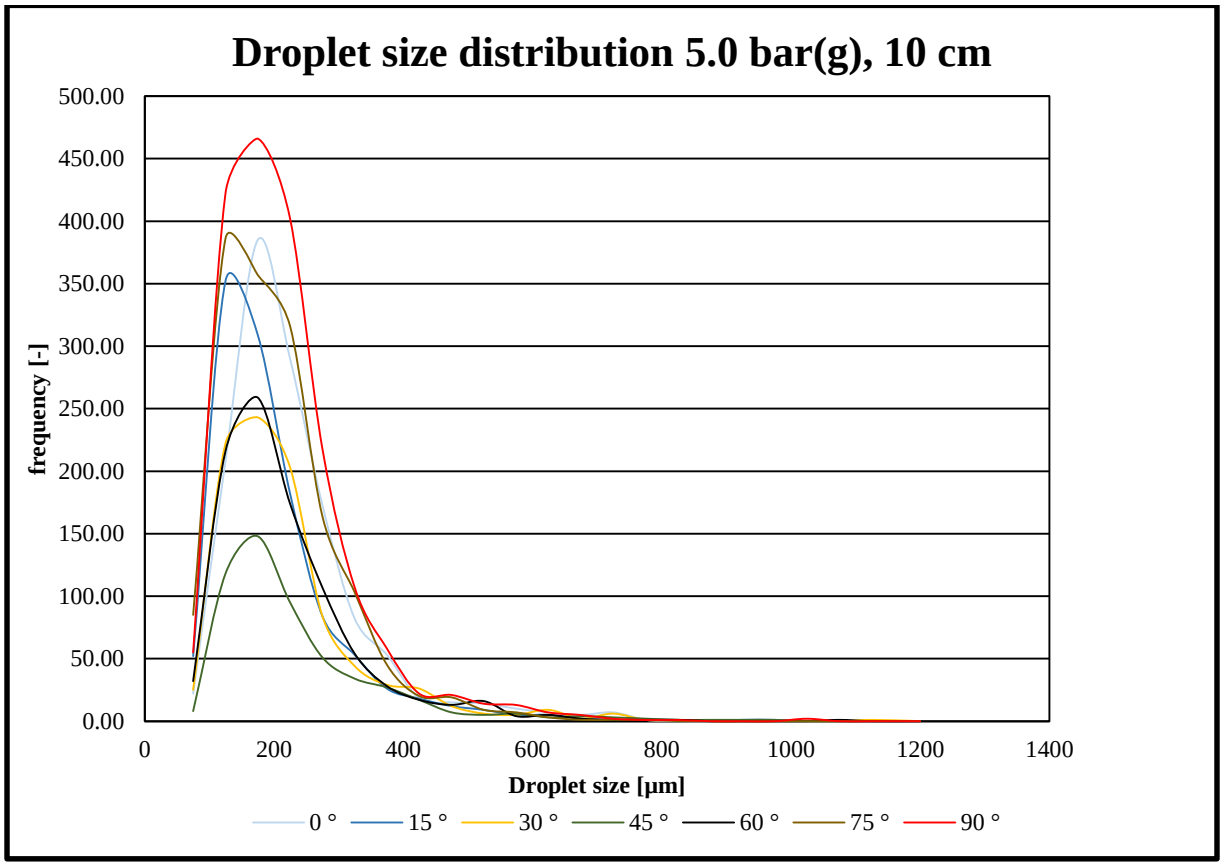
Droplet size distribution 5.0 bar(g), 10 cm
500.00
450.00
400.00
350.00
300.00
250.00
200.00
150.00
100.00
50.00
0.00
frequency [-]
0
200
400
600
800
1000
1200
1400
Droplet size [µm]
0 °
15 °
30 °
45 °
60 °
75 °
90 °

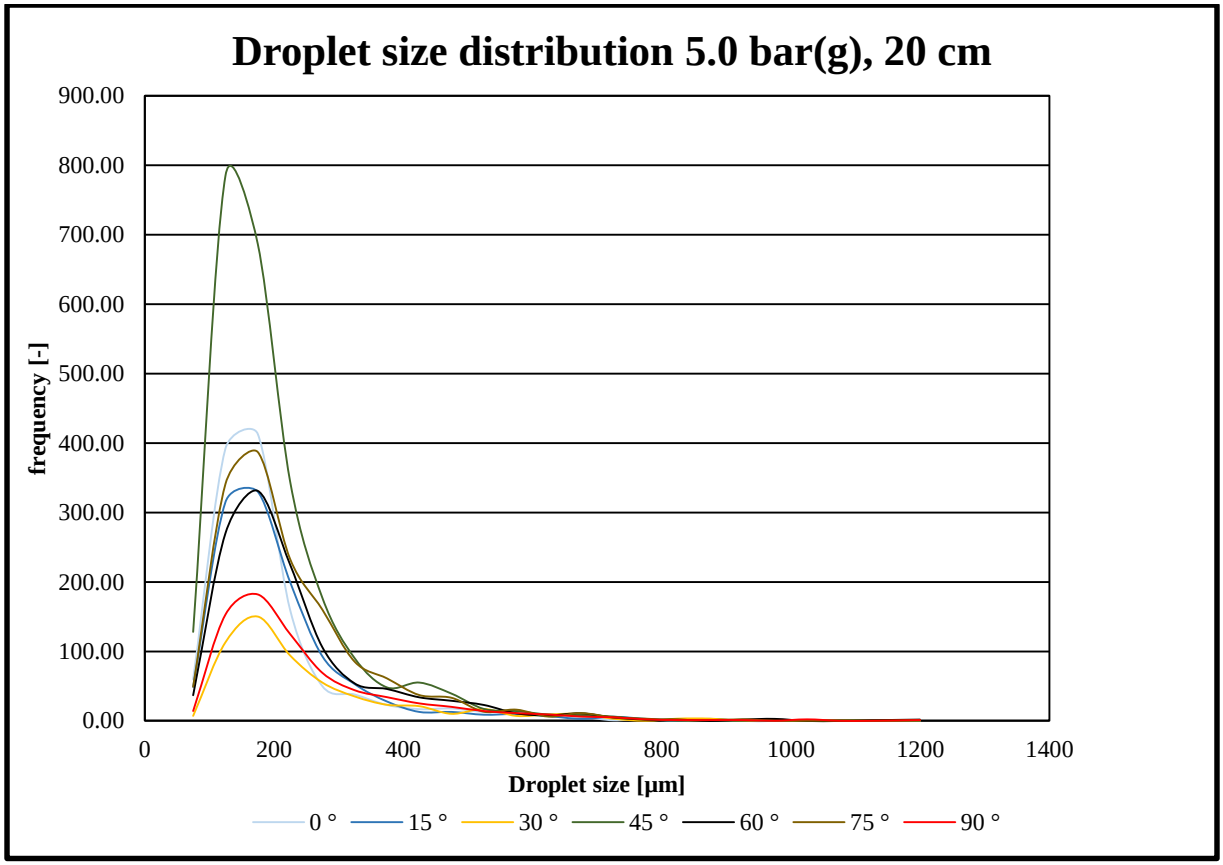
Droplet size distribution 5.0 bar(g), 20 cm
900.00
800.00
700.00
600.00
500.00
400.00
300.00
200.00
100.00
0.00
frequency [-]
0
200
400
600
800
1000
1200
1400
Droplet size [µm]
0 °
15 °
30 °
45 °
60 °
75 °
90 °

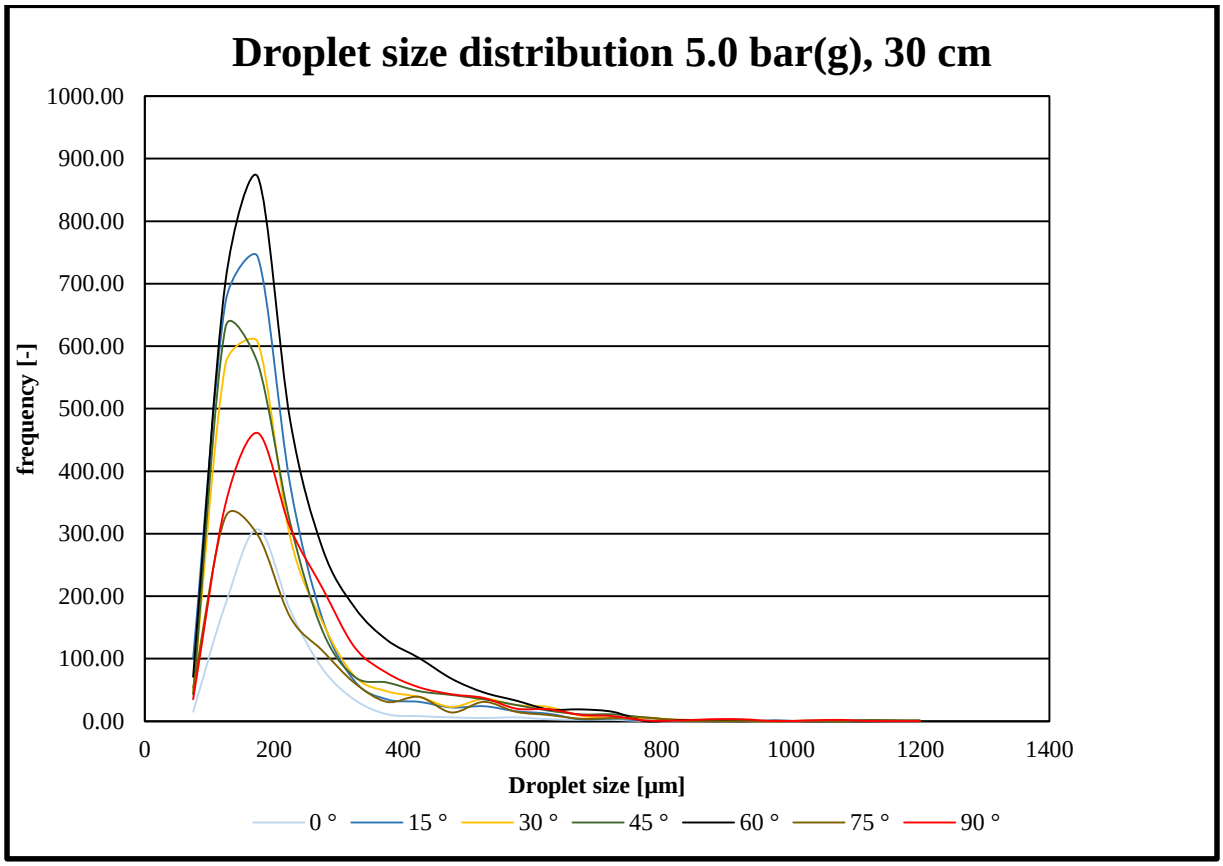
Droplet size distribution 5.0 bar(g), 30 cm
1000.00
900.00
800.00
700.00
600.00
500.00
400.00
300.00
200.00
100.00
0.00
frequency [-]
0
200
400
600
800
1000
1200
1400
Droplet size [µm]
0 °
15 °
30 °
45 °
60 °
75 °
90 °

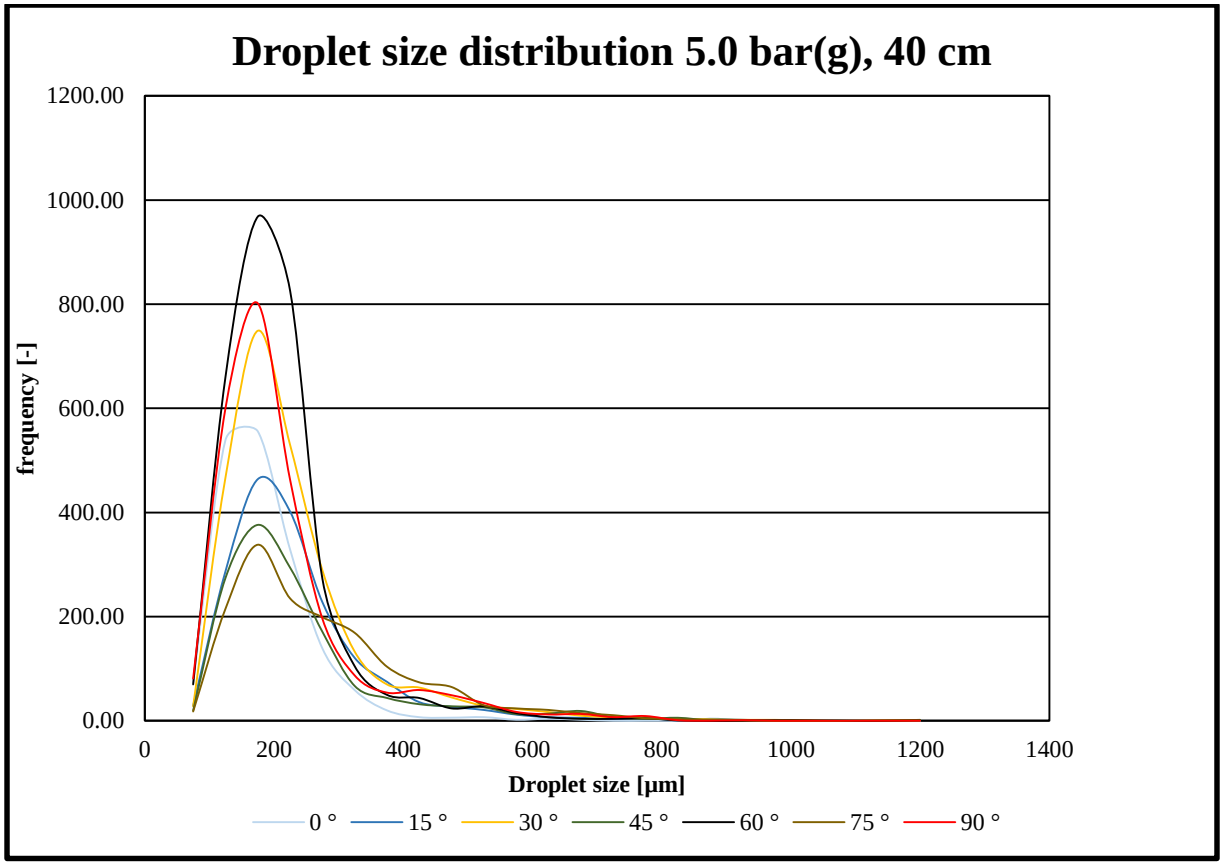
Droplet size distribution 5.0 bar(g), 40 cm
1200.00
1000.00
800.00
600.00
400.00
200.00
0.00
frequency [-]
0
200
400
600
800
1000
1200
1400
Droplet size [µm]
0 °
15 °
30 °
45 °
60 °
75 °
90 °

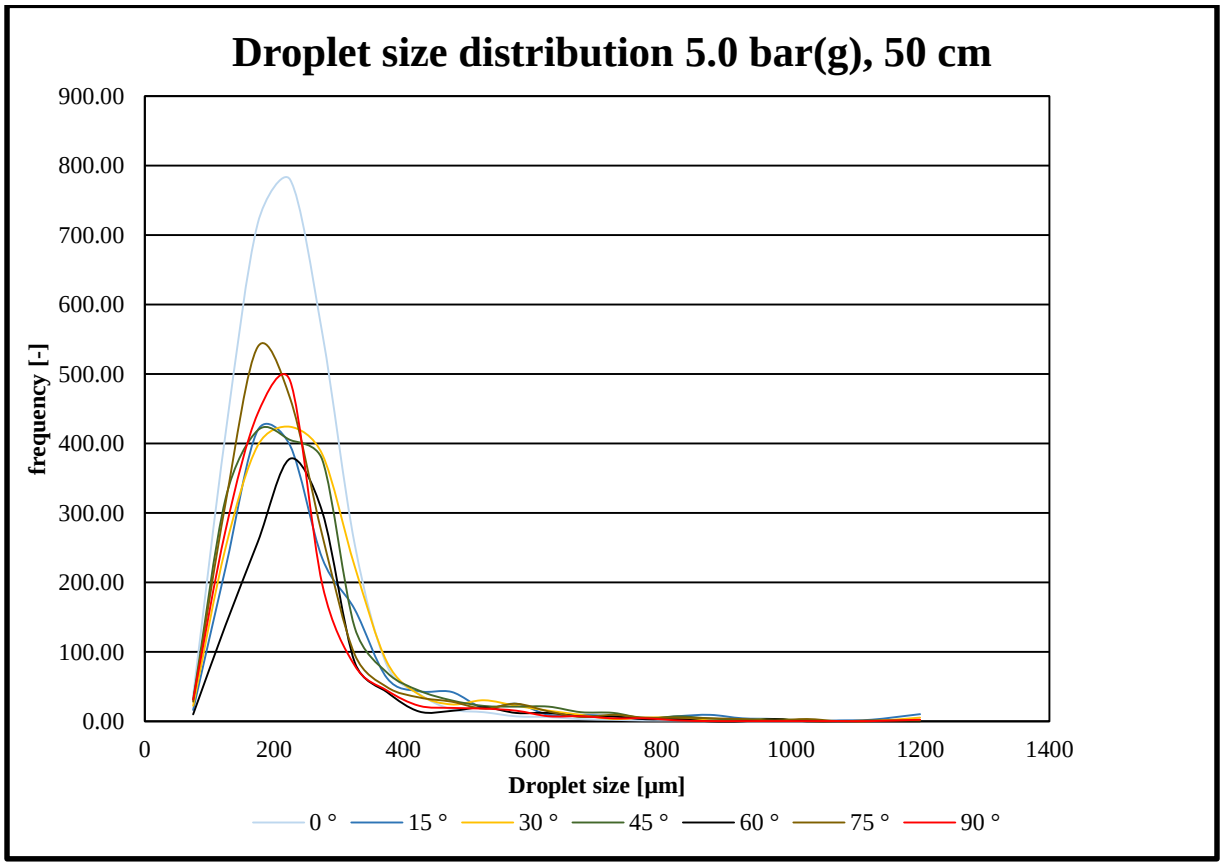
Droplet size distribution 5.0 bar(g), 50 cm
900.00
800.00
700.00
600.00
500.00
400.00
300.00
200.00
100.00
0.00
frequency [-]
0
200
400
600
800
1000
1200
1400
Droplet size [µm]
0 °
15 °
30 °
45 °
60 °
75 °
90 °

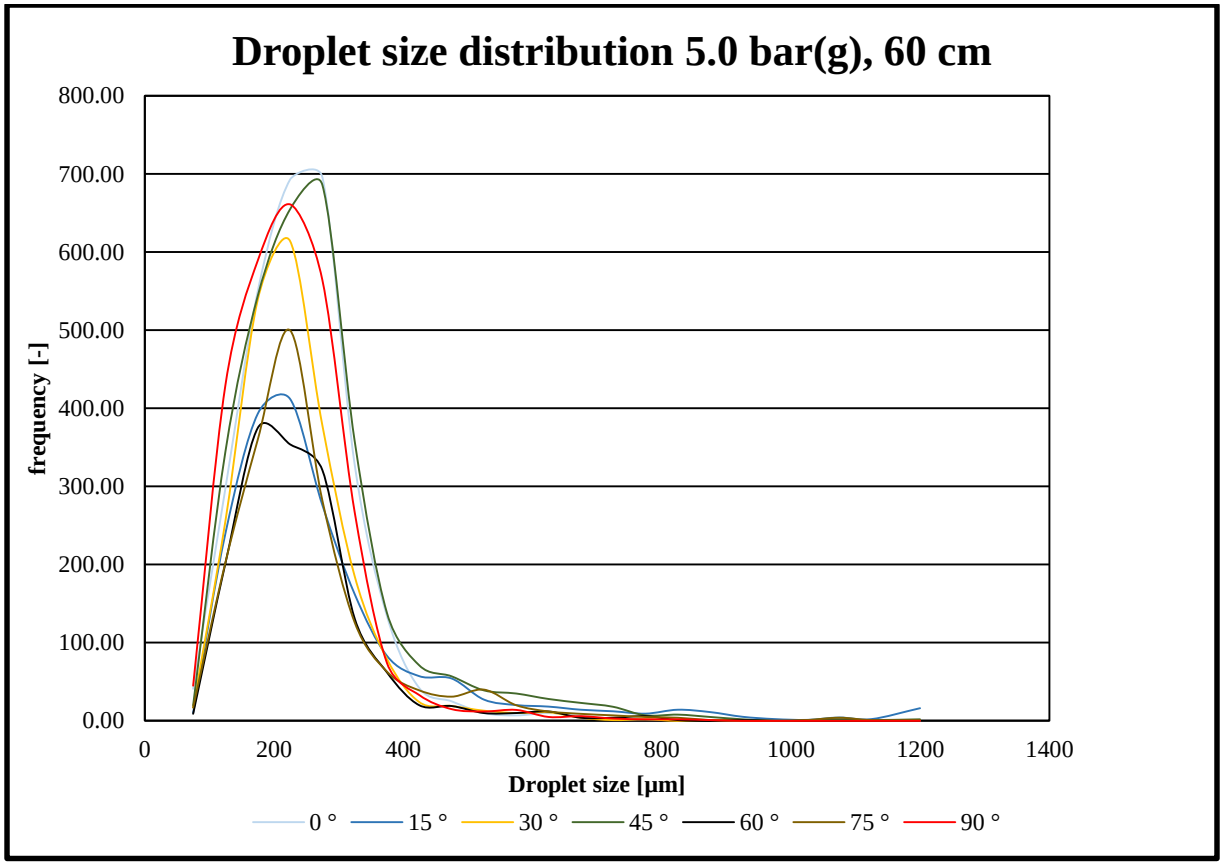
Droplet size distribution 5.0 bar(g), 60 cm
800.00
700.00
600.00
500.00
400.00
300.00
200.00
100.00
0.00
frequency [-]
0
200
400
600
800
1000
1200
1400
Droplet size [µm]
0 °
15 °
30 °
45 °
60 °
75 °
90 °

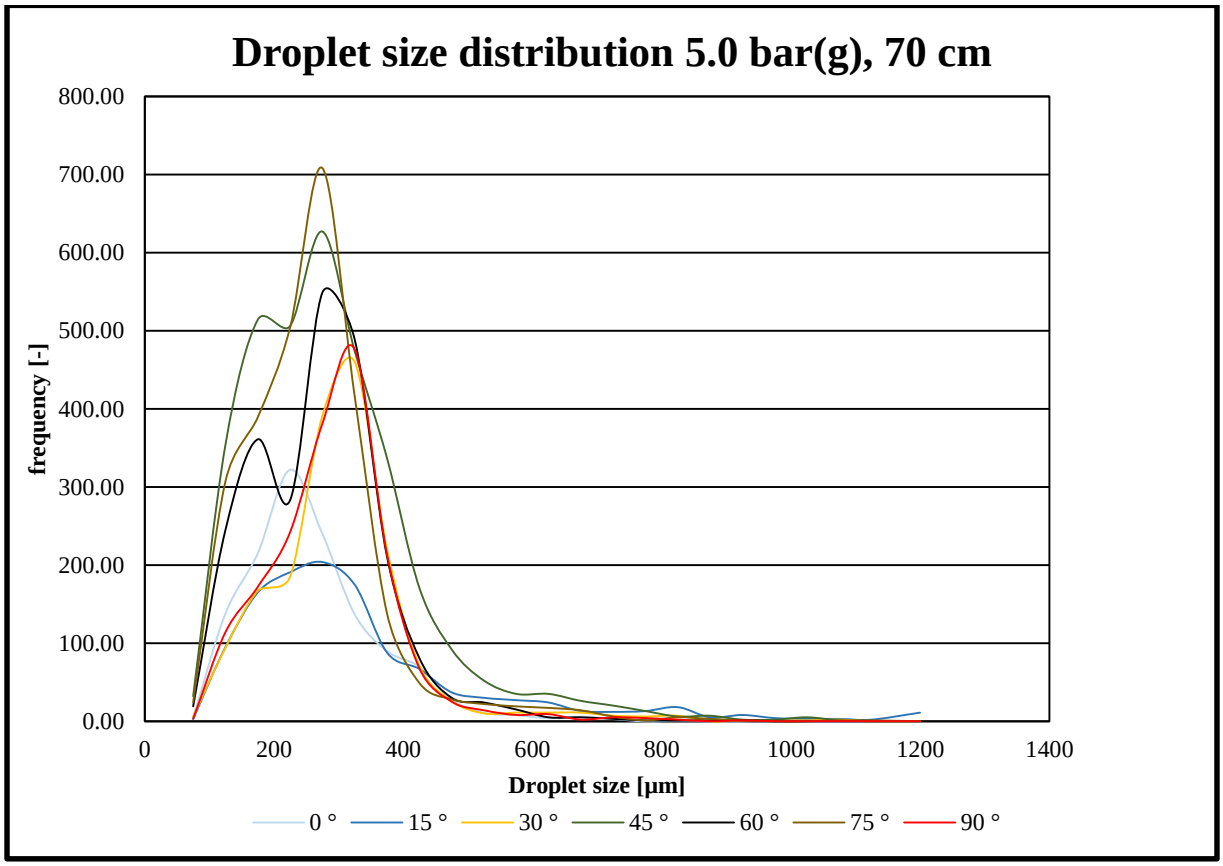
Droplet size distribution 5.0 bar(g), 70 cm
800.00
700.00
600.00
500.00
400.00
300.00
200.00
100.00
0.00
frequency [-]
0
200
400
600
800
1000
1200
1400
Droplet size [µm]
0 °
15 °
30 °
45 °
60 °
75 °
90 °

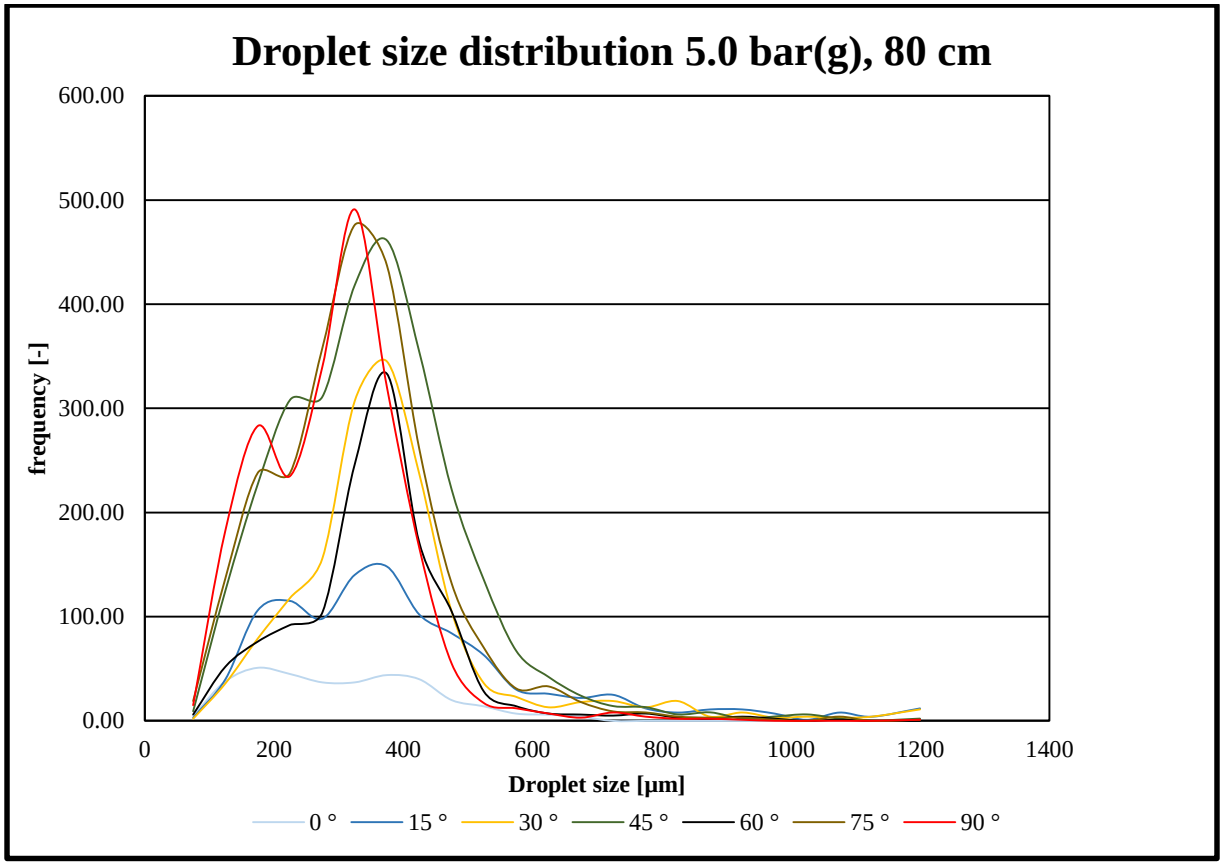
Droplet size distribution 5.0 bar(g), 80 cm
600.00
500.00
400.00
300.00
200.00
100.00
0.00
frequency [-]
0
200
400
600
800
1000
1200
1400
Droplet size [µm]
0 °
15 °
30 °
45 °
60 °
75 °
90 °

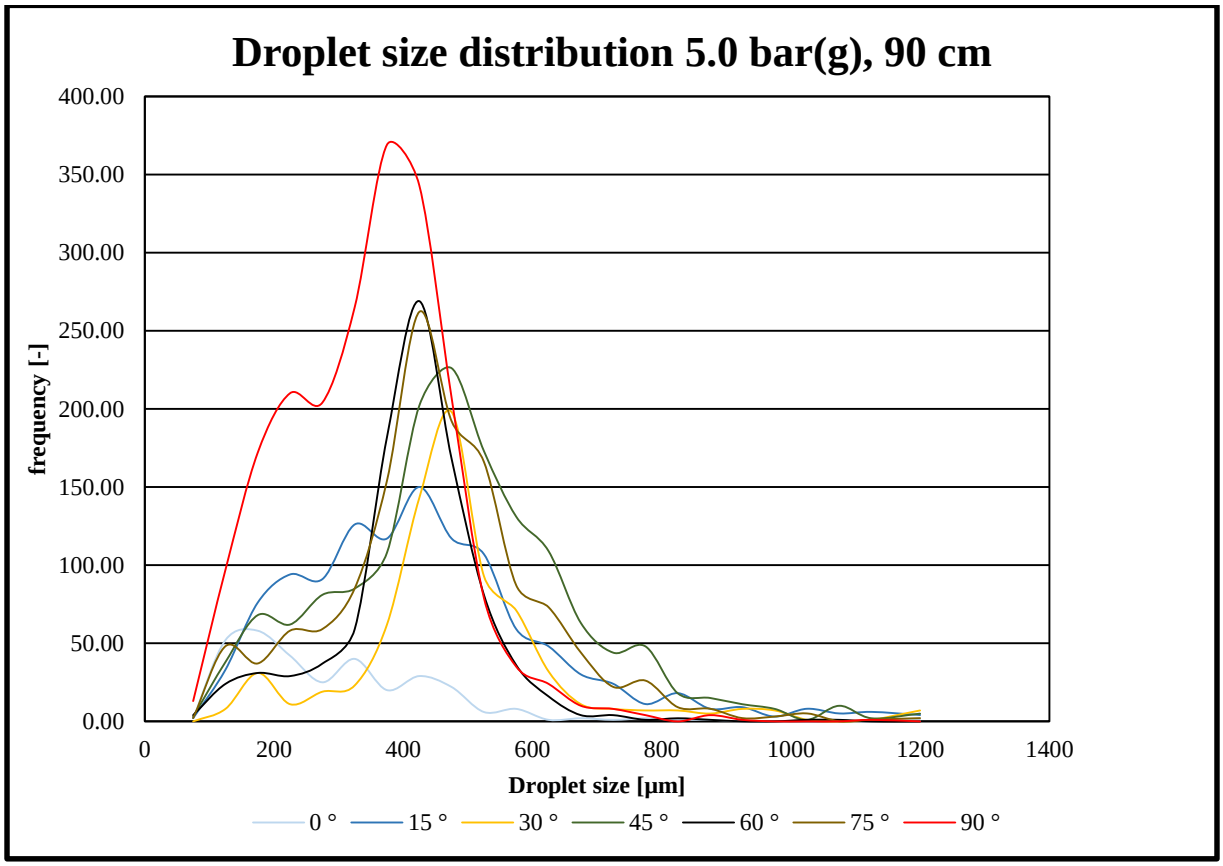
Droplet size distribution 5.0 bar(g), 90 cm
400.00
350.00
300.00
250.00
200.00
150.00
100.00
50.00
0.00
frequency [-]
0
200
400
600
800
1000
1200
1400
Droplet size [µm]
0 °
15 °
30 °
45 °
60 °
75 °
90 °

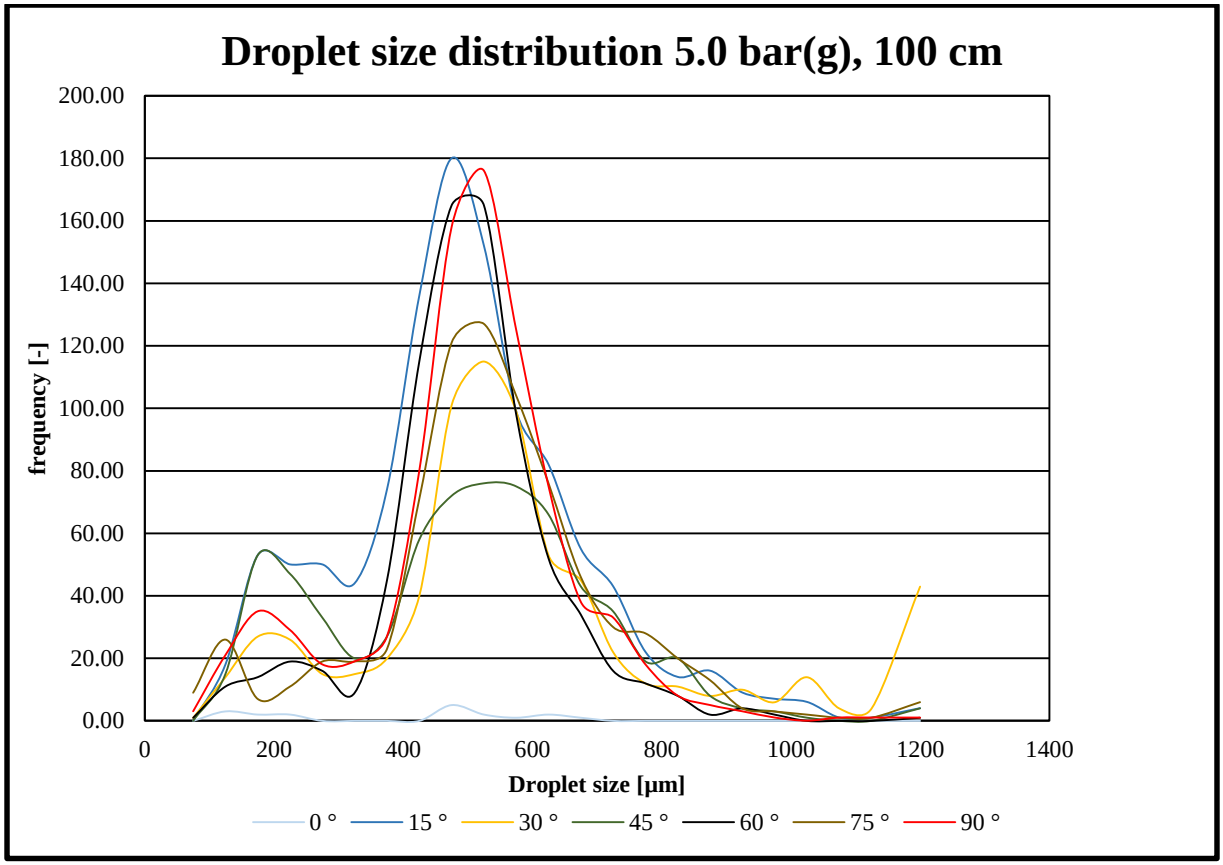
Droplet size distribution 5.0 bar(g), 100 cm
200.00
180.00
160.00
140.00
120.00
100.00
80.00
60.00
40.00
20.00
0.00
frequency [-]
0
200
400
600
800
1000
1200
1400
Droplet size [µm]
0 °
15 °
30 °
45 °
60 °
75 °
90 °

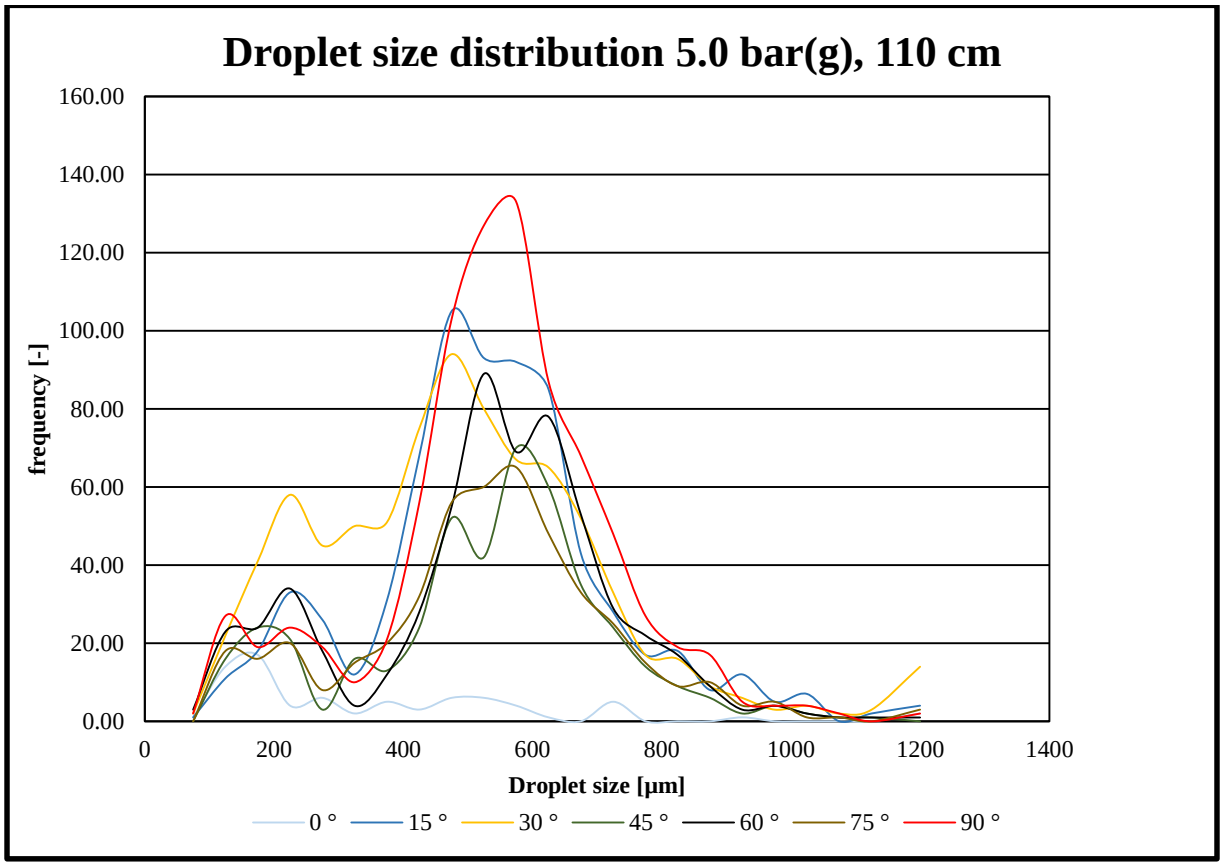
Droplet size distribution 5.0 bar(g), 110 cm
160.00
140.00
120.00
100.00
80.00
60.00
40.00
20.00
0.00
frequency [-]
0
200
400
600
800
1000
1200
1400
Droplet size [µm]
0 °
15 °
30 °
45 °
60 °
75 °
90 °

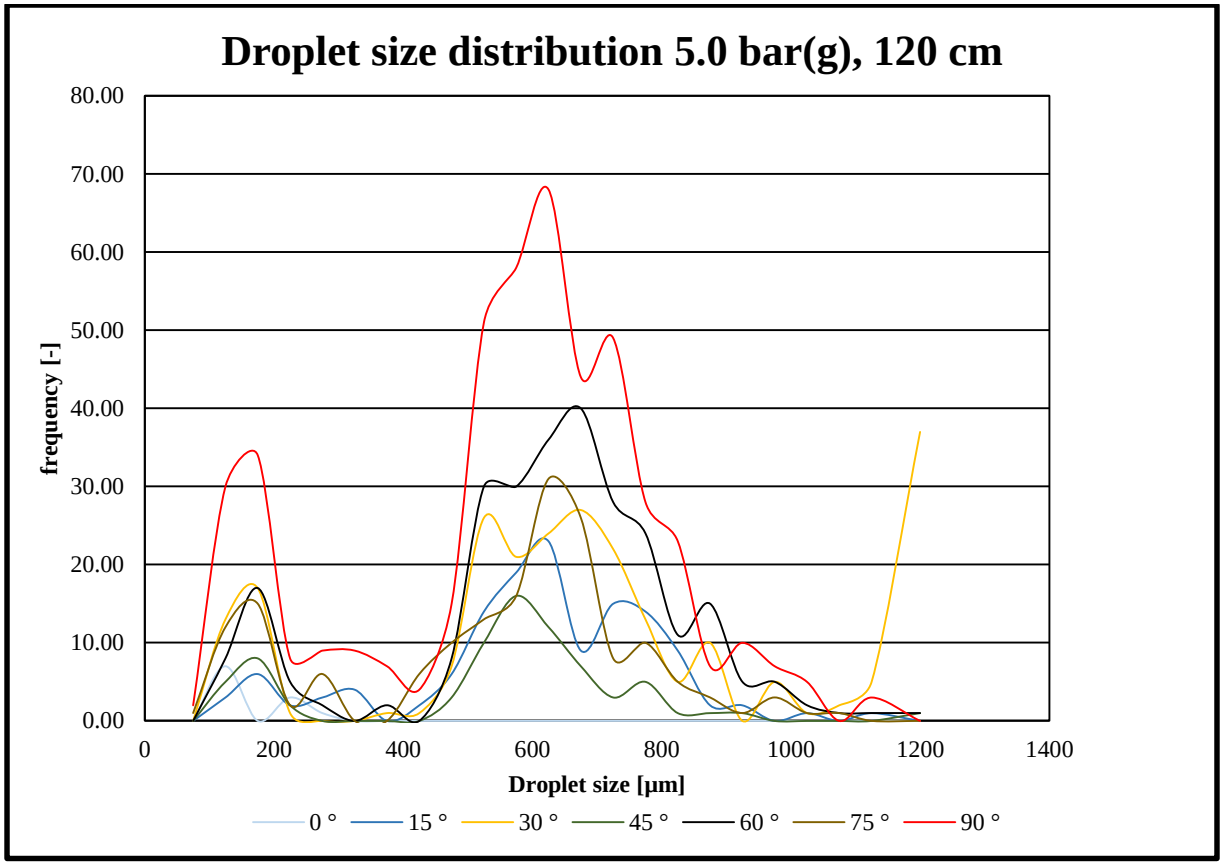
Droplet size distribution 5.0 bar(g), 120 cm
frequency [-]
80.00
70.00
60.00
50.00
40.00
30.00
20.00
10.00
0.00
0
200
400
600
800
1000
1200
1400
Droplet size [µm]
0 °
15 °
30 °
45 °
60 °
75 °
90 °

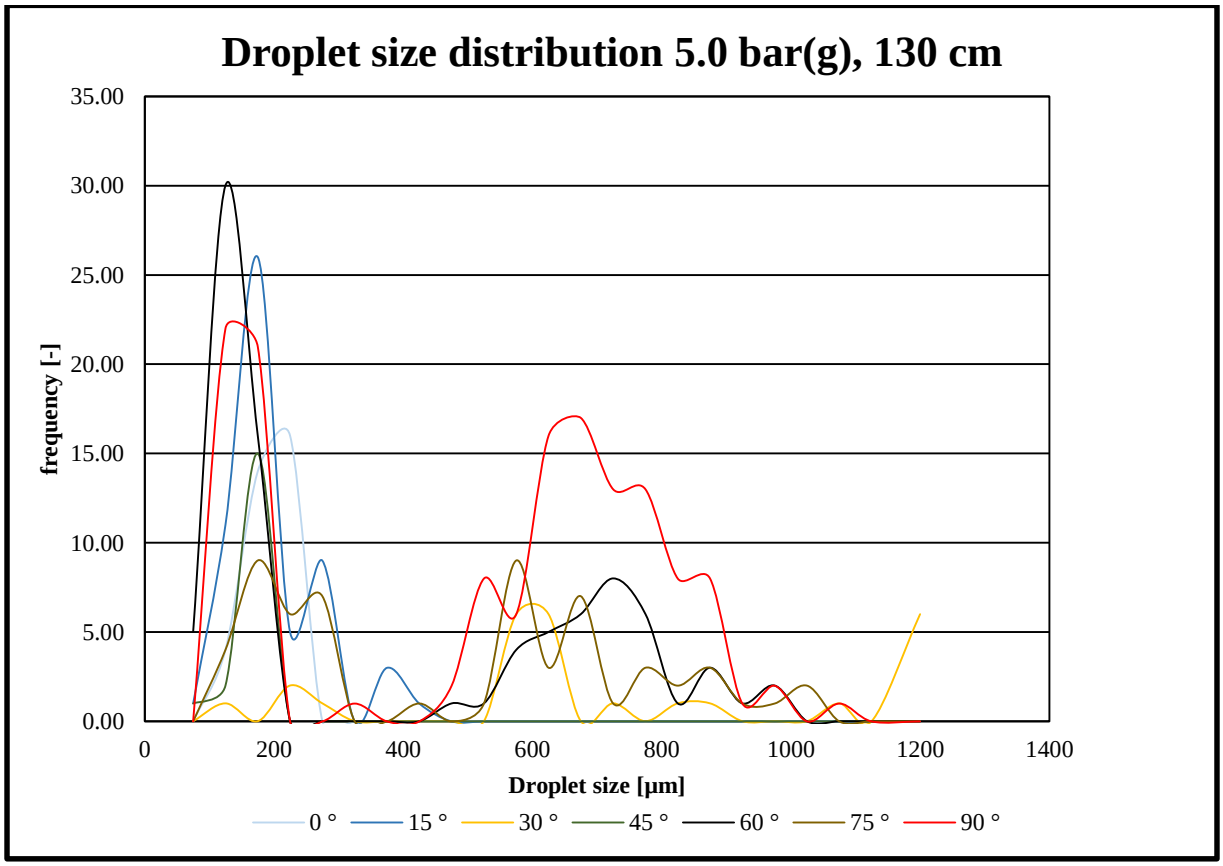
Droplet size distribution 5.0 bar(g), 130 cm
frequency [-]
35.00
30.00
25.00
20.00
15.00
10.00
5.00
0.00
0
200
400
600
800
1000
1200
1400
Droplet size [µm]
0 °
15 °
30 °
45 °
60 °
75 °
90 °

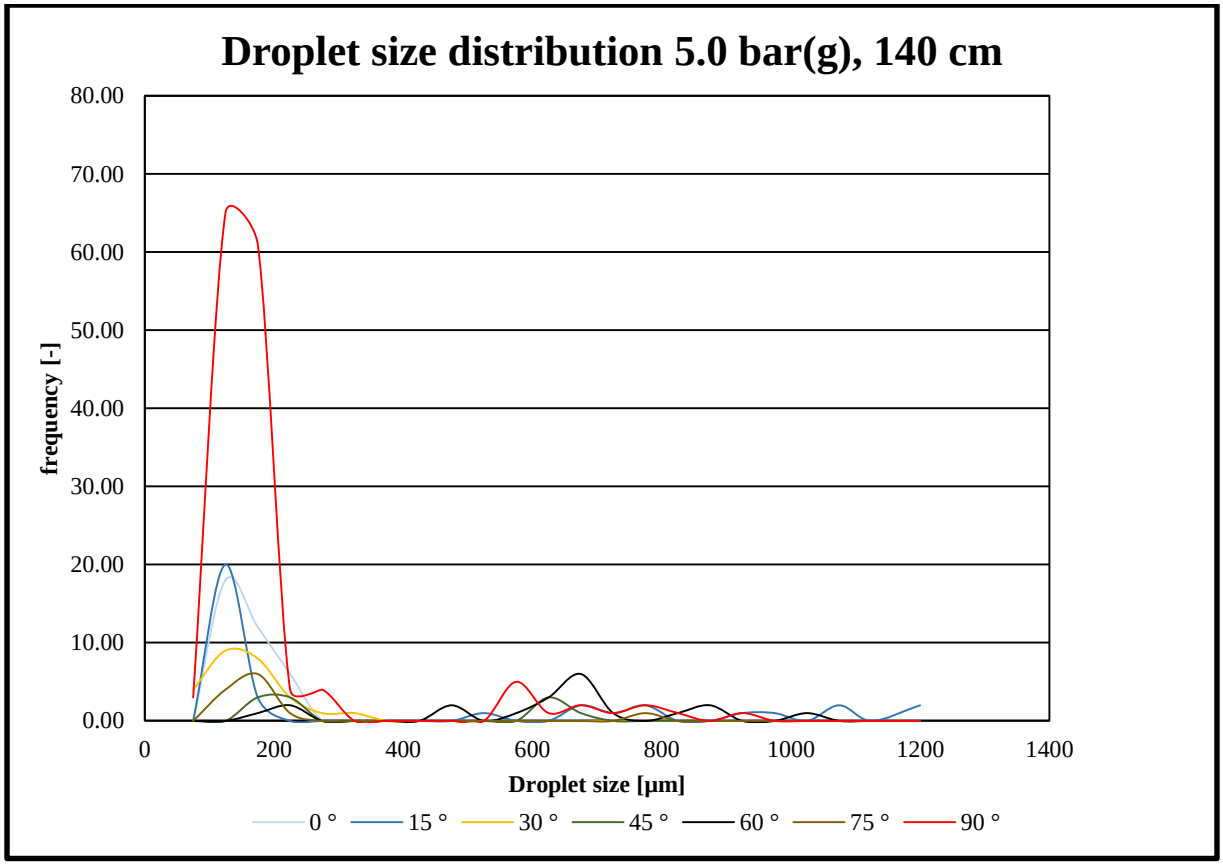
Droplet size distribution 5.0 bar(g), 140 cm
frequency [-]
80.00
70.00
60.00
50.00
40.00
30.00
20.00
10.00
0.00
0
200
400
600
800
1000
1200
1400
Droplet size [µm]
0 °
15 °
30 °
45 °
60 °
75 °
90 °

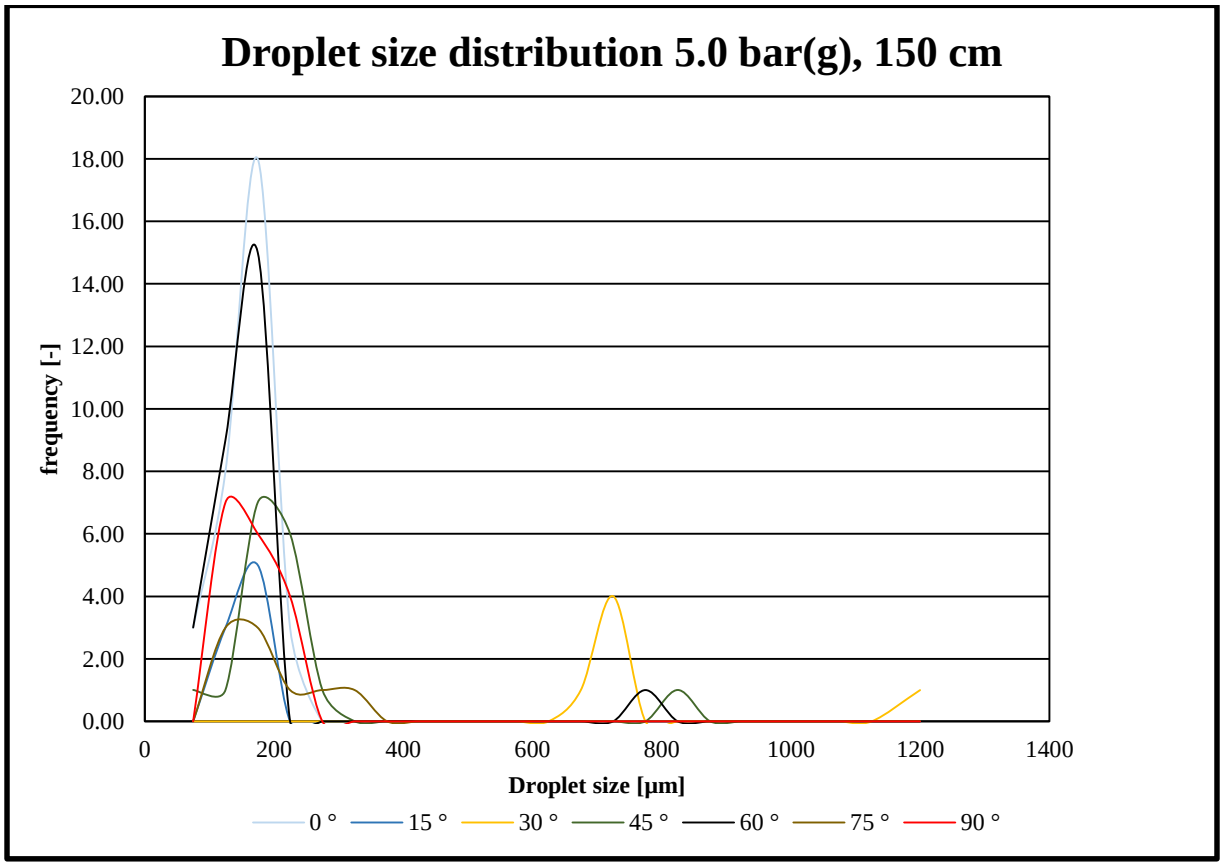
Droplet size distribution 5.0 bar(g), 150 cm
frequency [-]
20.00
18.00
16.00
14.00
12.00
10.00
8.00
6.00
4.00
2.00
0.00
0
200
400
600
800
1000
1200
1400
Droplet size [µm]
0 °
15 °
30 °
45 °
60 °
75 °
90 °

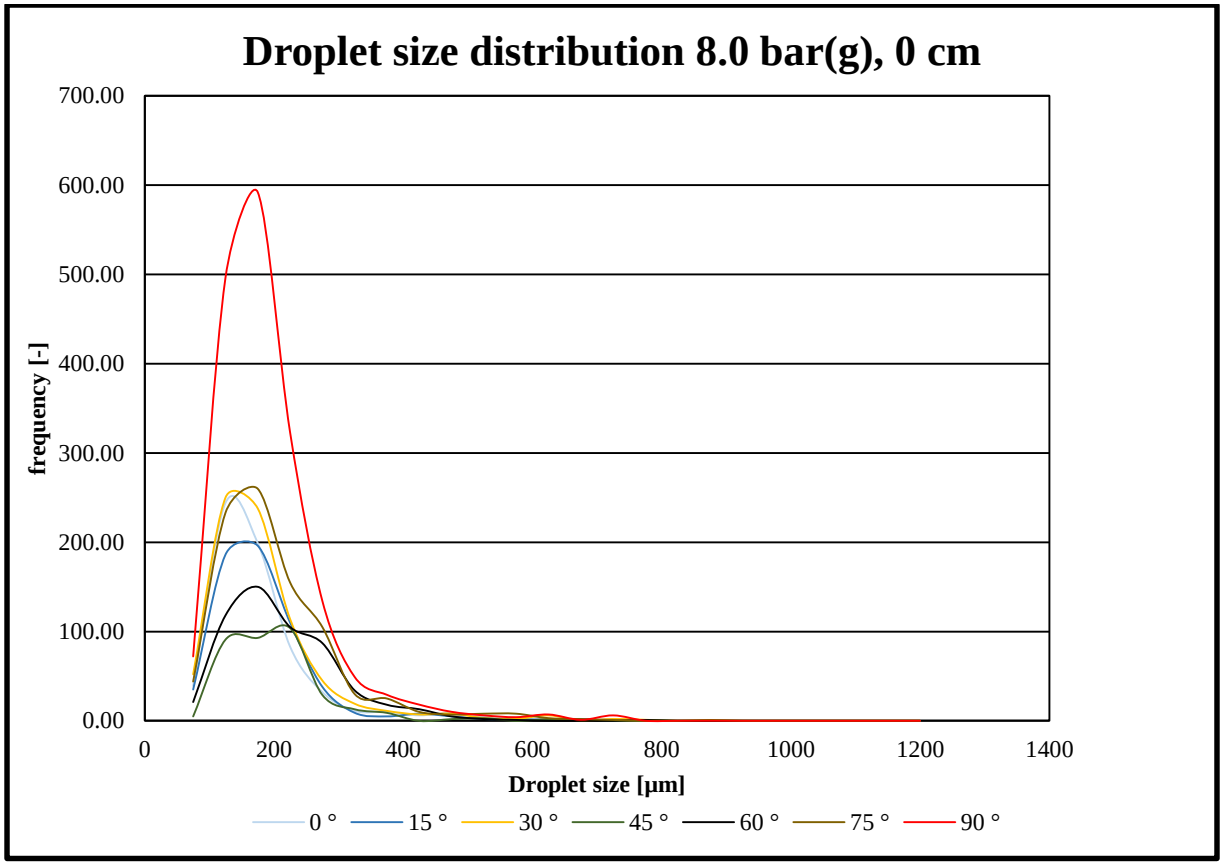
Droplet size distribution 8.0 bar(g), 0 cm
700.00
600.00
500.00
400.00
300.00
200.00
100.00
0.00
frequency [-]
0
200
400
600
800
1000
1200
1400
Droplet size [µm]
0 °
15 °
30 °
45 °
60 °
75 °
90 °

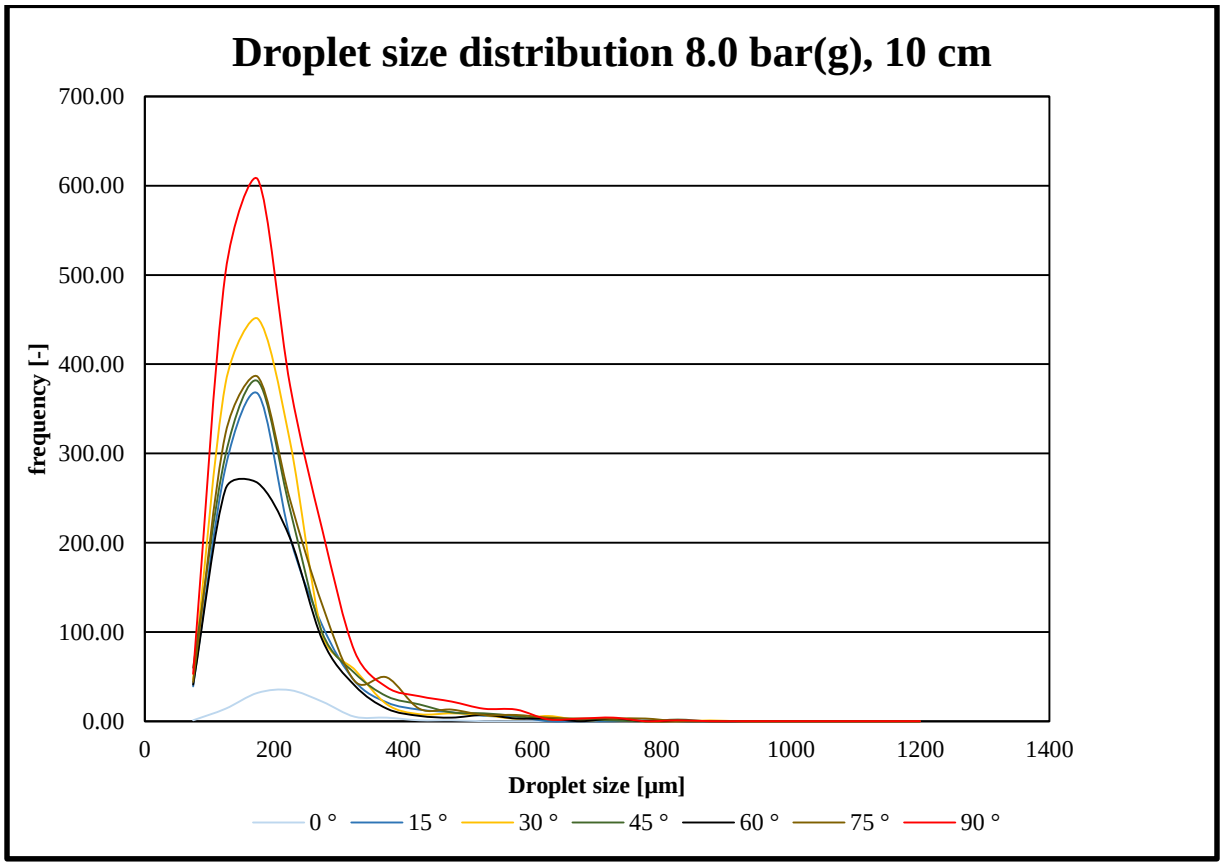
Droplet size distribution 8.0 bar(g), 10 cm
700.00
600.00
500.00
400.00
300.00
200.00
100.00
0.00
frequency [-]
0
200
400
600
800
1000
1200
1400
Droplet size [µm]
0 °
15 °
30 °
45 °
60 °
75 °
90 °

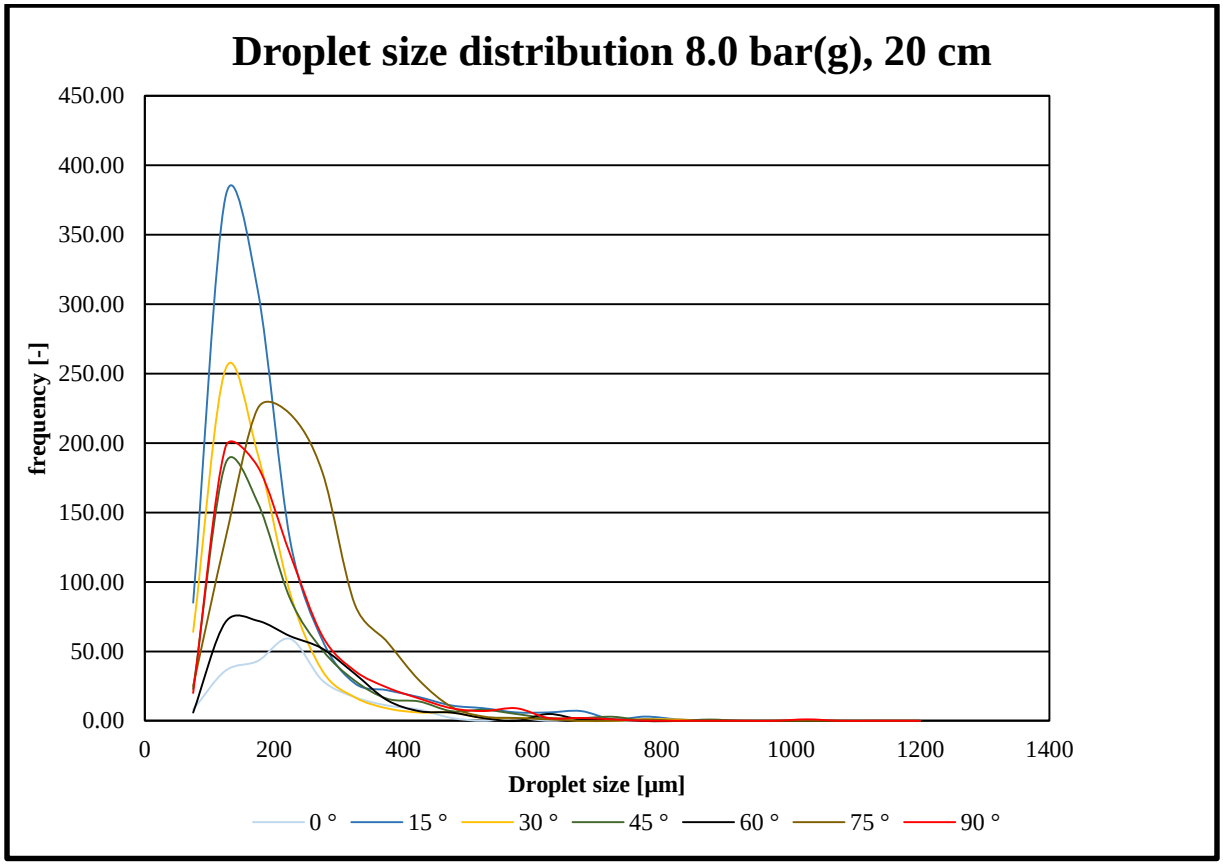
Droplet size distribution 8.0 bar(g), 20 cm
450.00
400.00
350.00
300.00
250.00
200.00
150.00
100.00
50.00
0.00
frequency [-]
0
200
400
600
800
1000
1200
1400
Droplet size [µm]
0 °
15 °
30 °
45 °
60 °
75 °
90 °

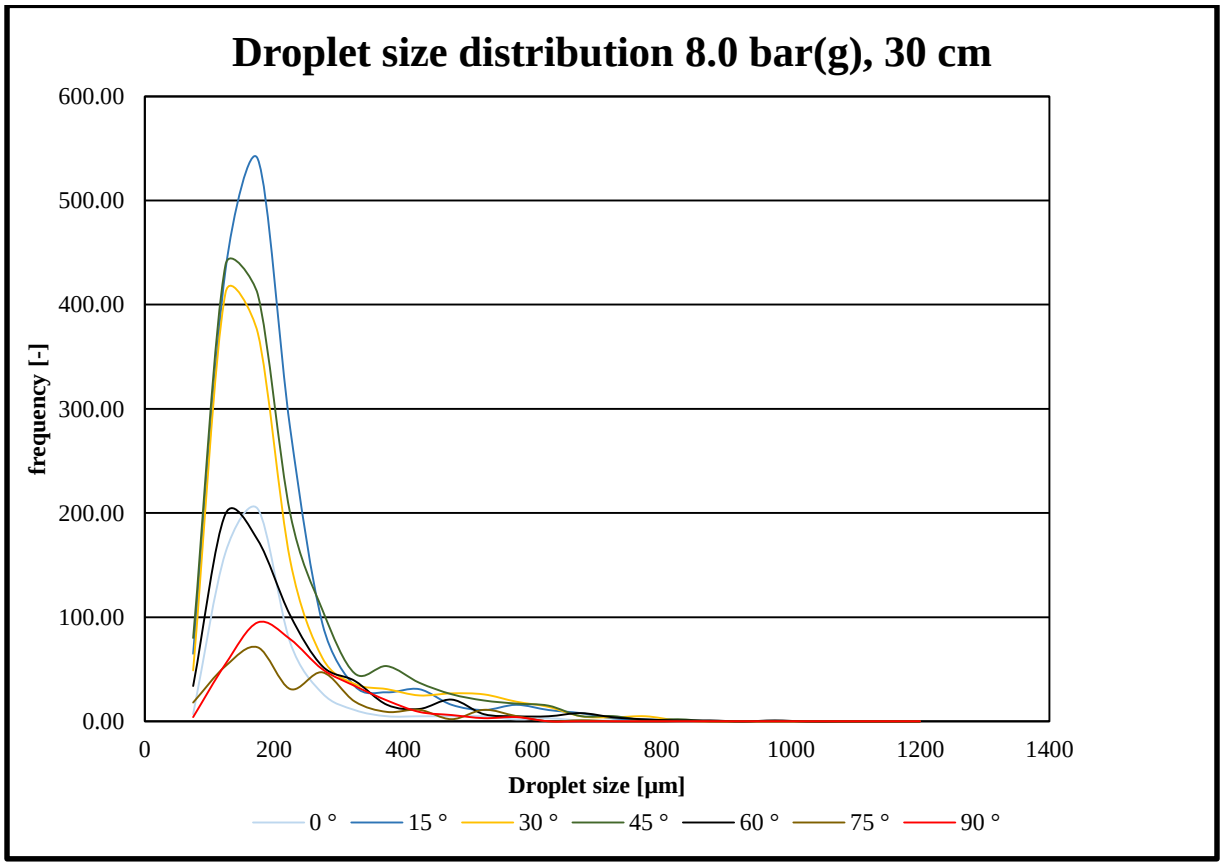
Droplet size distribution 8.0 bar(g), 30 cm
600.00
500.00
400.00
300.00
200.00
100.00
0.00
frequency [-]
0
200
400
600
800
1000
1200
1400
Droplet size [µm]
0 °
15 °
30 °
45 °
60 °
75 °
90 °

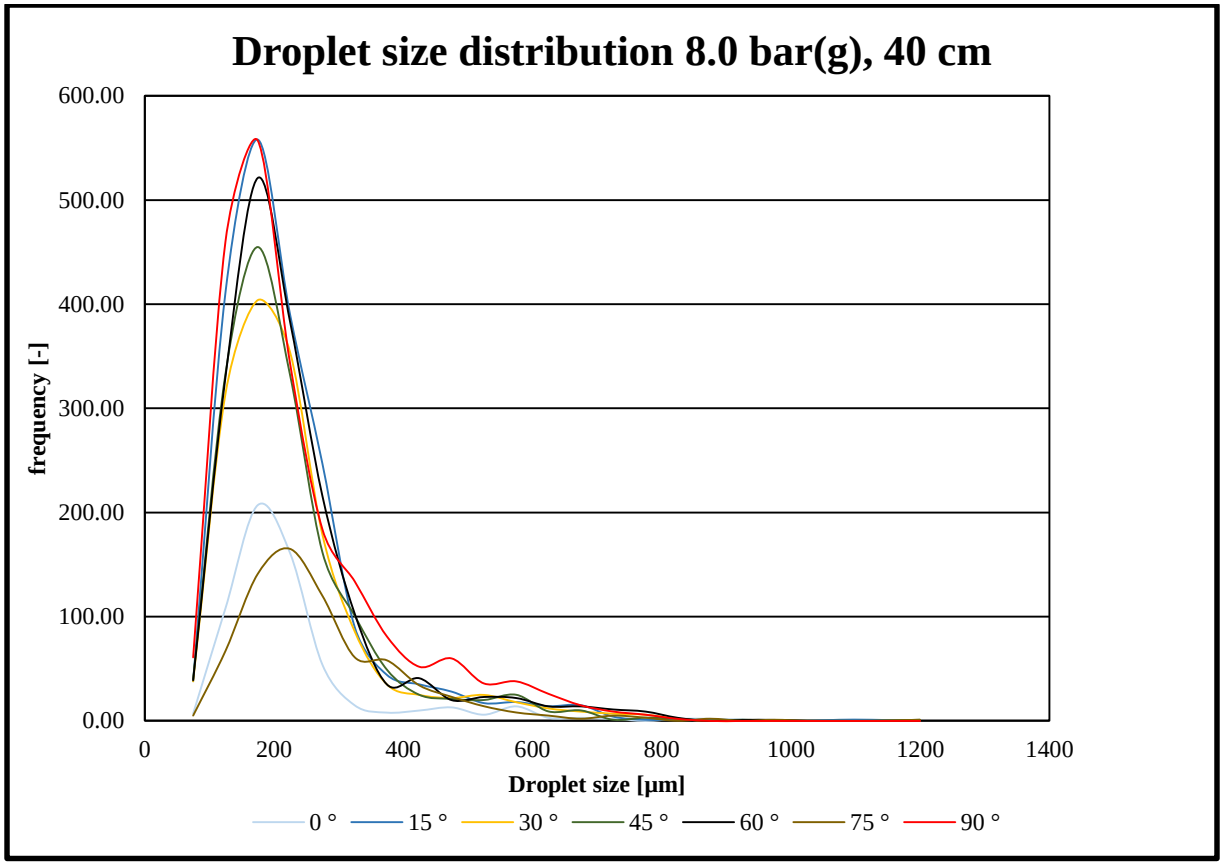
Droplet size distribution 8.0 bar(g), 40 cm
600.00
500.00
400.00
300.00
200.00
100.00
0.00
frequency [-]
0
200
400
600
800
1000
1200
1400
Droplet size [µm]
0 °
15 °
30 °
45 °
60 °
75 °
90 °

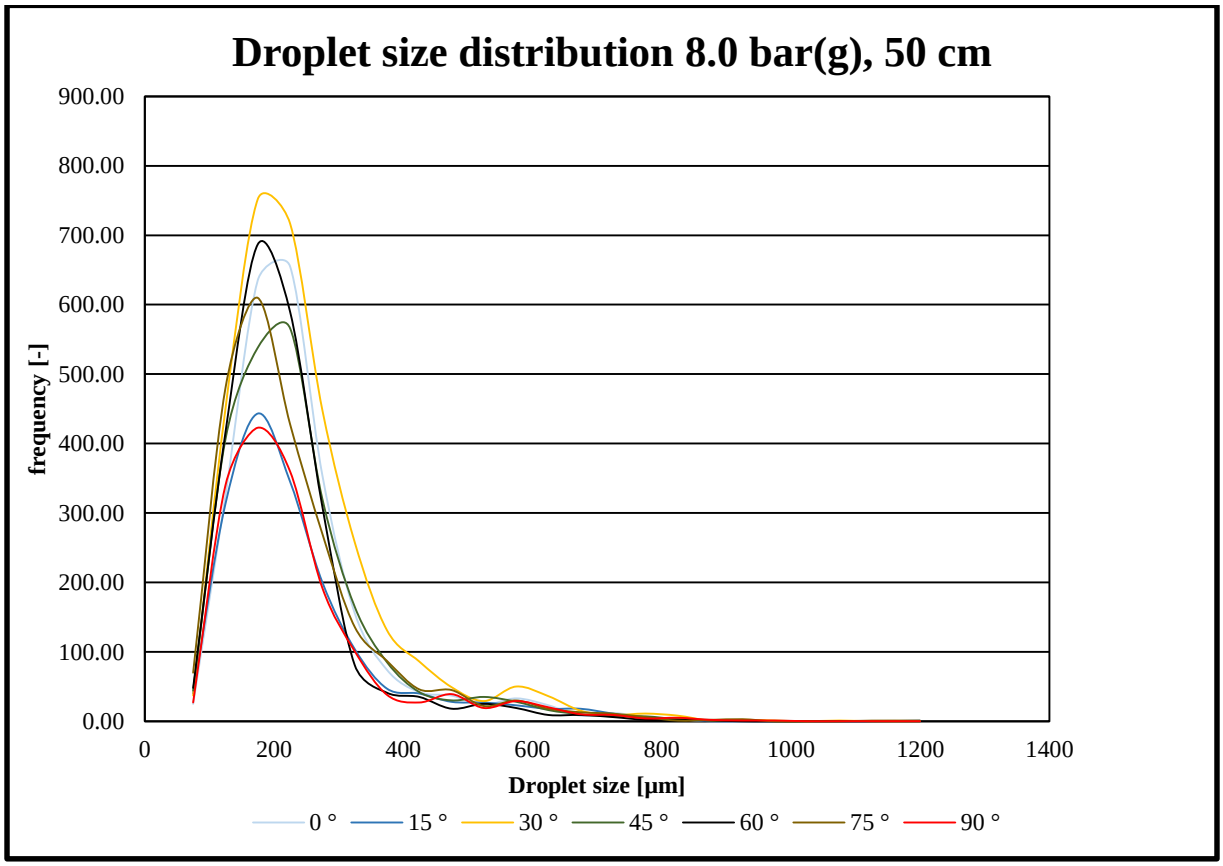
Droplet size distribution 8.0 bar(g), 50 cm
900.00
800.00
700.00
600.00
500.00
400.00
300.00
200.00
100.00
0.00
frequency [-]
0
200
400
600
800
1000
1200
1400
Droplet size [µm]
0 °
15 °
30 °
45 °
60 °
75 °
90 °

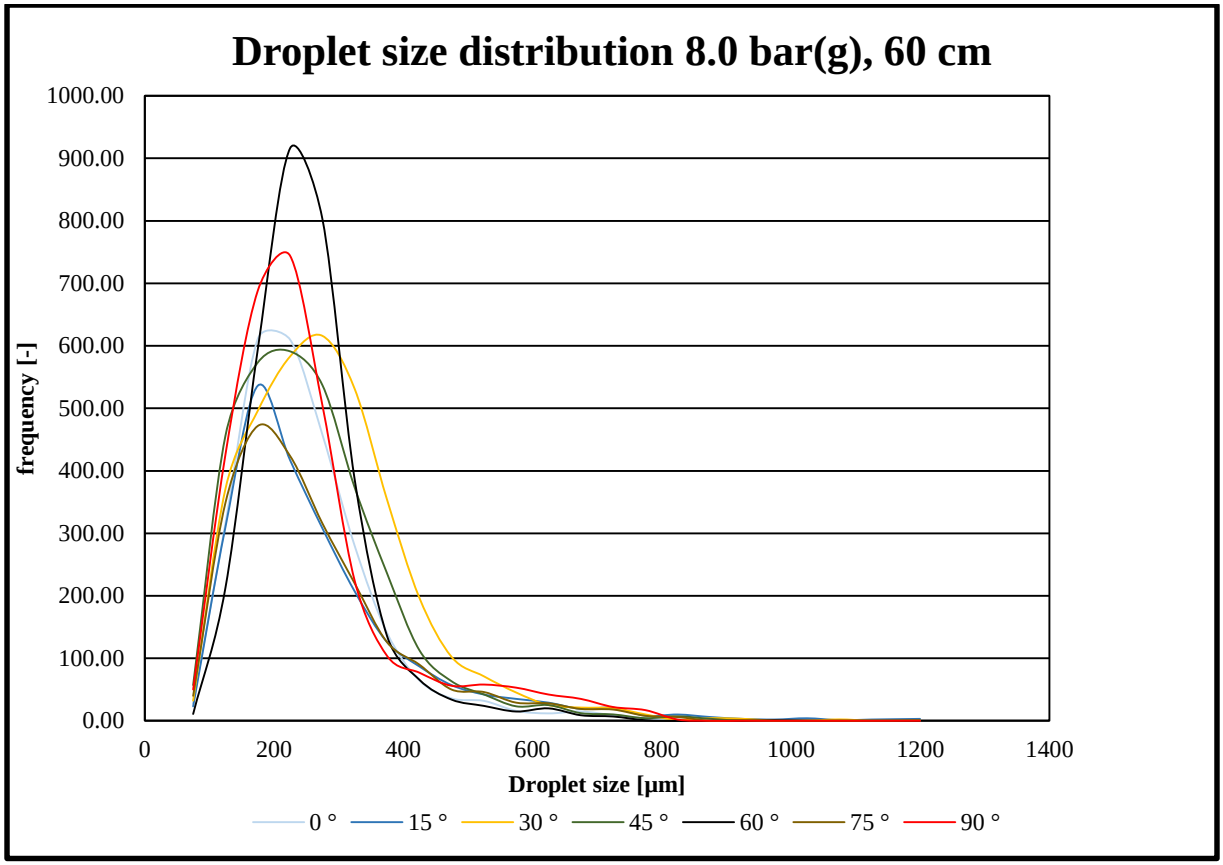
Droplet size distribution 8.0 bar(g), 60 cm
1000.00
900.00
800.00
700.00
600.00
500.00
400.00
300.00
200.00
100.00
0.00
frequency [-]
0
200
400
600
800
1000
1200
1400
Droplet size [µm]
0 °
15 °
30 °
45 °
60 °
75 °
90 °

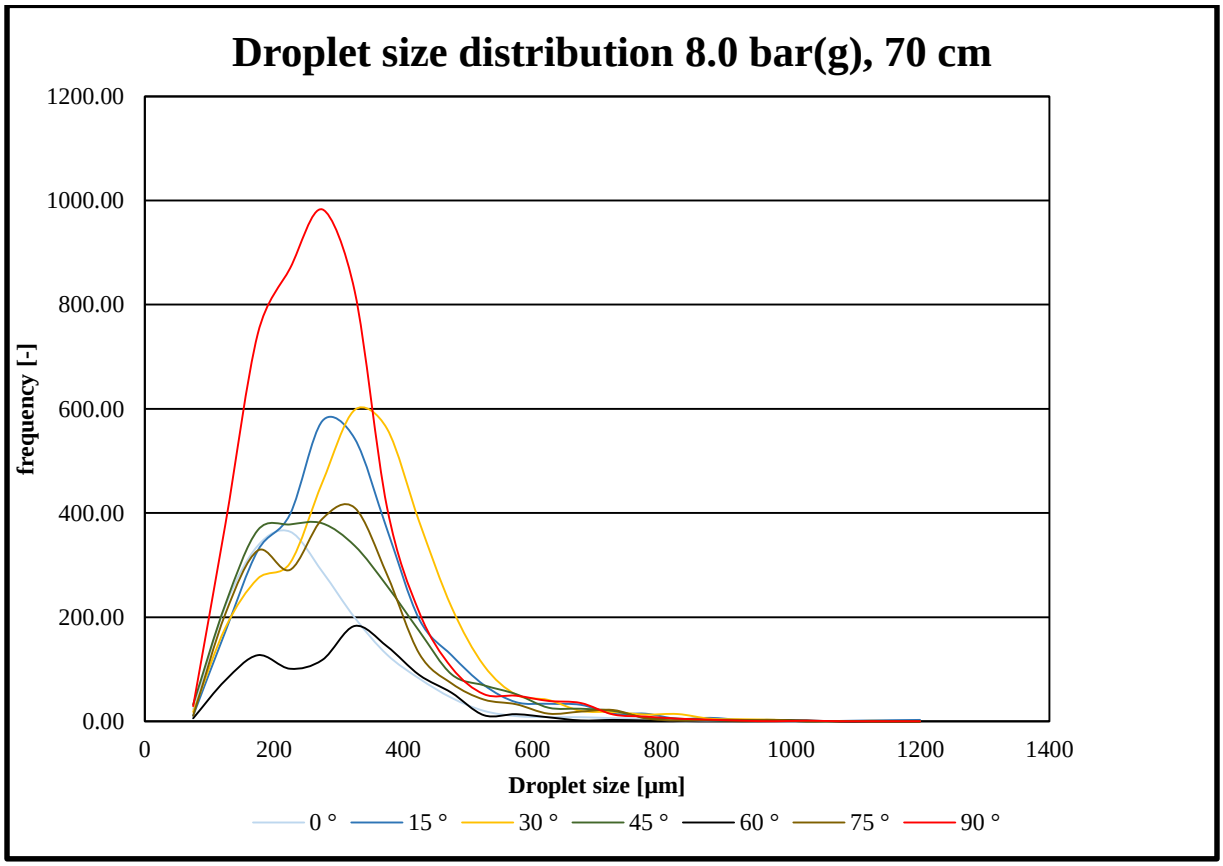
Droplet size distribution 8.0 bar(g), 70 cm
1200.00
1000.00
800.00
600.00
400.00
200.00
0.00
frequency [-]
0
200
400
600
800
1000
1200
1400
Droplet size [µm]
0 °
15 °
30 °
45 °
60 °
75 °
90 °

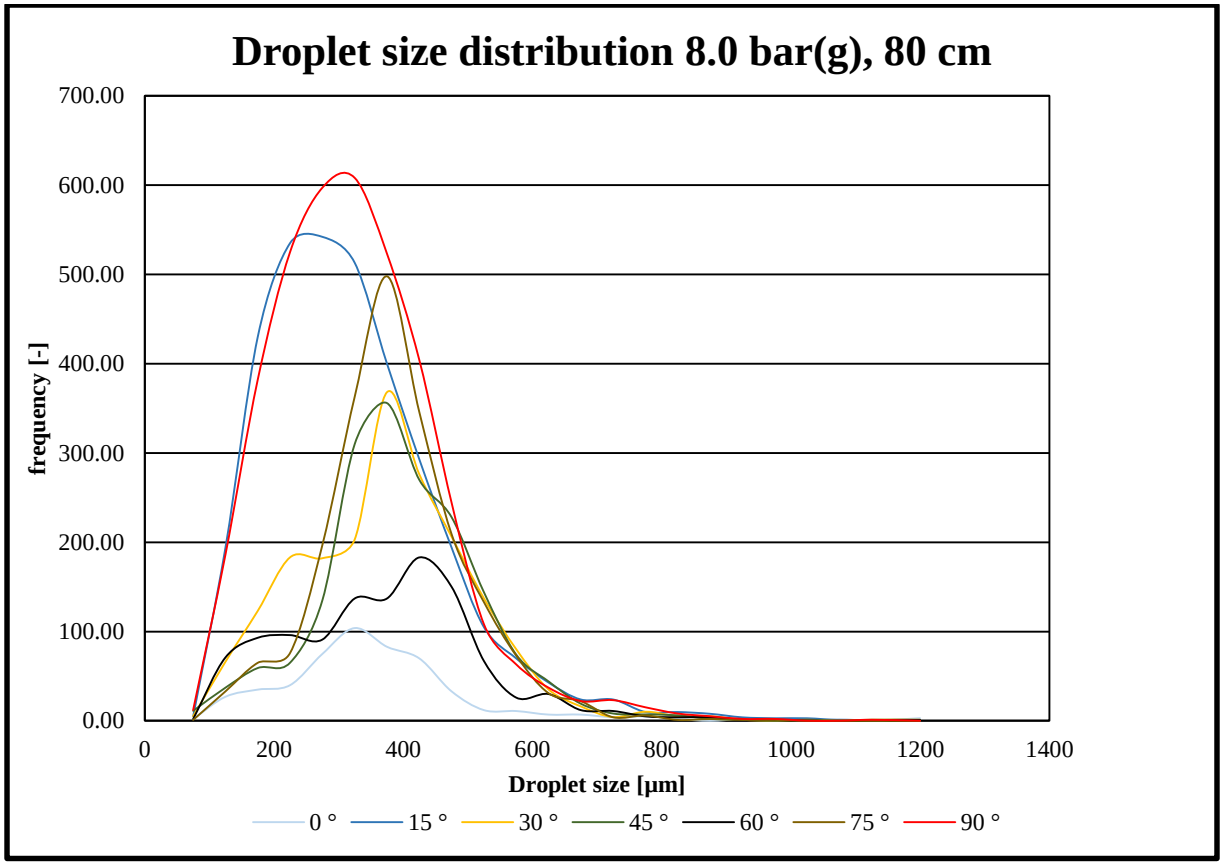
Droplet size distribution 8.0 bar(g), 80 cm
700.00
600.00
500.00
400.00
300.00
200.00
100.00
0.00
frequency [-]
0
200
400
600
800
1000
1200
1400
Droplet size [µm]
0 °
15 °
30 °
45 °
60 °
75 °
90 °

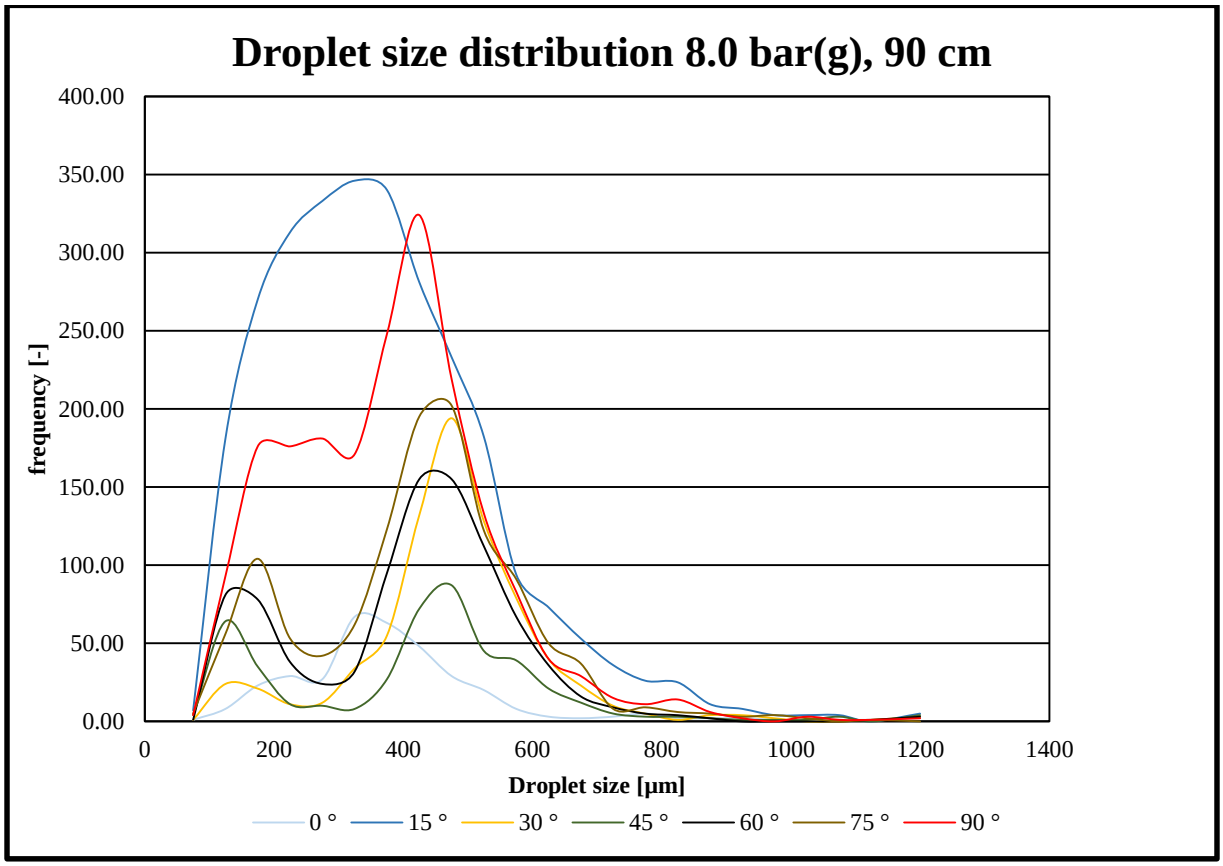
Droplet size distribution 8.0 bar(g), 90 cm
400.00
350.00
300.00
250.00
200.00
150.00
100.00
50.00
0.00
frequency [-]
0
200
400
600
800
1000
1200
1400
Droplet size [µm]
0 °
15 °
30 °
45 °
60 °
75 °
90 °

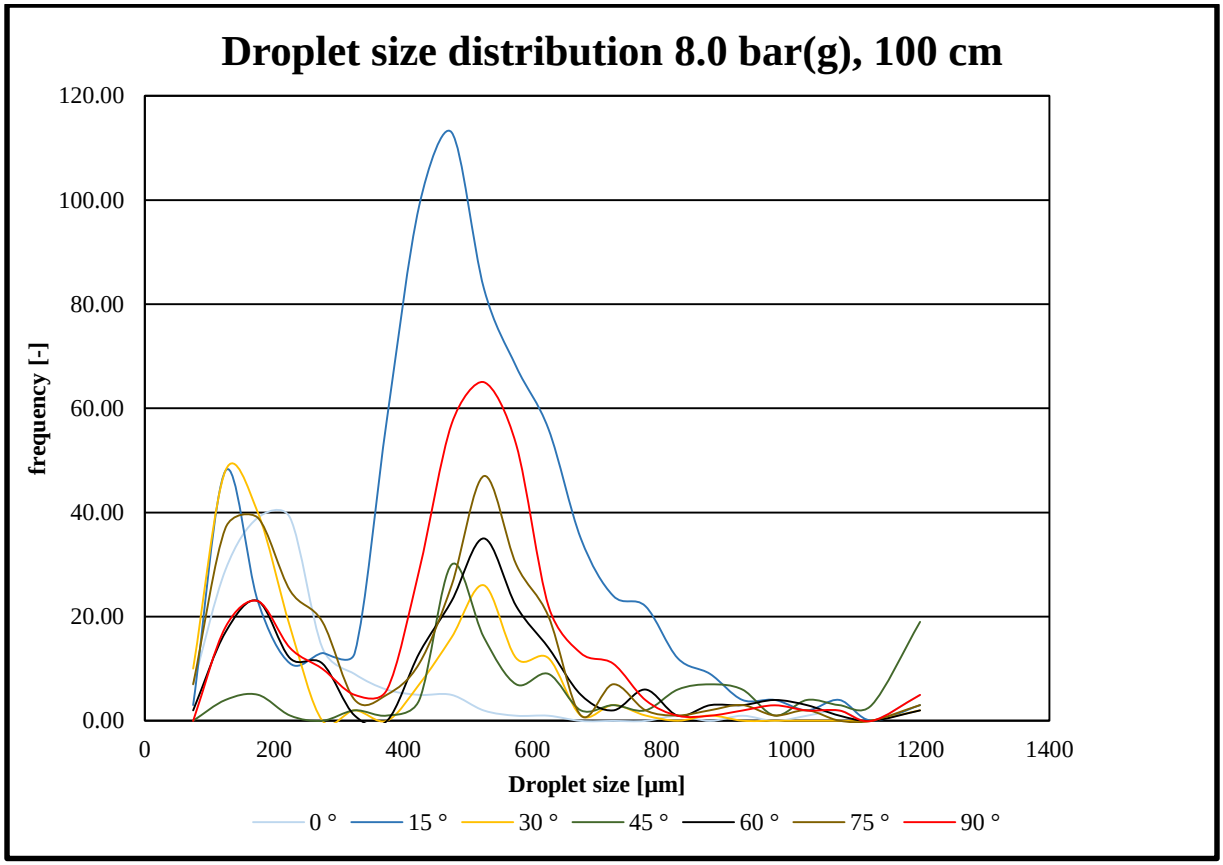
Droplet size distribution 8.0 bar(g), 100 cm
120.00
100.00
80.00
60.00
40.00
20.00
0.00
frequency [-]
0
200
400
600
800
1000
1200
1400
Droplet size [µm]
0 °
15 °
30 °
45 °
60 °
75 °
90 °

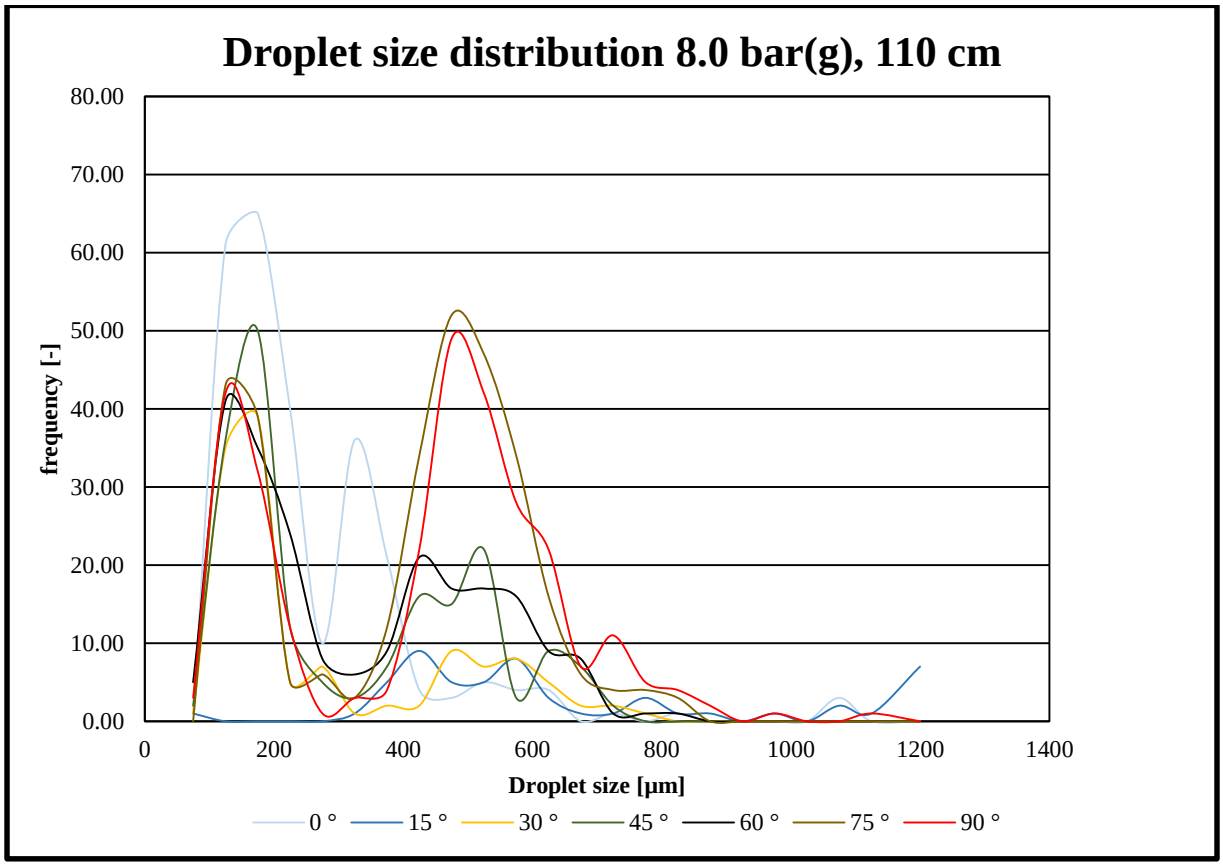
Droplet size distribution 8.0 bar(g), 110 cm
80.00
70.00
60.00
50.00
40.00
30.00
20.00
10.00
0.00
frequency [-]
0
200
400
600
800
1000
1200
1400
Droplet size [µm]
0 °
15 °
30 °
45 °
60 °
75 °
90 °

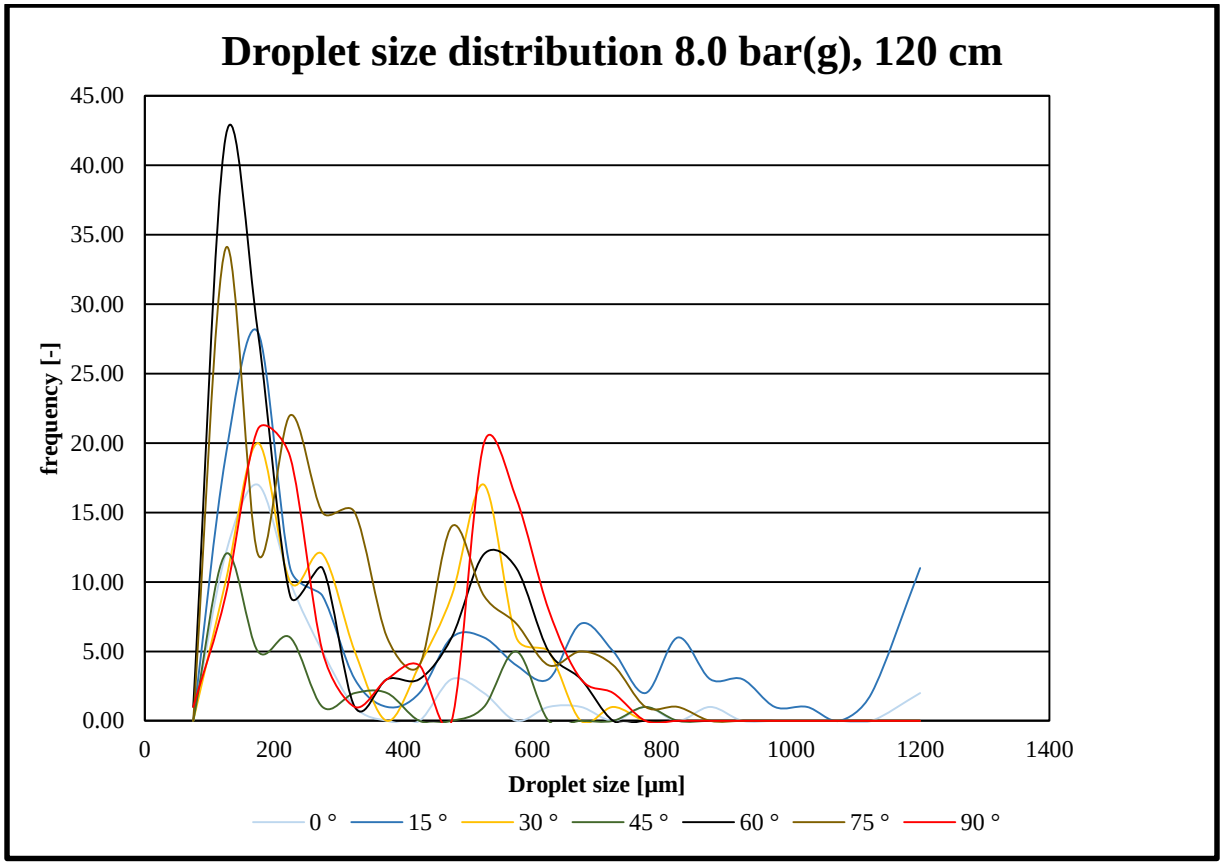
Droplet size distribution 8.0 bar(g), 120 cm
45.00
40.00
35.00
30.00
25.00
20.00
15.00
10.00
5.00
0.00
frequency [-]
0
200
400
600
800
1000
1200
1400
Droplet size [µm]
0 °
15 °
30 °
45 °
60 °
75 °
90 °

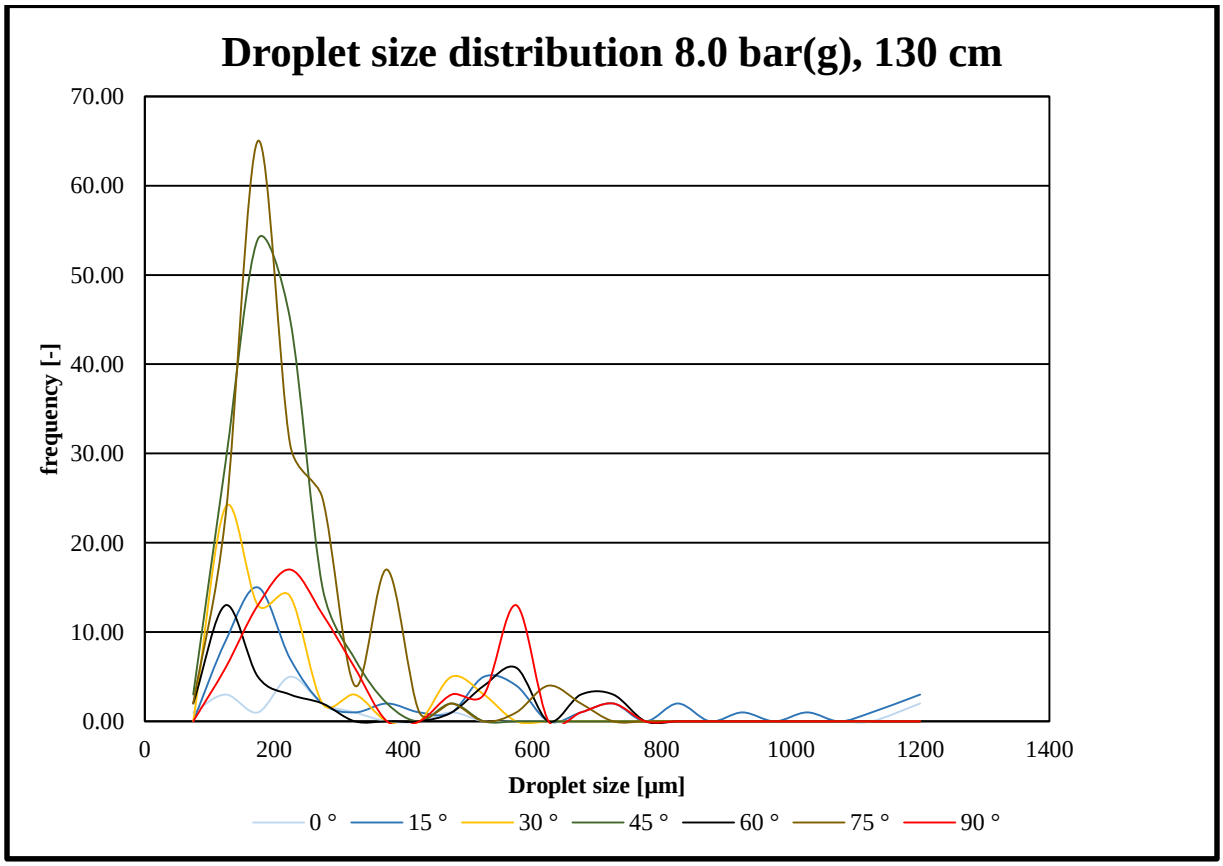
Droplet size distribution 8.0 bar(g), 130 cm
70.00
60.00
50.00
40.00
30.00
20.00
10.00
0.00
frequency [-]
0
200
400
600
800
1000
1200
1400
Droplet size [µm]
0 °
15 °
30 °
45 °
60 °
75 °
90 °

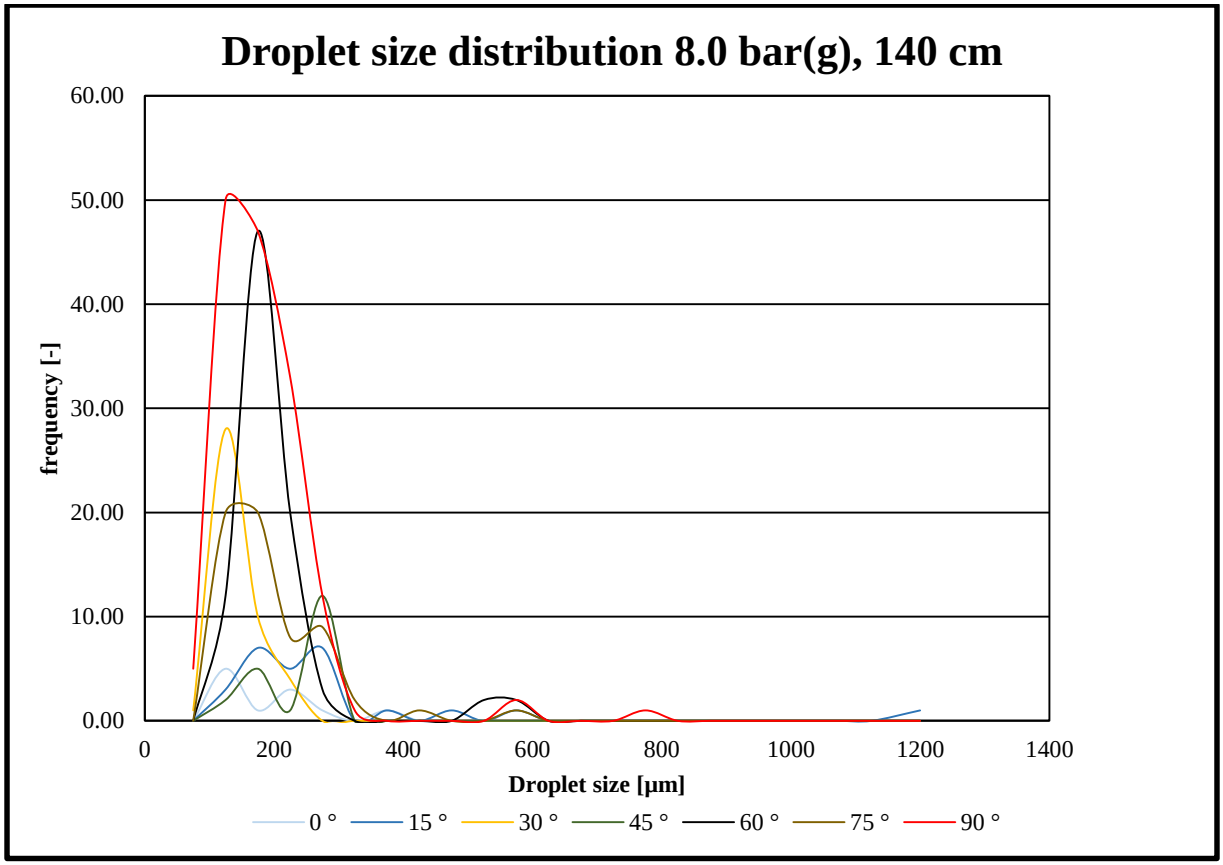
Droplet size distribution 8.0 bar(g), 140 cm
60.00
50.00
40.00
30.00
20.00
10.00
0.00
frequency [-]
0
200
400
600
800
1000
1200
1400
Droplet size [µm]
0 °
15 °
30 °
45 °
60 °
75 °
90 °

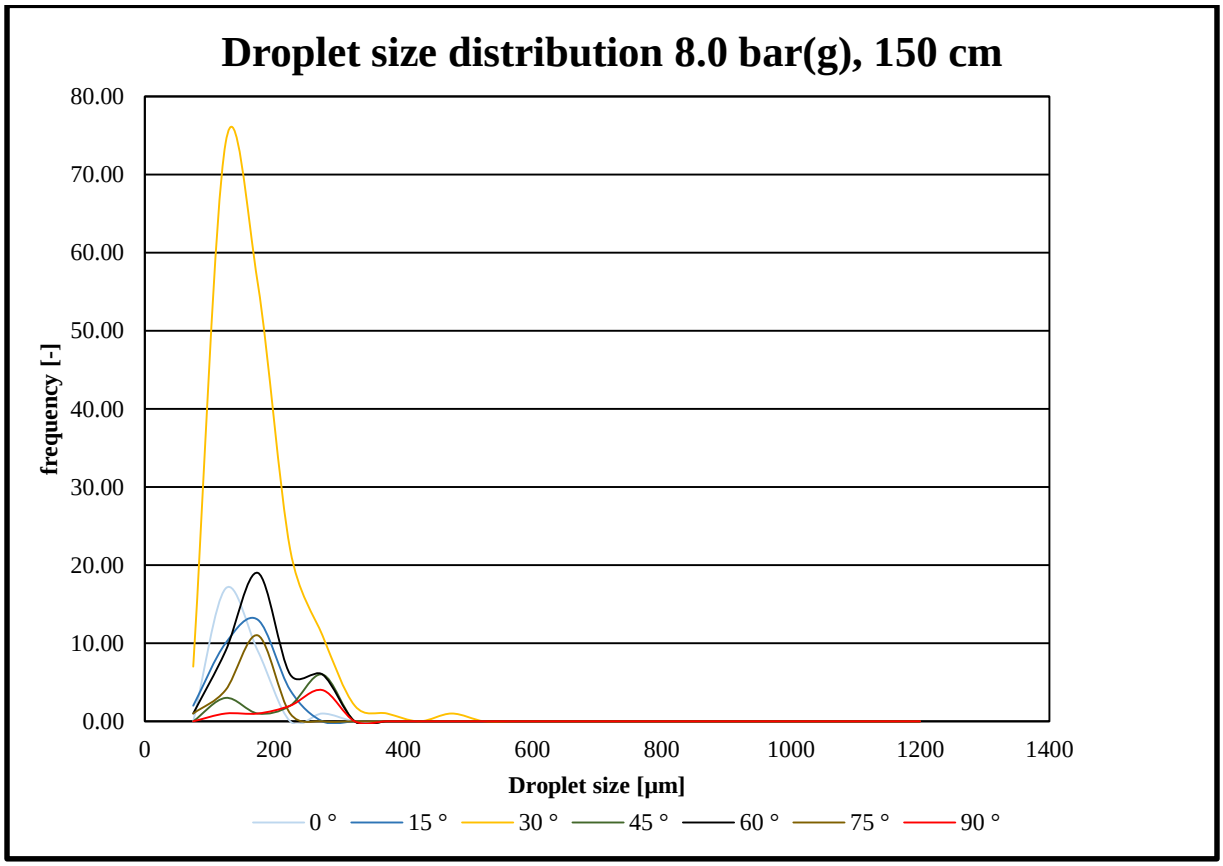
Droplet size distribution 8.0 bar(g), 150 cm
80.00
70.00
60.00
50.00
40.00
30.00
20.00
10.00
0.00
frequency [-]
0
200
400
600
800
1000
1200
1400
Droplet size [µm]
0 °
15 °
30 °
45 °
60 °
75 °
90 °

ISBN 978-82-7206-402-9
ISSN 1893-3068

www.hit.no
2015